Numerical simulation and experimental study of membrane chromatography for biomolecule separation

Chalore Teepakorn

Université Claude Bernard Lyon 1

UNIVERSITÉ DE LYON

N° d'ordre : 299 – 2015

Year: 2015

THESIS

Presented to

UNIVERSITY OF LYON I – CLAUDE BERNARD

In Partial Fulfillment of the Requirements for

THE DEGREE OF DOCTOR OF PHILOSOPHY

GRADUATE SCHOOL OF CHEMISTRY AT UNIVERSITY OF LYON

IN BIOPROCESS-PROCESS ENGINEERING

NUMERICAL SIMULATION AND EXPERIMENTAL STUDY OF MEMBRANE CHROMATOGRAPHY FOR BIOMOLECULE SEPARATION

Presented on 16/12/2015

By

Chalore Teepakorn

Supervisors:

Dr Catherine Charcosset	Directrice de recherche, CNRS, Lyon
Dr Koffi Fiaty	Maître de conférences, Université Lyon I, Lyon

Jury:

Pr Xavier Santarelli	Professeur, Université de Bordeaux, Bordeaux
Dr Marie-Pierre Belleville	Maître de conférences, Université de Montpellier, Montpellier
Pr François Puel	Professeur, Université Paris Saclay, Paris
Dr Denis Grenier	Ingénieur de recherche, CNRS, Lyon
Dr Catherine Charcosset	Directrice de recherche, CNRS, Lyon
Dr Koffi Fiaty	Maître de conférences, Université Lyon I, Lyon

(This page is intentionally left blank)

Université Claude Bernard Lyon 1

UNIVERSITÉ DE LYON

N° d'ordre : 299 - 2015

Année : 2015

THESE

Présentée à

L'UNIVERSITE CLAUDE BERNARD LYON 1

Pour l'obtention du

DIPLÔME DE DOCTORAT

(arrêté du 7 août 2006)

ECOLE DOCTORALE DE CHIMIE DE L'UNIVERSITE DE LYON

SPECIALITE : GENIE DES BIOPROCEDES-PROCEDES

SIMULATION NUMERIQUE ET ETUDE EXPERIMENTALE DE LA CHROMATOGRAPHIE MEMBRANAIRE POUR LA SEPARATION DE BIOMOLECULES

Présentée et soutenue publiquement le 16/12/2015

Par

Chalore Teepakorn

Directeurs de thèse:

Dr Catherine Charcosset	Directrice de recherche, CNRS, Lyon
Dr Koffi Fiaty	Maître de conférences, Université Lyon I, Lyon

Membres du jury :

Pr Xavier Santarelli	Professeur, Université de Bordeaux, Bordeaux	(Rapporteur)
Dr Marie-Pierre Belleville	Maître de conférences, Université de Montpellier, Montpellier	(Rapporteur)
Pr François Puel	Professeur, Université Paris Saclay, Paris	(Examinateur)
Dr Denis Grenier	Ingénieur de recherche, CNRS, Lyon	(Examinateur)
Dr Catherine Charcosset	Directrice de recherche, CNRS, Lyon	(Examinateur)
Dr Koffi Fiaty	Maître de conférences, Université Lyon I, Lyon	(Examinateur)

(This page is intentionally left blank)

UNIVERSITE CLAUDE BERNARD - LYON 1

Président de l'Université	**M. François-Noël GILLY**
Vice-président du Conseil d'Administration	M. le Professeur Hamda BEN HADID
Vice-président du Conseil des Etudes et de la Vie Universitaire	M. le Professeur Philippe LALLE
Vice-président du Conseil Scientifique	M. le Professeur Germain GILLET
Directeur Général des Services	M. Alain HELLEU

COMPOSANTES SANTE

Faculté de Médecine Lyon Est – Claude Bernard	Directeur : M. le Professeur J. ETIENNE
Faculté de Médecine et de Maïeutique Lyon Sud – Charles Mérieux	Directeur : Mme la Professeure C. BURILLON
Faculté d'Odontologie	Directeur : M. le Professeur D. BOURGEOIS
Institut des Sciences Pharmaceutiques et Biologiques	Directeur : Mme la Professeure C. VINCIGUERRA
Institut des Sciences et Techniques de la Réadaptation	Directeur : M. le Professeur Y. MATILLON
Département de formation et Centre de Recherche en Biologie Humaine	Directeur : Mme. la Professeure A-M. SCHOTT

COMPOSANTES ET DEPARTEMENTS DE SCIENCES ET TECHNOLOGIE

Faculté des Sciences et Technologies	Directeur : M. F. DE MARCHI
Département Biologie	Directeur : M. le Professeur F. FLEURY
Département Chimie Biochimie	Directeur : Mme Caroline FELIX
Département GEP	Directeur : M. Hassan HAMMOURI
Département Informatique	Directeur : M. le Professeur S. AKKOUCHE
Département Mathématiques	Directeur : M. le Professeur Georges TOMANOV
Département Mécanique	Directeur : M. le Professeur H. BEN HADID
Département Physique	Directeur : M. Jean-Claude PLENET
UFR Sciences et Techniques des Activités Physiques et Sportives	Directeur : M. Y.VANPOULLE
Observatoire des Sciences de l'Univers de Lyon	Directeur : M. B. GUIDERDONI
Polytech Lyon	Directeur : M. P. FOURNIER
Ecole Supérieure de Chimie Physique Electronique	Directeur : M. G. PIGNAULT
Institut Universitaire de Technologie de Lyon 1	Directeur : M. le Professeur C. VITON
Ecole Supérieure du Professorat et de l'Education	Directeur : M. le Professeur A. MOUGNIOTTE
Institut de Science Financière et d'Assurances	Directeur : M. N. LEBOISNE

(This page is intentionally left blank)

Résumé

La chromatographie membranaire est une alternative à la chromatographie classique sur résine basée sur le transport convectif des solutés à travers une membrane microporeuse plutôt que par le transport diffusif des solutés dans les particules de résines. Cette technique présente les avantages de diminuer les phénomènes de diffusion, de réduire les temps de séjour et les pertes de charge, et de permettre la purification rapide de quantités importantes de molécules. La chromatographie membranaire connaît un fort succès commercial. Une gamme importante de membranes chromatographiques mettant en jeu différents mécanismes de rétention (échange d'ions, affinité, etc.) et différentes géométries (feuille, spirale, etc.) est actuellement commercialisée. Malgré ce succès, différents aspects relatifs à la chromatographie membranaire restent mal connus. Cette thèse de doctorat se propose de répondre à certaines questions relatives à cette technique.

Dans une première partie, l'adsorption de l'albumine sérique bovine (BSA) sur une membrane chromatographique échangeuse d'ion est étudiée expérimentalement pour déterminer l'influence des conditions opératoires (débit de circulation, concentration initiale) sur la courbe de perçage. Deux types de géométries différentes (module plan ou module en spiral) ont été utilisés et ont permis de mettre en évidence l'influence du type d'écoulement (axial ou radial) sur la séparation ainsi que l'influence des paramètres géométriques des modules (épaisseur de la membrane, diamètre des modules). Afin de comprendre les phénomènes observés, de prédire les performances des différents modules et de mettre au point un outil destiné à l'amélioration de la conception des capsules de chromatographie membranaire, un modèle mathématique de CFD a été développé, basé sur les équations de Navier-Stokes, de convection-diffusion des solutés, couplé à une isotherme d'adsorption de Langmuir ou bi-Langmuir. Les courbes de perçage ainsi calculées et mesurées expérimentalement sont comparées, une bonne adéquation entre les valeurs expérimentales et calculées est observée pour une large gamme de paramètres opératoires.

Dans une deuxième partie, la chromatographie membranaire a été appliquée à la séparation d'un mélange de deux protéines de taille moléculaire voisine : le BSA et la lactoferrine (LF). La lactoferrine est une protéine présente dans le lait avec de nombreuses applications dans les domaines agroalimentaire et médical. L'objectif de cette étude est d'optimiser l'efficacité de la séparation en termes de capacité d'adsorption, sélectivité, temps nécessaire à la séparation et rendement en protéine purifiée. L'influence de différents paramètres expérimentaux (pH, force ionique, débit de circulation et concentration initiale) est étudiée afin d'augmenter la capacité d'adsorption et diminuer la durée du procédé. L'influence des conditions d'élution est testée pour différents débits de circulation et différents effets d'élution (augmentation de la force ionique, ajustement de pH) afin d'améliorer le rendement en protéine purifiée. Les résultats confirment que la chromatographie membranaire est une technique rapide qui permet d'obtenir un rendement en protéine purifiée élevé.

La troisième partie de cette thèse de doctorat porte sur la comparaison entre les chromatographies membranaire et monolithique, deux techniques alternatives à la chromatographie sur résine échangeuse d'ions. Les deux supports microporeux, membrane et monolithe, ont des caractéristiques similaires avec un transport de solutés principalement convectif. La comparaison des deux supports est très peu étudiée dans la littérature. Afin de combler cette lacune, la séparation d'un mélange BSA-LF a été étudiée pour les deux supports

placés dans un même module. Pour caractériser théoriquement la fixation de la LF par les supports, le modèle de CFD a été appliqué. L'ensemble des résultats montre qu'une distribution homogène du fluide d'alimentation dans le module chromatographique, ainsi que la conception de module, sont des points clés pour améliorer l'efficacité de la séparation chromatographique.

Dans une dernière partie, afin de vérifier la précision des résultats de CFD, l'imagerie par résonance magnétique (IRM) a été mise en œuvre pour caractériser la géométrie de deux types de modules chromatographiques (axial et radial) ainsi que la mesure du champ de vitesse dans ces deux types de modules. Le profil de vitesse du fluide dans le module membranaire calculé par CFD a été comparé avec le champ de vitesse obtenu expérimentalement par IRM. Les deux approches permettent d'obtenir des résultats similaires, ce qui nous permet de conclure à la fiabilité du modèle CFD pour le calcul des champs de vitesse, et de discuter de l'optimisation des modules chromatographiques.

Mots-clés:

Chromatographie membranaire, Echange d'ions, Courbe de perçage, Capacité d'adsorption, Chromatographie à flux axial, Chromatographie à flux radial.

Abstract

Membrane chromatography (MC) is an alternative to traditional resin packed columns chromatography. The solute mass transport in the membrane occurs in convective through-pores rather than in stagnant fluid inside the pores of the resins particles, which is limited by the slow diffusive transport. MC offers the main advantage of reducing diffusion phenomena, shorter residence time and lowered pressures drops, and thus, facilitates rapid purification of large quantities of molecules. A wide range of chromatographic membranes involving different molecules retention mechanisms (ion exchange, affinity, etc...) is now commercialized. Despite their success, the influence of the geometry of the membrane chromatography devices remains relatively unexplored from a theoretical point of view. This doctoral thesis is aimed to clarify some ambiguous points related to this technique.

At the first step, the adsorption of bovine serum albumin (BSA) was experimentally investigated using the ion exchange MC in order to evaluate the influence of the different operating conditions (fluid flow rate, initial concentrations) on the breakthrough curves. Two types of geometries (stack sheet and spiral wound module) were used and helped to highlight the influence of the type of flow (axial or radial flow) on separation, and thus the geometric parameters of the MC devices (bed height of membrane stack, diameter of module). Furthermore, a mathematical model of CFD was developed, based on the Navier-Stokes equations, convection-diffusion solute mass transport, and coupled binding kinetics models like Langmuir or bi-Langmuir isotherm adsorption. This CFD model could help to understand the solute mass transport phenomena, to predict the performance of different module and to obtain a simulation tool to improve the MC device design. The experimental and predicted breakthrough curves were compared, the results showed a good prediction of the experimental data using the CFD model at the different MC device scales and operating conditions.

In the second part, MC was used for the separation of a binary protein mixture with similar size as BSA and lactoferrin (LF). LF is a minor protein found in milk with several nutritional and medical applications. This study is intended to optimize the efficiency of the BSA-LF mixture separation, evaluating the protein binding capacity, selectivity, process time and yield of separated protein. The influence of the different experimental parameters (pH, ionic force, flow rate, and initial concentration of protein) was studied, resulting in the increase in protein binding capacity and the shortening process duration. Different eluents were tested at different flow rates using different elution effect (increasing ionic force, pH shift), which improved yield of eluted protein mass. The results confirmed that MC can increase protein productivity with high purity.

The third part of this thesis describes the comparison between membrane and monolith chromatography, which are two alternatives supports instead of the traditional ion exchange resins. These two microporous supports, membrane and monolith have similar characteristics with solute mass transport dominated by convection. In the literature, the comparison between these two supports has been very few studied. In order to fulfill this gap, the separation of the BSA-LF mixture was carried out using the membrane and monolith supports placed in the same housing. The CFD model was established for prediction of the protein adsorption on the supports. Overall, the results pointed out that the uniform flow distribution inside the chromatographic device, and thus the housing design played an important role to improve the

performance of the chromatographic separation.

In the last study, magnetic resonance imaging (MRI) was applied to visualize the internal geometry of the two types MC devices (axial and radial), and then to measure the velocity field inside these devices. The calculated velocity profile inside the MC device was compared with the experimental results obtained from the MRI measurements. These two methods gave similar results; which confirms the accuracy of the CFD model for the prediction of the velocity field, while the chromatographic device optimization was discussed.

Keywords:

Membrane chromatography, Ion exchange, Breakthrough curve, Dynamic binding capacity, Axial flow chromatography, Radial flow chromatography

Abbreviations

BV	: Bed Volume
BSA	: Bovine Serum Albumin
Bw	: Bandwidth
C	: Carboxyl
CFD	: Computational Fluid Dynamics
CSTR	: Continuously Stirred Tank Reactor
DEAE	: Diethylaminoethyl
DBC	: Dynamic Binding Capacity
$DBC_{10\%}$	: Dynamic Binding Capacity at 10% breakthrough
DBC_{Tot}	: Dynamic Binding Capacity at Total breakthrough
FEM	: Finite Element Method
FLASH	: Fast Low-Angle Shot
FOV	: Filed Of View
HCP	: Host Cell Protein
HIC	: Hydrophobic Interaction Chromatography
HPLC	: High Performance Liquid Chromatography
IEX	: Ion Exchange
IgG	: Immunoglobulin G
IgM	: Immunoglobulin M
pI	: Isoelectric point
LF	: Lactoferrin
LP	: Lactoperoxidase
MBR	: Membrane Bioreactor
MC	: Membrane Chromatography
MMM	: Mixed Matrix Membrane
MRI	: Magnetic Resonance Imaging
PBS	: Phosphate Buffer Saline
PDE	: Partial Differential Equation
PFR	: Plug Flow Reactor
PIV	: Particle Image Velocimetry
Q	: Quaternary ammonium
RP-HPLC	: Reversed-Phase High Performance Liquid Chromatography
S	: Sulfonic acid
SNOPT	: Sparse Nonlinear OPTimizer algorithm
TE	: Echo time
TR	: Repetition time
ZRM	: Zonal Rate Model

Symbols

A or Ab	: Measured UV absorbance
b	: Ratio of forward to reverse sorption constant (k_a/k_d)
B_0	: Static magnetic field
c	: Solute concentration in liquid phase
c_0	: Initial solute concentration in liquid phase
c_e	: Solute concentration in liquid phase at equilibrium
c_{ef}	: Solute concentration in collected effluent
$\bar{c}$	: Average concentration in liquid phase
D_a	: Axial diffusion coefficient
D or D_m	: Membrane diameter
I	: Identity matrix
k_a	: Forward adsorption rate constant
k_d	: Reverse desorption rate constant
K_i	: Absorbance calibration constant of protein i
K_{prot}	: Constant of the Polson correlation
m_0	: Initial solute masse
$m_{loading}$	: Loading solute masse
M_w	: Molecular weight
P	: Pressure
Pe	: Peclet number
q	: Solute concentration in solid phase
q_e	: Solute concentration in solid phase at equilibrium
q_m	: Maximum solute concentration in solid phase
Q	: Flow rate
R_{in}	: Inlet radius of a membrane device
N	: Spiral wound length
u	: Superficial velocity
V or $V_{loading}$	: Loading volume
V_0	: Void volume
$V_{10\%}$	: Loading volume at 10% breakthrough
α	: Selectivity in Chapter 4, Flip angle in Chapter 6
β	: Ratio of the membrane surface area occupied by binding site 2 relative to that on the site 1 for the spreading model
ε	: Porous media porosity
κ	: Porous media permeability
ϒ	: Magnetogyric ratio
φ_v	: Accumulated phase
ρ	: Liquid density
τ	: Residence time
μ	: Liquid dynamic viscosity
ν	: Interstitial velocity
ω	: Pulsation of the precession

Contents

ACKNOWLEDGEMENTS

I would like to express my sincere gratitude to my advisors Dr. Catherine Charcosset and Dr. Koffi Fiaty for giving me the opportunity to pursue my PhD thesis with their guidance, continuous support and sympathetic research environment. Thanks to their expertise, encouragement and taking time to review my progress, this thesis could be completed with my development as a researcher.

Similarly, I would like to thank Pr. François Puel, who is very supportive and enthusiastic teacher. Due to his advice and recommendation, I obtained the funding sources to complete this PhD.

My special thanks go to Dr. Denis Grenier for his contributions, providing useful information and participating the experiments on the Magnetic Resonance Imaging (MRI) technique. Because of his innovative idea and straightforward explanation, this thesis becomes unique and interesting by applying the MRI technique to measure the internal geometry and velocity field inside the membrane chromatography modules. He demonstrated his great creation to resolve some problems and it is a pleasure to have the opportunity to work with a multidisciplinary scientist like him.

I would like also to thank Dr. Marie-Pierre Belleville and Pr. Xavier Santarelli with their generous acceptance to be the jury and reviewers of my thesis. Due to their useful comments and suggestions, I could improve my thesis quality and obtain many perspectives to develop my research project in the future.

Next, I would like to express my gratitude to the Royal Thai Government and Campus France for providing the financial aid during the past three years. Moreover, they provided me the new knowledge and cultural understanding, and much assistance to set up in France.

I am thankful to the entire LAGEP teams and staffs for their contributions and providing an informative and pleasurable work atmosphere. I have to thank the engineers and technicians in LAGEP; Géraldine Agusti, Sebastian Urbaniak and Jean-Pierre Valour to fulfill my experimental study. For all special kindness and supports during my stay in LAGEP, I would like to thank to all friends in the 231 office; Thouaiba Htira, Mohamed Benlahrache, Jing Wu, Assma Alharati and Pierre Verhlac. I have to thank also to all of my friends in Lyon, who are always beside me for many years.

Finally, I have to thank to David Verard for his unwavering support to my PhD thesis and professional career and being my inspiration and strength. I have no word to thank my beloved family for their unconditional understanding to my long journey and academic career in France.

THESIS INTRODUCTION

This PhD thesis focuses on the characterization and modeling of membrane chromatography (MC) as a chromatographic technique for biomolecules purification. Due to the advances in upstream bioprocesses, the major cost of bioprocesses (around 50-90%) has shifted toward downstream purification. In the last decade, MC has been increasingly used in unit operation in the biopharmaceutical industry. Indeed, MC is an interesting alternative to resin packed column chromatography for applications such as antibody polishing, purification of therapeutic proteins as well as large molecules such as viruses and plasmid DNA. The main advantages of MC are the reduced mass transfer resistance and the fast binding, which depends on the operating flow rate. Thus, operating at high flow rate is possible to optimize the productivity and the operational cost. Another interesting advantage of MC is its single-use ability, as the cleaning and regeneration steps are avoided and the contamination risk and manufacturing costs are reduced.

The objectives of this thesis are to contribute to a better understanding of the hydrodynamics, mass transfer and protein binding of ion-exchange membranes using an experimental and mathematical approach. MC is used in many applications and different devices are commercialized with either axial or radial flow. In the literature, the flow effect on the MC performance has been previously studied as well as the device geometry effect. This leads to optimized operating parameters and to the development of new design of MC devices. Several aspects related to chromatography for biomolecule separation and to MC are recalled in Chapter 1.

In Chapter 2, we compared axial and radial flow anion ion-exchange MC devices for bovine serum albumin (BSA) binding. For both axial and radial flow devices, three devices with different scales were compared. The effect of flow rates and BSA loading concentrations on BSA mass transfer and binding behavior was also investigated. Based on these experimental results, the advantages and limits of both geometries were discussed.

A mathematical model was developed in Chapter 3 using Computational Fluid Dynamics (CFD) to predict the breakthrough curves under non-binding and BSA binding conditions. The CFD model accounted for flow non-idealities inside the MC devices. Consequently, the influence of axial and radial flow was characterized on the hydrodynamics, BSA mass transfer and BSA binding behavior. The CFD model was also extended to predict the BSA binding at different flow rates and BSA initial concentrations.

In Chapter 4, MC is applied to biomolecules separation, which is an interesting and challenging topic. To this end, the separation of two similar-sized proteins, BSA and lactoferrin (LF), was carried out using anion and cation exchange MC. LF is a minor milk protein with numerous nutritional and medical applications. The influence of operating (flow rate, loading concentration ratio) and buffer conditions (pH, ionic strength) on BSA-LF mixture separation performance was studied using the two proteins, representative of whey concentrates. The breakthrough curve, dynamic binding capacity at 10% breakthrough ($DBC_{10\%}$), selectivity and productivity of the BSA-LF mixture separation were measured at various experimental conditions. Furthermore, the choice of the eluent was investigated to optimize the yield of the bound

proteins. The advantages and limits to use the MC devices in the milk industry were then discussed.

In the next part of this thesis, Chapter 5, we investigated the performance of two chromatographic stationary phases, membrane and monolith, which have been increasingly used in various applications due to their fast mass transfer. However, the comparison of the performances of these two stationary phases has been very little investigated in the literature. The separation of the BSA-LF mixture was studied using strong cation exchange membranes and monoliths packed in the same housing, as well as commercialized devices. The scaling-up of membrane and monolithic supports was performed by increasing the bed height. Additionally, a CFD model was developed and used to predict the flow distribution and breakthrough curves for both membrane and monolith media.

In the last part, Chapter 6, the hydrodynamics within the MC devices was measured experimentally using a non-invasive technique and predicted using the CFD model. This study was aimed at better understanding the mass transport and flow pattern within the MC devices. Magnetic resonance imaging (MRI) was selected as the experimental method, and the flow distribution was measured for both axial flow and radial flow devices. The velocity field obtained using the CFD simulations from 2D and 3D geometries was found in good agreement with the measured MRI velocities. Finally, the advantages and limits of both flow visualization methods were discussed.

Finally, the general conclusion and perspectives are presented at the end, closing this research report.

(This page is intentionally left blank)

Chapter 1

THESIS BACKGROUND

(This page is intentionally left blank)

Chapter 1
THESIS BACKGROUND

The purification of biomolecules is a very complex operation due in part to thier complex physical and chemical properties. The native conformation, stability and biological activity of the target biomolecules must be maintained during the purification. In addition, several types of contaminants, such as DNA, viral elements, endotoxin and other cellular material have to be eliminated as well as other contaminants which can interfere at the following steps such as inhibitors, and denaturants, etc [1,2]. Downstream processing of biomolecules relies on chromatography techniques and uses many types of chromatography in series. For example, the purification of recombinant factor VIII was reported with four steps: capture, affinity purification, anion exchange chromatography and gel filtration [3]. The high purification efficiency obtained relied mainly on the affinity and anion exchange chromatographic steps.

1.1 Chromatographic stationary phases

The development of techniques and methods for the separation and purification of biological macromolecules such as proteins has been an important prerequisite for many of the advancements made in bioscience and biotechnology over the past five decades. Improvements in materials have been extensively studied [1]. Conventionally, packed-bed chromatography using micro-sized resins (or gels) as porous matrix is found in industrial biopharmaceutical purification due to its good capacity, outstanding resolving capability, robustness and reliability [4]. However, the resin potential is restricted by poor mass transfer and physical characteristics. The development of new chromatographic stationary phases has been extensively reported since the 1980s. This has resulted in novel stationary phases such as membrane and monolith with high efficiencies and short processing times. The schema of each stationary phase is given in Fig. 1.1.

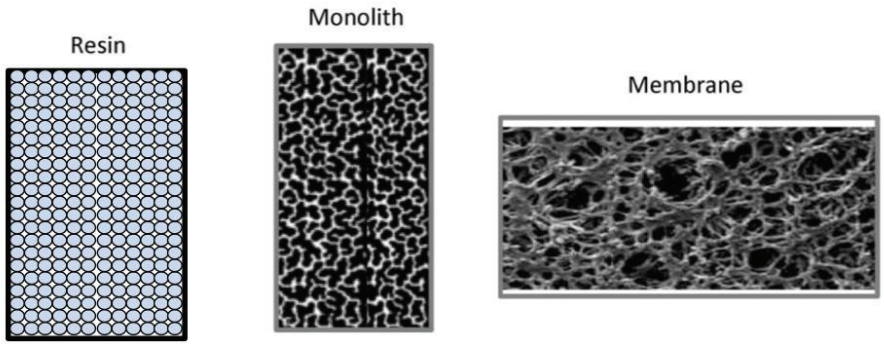

Fig. 1.1 Schema of the available chromatographic stationary phases.

- **Resin packed-bed chromatography**

Traditionally, resins or gels are bead-shaped, with average particle diameters ranging from a few to 100 μm. A wide variety of materials have been used for the design of chromatography matrices. They can be classified as inorganic materials, synthetic organic polymers, or polysaccharides. The most common chromatography stationary phase used in chromatography is porous silica resin. High mechanical strength is a strong advantage of silica particles, allowing the formation of packed beds that are stable for long periods and high operating pressures. Another advantage of silica is that it can be bonded with different ligands (C8, C18, phenyl, and cyano) for use with different samples and to change separation selectivity. Silica-based columns are compatible with all organic solvents and water, and do not swell or shrink with a change of solvent. Silica particles are especially suited for gradient elution, where the mobile-phase composition changes during the separation [5]. Furthermore, for packed beds with soft chromatography beads, scale-up is limited by mechanical factors such as bed instability [6].

Significant medium compression and increasing pressure drops are observed with increasing bed height [7]. An important limitation of traditional chromatography is the mass transfer due to diffusion in resin pores. This increases the process time during biomolecule purification. The pressure drop over the column is high even at low flow rates and increases during processing due to bed consolidation and column blinding [8]. Decrease in binding capacity and throughput are also observed using large biomolecules and highly concentrated feed-stocks [9,10].

- **Monolithic chromatography**

A monolithic stationary phase is a porous structure prepared by in situ polymerization or consolidation inside a column tubing [11]. Monoliths have been produced using a large range of materials, including polymethacrylate, polyacrylate, polyacrylamide, polystyrene, cellulose and silica [12–14]. Most monoliths for chromatography are made from polymethacrylate [13,14]. Monoliths have been increasingly used in liquid chromatography in recent years due to their simple preparation procedure, unique properties and excellent performance, especially for separation of biomolecules [15]. The mobile phase is forced to flow through the large pores; as a consequence, mass transport is mainly based on convection, and high flow rates can be obtained without negative effect on separation performance. Due to the large pore size and short bed of monolith supports, the separation time can be reduced, as well as the pressure drop compared to traditional resin columns [13,16–18]. Moreover, the dynamic binding capacity is not affected by flow rate, molecule size and feed concentration. This is a strong indication that adsorption is not limited by mass transfer due to the convective transport through the channels with diameter above 1000 nm.

Monoliths can be applied for all kinds of chromatography techniques, except size exclusion chromatography because monoliths rely on convection, while size exclusion chromatography is based on differences between diffusivity of individual molecules into the pore. Today, monolithic columns have been used for all kinds of biomolecule separations, especially the large biomolecules such as proteins, protein aggregates, plasmid DNA, and viruses. Monolithic columns up to 8 L in size are already commerciallized [24]. Although the monolithic stationary

phases possess a number of unique properties compared to traditional stationary phases, some disadvantages and limitations are inevitable. Most of the polymeric monolithic stationary phases are known to swell in organic solvents. This frequently leads to a lack of stability. Furthermore, the preparation of polymeric monoliths usually leads to micropores, which negatively affect the efficiency and peak symmetry of the column. Therefore, it is not easy to obtain high efficiency for small molecules. The low column capacity may be another significant disadvantage, which may be attributed to their low specific surface area compared to traditional packed-bed chromatography, although some attempts have been made to increase the specific surface area [15,25,26].

- **Membrane chromatography (MC)**

Membrane chromatography (MC) was introduced since over two decades as a novel chromatographic technique based on the integration of membrane filtration and liquid chromatography into a single-step operation [4,8,12,27]. Nowadays, MC is being employed for the purification and polishing of a large range of biomolecule species, including purification of monoclonal antibodies, DNA, protein purification and virus capture. MC devices are commercially available from several suppliers, ranging from laboratory scale to process scale. Several membrane materials have been tested as chromatographic supports: inorganic-organic (e.g. an alkoxysilane coated on glass fiber and alumina membranes [28]) and organic materials (e.g. cellulose and its derivatives, nylon, polyethersulfone, polypropylene, polyvinylidene, etc. [24,28]). Most membrane chromatography devices, especially for ion-exchange, are made from regenerated cellulose [28].

The main advantage of the method is attributed to short diffusion times, as the interactions between molecules and active sites in the membrane occur in convective through-pores rather than in stagnant fluid inside the resin pores. Therefore, membrane chromatography has the potential to operate at high flow rates and low pressure drops, to purify large biomolecules with small diffusivities, to reduce biomolecules degradation and denaturation, and buffer usages [4,8,29]. Other benefits of MC include the ability to replace each device completely, which makes it easier to assemble process trains for new products in existing premises without worrying about cross-contamination. This flexibility is of interest during scale-up, because the MC devices are available in a number of different sizes. Scale-up is linear for parameters such as the frontal surface area, bed volume, flow rate, and static binding capacity, while normalized dynamic capacity remains fairly constant [1].

Another interesting feature of MC devices for biopharmaceutical applications is their single-use ability, as the elimination of cleaning and regeneration steps reduces the contamination risk and manufacturing costs. It has been estimated that single-use techniques can reduce by up to 40 % the capital costs of production facilities in the biopharmaceutical manufacturing. Its advantages have made MC to have the highest market growth among all commercial disposable devices, such as mixing systems and bioreactors, with an annual growth rate of nearly 27% between 2006 and 2012 [30]. Nevertheless, further developments are still required due to several identified drawbacks, including poor binding capacities, ineffective device design, and irregular physical characteristics of the membrane such as pore size distribution, membrane thickness, and ligand density [4].

1.2 Interaction modes in membrane chromatography

Different separation mechanisms are available, including ion-exchange, affinity and hydrophobic interaction. The methods often have very different requirements regarding to chromatographic conditions including ionic strength, pH and various additives such as detergents, reducing agent and metals. The affinity and ion exchange chromatography are the most selected techniques for protein purification [1]. Chromatographic membranes based on above mentioned separation mechanisms are commercially available.

- **Ion-exchange (IEX) chromatography**

IEX chromatography is one of the most widely used and universal unit operation in the biopharmaceutical industry for the downstream processing of biomolecules for the capture, intermediate and polishing steps [31–33]. IEX separation is based on the differences in net surface charge between the functional groups on the chromatographic media and biomolecules. The charged groups within a biomolecule that contribute to the net surface charge possess different pKa values depending on their structure and chemical microenvironment. All molecules with ionizable groups have their net surface charge, which is highly pH dependent. A protein that has no net charge at pH equivalent to its isoelectric point (pI) will not interact with a charged medium. However, at pH above its isoelectric point, a protein will bind to a positively charged medium or anion exchanger and, at a pH below its pI, a protein will bind to a negatively charged medium or cation exchanger [34]. The strength of the interaction depends upon the charge of the proteins and the ion exchangers, the dielectric constant of the medium, and the competition from other ions from the charged group. The most common technique in IEX is adsorption of target biomolecule from a buffer of low ionic strength and desorption with a more concentrated buffer, commonly NaCl or NaOH [1].

The advantages of IEX chromatography include its simple separation principle, high separation resolution, high biomolecule binding capacity and ease of operation. Several IEX membranes are available: quaternary ammonium (Q) as strong anion-exchangers, sulfonated (S) as strong cation-exchangers, diethylaminoethyl (DEAE) as weak anion-exchangers, and carboxyl (C) as weak cation-exchangers [12]. IEX MC was performed successfully in many applications. For example, Suck et al. [35] separated successfully two model proteins, human serum albumin (HSA) and immunoglobulin G (IgG) using anion exchange MC at pH 6.0. The same authors isolated Penicillin acylase from a crude Escherichia coli supernatant in one step using an anion exchange spin column, designed for centrifugation. Santarelli et al. [25] characterized the separation performance of immunoglobulin M (IgM) from the supernatant of a human hybridoma cell culture using strong cation and anion ion-exchange membranes at different flow rates. Bhut et al. [31] reported the application of a novel weak anion exchange device for the separation of anthrax protective antigen protein from E. coli lysate at high binding capacity, high throughput, and good separation resolution.

IEX chromatographic membranes are used during polishing steps, which are conducted for extensive clearance of the remaining impurities, such as host cell proteins (HCPs), endotoxins, nucleic acids, and viruses, after major capture or purification of the target molecules [4]. The relatively dilute and large volumes of bioprocess streams highlight the importance of MC fast flowrates for this step. Various polishing applications based on the use of strong cation Q IEX membranes were reported [36–39]. Strong cation (S) and weak anion exchangers (DEAE) were

investigated for the host cell proteins (HCPs) and DNA clearance during monoclonal antibody purification [40,41]. Anion exchange chromatography was shown to be very efficient for the purification of plasmid DNA (pDNA). The pDNA purification takes advantage of the interaction between negatively charged phosphate groups on the DNA backbone and positively charged ligands of anion exchangers [42]. However, complete separation between pDNA and other nucleic acid impurities, especially RNA, becomes difficult for most chromatographic methods due to the similarity in size and chemical properties. Recently, anion-exchange MC was shown to be a promising tool for the separation of pDNA and RNA in cell lysate. Several strong (Q) and weak (DEAE) IEX chromatographic membranes have been investigated to improve pDNA purification efficiency [28,43–45].

- **Affinity chromatography**

Affinity chromatography separates biomolecules on the basis of a reversible interaction between a target biomolecule and a specific ligand coupled to a chromatographic media. The technique offers high selectivity, hence high resolution, and usually high capacity for the biomolecule of interest. It is used most often for initial product capture. The purification processes that would otherwise be time-consuming, difficult or even impossible using other techniques can often be easily achieved with affinity chromatography. To elute the target molecule from the affinity medium the interaction can be reversed, either specifically using a competitive ligand, or non-specifically, by changing the pH, ionic strength or polarity. In a single step, affinity purification can offer time-saving over less selective multistep procedures [1].

Common affinity ligands include protein A for purification of immunoglobulins (IgGs), immobilized metals for purification of his-tagged proteins, dyes, and specialized ligands [4]. Dye-affinity membranes vary in the type of interaction that dictates the separation behavior and Cibacron Blue F3GA specific to serum albumins is particularly common. Other ligands of interest are the mimetic ligands A2P monochloride, B14 monochloride, and Ligand 22/8 which are alternatives to protein A for immunoglobulin purification [46,47].

- **Hydrophobic interaction chromatography (HIC)**

Hydrophobic interaction chromatography (HIC) is widely used in biomolecule purification as a complement to other techniques. The separation is based on the interactions between hydrophobic groups on the surface of biomolecules and hydrophobic ligands displayed on the stationary phase. The technique is an ideal next step when samples have been subjected to ammonium sulfate precipitation or after separation by IEX chromatography. In both situations, the sample contains a high salt concentration and can be applied directly to the HIC column with little or no additional preparation. The elevated salt level enhances the interaction between the hydrophobic components of the sample and the chromatography medium. For selective elution, the salt concentration is lowered gradually and the sample components elute in order of hydrophobicity [1].

Hydrophobic interaction is less common in MC as higher resolutions can be obtained by resin chromatography. While the functionalized group on the support matrix can have certain hydrophobicity, alkyl chains are often grafted for hydrophilic supports. Major applications include separation of aggregates and inactive product isoforms with hydrophobicity different from their bioactive form and such separation often requires high resolutions that are difficult to achieve with membrane supports [4].

1.3 Membrane chromatography devices

The efficiency of MC is critically dependent on membrane module design. Inlet fluid distribution and outlet fluid collection inadequacies result in broad breakthrough curves and poor utilization of membrane binding capacity [12]. From the beginning of the 1990s, MC has been extensively designed and evaluated in different geometries such as flat sheet systems and stacks of membranes, hollow fibers, radial flow cartridges, and different interaction modes as explained earlier [4,48–50]. The available MC devices are displayed and summarized in Fig. 1.2. The flow patterns inside the MC devices include axial, radial and tangential flow. Axial flow devices containing stacked membrane disks are commonly used at laboratory scale and are commercialized with different membrane volumes. For example, better flow distribution was obtained by alternating the membrane sheets with spacers in Memsep modules (Millipore), consisting of a stack of modified cellulose membranes housed in an 18 mm module [51]. The dead volumes for stacked membrane sheet modules were minimized by Tennikova and Svec [52]. Besides, Ghosh and Wong [48] proposed the incorporation of fluid distributors and collectors above and below the membrane stack, respectively. This led to the increase in lysozyme binding efficiency compared to the corresponding conventional modules [53]. However, membrane axial flow devices are usually used at small scale, as the scaling-up of these devices is difficult because increasing the number of membrane layers results in an increasing pressure drop [49]. At the same time, poor flow distribution results of the increasing membrane diameter.

For large scale applications, radial flow devices are preferred due to easiest scaling-up. Radial flow devices were reported first in the 1980s [55]. Nowadays, several radial flow MC devices are commercialized with large bed volumes up to 1-5 L in different geometries such as hollow fiber, spiral wound and pleated sheet [4]. It is generally accepted that radial flow chromatography provides advantages over axial chromatography because of lowered pressure drops and high flow rates due to the large cross-sectional area and the short flow path. Indeed, radial flow chromatography can operate at higher volumetric flow rates than axial flow chromatography at the same pressure drop and same bed volume. Therefore, higher productivity in biomolecule purification has been successfully obtained using radial flow chromatography [56,57].

Tangential flow device is another possible alternative for industrial applications and could reduce membrane fouling [58]. Recently, Madadkar et al. [54] presented a novel configuration using stacked membrane sheets with lateral fed, to obtain a more uniform flow distribution, and therefore higher resolution of elution peaks.

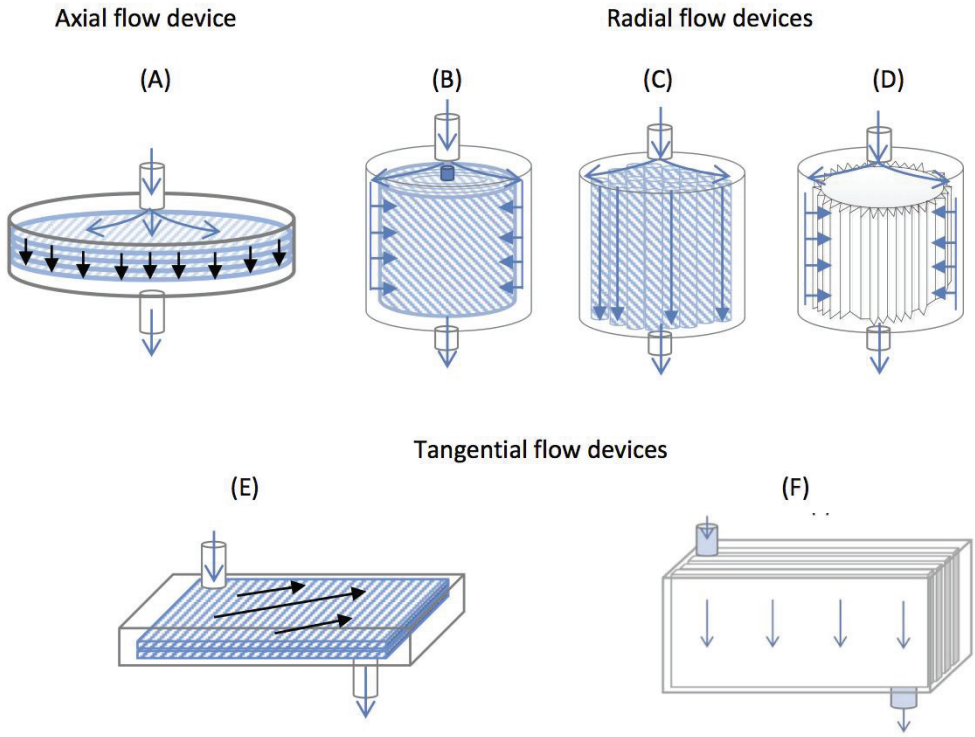

Fig. 1.2 Available MC devices into the different geometry. The axial flow device into (A) stacked sheets of membrane, the radial flow devices into the different membrane arrangements such as (B) spiral wound, (C) hollow-fiber, and (D) pleated sheet, and the tangential flow devices into (E) cross-flow flat sheet cassette and (F) latterally-fed device [Adapted from 4,54].

1.4 Modeling of membrane chromatography

A chromatographic separation is commonly performed in four steps: loading, washing, elution and regeneration as displayed in Fig. 1.3. The breakthrough curve and elution peak are commonly used to characterize the chromatographic performance. The breakthrough curve is the concentration profile during the loading step [12]. Breakthrough is defined as the point at which the solute being purified appears in the effluent solution. Most breakthrough curves present a S shape. Initially, the solute concentration in the effluent is zero, reflecting complete adsorption of the molecules by the stationary phase. As the loading step proceeds and binding sites become occupied, the species appear in the effluent. Afterward, the species concentration in the effluent increases rapidly and then more slowly as solute concentration asymptotically approaches to the initial concentration. At this point, steady state is achieved and no further adsorption occurs. Ideal breakthrough would increase sharply or almost vertically from zero to the loading concentration.

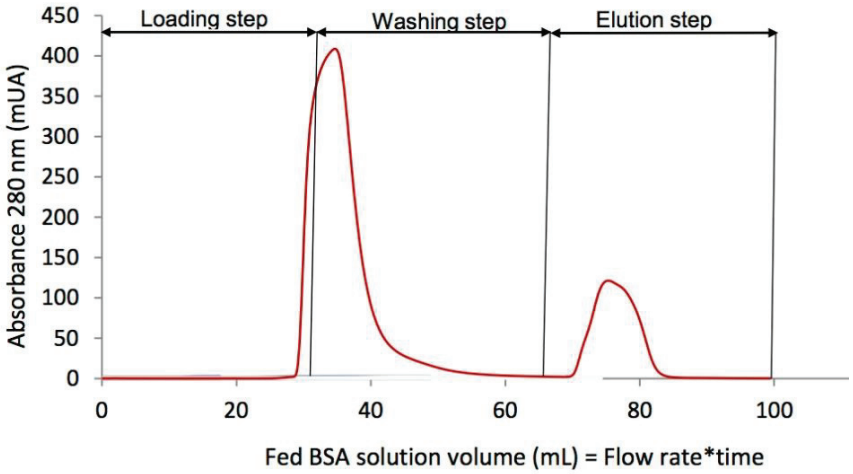

Fig. 1.3 Typical experimental chromatogram includes loading,washing and elution steps [12].

Mathematical models of MC are important tools to accurately predict and optimize the hydrodynamic, binding, housing design and scaling-up of MC devices. In MC devices, the flow is non-uniform, mainly due to the difference of the cross-sections between the inlet and outlet tubes and the membrane bed diameter. This leads to inefficient flow distribution in the membrane bed, which broadens the breakthrough curves and thus inefficient performance of MC processes [8,53,59]. In the past decades, many works have been devoted to the development of mathematical models for the prediction of elution peaks and breakthrough curves for MC devices.

MC has been first modeled by considering only the axial coordinate [5–8]. The effects of void volumes and dispersion from the external system (i.e. pumps, tubes, valves, etc.) were taken into account by connecting a plug flow model (PFR) in series with the membrane stack and with one or two continuously stirred tank reactors (CSTR) for the dispersion effect as displayed in Fig. 1.4. These one-dimensional models assumed flow homogeneity over the entire membrane cross-section, which in practice is difficult to achieve [60].

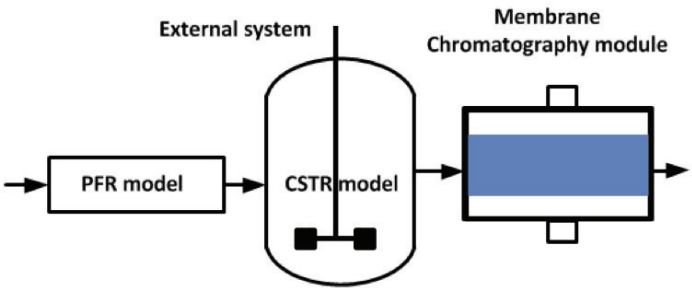

Fig. 1.4 Model configuration of the membrane stack device connected in series with a plug flow reactor (PFR) and a continouous stirred tank reactor (CSTR) in order to account for void volume and dispersion effects from the external system.

Usually, mathematical model of MC describes the transport phenomenon only in the membrane region based on one dimensional diffusion-convection equation and a binding kinetics equation. Typical binding kinetics are based on the single and multicomponent Langmuir isotherms to simulate the breakthrough curves for affinity [57] and ion-exchange MC [61,62]. The adsorption of proteins from aqueous solution onto porous and often chemically heterogeneous solid matrices is considerably more complex. For example, the much greater size and configurational degrees of freedom of proteins, the competition between the protein macro-ion and the solvent for surface binding sites of the same surface energy or differing surface energies, the potential for either orientationally specific or random binding of the sorbate, the ability or inability of the adsorbed protein to diffuse on the sorbent surface, and the non-ideal interactions between components within the solution and bound at the sorbent surface may all contribute to the adsorption rate, energetics and equilibria [2]. Several other binding kinetic models have been evaluated to try to account for these non-ideal contributions, such as steric hindrance [63], spreading equations [64] and bi-Langmuir adsorption equation [65].

Many mathematical models have been developed to account for non-uniform flow within MC devices and their external system. For example, Boi et al. [65] considered the effect of non-uniform flow on the dynamic binding behavior of MC devices using a combination in series of a CSTR and of a PFR model before the MC device. The modeling parameters including CSTR and PFR residence times were determined by fitting the model data to the experimental breakthrough curve under non-binding condition. The breakthrough curve under binding condition was simulated using the bi-Langmuir isotherm model for affinity MC. This approach was further tested to predict the breakthrough curves during the purification of IgG from a complex mixture [66,67]. The simulated results showed a good agreement with the experimental data. In addition, a non-uniform flow at the MC device inlet could be described using a polynomial equation as reported by Schneiderman et al. [68]. The accurate prediction of non-uniform and unsymmetrical breakthrough curves was obtained. A network of multi-tanks of CSTR connected in series and parallels was introduced in the zonal rate model (ZRM) to describe non-ideal flow in MC devices. The ZRM model was further applied to analyze the hydrodynamics and the performance of the axial flow device under different operating conditions [69,70]. The breakthrough curve prediction was achieved for both axial and radial flow MC [71,72].

Computational fluid dynamics (CFD) provides qualitative and quantitative prediction of fluid flows, in which mathematical modeling, numerical methods and software tools are employed to solve the problems. CFD can accurately characterize fluid hydrodynamics in complex geometries, thus CFD is a powerful tool in several modeling bioprocesses [73]; for example, bioreactors of various different configurations (i.e. stirred tanks [74,75], bubble columns [76,77], airlift reactors [78,79]). Hydrodynamics of many flat sheet and hollow membrane bioreactors (MBR) at a large scale were investigated by CFD [80–82]. Furthermore, CFD can be used to simulate the flow and concentration fields in membrane filtration devices [83–86] and chromatographic columns [87]. Recently, CFD has been applied to MC modeling. Ghosh et al. [60,88] used a CFD model to describe flow distribution within a MC device, connected in series with CSTR and PFR models. The results obtained showed flow distribution, which could be distinguished from binding kinetic effects by accounting for accurate internal geometry of the MC device. Moreover, the CFD model was applied to predict the binding behavior for axial and radial flow MC devices.

1.5 References

[1] J.-C. Janson, Protein Purification: Principles, High Resolution Methods, and Applications,John wiley & sons, 2012.

[2] P. Francis, Modeling of controlled-shear affinity filtration using computational fluid dynamics and a novel zonal rate model for membrane chromatography, 2011.

[3] L. Thim, B. Vandahl, J. Karlsson, N.K. Klausen, J. Pedersen, T.N. Krogh, et al., Purification and characterization of a new recombinant factor VIII (N8), Haemoph. Off. J. World Fed. Hemoph. 16 (2010) 349–359. doi:10.1111/j.1365-2516.2009.02135.x.

[4] V. Orr, L. Zhong, M. Moo-Young, C.P. Chou, Recent advances in bioprocessing application of membrane chromatography, Biotechnol. Adv. 31 (2013) 450–465. doi:10.1016/j.biotechadv.2013.01.007.

[5] L.R. Snyder, J.J. Kirkland, J.W. Dolan, Introduction to modern liquid chromatography, John wiley & sons, 2011.

[6] K. Brorson, J. Brown, E. Hamilton, K.E. Stein, Identification of protein A media performance attributes that can be monitored as surrogates for retrovirus clearance during extended re-use, J. Chromatogr. A. 989 (2003) 155–163. doi:10.1016/S0021-9673(02)01697-7.

[7] J.J. Stickel, A. Fotopoulos, Pressure-flow relationships for packed beds of compressible chromatography media at laboratory and production scale, Biotechnol. Prog. 17 (2001) 744–751. doi:10.1021/bp010060o.

[8] R. Ghosh, Protein separation using membrane chromatography: opportunities and challenges, J. Chromatogr. A. 952 (2002) 13–27. doi:10.1016/S0021-9673(02)00057-2.

[9] A.K. Hunter, G. Carta, Protein adsorption on novel acrylamido-based polymeric ion-exchangers: IV. Effects of protein size on adsorption capacity and rate, J. Chromatogr. A. 971 (2002) 105–116. doi:10.1016/S0021-9673(02)01027-0.

[10] A. Jungbauer, R. Hahn, Polymethacrylate monoliths for preparative and industrial separation of biomolecular assemblies, J. Chromatogr. A. 1184 (2008) 62–79. doi:10.1016/j.chroma.2007.12.087.

[11] I. Gusev, X. Huang, C. Horváth, Capillary columns with in situ formed porous monolithic packing for micro high-performance liquid chromatography and capillary electrochromatography, J. Chromatogr. A. 855 (1999) 273–290. doi:10.1016/S0021-9673(99)00697-4.

[12] C. Charcosset, Membrane processes in biotechnology and pharmaceutics, Elsevier, 2012.

[13] A. Jungbauer, R. Hahn, Monoliths for fast bioseparation and bioconversion and their applications in biotechnology, J. Sep. Sci. 27 (2004) 767–778. doi:10.1002/jssc.200401812.

[14] A. Podgornik, M. Barut, A. Strancar, D. Josić, T. Koloini, Construction of large-volume monolithic columns, Anal. Chem. 72 (2000) 5693–5699.

[15] H. Zou, X. Huang, M. Ye, Q. Luo, Monolithic stationary phases for liquid chromatography and capillary electrochromatography, J. Chromatogr. A. 954 (2002) 5–32. doi:10.1016/S0021-9673(02)00072-9.

[16] F. Svec, J.M.J. Fréchet, Modified poly(glycidyl metharylate-co-ethylene dimethacrylate) continuous rod columns for preparative-scale ion-exchange chromatography of proteins, J. Chromatogr. A. 702 (1995) 89–95. doi:10.1016/0021-9673(94)01021-6.

[17] A. Strancar, A. Podgornik, M. Barut, R. Necina, Short Monolithic Columns as Stationary Phases for Biochromatography, in: P.D.R. Freitag (Ed.), Mod. Adv. Chromatogr., Springer Berlin Heidelberg, 2002: pp. 49–85.

[18] P. Gagnon, Technology trends in antibody purification, J. Chromatogr. A. 1221 (2012) 57–70. doi:10.1016/j.chroma.2011.10.034.
[19] R. Hahn, A. Jungbauer, Peak broadening in protein chromatography with monoliths at very fast separations, Anal. Chem. 72 (2000) 4853–4858. doi:10.1021/ac000688y.
[20] R. Hahn, M. Panzer, E. Hansen, J. Mollerup, A. Jungbauer, Mass transfer properties of monoliths, Sep. Sci. Technol. 37 (2002) 1545–1565. doi:10.1081/SS-120002736.
[21] G. Iberer, R. Hahn, A. Jungbauer, Monoliths as stationary phases for separating biopolymers : Fourth-generation chromatography sorbents, LC GC. 17 (n.d.) 998–1005.
[22] I. Mihelič, D. Nemec, A. Podgornik, T. Koloini, Pressure drop in CIM disk monolithic columns, J. Chromatogr. A. 1065 (2005) 59–67. doi:10.1016/j.chroma.2004.10.054.
[23] I. Junkar, T. Koloini, P. Krajnc, D. Nemec, A. Podgornik, A. Štrancar, Pressure drop characteristics of poly(high internal phase emulsion) monoliths, J. Chromatogr. A. 1144 (2007) 48–54. doi:10.1016/j.chroma.2007.01.003.
[24] A. Jungbauer, R. Hahn, Polymethacrylate monoliths for preparative and industrial separation of biomolecular assemblies, J. Chromatogr. A. 1184 (2008) 62–79. doi:10.1016/j.chroma.2007.12.087.
[25] M.-J. Jacobin, X. Santarelli, J. Laroche-Traineau, G. Clofent-Sanchez, Production of a human monoclonal IgM directed against human cardiac myosin in a hollow-fiber bioreactor for membrane anion exchange chromatography one-step purification, Human Antibodies. 13 (2004) 69–79.
[26] S. Xie, F. Svec, J.M.J. Fréchet, Porous polymer monoliths: Preparation of sorbent materials with high-surface areas and controlled surface chemistry for high-throughput, online, solid-phase extraction of polar organic compounds, Chem. Mater. 10 (1998) 4072–4078. doi:10.1021/cm9804867.
[27] S. Brandt, R.A. Goffe, S.B. Kessler, J.L. O'Connor, S.E. Zale, Membrane-based affinity technology for commercial scale purifications, Nat. Biotechnol. 6 (1988) 779–782. doi:10.1038/nbt0788-779.
[28] C.-S. Chang, H.-S. Ni, S.-Y. Suen, W.-C. Tseng, H.-C. Chiu, C.P. Chou, Preparation of inorganic–organic anion-exchange membranes and their application in plasmid DNA and RNA separation, J. Membr. Sci. 311 (2008) 336–348. doi:10.1016/j.memsci.2007.12.034.
[29] J. Thömmes, M.-R. Kula, Membrane chromatography—An integrative concept in the downstream processing of proteins, Biotechnol. Prog. 11 (1995) 357–367. doi:10.1021/bp00034a001.
[30] Research and Markets: 9th annual report and survey of biopharmaceutical manufacturing capacity and production, Reuters. (2012). http://www.reuters.com/article/2012/07/03/idUS126634+03-Jul-2012+BW20120703 (accessed October 10, 2014).
[31] B.V. Bhut, K.A. Christensen, S.M. Husson, Membrane chromatography: Protein purification from E. coli lysate using newly designed and commercial anion-exchange stationary phases, J. Chromatogr. A. 1217 (2010) 4946–4957. doi:10.1016/j.chroma.2010.05.049.
[32] Curling, J., Gottschalk, U., Process chromatography: Five decades of innovation, BioPharm. Int., 2007. http://www.biopharminternational.com/process-chromatography-five-decades-innovation (accessed October 11, 2015).
[33] G. Subramanian, Bioseparation and bioprocessing: A handbook, 2 volume set, 2nd, Wiley-VCH, 2007.
[34] GE life sciences, Ion exchange chromatography and chromatofucusing principles and methods,http://www.gelifesciences.com/webapp/wcs/stores/servlet/catalog/en/GELifeScie

nces-fr/service-and-support/handbooks/ (accessed October 11, 2015).
[35] K. Suck, J. Walter, F. Menzel, A. Tappe, C. Kasper, C. Naumann, et al., Fast and efficient protein purification using membrane adsorber systems, J. Biotechnol. 121 (2006) 361–367. doi:10.1016/j.jbiotec.2005.07.023.
[36] B.V. Bhut, J. Weaver, A.R. Carter, S.R. Wickramasinghe, S.M. Husson, The role of polymer nanolayer architecture on the separation performance of anion-exchange membrane adsorbers: I. Protein separations, Biotechnol. Bioeng. 108 (2011) 2645–2653. doi:10.1002/bit.23221.
[37] J. Weaver, S.M. Husson, L. Murphy, S.R. Wickramasinghe, Anion exchange membrane adsorbers for flow-through polishing steps: Part I. Clearance of minute virus of mice, Biotechnol. Bioeng. 110 (2013) 491–499. doi:10.1002/bit.24720.
[38] M. Woo, N.Z. Khan, J. Royce, U. Mehta, B. Gagnon, S. Ramaswamy, et al., A novel primary amine-based anion exchange membrane adsorber, J. Chromatogr. A. 1218 (2011) 5386–5392. doi:10.1016/j.chroma.2011.03.068.
[39] R. Chen, J. John, A. Lavrentieva, S. Müller, M. Tomala, Y. Zhao, et al., Cytokine production using membrane adsorbers: Human basic fibroblast growth factor produced by Escherichia coli, Eng. Life Sci. 12 (2012) 29–38. doi:10.1002/elsc.201100045.
[40] H.F. Liu, B. McCooey, T. Duarte, D.E. Myers, T. Hudson, A. Amanullah, et al., Exploration of overloaded cation exchange chromatography for monoclonal antibody purification, J. Chromatogr. A. 1218 (2011) 6943–6952. doi:10.1016/j.chroma.2011.08.008.
[41] H. Shirataki, C. Sudoh, T. Eshima, Y. Yokoyama, K. Okuyama, Evaluation of an anion-exchange hollow-fiber membrane adsorber containing γ-ray grafted glycidyl methacrylate chains, J. Chromatogr. A. 1218 (2011) 2381–2388. doi:10.1016/j.chroma.2010.10.071.
[42] M.M. Diogo, J.A. Queiroz, D.M.F. Prazeres, Chromatography of plasmid DNA, J. Chromatogr. A. 1069 (2005) 3–22. doi:10.1016/j.chroma.2004.09.050.
[43] P. Guerrero-Germán, D.M.F. Prazeres, R. Guzmán, R.M. Montesinos-Cisneros, A. Tejeda-Mansir, Purification of plasmid DNA using tangential flow filtration and tandem anion-exchange membrane chromatography, Bioprocess Biosyst. Eng. 32 (2009) 615–623. doi:10.1007/s00449-008-0284-7.
[44] P.-O. Syrén, A. Rozkov, S.R. Schmidt, P. Strömberg, Milligram scale parallel purification of plasmid DNA using anion-exchange membrane capsules and a multi-channel peristaltic pump, J. Chromatogr. B. 856 (2007) 68–74. doi:10.1016/j.jchromb.2007.05.033.
[45] L. Zhong, K. Srirangan, J. Scharer, M. Moo-Young, D. Fenner, L. Crossley, et al., Developing an RNase-free bioprocess to produce pharmaceutical-grade plasmid DNA using selective precipitation and membrane chromatography, Sep. Purif. Technol. 83 (2011) 121–129. doi:10.1016/j.seppur.2011.09.024.
[46] T. Barroso, M. Temtem, A. Hussain, A. Aguiar-Ricardo, A.C.A. Roque, Preparation and characterization of a cellulose affinity membrane for human immunoglobulin G (IgG) purification, J. Membr. Sci. 348 (2010) 224–230. doi:10.1016/j.memsci.2009.11.004.
[47] C. Boi, S. Dimartino, S. Hofer, J. Horak, S. Williams, G.C. Sarti, et al., Influence of different spacer arms on Mimetic Ligand™ A2P and B14 membranes for human IgG purification, J. Chromatogr. B. 879 (2011) 1633–1640. doi:10.1016/j.jchromb.2011.03.059.
[48] C. Charcosset, Membrane processes in biotechnology: An overview, Biotechnol. Adv. 24 (2006) 482–492. doi:10.1016/j.biotechadv.2006.03.002.
[49] C. Boi, Membrane adsorbers as purification tools for monoclonal antibody purification, J. Chromatogr. B Analyt. Technol. Biomed. Life. Sci. 848 (2007) 19–27. doi:10.1016/j.jchromb.2006.08.044.

[50] J.X. Zhou, T. Tressel, Basic Concepts in Q Membrane Chromatography for Large-Scale Antibody Production, Biotechnol. Prog. 22 (2006) 341–349. doi:10.1021/bp050425v.
[51] E. Klein, Affinity membranes: a 10-year review, J. Membr. Sci. 179 (2000) 1–27. doi:10.1016/S0376-7388(00)00514-7.
[52] T.B. Tennikova, F. Svec, High-performance membrane chromatography: Highly efficient separation method for proteins in ion-exchange, hydrophobic interaction and reversed-phase modes, J. Chromatogr. A. 646 (1993) 279–288. doi:10.1016/0021-9673(93)83340-X.
[53] R. Ghosh, T. Wong, Effect of module design on the efficiency of membrane chromatographic separation processes, J. Membr. Sci. 281 (2006) 532–540. doi:10.1016/j.memsci.2006.04.023.
[54] P. Madadkar, Q. Wu, R. Ghosh, A laterally-fed membrane chromatography module, J. Membr. Sci. 487 (2015) 173–179. doi:10.1016/j.memsci.2015.03.056.
[55] S. Huang, S. Roy, K. Hou, G. Tsao, Scaling-up of affinity-chromatography by radial-flow cartridges, Biotechnol. Prog. 4 (1988) 159–165. doi:10.1002/btpr.5420040306.
[56] V. Chen, H. Li, A.G. Fane, Non-invasive observation of synthetic membrane processes – a review of methods, J. Membr. Sci. 241 (2004) 23–44. doi:10.1016/j.memsci.2004.04.029.
[57] S.-Y. Suen, M.R. Etzel, A mathematical analysis of affinity membrane bioseparations, Chem. Eng. Sci. 47 (1992) 1355–1364. doi:10.1016/0009-2509(92)80281-G.
[58] V. Orr, J. Scharer, M. Moo-Young, C.H. Honeyman, D. Fenner, L. Crossley, et al., Simultaneous clarification of Escherichia coli culture and purification of extracellularly produced penicillin G acylase using tangential flow filtration and anion-exchange membrane chromatography (TFF-AEMC), J. Chromatogr. B. 900 (2012) 71–78. doi:10.1016/j.jchromb.2012.05.039.
[59] S.-Y. Suen, Y.-C. Liu, C.-S. Chang, Exploiting immobilized metal affinity membranes for the isolation or purification of therapeutically relevant species, J. Chromatogr. B. 797 (2003) 305–319. doi:10.1016/S1570-0232(03)00490-2.
[60] P. Ghosh, K. Vahedipour, M. Lin, J.H. Vogel, C. Haynes, E. von Lieres, Computational fluid dynamic simulation of axial and radial flow membrane chromatography: Mechanisms of non-ideality and validation of the zonal rate model, J. Chromatogr. A. 1305 (2013) 114–122. doi:10.1016/j.chroma.2013.07.004.
[61] K.H. Gebauer, J. Thömmes, M.R. Kula, Breakthrough performance of high-capacity membrane adsorbers in protein chromatography, Chem. Eng. Sci. 52 (1997) 405–419. doi:10.1016/S0009-2509(96)00426-5.
[62] A. Shiosaki, M. Goto, T. Hirose, Frontal analysis of protein adsorption on a membrane adsorber, J. Chromatogr. A. 679 (1994) 1–9. doi:10.1016/0021-9673(94)80306-4.
[63] C. Frerick, P. Kreis, A. Górak, A. Tappe, D. Melzner, Simulation of a human serum albumin downstream process incorporating ion-exchange membrane adsorbers, Chem. Eng. Process. Process Intensif. 47 (2008) 1128–1138. doi:10.1016/j.cep.2007.07.013.
[64] H. Yang, M.R. Etzel, Evaluation of three kinetic equations in models of protein purification using ion-exchange membranes, Ind. Eng. Chem. Res. 42 (2003) 890–896. doi:10.1021/ie020561u.
[65] C. Boi, S. Dimartino, G.C. Sarti, Modelling and simulation of affinity membrane adsorption, J. Chromatogr. A. 1162 (2007) 24–33. doi:10.1016/j.chroma.2007.02.008.
[66] S. Dimartino, C. Boi, G.C. Sarti, A validated model for the simulation of protein purification through affinity membrane chromatography, J. Chromatogr. A. 1218 (2011) 1677–1690. doi:10.1016/j.chroma.2010.11.056.
[67] S. Dimartino, C. Boi, G.C. Sarti, Influence of protein adsorption kinetics on breakthrough broadening in membrane affinity chromatography, J. Chromatogr. A. 1218 (2011) 3966–

3972. doi:10.1016/j.chroma.2011.04.062.
[68] S. Schneiderman, H. Varadaraju, L. Zhang, H. Fong, T.J. Menkhaus, Mathematical model using non-uniform flow distribution for dynamic protein breakthrough with membrane adsorption media, J. Chromatogr. A. 1218 (2011) 9121–9127. doi:10.1016/j.chroma.2011.10.063.
[69] P. Francis, E. von Lieres, C.A. Haynes, Zonal rate model for stacked membrane chromatography. I: Characterizing solute dispersion under flow-through conditions, Biotechnol. Bioeng. 1218 (2011) 5071–5078. doi:10.1016/j.chroma.2011.05.017.
[70] P. Francis, E. von Lieres, C. Haynes, Zonal rate model for stacked membrane chromatography part II: characterizing ion-exchange membrane chromatography under protein retention conditions, Biotechnol. Bioeng. 109 (2012) 615–629. doi:10.1002/bit.24349.
[71] P. Ghosh, K. Vahedipour, M. Lin, J.H. Vogel, C.A. Haynes, E. von Lieres, Zonal rate model for axial and radial flow membrane chromatography. Part I: Knowledge transfer across operating conditions and scales, Biotechnol. Bioeng. 110 (2013) 1129–1141. doi:10.1002/bit.24771.
[72] P. Ghosh, M. Lin, J.H. Vogel, D. Choy, C. Haynes, E. von Lieres, Zonal rate model for axial and radial flow membrane chromatography, part II: Model-based scale-up, Biotechnol. Bioeng. 111 (2014) 1587–1594. doi:10.1002/bit.25217.
[73] P. Ghosh, K. Vahedipour, M. Leuthold, E. von Lieres, Model-based analysis and quantitative prediction of membrane chromatography: Extreme scale-up from 0.08 ml to 1200 ml, J. Chromatogr. A. 1332 (2014) 8–13. doi:10.1016/j.chroma.2014.01.047.
[73] C. Sharma, D. Malhotra, A.S. Rathore, Review of Computational fluid dynamics applications in biotechnology processes, Biotechnol Progress. 27 (2011) 1497–1510. doi:10.1002/btpr.689.
[74] H. Hartmann, J.J. Derksen, H.E.A. van den Akker, Mixing times in a turbulent stirred tank by means of LES, AIChE J. 52 (2006) 3696–3706. doi:10.1002/aic.10997.
[75] F. Kerdouss, A. Bannari, P. Proulx, CFD modeling of gas dispersion and bubble size in a double turbine stirred tank, Chem. Eng. Sci. 61 (2006) 3313–3322. doi:10.1016/j.ces.2005.11.061.
[76] P. Chen, J. Sanyal, M.P. Duduković, Numerical simulation of bubble columns flows: effect of different breakup and coalescence closures, Chem. Eng. Sci. 60 (2005) 1085–1101. doi:10.1016/j.ces.2004.09.070.
[77] J. Sanyal, S. Vásquez, S. Roy, M.P. Dudukovic, Numerical simulation of gas–liquid dynamics in cylindrical bubble column reactors, Chem. Eng. Sci. 54 (1999) 5071–5083. doi:10.1016/S0009-2509(99)00235-3.
[78] W. Feng, J. Wen, C. Liu, Q. Yuan, X. Jia, Y. Sun, Modeling of local dynamic behavior of phenol degradation in an internal loop airlift bioreactor by yeast Candida tropicalis, Biotechnol. Bioeng. 97 (2007) 251–264. doi:10.1002/bit.21215.
[79] R. F. Mudde, H. E. A. Van Den Akker, 2D and 3D simulations of an internal airlift loop reactor on the basis of a two-fluid model, Chem. Eng. Sci. 56 (2001) 6351–6358. doi:10.1016/S0009-2509(01)00222-6.
[80] Y. Wang, M. Brannock, S. Cox, G. Leslie, CFD simulations of membrane filtration zone in a submerged hollow fibre membrane bioreactor using a porous media approach, J. Membr. Sci. 363 (2010) 57–66. doi:10.1016/j.memsci.2010.07.008.

[81] M. Brannock, Y. Wang, G. Leslie, Mixing characterisation of full-scale membrane bioreactors: CFD modelling with experimental validation, Water Research. 44 (2010) 3181–3191. doi:10.1016/j.watres.2010.02.029.

[82] P. Wei, K. Zhang, W. Gao, L. Kong, R. Field, CFD modeling of hydrodynamic characteristics of slug bubble flow in a flat sheet membrane bioreactor, J. Membr. Sci. 445 (2013) 15–24. doi:10.1016/j.memsci.2013.05.036.

[83] R. Ghidossi, J.V. Daurelle, D. Veyret, P. Moulin, Simplified CFD approach of a hollow fiber ultrafiltration system, Chem. Eng. J. 123 (2006) 117–125. doi:10.1016/j.cej.2006.07.007.

[84] M. Rahimi, S.S. Madaeni, M. Abolhasani, A.A. Alsairafi, CFD and experimental studies of fouling of a microfiltration membrane, Chem. Eng. Proc. Intens. 48 (2009) 1405–1413. doi:10.1016/j.cep.2009.07.008.

[85] B. Marcos, C. Moresoli, J. Skorepova, B. Vaughan, CFD modeling of a transient hollow fiber ultrafiltration system for protein concentration, J. Membr. Sci. 337 (2009) 136–144. doi:10.1016/j.memsci.2009.03.036.

[86] A.R. Rajabzadeh, C. Moresoli, B. Marcos, Fouling behavior of electroacidified soy protein extracts during cross-flow ultrafiltration using dynamic reversible–irreversible fouling resistances and CFD modeling, J. Membr. Sci. 361 (2010) 191–205.

(This page is intentionally left blank)

Chapter 2

EFFECT OF GEOMETRY AND SCALE FOR AXIAL AND RADIAL FLOW MEMBRANE CHROMATOGRAPHY – EXPERIMENTAL STUDY OF BOVIN SERUM ALBUMIN ADSORPTION

(This page is intentionally left blank)

Chapter 2

EFFECT OF GEOMETRY AND SCALE FOR AXIAL AND RADIAL FLOW MEMBRANE CHROMATOGRAPHY - EXPERIMENTAL STUDY OF BOVIN SERUM ALBUMIN ADSORPTION

2.1 Abstract

During the last 10 years, membrane chromatography (MC) has been increasingly reported for biomolecule purification at both small and large scales. Although, several axial and radial flow MC devices are commercialized, the effect of the device dimensions on the adsorption performance has not been fully investigated. In this study, axial and radial flow anion ion-exchange MC devices were used for bovine serum albumin (BSA) adsorption. For both axial and radial flow, three devices at different scales were compared, two having similar diameter and two similar bed height. The pressure drop and the flow distribution using acetone as a non-binding solute were measured, as well as BSA breakthrough curves at different flow rates and BSA loading concentrations. For all devices, it was observed that the flow rate had no effect on the breakthrough curve, which confirms the advantage of MC to be used at high flow rates. In addition, the BSA binding capacity increased with increasing BSA concentration, which suggests that it could be preferable to work with concentrated solutions rather than with very dilute solutions, when using buffer at high phosphate concentration. For both axial and radial flow, the bed height had a negative impact on the binding capacity, as the lowest binding capacities per membrane volume were obtained with the devices having the highest bed height. Radial flow MC has potential at large-scale applications, as a short bed thickness can be combined with a large inlet surface area.

Keywords :

Membrane chromatography, Breakthrough curve, Dynamic binding capacity, Axial flow chromatography, Radial flow chromatography

2.2 Introduction

Membrane chromatography (MC) was introduced in the late 1980s as a novel chromatographic technique based on the integration of membrane filtration and liquid chromatography into a single-step operation [1]. From the beginning of the 1990s, MC has been extensively designed and evaluated in different geometries such flat sheet systems and stacks of membranes, hollow fibers, radial flow cartridges, and different interaction modes including affinity interaction, ion exchange, hydrophobic interaction, reversed-phase and multistage chromatography [2, 3, 4 ,5]. Nowadays, MC is being employed for the purification and polishing of a large range of biomolecular species, including purification of monoclonal antibodies, DNA, and virus capture. MC devices are commercially available from several suppliers, ranging from laboratory scale to process scale.

The benefit of MC over conventional resin chromatography is mainly attributed to the shorter diffusion times, as the interactions between molecules and active sites in the membrane occur in convective through-pores rather than in stagnant fluid inside the pores of the adsorbent particles. Therefore, MC has the potential to maintain high efficiencies both at high flow rates and for use of large biomolecules with small diffusivities, reducing biomolecules degradation and denaturation. Low pressure drop associated with high flow rate, as compared to packed bed chromatography, reduced buffer usages due to low void volume and scalability for process development are other key advantages of MC. In addition, MC devices can be used as single-use units to eliminate the requirement for cleaning and regeneration and to reduce contamination risk. It has been estimated that single-use techniques can reduce by up to 40 % the capital costs of production facilities in the biopharmaceutical manufacturing. Its advantages have made MC to have the highest market growth among all commercial disposable devices, such as mixing systems and bioreactors, with an annual growth rate of nearly 27% between 2006 and 2012 [6].

MC devices are often characterized by the shape of their breakthrough curves. The breakthrough curve shape is governed by adsorption kinetics within the functionalized membrane and by fluid hydrodynamics in the hold-up volumes of the MC devices. Commercial MC devices are optimized such as to obtain breakthrough curves that are as sharp as possible, in order to minimize buffer consumption and to maximize the utilized membrane capacity. Significant developments in MC devices have been obtained by considering advanced materials [7,8], polymer grafting of the surface of the pore walls [9,10], fluid flow distribution and collection within the MC device [11][12], as well as optimized geometry [13,14].

The scaling up of MC devices has been reported in several studies. For example, Briefs and Kula [15] increased the membrane diameter from 90 mm to 142 mm of a stack of 96 membranes without any change in the anion exchange membrane capacity. Using devices having two different diameters of 15 and 25 mm, a good resolution was obtained compared to DEAE-Sephacel gel for pyruvate decarboxylase purification. Huang et al. [16] investigated the radial flow MC devices made from modified cellulose for trypsin removal. The trypsin binding capacity was found linearly related to the bed volume for 250, 800 and 3200 ml devices. Puthirasigamany

et al. [17] measured the binding capacity of two Nano Sartobind Q devices with different bed volume: 1 ml and 3 ml. For the 3 ml device, the dynamic binding capacity per unit of membrane volume was found around 20 % lower than the one obtained with the 1 ml device, although this result was not discussed. Ghosh et al. [14] used two MC devices with a scale-up factor of 15,000: an axial flow Sartobind Pico MC capsule with 0.08 ml bed volume and a radial flow Sartobind 1.2 l MC capsule. A simulation based on CFD and on the spreading binding model was developed for analyzing MC at the very small scale, and transferring the identified binding mechanism and parameters for predicting the performance of the very large scale device. These authors underlined that the introduction of appropriate flow distribution and binding mechanism for each device was necessary to obtain a good fit between modeling and experimental values.

The effect of membrane diameter and bed height of membrane absorbers has also been investigated by some authors. For example, Josić et al. [18] used anion exchange MC devices made from poly(glycidyl methacrylate) membranes for separations of standard proteins. The thickness of the membrane layers was between 1 and 7 mm and the disc diameter between 10 and 50 mm. The results obtained showed that with increasing thickness better separation was achieved. The separation obtained with a 10 mm diameter disc could also be achieved with a 50 mm diameter disc. Knudsen et al. [13] determined the breakthrough capacities of Sartobind cation-exchange membranes as a function of layer number, from 1 to 60. The continued rise in breakthrough capacity was explained by the inefficient flow distribution within the MC devices and/or the housing and the experimental system.

The comparison between axial and radial flow has been little studied using MC devices. For example, Ghosh et al.[14] used two MC devices: an axial flow Sartobind Pico MC capsule and a radial flow Sartobind 1.2 L MC capsule. However, due to the very different scales, the comparison between the two devices was difficult. On the contrary, comparison of radial flow over axial flow chromatography using traditional resin columns has been largely investigated (e.g. Besselink et al. [19], Tharakan [20]). A radial flow column typically consists of two concentric cylinders between which the resin bed is packed. The liquid is directed from outside inwards or vice versa, resulting in horizontal, radial flow. In a recent study, Besselink et al. [19] compared axial and radial flow affinity chromatography using columns packed with affinity resin to adsorb BSA. No difference in performance between the two columns was observed. The authors concluded that for small-scale processes, axial flow chromatography may be preferable, for resin volumes of at least several tens of litres, radial flow chromatography is probably the best choice. Unlike radial flow chromatography, axial flow chromatography has significant limitation of scaling up because high volumes can be obtained by varying only the membrane diameter, while the bed height is maintained constant. Higher scalability is obtained using radial flow geometry by increasing both column height and diameter [20].

In this work, the effect of axial and radial flow, membrane area, membrane diameter, and bed height on the MC device performance is investigated. Commercialized strong anion ion-exchange MC is used for bovine serum albumin (BSA) adsorption. For both axial and radial flow, three devices with different membrane area are tested, two having similar diameter, and two

similar bed height. The flow distribution is first observed under a non-binding condition loading an acetone solution. BSA breakthrough curves are then compared at different flow rates and BSA loading concentrations. The dynamic binding capacity at 10% breakthrough is calculated and compared for the various devices. Finally, the effect of flow configuration, dimensions of MC devices on flow distribution and binding capacity is discussed.

2.3 Materials and Methods

2.3.1 Materials

BSA lyophilized powder (≥ 98.00% purity) was purchased from MP Biomedical (France). BSA was dissolved in a phosphate buffer prepared from 100 mM solution of K_2HPO_4 and KH_2PO_4, adjusted to pH 7.0. The elution buffer was phosphate buffer saline (PBS), prepared by adding 1 M NaCl to the above buffer, and adjusted at pH 7.0. The washing and regeneration buffers were 1 M NaOH. Except BSA, all chemical reagents used in this study were purchased from Sigma Aldrich (France). Ultra-pure water was obtained using a Milli-Q system (Millipore, France). Prior to use, all buffer solutions were filtered through a hydrophobic membrane filter with a 0.45 µm pore size (Millipore, France). A 0.22 µm polyethersulfone hydrophilic Millex-GP filter unit (Millipore, France) was set-up before the MC device to remove fine particles from solutions during the experiments.

The experiments were carried out on the Äktaprime Plus chromatography system (GE Healthcare Life Sciences, France) as displayed in Fig. 2.1, which includes a system pump, a fraction collector, a pressure sensor, and monitors for UV and conductivity. Valves for buffer selection, sample injection, gradient formation, and flow diversion are integrated into the system.

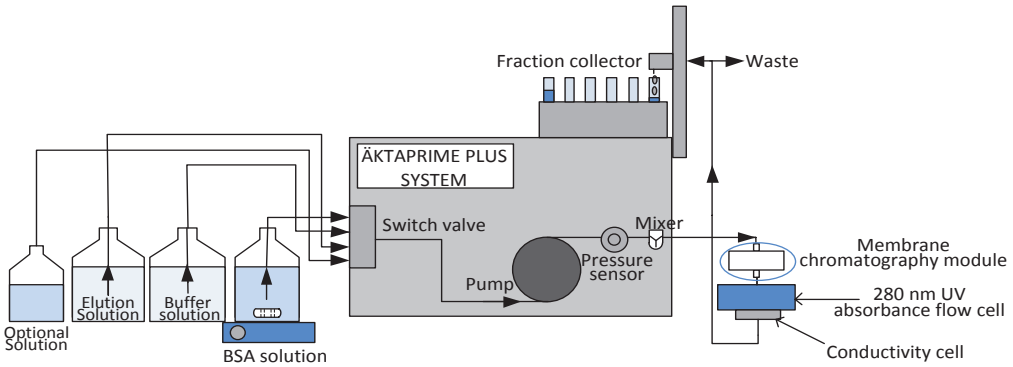

Fig. 2.1 Membrane chromatography experiment set-up under the control of Aktaprime Plus FHLC system

2.3.2 Strong anion ion exchange MC

All MC devices were obtained from Sartorius Stedim Biotech GmbH (Goettingen, Germany). They contain a stabilized reinforced cellulose membrane with thickness 275 µm and pore size around 3 - 5 µm. Functionalized quaternary ammonium (Q) groups are bound covalently to a grafted polymer layer.

The characteristics of the MC devices provided by the manufacturer are summarized in Table 2.1. For the radial flow devices, the outer diameters and the cylindrical heights were obtained from magnetic resonance imaging. For both axial and radial flow, three different devices were investigated. The flow configuration is shown in Fig. 2.2. Axial flow devices are composed of several stacked membrane sheets in capsules. The flow goes from top through the membrane bed to the outlet. Inside radial flow devices, the membrane is in the form of spiral wound or rolled around a cylindrical core. The flow pattern is from outside of the membrane cylinder through the membrane bed to the inside core of the membrane cylinder. The superficial velocity on each MC device was determined using the flow rate devised with the cross-section area. For the axial flow MC, the cross section was the disc surface, which is equal to $\frac{\pi}{4}D_m^2$. The outer surface of cylinder shape or $\pi N D_m$ was the cross section for the radial flow MC.

Table 2.1 Characteristics of the radial and axial flow MC devices

	Axial flow MC			**Radial flow MC**		
	Sartobind Q15	Sartobind Q75	Sartobind Q100	Sartobind Nano1mL	Sartobind Nano3mL	Sartobind Mini
Ligand	$R\text{-}CH_2\text{-}N^+(CH_3)_3$					
Membrane bed volume (ml)	0.41	2.10	2.80	1.00	3.00	7.00
Void volume (ml)	1.00	1.30	4.20	5.00	4.00	20.0
Bed height-H (mm)	0.8	4.0	1.4	4.0	8.0	4.0
Membrane bed diameter-D_m (mm)	25.0	25.0	50.0	22.0*	22.0*	36.0*
Spiral wound height-N (mm)	-	-	-	6.5*	8.0*	30.0*
Membrane area (cm^2)	15.0	75.0	100.0	36.4	110.0	250.0
Number of layers	3	15	5	-	-	-

* : dimensions obtained from magnetic resonance imaging

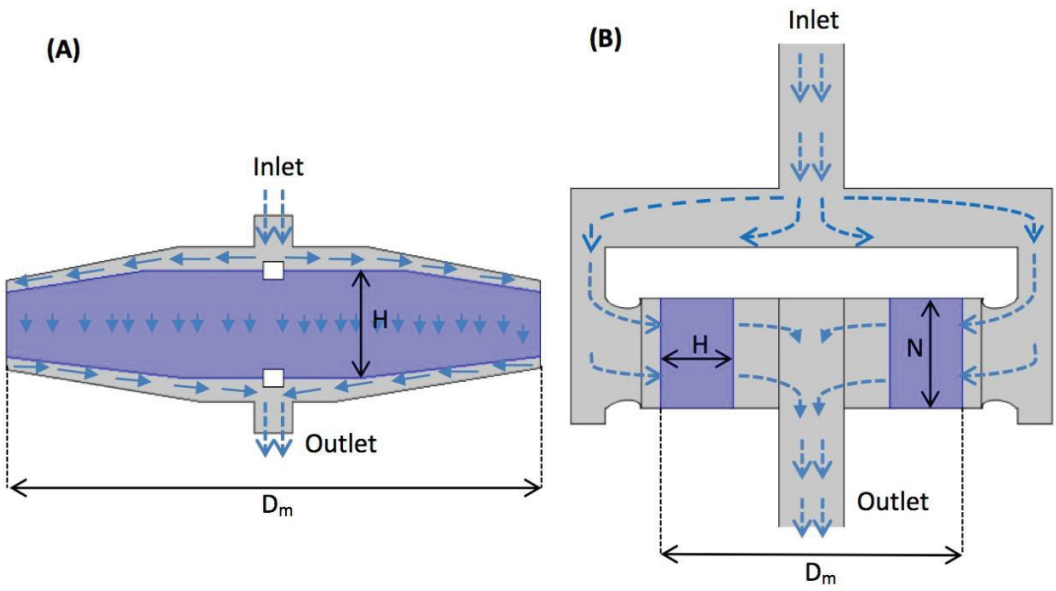

Fig. 2.2 Geometry and flow paths of: (A) axial flow MC (Sartobind Q 75), and (B) radial flow chromatography (Sartobind Nano1mL).

2.3.3 Breakthrough curves under non-binding conditions

The system dispersion curve was measured using a phosphate buffer containing 5.00 v.% acetone. Similarly to binding experiments, the non-binding breakthrough curves were monitored by reading the UV absorbance at 280 nm. A wash step was then performed using a 100 mM phosphate buffer at pH 7.0.

The non-binding breakthrough curves were fitted to Eq. 1 to determine the Peclet number (Pe) using least squares regression [7,21]. In Eq. 1, c is the outlet effluent concentration, c_0 is the solute loading concentration, V is the volume of acetone solution loaded, and V_{50} is the loaded volume when c/c_0=0.50. The dimensionless number Pe is the ratio between the rate of convective flow (mean velocity, u, multiplied by bed height, H) and the rate of diffusive flow (axial dispersion, D).

$$\frac{c}{c_0} = \frac{1}{2}\left\{1 + erf\left(\frac{Pe^{1/2}(V - V_{50})}{2(VV_{50})^{1/2}}\right)\right\} \quad \text{Eq. 1}$$

High Pe values are associated with uniform distribution of flow to the inlet surface of the MC device as well as uniform distribution of the binding site properties. Low Pe number values are associated with poor flow distribution, large flow dispersive characteristics of the MC devices, and/or large binding mechanism distribution [21]. In addition to the determination of Pe numbers, the non-binding experiments were used to determine the dead volume of the experimental set-up and device, V_0, from the breakthrough at 10 %.

2.3.4 Protein dynamic adsorption

BSA breakthrough curves were measured at different BSA concentrations (0.5, 2.0, 4.0 and 8.0 $mgmL^{-1}$) and flow rates (5.0, 10.0, 20.0, 30.0 $mLmin^{-1}$). After the loading step, the membrane was washed using 1 M NaOH solution for 1 h at a flow rate of 1 bed volume $(BV)min^{-1}$, followed by the elution and phosphate buffers for 10 BV of each.

To compare the adsorption performance of the different MC devices, the dynamic binding capacity at 10% breakthrough ($DBC_{10\%}$) was calculated using Eq. 2, where c is the BSA outlet concentration, c_0 is the BSA loading concentration, $V_{10\%}$ is the loading volume of BSA solution when c/c_0= 0.10 and V_0 is the dead volume of the MC device and external system. In addition, the dynamic binding capacity at total breakthrough (DBC_{Total}) was determined using Eq. 3.

$$DBC_{10\%} = \int_0^{V_{10\%}} (c_0 - c)dV_{loading} - c_0V_0 \quad \text{Eq. 2}$$

$$DBC_{Total} = \int_0^{V_{Total}} (c_0 - c)dV_{loading} - c_0V_0 \quad \text{Eq. 3}$$

2.4 Results and discussion

2.4.1 Operational pressure

Fig. 2.3 shows the operational pressure (P) as a function of superficial velocity for the different devices. The pressures were lower than 0.6 MPa and 0.7 MPa for axial flow and radial flow devices, respectively. This low pressure is a major advantage of MC and is due to the large membrane pore size around 3 -5 μm. Both axial and radial flow devices show similar pressure values, as well as similar effect of velocity. For all devices, the operational pressure increased linearly with increasing superficial velocity, which has been also reported previously, e.g. with nylon-based microporous membranes from Pall of two different mean pore size 1.2 and 3 μm [15], radial flow cartridges made of modified cellulose [16] and Sartobind Q Nano1mL and 3mL [17].

For axial flow devices, the effect of bed height can be seen by comparing the operational pressure obtained with the Sartobind Q75 device (bed height 4 mm) to the Q15 devices (bed height of 0.8). Fig. 2.3 shows that the pressure was slightly higher with the Sartobind Q 75 device. In addition, the very lower velocity was obtained on the Sartobind Q100 due to the increasing diameter effect. This could be explained by the larger cross-section area of the Q100 device for double folds, which thus decreased the velocity for four times.

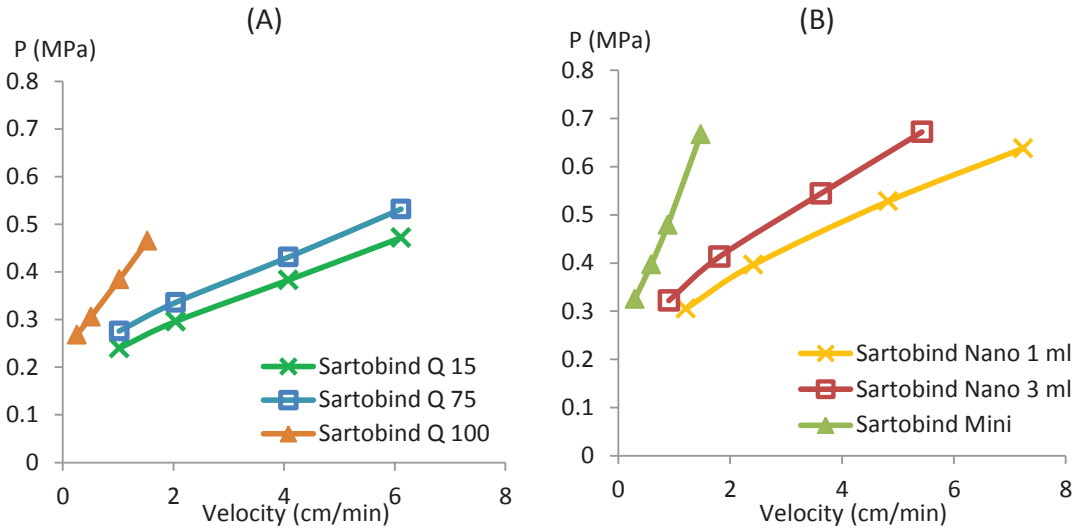

Fig. 2.3 Operational pressures at different superficial velocities for the different scales of: (A) axial flow devices and (B) radial flow devices.

For radial flow geometry, the increase in operational pressure with bed height can be seen with the Sartobind Nano 3 mL device (bed height 8 mm) compared to the Nano1mL devices (bed height 4 mm). The Sartobind Nano1mL and Nano3mL devices showed similar superficial velocity, due to the close lateral surface of both devices. Identically to the axial flow devices, the lowest velocity was obtained with the Sartobind Mini device, which has the largest cross section area. However, the similar operational pressure to the Sartobind Nano1mL was observed due to their identical bed height.

2.4.2 Flow distribution analysis

For each device, the acetone breakthrough curve was measured under non-binding conditions. Fig. 2.4 shows that the acetone breakthrough curves obtained for both axial (Sartobind Q 15 and Q75) and both radial flow devices (Sartobind Nano1mL and 3mL) were identical. For the two larger devices, Sartobind Q 100 and Mini, the breakthrough occurred later due to their larger void volumes.

Pe values were estimated from Eq. 1 and summarized in Table 2.2. For axial flow devices, Pe values were almost identical, between 33 and 35. The radial flow devices led to higher Pe, between 45 and 77. As mentioned previously, higher Pe are preferred as they are associated with uniform distribution of flow to the inlet surface of the MC device as well as uniform distribution of the binding site properties. Phillips [21] stated that for higher Pe values, such as above 100, the breakthrough curve begins to approach ideality and breakthrough corresponds to the capacity of the device, i.e. high efficiency. Considering the Pe criteria, our results suggest that the radial flow devices are more efficient than the axial ones. Pe values of 102 and 88 were reported by Schneiderman et al. [7] when using MC devices Mustang S (Pall Corporation) and homemade nanofiber supports, respectively. Using commercial MC devices, Phillips [21] measured Pe numbers on the order of 20 and 100. Therefore, our Pe values were in the range of previously reported data for MC devices.

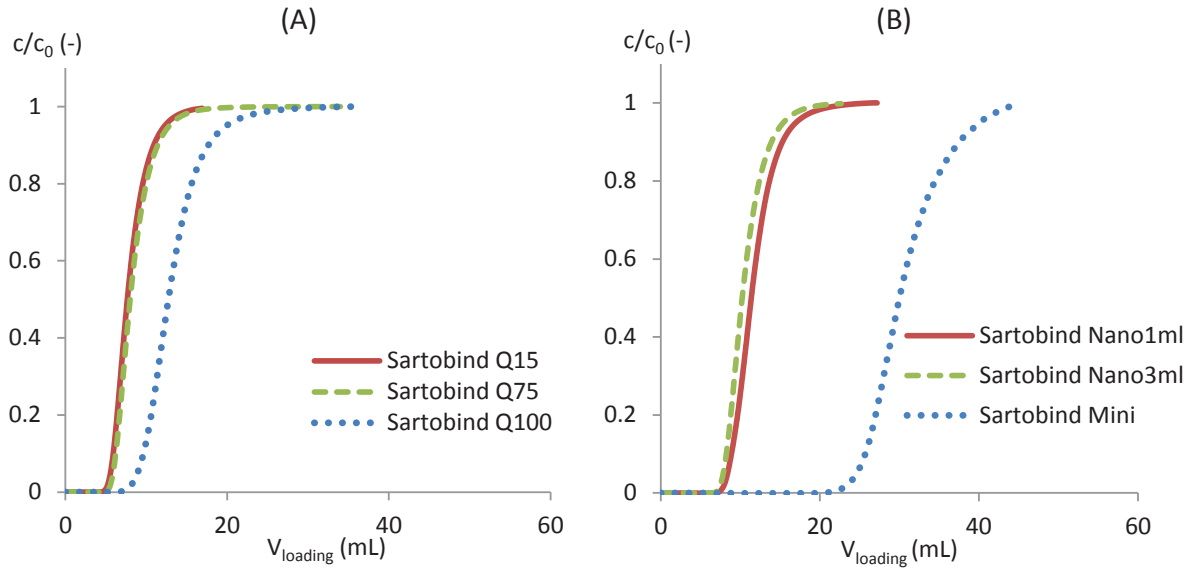

Fig. 2.4 Non-binding breakthrough curves: (A) axial flow devices and (B) radial flow devices at a flow rate of 10 mLmin^{-1} and acetone loading concentration of 5 v.%.

Table 2.2 Peclet numbers, velocities and dead volumes of the MC devices and external system measured at the flow rate of 5 mLmin^{-1} under a non-binding condition with 5 v.% of acetone. The dead volume, V_0, was obtained, when the breakthrough concentration reached to 10 %.

Membrane chromatography modules	**Axial flow module**			**Radial flow module**		
	Sartobind Q 15	Sartobind Q 75	Sartobind Q 100	Sartobind Nano1mL	Sartobind Nano3mL	Sartobind Mini
Dead volume of MC device and external system-V_0 (mL)	5.94	6.25	9.75	8.88	8.25	25.28
Superficial velocity (cmmin^{-1})	1.02	1.02	0.25	1.20	0.90	0.15
Pe (-)	33	33	35	45	46	77

2.4.3 BSA breakthrough curves at different operating conditions

The obtained BSA breakthrough curves showed the same shape as usually observed (i.e. van Beijeren et al. [22], Puthirasigamany et al. [17]. The shape of the BSA breakthrough curves was not rectangular, as it would happen for an ideal adsorbent [22], but was initially steep and became gradually broader. One reason for such a behavior is usually admitted to be dispersion effects due to pore size and length distribution. Another reason could be the slow adsorption kinetic on the grafted polymer layers at the membrane surface. The amount of BSA that breakthrough at a certain point loaded depends on the amount of already adsorbed proteins. Thus, the adsorption of BSA seems to reduce the accessibility of the binding sites and increases mass transport limitations [22].

- **BSA adsorption at different flow rates**

To observe the influence of flow rate on BSA breakthrough curves, dynamic adsorption experiments were performed at flow rate between 5.00 $mLmin^{-1}$ and 30.0 $mLmin^{-1}$, except for the Sartobind Mini device for which the flow rate was set between 10.0 to 50.0 $mLmin^{-1}$. The BSA loading concentration was maintained at 2.00 $mgmL^{-1}$. The experimental breakthrough curves obtained were plotted against the BSA loading volume per bed volume of the MC devices for the axial flow devices (Fig. 2.5) and the radial flow devices (Fig. 2.6). For both axial and radial flow devices, and even for the larger scales, the breakthrough curves were unaffected by flow rate from 5 to 30 $mLmin^{-1}$ (50 $mLmin^{-1}$ for the radial flow Mini device). This confirms that it is possible to obtain high throughput using MC without any flow rate effect. The absence of flow rate effect on the experimentally observed breakthrough curves has been reported previously, for MC devices (e.g. Knudsen et al. [13], van Beijeren et al. [22], Puthirasigamany et al. [17]). This phenomenon is generally explained by the absence of diffusive transport limitation.

The lowest residence time of the mobile phase in the void volume, which was measured loading acetone solution as an inert tracer, was obtained with the Sartobind Q 15 device at the flow rate of 30 $mLmin^{-1}$ and was equal to 2.00 s. This confirms the high rate of mass transport in MC devices in comparison to conventional resins, where residence times of several minutes are required to obtain sufficient dynamic binding capacities. The residence time of 2.00 s is slightly lower than that reported at 3.12 s by van Beijeren et al. [22] using a Sartobind Q75 device.

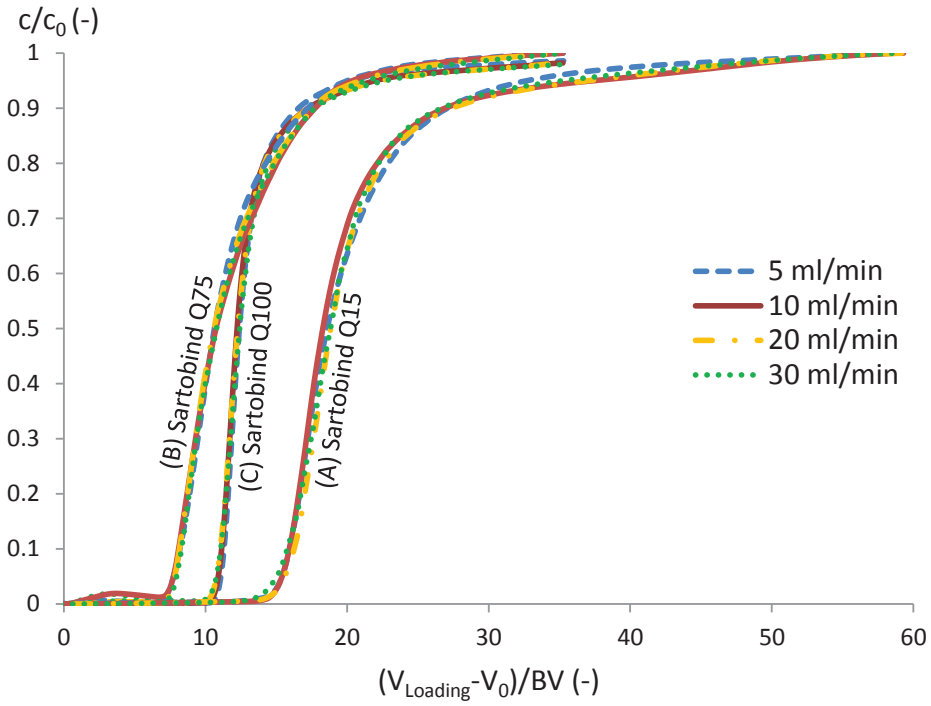

Fig. 2.5 BSA breaktrough curves of the axial flow devices: (A) Sartobind Q15, (B) Sartobind Q75, and (C) Sartobind Q100 at different flow rates 5, 10, 20 and 30 mLmin^{-1}.

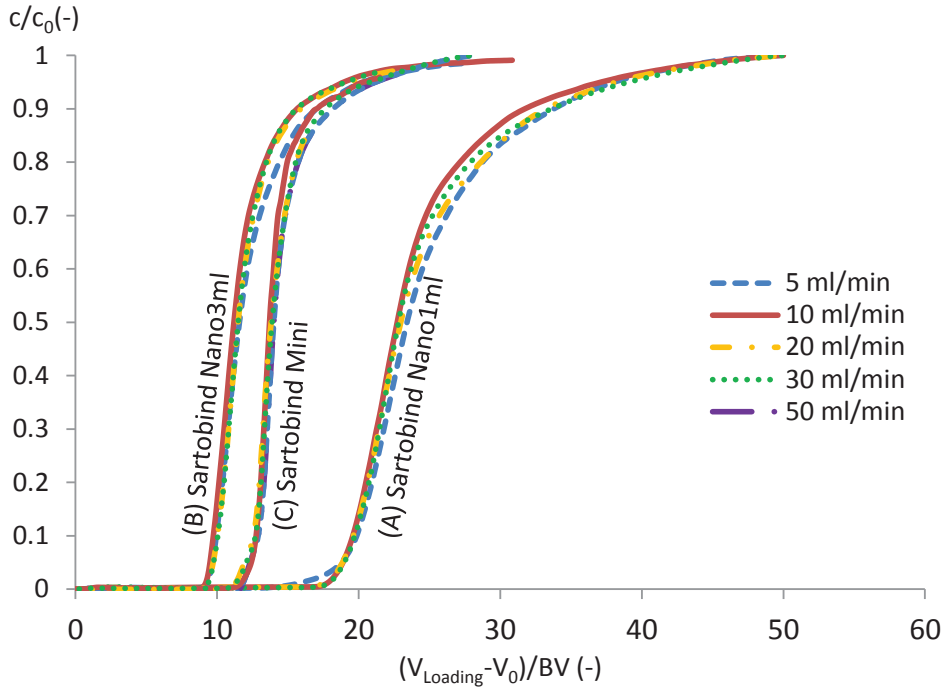

Fig. 2.6 Breaktrough curves of the radial flow devices; (A) Sartobind Nano1mL, (B) Sartobind Nano3mL, and (C) Sartobind Mini at different flow rates 5,10,20, 30 and 50 mLmin^{-1}.

- **BSA adsorption at different BSA loading concentrations**

The effect of BSA loading concentration on breakthrough curves was studied at 0.5, 2, 4 and 8 $mgmL^{-1}$ BSA, except for the largest radial flow device (Sartobind Mini) for which the lower BSA concentration of 0.5 $mLmin^{-1}$ was not tested. The flow rate was maintained at 10 $mLmin^{-1}$. The breakthrough curves were compared by plotting c/c_0 as a function of the loading mass of BSA corrected for the BSA mass loss in the void volume (m_0)/BV, i.e. the loading volume of BSA solution ($V_{loading}$) corrected by V_0 , multiplied by the inlet concentration (c_0) and divided by BV.

Fig. 2.7 and Fig. 2.8 show the BSA breakthrough curves at different BSA feed concentrations, for the axial and radial flow devices, respectively. For both geometries, the shape of the breakthrough curves was unaffected by the feed concentration. However, for all devices, the breakthrough curves appeared earlier at lower loading concentrations. This effect was already observed, i.e. for the adsorption of BSA on a Sartobind Q device: below 1 $mgmL^{-1}$ BSA feed concentration, breakthrough occurred earlier at low feed concentrations. The difference in dynamic capacity at different BSA concentrations may be due to the high amount of phosphate (100 mM) present.

The strong anion exchange ammonium quaternary groups have a high preference for phosphate ions due to their smaller size and easier access to the binding sites compared to the large BSA molecules. Many studies have pointed out that BSA has the ability to bind with numerous organic and inorganic ions [23-25]. Klotz et al. [23] highlighted complexes formation between BSA molecules and phosphate ions, which could reduce the BSA binding capacity on the dyes. With increasing BSA concentration, the preference for BSA over phosphate ions shifts resulting in a later breakthrough and higher dynamic capacity. Van Beijeren et al. [22] also reported an increase in BSA binding capacity with increasing BSA loading concentration and decreasing the acetate buffer concentration.

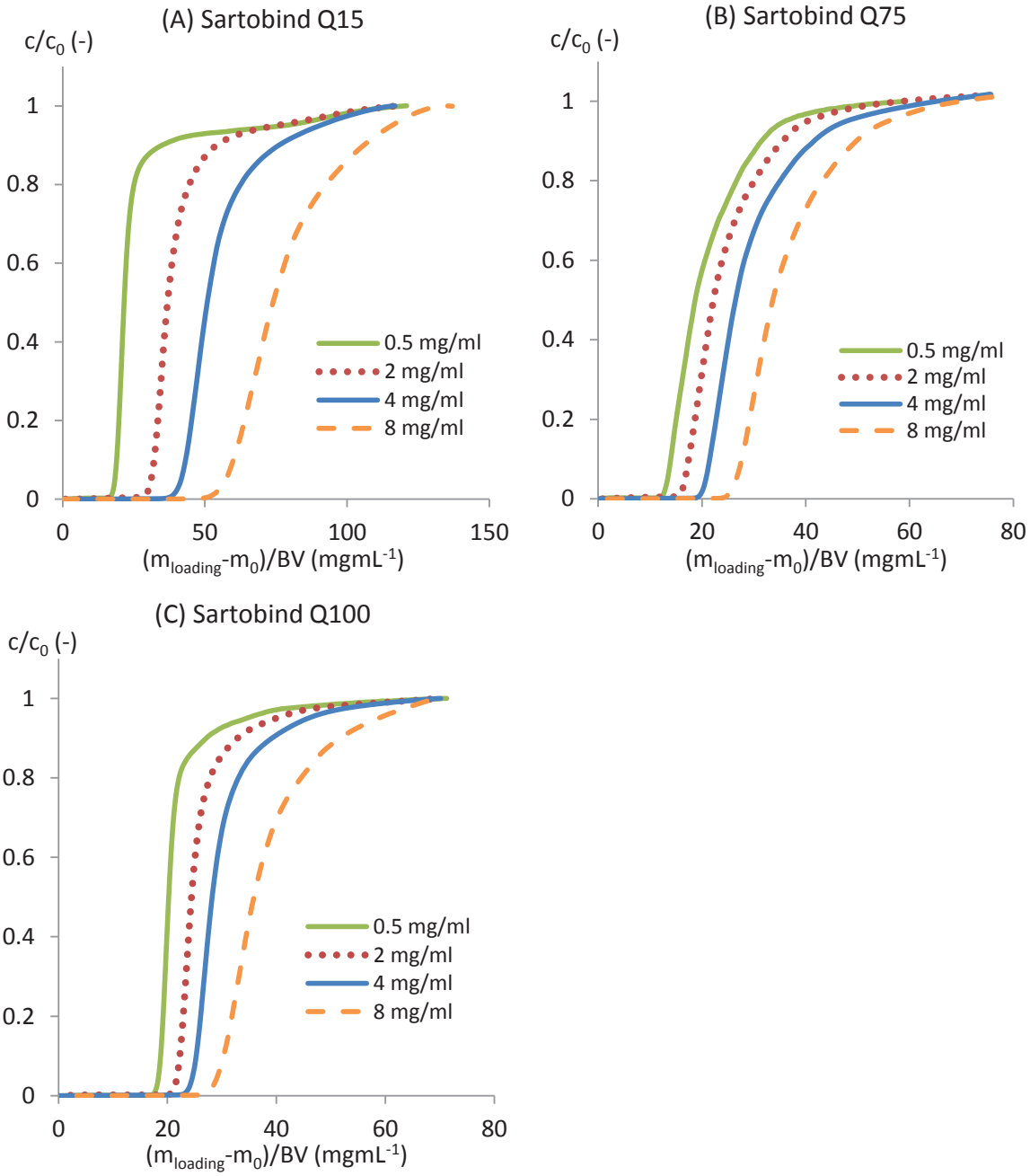

Fig. 2.7 Experimental breakthrough curves of the axial flow devices: (A) Sartobind Q15, (B) Sartobind Q75, and (C) Sartobind Q100 under different BSA loading concentrations at 0.5, 2.0, 4.0 and 8.0 $mgmL^{-1}$.

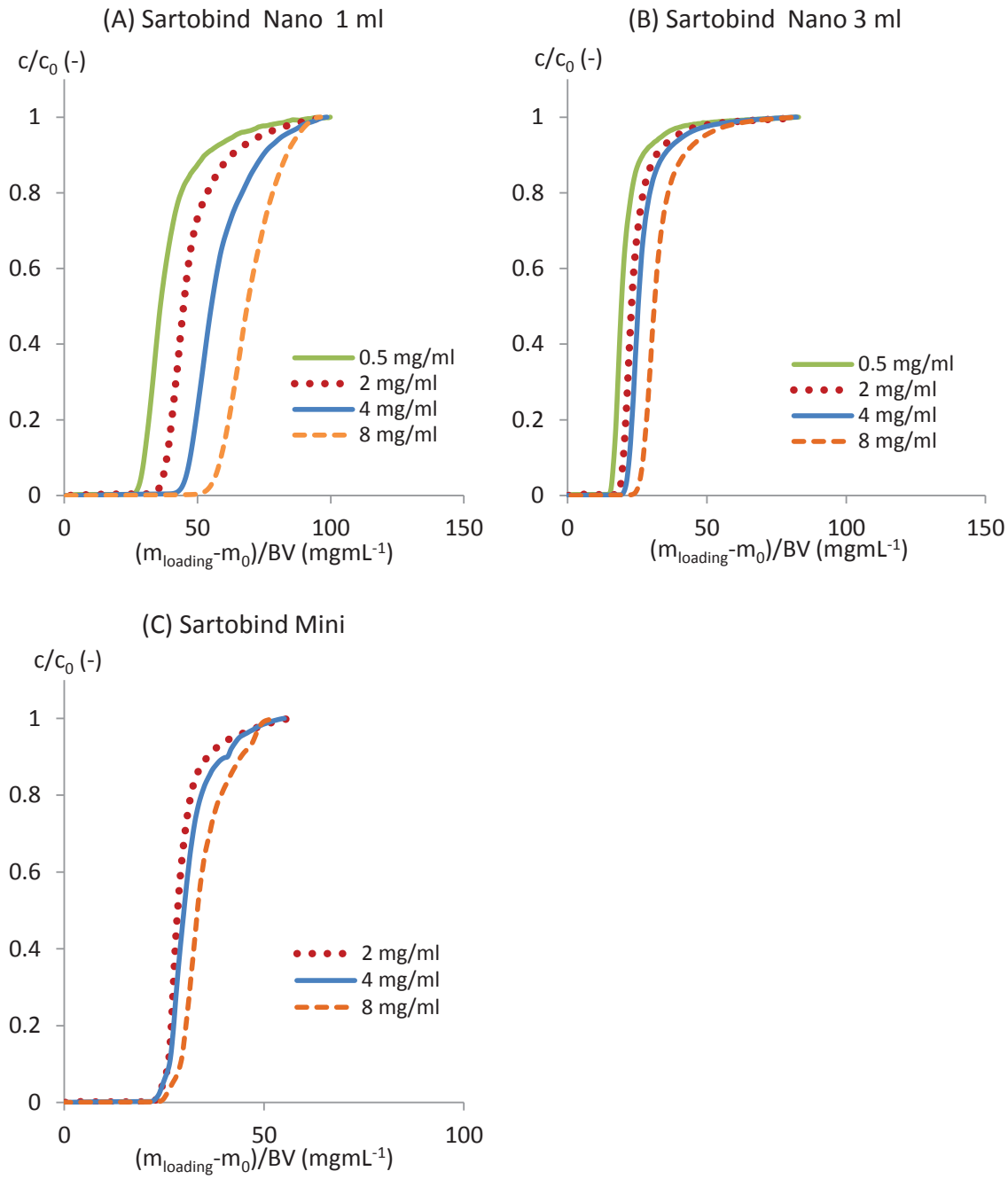

Fig. 2.8 Experimental breakthrough curves of the radial flow devices: (A) Sartobind Nano1mL, (B) Sartobind Nano3mL, and (C) Sartobind Mini under different BSA loading concentrations at 0.5, 2.0, 4.0 and 8.0 $mgmL^{-1}$.

2.4.4 Dynamic binding capacity

For each device, the dynamic binding capacities at 10 % breakthrough ($DBC_{10\%}$) and at the end of the loading step (DBC_{Total}) were determined from the breakthrough curves obtained at different flow rates. $DBC_{10\%}$ and DBC_{Total} divided by the BV were plotted as a function of superficial velocity in Fig. 2.9. As mentioned previously, the BSA dynamic capacity remained almost constant as a function of flow rate for both axial and radial flow and for each scales.

For axial and radial flow devices, the highest capacities $DBC_{10\%}$ and DBC_{Total} were obtained for the devices with the lowest bed volume (respectively, Sartobind Q15 and Nano1mL). In addition, for axial flow, the capacity of the Q75 device (bed height 4 mm, bed volume 2.10 mL) was found lower than the Q100 device (bed height 1.4 mm, bed volume 2.80 mL). A similar effect was observed with the radial flow devices, where the binding capacity of the Nano 3 mL device (bed height 8 mm, bed volume 3.00 mL) was lower than that of the Mini device (bed height 4 mm, bed volume 7 mL). This effect was already observed by Puthirasigamany et al. [17] for the 3 mL device, the BSA binding capacity per unit of membrane volume was found around 20 % lower than the one obtained with the 1 mL device. Thus, the bed height appears as a main parameter for MC device design: an increase in bed height (from 1.4 to 4 mm for axial flow and from 4 to 8 mm for radial flow) decreases the binding capacity. This effect is probably due to the more difficult access of molecules to binding sites at the bottom of the thicker membrane.

Similar binding capacities were found with both axial and radial flow devices: around 40-45 $mgmL^{-1}$ for the smallest Q 15 and Nano1mL device, and around 25 $mgmL^{-1}$ for the two intermediate devices Q75 and Nano3mL. For the Sartobind Q 75 device, the observed binding capacity of for BSA at 10% breakthrough was 20 $mgmL^{-1}$, which increased to 25 $mgmL^{-1}$at the end of loading. The first value was very close to the one reported by [22] for the same MC device (19.1 $mgmL^{-1}$). Moreover, for the Nano1mL and 3mL, the observed binding capacity of for BSA at 10% breakthrough was respectively equal to 31 and 20 $mgmL^{-1}$. These values are in agreement with the ones obtained by Puthirasigamany et al. [17], who found respectively around 32 and 25 $mgmL^{-1}$.

The dynamic binding capacity was also measured as a function of BSA loading concentration. Fig. 2.10 shows the concentration effect for the different axial and radial flow devices. For the smallest bed volume devices, Sartobind Q15 and Nano1mL, the $DBC_{10\%}$ increased significantly with the BSA loading concentration. The $DBC_{10\%}$ at 0.5 $mgmL^{-1}$ were 19 and 21 $mgmL^{-1}$ for the Sartobind Q15 and Nano1mL devices, respectively. At 8.0 $mgmL^{-1}$, these values increased to 59.4 and 58.4 $mgmL^{-1}$, corresponding to an increase in binding capacity of 213% and 178%, as the initial concentration increased. As previously explained, a higher BSA concentration in the phosphate buffer (100 mM) led to an increase in $DBC_{10\%}$/BV.

The binding capacity was less important for the intermediate (Sartobind Q75 and Nano3 mL) and larger scale devices (Sartobind Q100 and Mini). Moreover, the observed breakthrough curves at loading concentration between 0.5 and 8 $mgmL^{-1}$ confirms the result obtained previously at a concentration of 2 $mgmL^{-1}$. At these various loading concentrations, the binding

capacities were lowest with the Sartobind Q75 and Nano3mL devices, due to their higher bed height, respectively 4 and 8 mm.

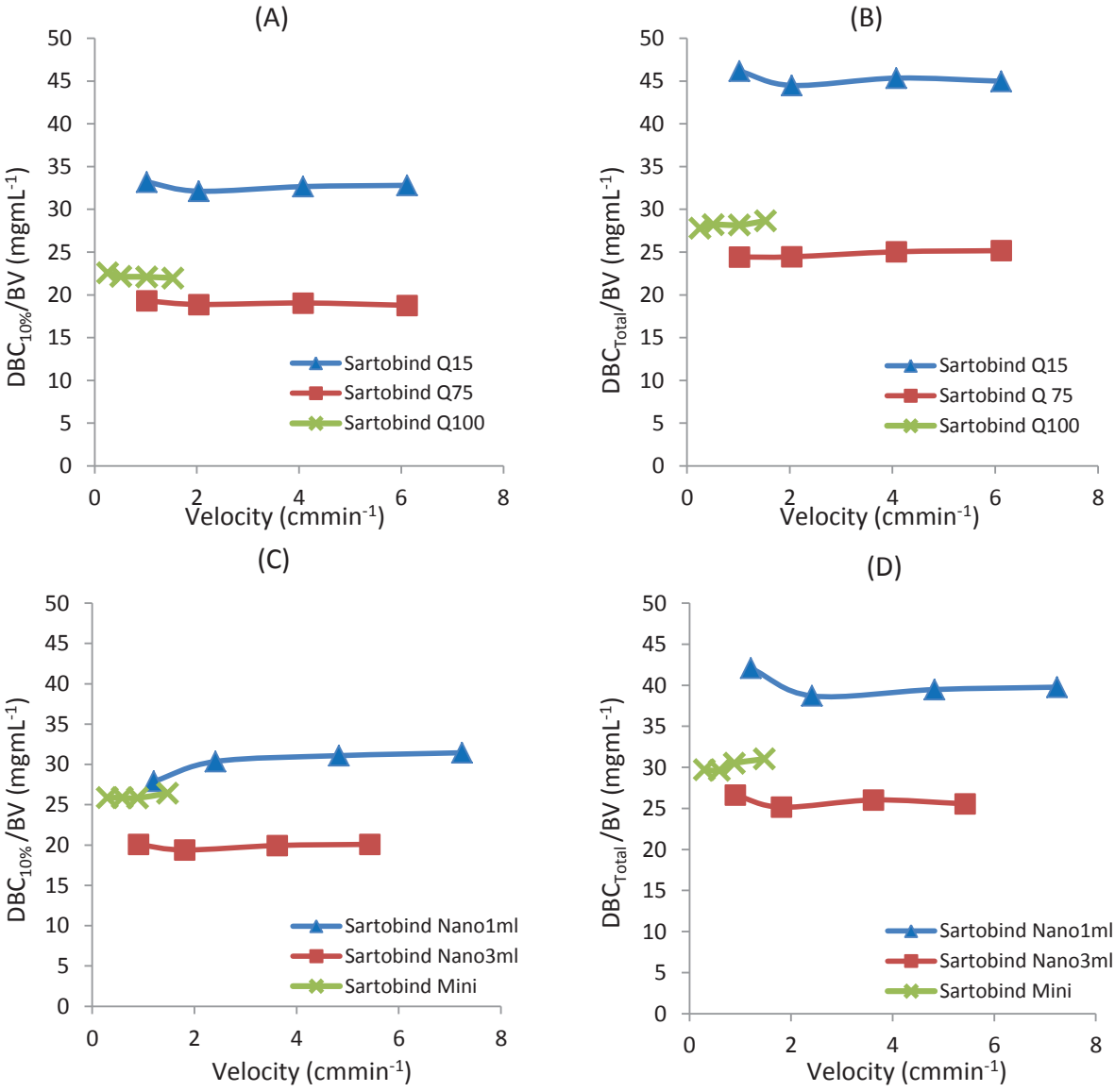

Fig. 2.9 Effect of flow rate for the axial flow devices: (A) dynamic binding capacity at 10% of breakthrough ($DBC_{10\%}$) per BV and (B) dynamic binding capacity at total breakthrough (DBC_{Total}) per BV. For the radial flow devices: (C) $DBC_{10\%}$/BV and (D) DBC_{Total}/BV. BSA loading concentration 2.0 $mgmL^{-1}$.

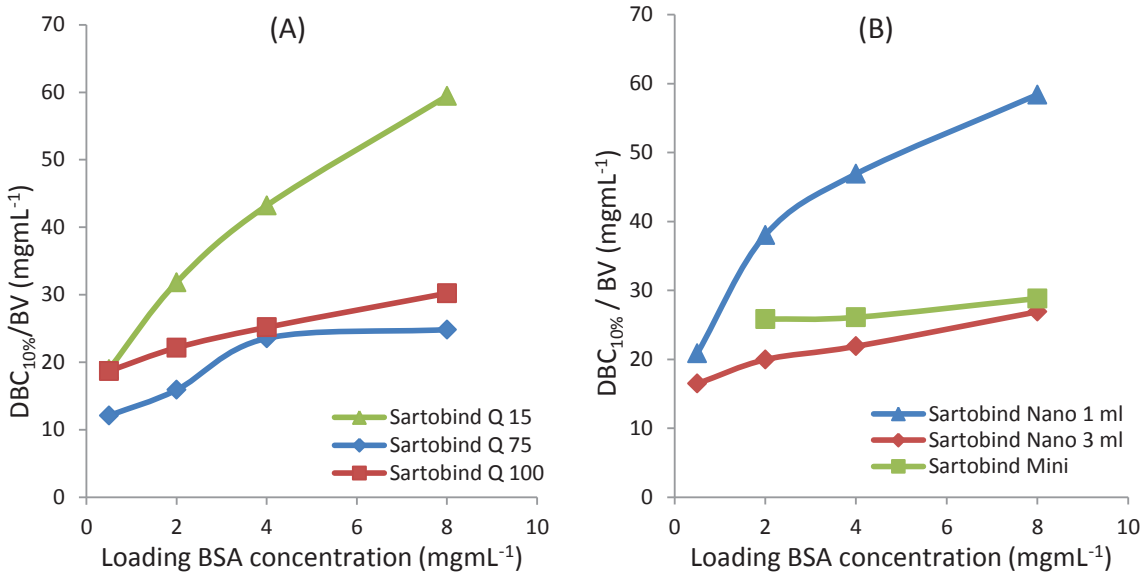

Fig. 2.10 Effect of BSA loading concentration for axial flow devices on the dynamic binding capacity at 10% of breakthrough ($DBC_{10\%}$) for (A) axial flow MC and (B) radial flow MC. Flow rate 10 $mLmin^{-1}$.

2.4.5 Scaling-up of MC devices

For both axial and radial flow, Fig. 2.11 demonstrates the $DBC_{10\%}$ values as a function of bed volume at the different velocity. The $DBC_{10\%}$ values provided by the manufacturer were obtained with the Sartobind Q 15 device at 10 ml/min with BSA in 20 mM Tris/HCl and pH at 7.5. This value (12 mg/unit) compared well with the one obtained in the present study (13 mg/unit). The same result was obtained with the Nano1mL device. At the same experimental conditions, the values provided by the manufacturer (29 mg/unit) compared well with the one obtained in this study.

From Fig. 2.11, it can be seen that the experimental $DBC_{10\%}$ increased nonlinearly as a function of bed volume. Moreover, the difference between experimental and $DBC_{10\%}$ values provided by the manufacturer was larger with the axial flow devices than with the radial flow ones. This may be a consequence of a better flow distribution throughout the radial flow devices than the axial ones. This difference was also slightly higher for the two devices with the higher bed height (Sartobind Q 75 and Nano 3 ml). This may be due to the negative effect of bed height, as previously mentioned.

The radial flow column has potential at large-scale applications, as a short bed height can be combined with a large surface area. Therefore, the axial flow device is scaled up in diameter, while the radial flow device can be scaled up vertically. This allows for the large scale radial flow MC device to be easier to handle than the equivalent axial flow device. Similar conclusions were recently obtained with packed bed resins for the comparison between axial and radial flow chromatography [19]. An advantage of MC devices over resins column is that the height of the

radial flow column may be not limited, contrary to resin packing which may limit the height of the radial flow column.

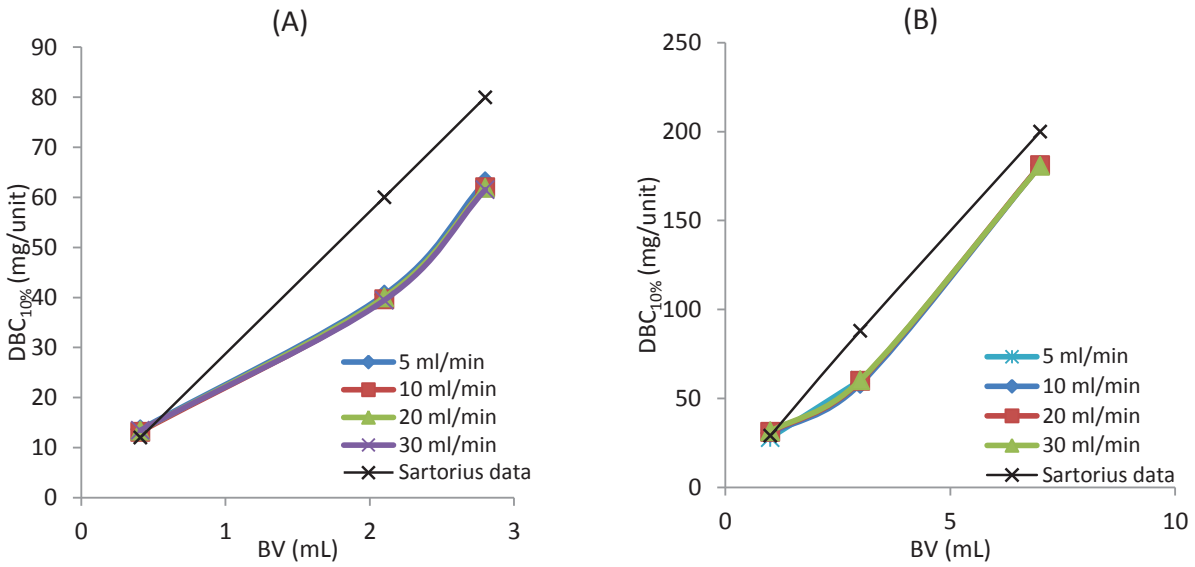

Fig. 2.11 Dynamic binding capacity at 10% of breakthrough as a function of bed volume for different device scales: (A) axial flow devices and (B) radial flow devices.

2.5 Conclusion

In this work, various axial and radial flow anion exchange devices have been selected for their different scales, membrane diameters and bed heights. For the different devices, BSA break-through curves were measured at various flow rates and BSA feed concentrations. It was observed that the BSA dynamic binding capacity at 10% and the total breakthrough capacity were independent upon flow rates for the two geometries at the different scales. This confirms the advantage of MC devices, for which high flow rates can be used without decreasing the dynamic binding capacity. In addition, the dynamic binding capacity increased at higher BSA concentration, which may be due to the competitive adsorption between phosphate ions, at the high concentration used, and BSA.

The axial flow MC devices showed slightly lower pressure drops than the radial flow MC devices at identical flow rates. Moreover, lower Peclet number values were obtained than for axial flow devices, which may be explained by the uneven flow distribution over the membrane surface. In addition, the device with the highest bed height (Sartobind Q75) showed the lowest dynamic binding capacity per membrane volume. This is a main limitation of axial flow devices, for which scaling-up has to rely upon increasing the diameter, which leads to lower velocities. However, the axial flow devices have the advantage to be simplest to produce; they are then preferred at small scale to radial flow devices.

With the radial flow devices, the pressure drop increased slightly with increasing bed height. In addition, slightly higher Peclet numbers were obtained, which may confirm reduced flow non-idealities compared to axial flow devices. As observed for axial flow devices, by increasing the bed height (Nano 3 ml device), the dynamic binding capacity decreased because of non-ideal flow distribution. However, the difference between experimental and theoretical BSA binding capacities, was slightly lower in case of radial flow devices. In addition, the radial flow devices can be scaled up by increasing the length of the radial flow column and not only the bed height. Radial flow devices are then preferred at industrial scales.

2.6 References

[1] S. Brandt, R.A. Goffe, S.B. Kessler, J.L. O'Connor, S.E. Zale, Membrane-Based Affinity Technology for Commercial Scale Purifications, Nat. Biotech. 6 (1988) 779–782. doi:10.1038/nbt0788-779.

[2] C. Boi, Membrane adsorbers as purification tools for monoclonal antibody purification, J. Chromatogr. B. 848 (2007) 19–27. doi:10.1016/j.jchromb.2006.08.044.

[3] C. Charcosset, Membrane Processes in Biotechnology and Pharmaceutics, Elsevier, 2012.

[4] V. Orr, L. Zhong, M. Moo-Young, C.P. Chou, Recent advances in bioprocessing application of membrane chromatography, Biotechnol. Adv. 31 (2013) 450–465. doi:10.1016/j.biotechadv.2013.01.007.

[5] J.X. Zhou, T. Tressel, Basic Concepts in Q Membrane Chromatography for Large-Scale Antibody Production, Biotechnol. Progr. 22 (2006) 341–349. doi:10.1021/bp050425v.

[6] Research and Markets: 9th Annual Report and Survey of Biopharmaceutical Manufacturing Capacity and Production, Reuters. (2012). http://www.reuters.com/article/2012/07/03/idUS126634+03-Jul-2012+BW20120703 (accessed October 10, 2014).

[7] S. Schneiderman, H. Varadaraju, L. Zhang, H. Fong, T.J. Menkhaus, Mathematical model using non-uniform flow distribution for dynamic protein breakthrough with membrane adsorption media, J. Chromatogr. A. 1218 (2011) 9121–9127. doi:10.1016/j.chroma.2011.10.063.

[8] C.-S. Chang, H.-S. Ni, S.-Y. Suen, W.-C. Tseng, H.-C. Chiu, C.P. Chou, Preparation of inorganic–organic anion-exchange membranes and their application in plasmid DNA and RNA separation, J. Membr. Sci. 311 (2008) 336–348. doi:10.1016/j.memsci.2007.12.034.

[9] T. Kawai, K. Saito, W. Lee, Protein binding to polymer brush, based on ion-exchange, hydrophobic, and affinity interactions, J. Chromatogr. B. 790 (2003) 131–142. doi:10.1016/S1570-0232(03)00090-4.

[10] N. Singh, J. Wang, M. Ulbricht, S.R. Wickramasinghe, S.M. Husson, Surface-initiated atom transfer radical polymerization: A new method for preparation of polymeric membrane adsorbers, J. Membr. Sci. 309 (2008) 64–72. doi:10.1016/j.memsci.2007.10.007.

[11] R. Ghosh, T. Wong, Effect of module design on the efficiency of membrane chromatographic separation processes, J. Membr. Sci. 281 (2006) 532–540. doi:10.1016/j.memsci.2006.04.023.

[12] S.E. Bower, S.R. Wickramasinghe, Elimination of non-uniform, extra-device flow effects in membrane adsorbers, J. Membr. Sci. 330 (2009) 379–387. doi:10.1016/j.memsci.2009.01.020.

[13] H.L. Knudsen, R.L. Fahrner, Y. Xu, L.A. Norling, G.S. Blank, Membrane ion-exchange chromatography for process-scale antibody purification, J. Chromatogr. A. 907 (2001) 145–154. doi:10.1016/S0021-9673(00)01041-4.

[14] P. Ghosh, K. Vahedipour, M. Leuthold, E. von Lieres, Model-based analysis and quantitative prediction of membrane chromatography: Extreme scale-up from 0.08 ml to 1200 ml, J. Chromatogr. A. 1332 (2014) 8–13. doi:10.1016/j.chroma.2014.01.047.

[15] K.-G. Briefs, M.-R. Kula, Fast protein chromatography on analytical and preparative scale using modified microporous membranes, Chem. Eng. Sci. 47 (1992) 141–149. doi:10.1016/0009-2509(92)80208-T.

[16] S.H. Huang, S. Roy, K.C. Hou, G.T. Tsao, Scaling-up of affinity chromatography by radial-flow

cartridges, Biotechnol. Progr. 4 (1988) 159–165. doi:10.1002/btpr.5420040306.
[17] M. Puthirasigamany, M. Wirges, T. Zeiner, Membrane chromatography for the purification of laccase from the supernatant of Pleurotus sapidus, Biochem. Eng. J. 70 (2013) 180–187. doi:10.1016/j.bej.2012.11.003.
[18] D. Josić, J. Reusch, K. Löster, O. Baum, W. Reutter, High-performance membrane chromatography of serum and plasma membrane proteins, J. Chromatogr. A. 590 (1992) 59–76. doi:10.1016/0021-9673(92)87006-T.
[19] T. Besselink, A. van der Padt, A.E.M. Janssen, R.M. Boom, Are axial and radial flow chromatography different?, J. Chromatogr. A. 1271 (2013) 105–114. doi:10.1016/j.chroma.2012.11.027.
[20] M.B. J. Tharakan, Ligand efficiency in axial and radial flow immunoaffinity chromatography of factor IX, J. Chromatogr. A. 702 (1995) 191–196. doi:10.1016/0021-9673(94)01141-Z.
[21] M.W. Phillips, Method for determining an effective peclet number for a membrane adsorber device, US7281410 B2, 2007. http://www.google.com.ar/patents/US7281410 (accessed October 2, 2014).
[22] P. van Beijeren, P. Kreis, T. Zeiner, Ion exchange membrane adsorption of bovine serum albumin—Impact of operating and buffer conditions on breakthrough curves, J. Membr. Sci. 415–416 (2012) 568–576. doi:10.1016/j.memsci.2012.05.051.
[23] I.M. Klotz, J.M. Urquhart, The binding of organic ions by proteins. Buffer effects, J. Phys. Chem. 53 (1949) 100–114. doi:10.1021/j150466a008.
[24] L. Song, Influence of phosphate on the adsorption/desorption of bovine serum albumin on nano and bulk oxide particles, University of Massachusetts – Amherst, 2012.
[25] J.D. Teresi, The combination of organic anions with serum albumin. VII. The protein sites involved in the combination, J. Am. Chem. Soc. 72 (1950) 3972–3978. doi:10.1021/ja01165a040.

(This page is intentionally left blank)

Chapter 3

COMPUTATIONAL FLUID DYNAMIC SIMULATION TO CLARIFY THE AXIAL AND RADIAL FLOW DEVICE EFFECT ON PROTEIN ADSORPTION USING MEMBRANE CHROMATOGRPAHY

(This page is intentionally left blank)

Chapter 3
COMPUTATIONAL FLUID DYNAMIC SIMULATION TO CLARIFY THE AXIAL AND RADIAL FLOW DEVICE EFFECT ON PROTEIN ADSORPTION USING MEMBRANE CHROMATOGRPAHY

3.1 Abstract

For the last decades, membrane chromatography (MC) is being seen in many biomolecule purification downstream with several benefits such as fast biomolecule binding behavior, lowered pressure drop, single-use ability, etc. The employment of several MC geometric formats can be achieved such as a stack sheet, a spiral wound, etc. In this chapter, the effect of axial flow and radial flow geometry on the strong ion-exchange MC performance was studied via the experimental approach and numerical simulation using a CFD model. The different scales of axial flow and radial flow devices of the MC Sartobind units from Sartorius Stedim Biotech GmbH (Germany) were compared; two devices having the same diameter and two with the same bed height. The CFD model was developed to predict the breakthrough curves under for both non-binding and binding conditions using an inert tracer as acetone solution and bovine serum albumin (BSA), respectively. The results showed that the CFD model offered much useful information of hydrodynamics and flow distribution inside the MC devices. The accurate prediction of the BSA binding breakthrough curve could be achieved using the CFD model along with the bi-Langmuir isotherm model. Keeping the same kinetic parameters, the BSA binding behavior could be precisely predicted across the different scales and flow configurations. With the increasing bed height of membrane bed, the band-broadening of the breakthrough curve was more pronounced, which corresponded to the experimental results. This negative effect of the increasing bed height could come from the inhomogeneous binding sites of membrane and/or the non-uniform flow distribution, which gave more difficult access of molecules to binding sites at the bottom of the thicker membrane. Thus, the increase in bed height for a large scale MC device should be avoided. The scaling up of the axial flow devices has shifted to the increasing the diameter, which leads to lower velocities. For the radial flow devices, a large scale MC device with a high velocity could be obtained combining a shorter cylindrical length with a larger cylindrical diameter.

Keywords :

Membrane chromatography (MC), Bovine serum albumin (BSA), Breakthrough curve, Radial flow device, Axial flow device, Computational fluid dynamics (CFD) model

3.2 Introduction

Membrane chromatography (MC) has proved successful in biopharmaceutical industry for biomolecules purification due to fast biomolecule binding behavior. The solute transport on MC is conducted principally by convective fluid and is not limited by pore diffusion like in traditional bead-based chromatography [1,2]. High throughput and fast biomolecule purification process can be achieved using MC techniques. Another interest of MC is single-step application due to its generic feature for the membrane filtration, simultaneously with the implementation of liquid chromatography. While traditional chromatography requires extensive prior preparative steps, which may be time-consuming and costly as chromatographic operations [3,4]. Due to MC material properties, the employment of non-conventional geometry devices can be achieved like radial flow chromatography, which has been firstly developed for microfiltration and widely applied today as an alternative to a conventional axial flow chromatography. It is generally accepted that radial flow chromatography provides potential advantages over conventional axial flow devices such as the lowered-pressure drops and an appropriate system for fast-flow systems due to the large cross-sectional area and the short flow path. In axial flow chromatography, there is difficulty in increasing the cross sectional area or in shortening the flow path, because a minimum ratio of bed length to bed diameter has to be maintained to neglect wall effect [5]. Another major feature of radial flow chromatography is its ability to support higher volumetric flow rates than similar volume axial flow chromatography at the same pressure drop. A radial flow device usually provides higher volumetric flow rate, but it does not necessarily have larger linear flow velocities because its frontal area is much larger than axial flow chromatography. Therefore, radial flow chromatography could increase productivity in biomolecule purification processes [6,7].

High scalability was claimed as another advantage of radial flow chromatography that both increasing bed height and diameter could be achieved. For example; Saxena and Dunn [6] reported the scaling-up from 20 to 60 L of column volume using the radial flow column packed with histidyl-sepharose to recover anticoagulant. Similarly, Huang et al. [5] investigated radial flow devices made from modified cellulose to purify trypsin on affinity chromatography with the increasing bed volumes at 250, 800 and 3200 mL. In the study of Jungbauer et al. [8], the scaling-up factor of the radial flow devices was determined for IgG purification using ion-exchange MC. However, the difference between the experimental and predicted elution volume on the largest device was observed. Recently, Puthirasigamany et al. [9] observed around 20% lower BSA binding capacity per bed volume (BV) of the 3 mL radial flow device compared to the 1-mL device. Using axial flow devices, an increase in bed diameter can combine with a short bed height to provide high potential at large scale application. There are many studies that showed the good promising result with this method such as the scaling-up from 10 to 50 mm of bed diameter for DEAE ion-exchange MC [10], the increasing diameter from 15 to 25 mm of nylon-based affinity MC [11] and the increase in diameter from 35 to 45 cm by on diethylaminoethyl cellulose column [10].

MC has been extensively obtained attention from bioprocess industries. Nevertheless, non-uniform flow distribution remains a major limitation for both traditional and membrane chromatographic techniques. Uniform flow in MC is difficult to be obtained due to the difference of the cross-sections between the inlet tube and the membrane bed diameter. This leads to the inefficient flow distribution in membrane bed, which broadens the breakthrough curves and leads to the inefficient performance of MC processes [2,12,13]. In addition, non-ideal flow in MC

arises some difficulties to develop a mathematical model for characterizing the operational process, flow distribution, binding behavior and scaling-up for MC devices. Usually, the mathematical model of MC describes the transport phenomenon only on the membrane adsorbent zone basing on coupling the diffusion-convection equations with the binding kinetics models on the axial flow devices. Typical binding kinetic was represented using the single and multicomponent Langmuir isotherm model to simulate the breakthrough curves on affinity [14] and ion-exchange MC [15,16]. Several other binding kinetic models have been evaluated such as steric hindrance [17], spreading equations [18] and bi-Langmuir adsorption [19]. Many mathematical models have been developed to account for non-uniform flow of MC devices and their external system. For example; Boi et al. [19] considered the effect of non-uniform flow on the dynamic binding behavior of MC devices. The entire operational chromatographic system was taken into account by using a combination in series of an ideal continuously stirred tank reactor (CSTR) and of an ideal plug flow reactor (PFR) model before the MC device. The modeling parameters including CSTR and PFR residence times were determined by fitting the model data to the experimental breakthrough curve under a non-binding condition in order to account for dispersion and a void volume of the external system such as a pump, tubes, etc. The breakthrough curve under a binding condition was simulated using the bi-Langmuir isotherm model on the affinity MC. This approach was further examined to predict the breakthrough curves on the purification of IgG from a complex mixture [20,21]. The simulation results showed a good agreement to the experimental data. In addition, a non-uniform flow at the MC device inlet could be described using a polynomial equation as reported by Schneiderman et al. [23]. The accurate prediction of non-uniform and unsymmetrical breakthrough curves could be obtained. A network of multi-tanks of CSTR connected in series and parallels was introduced as the zonal rate model (ZRM) to describe non-ideal flow in MC devices. The ZRM model was further applied to analyze the hydrodynamics and the performance of the axial flow device under the different operating condition [24,25]. The breakthrough curve prediction was achieved for both axial and radial flow MC [26,27].

A computational fluid dynamic (CFD) model has been recently studied on MC application. Ghosh et al. [28,29] applied a CFD model to describe flow distribution inside a MC device and connected in series with the CSTR and PFR models. This allows separately analyzing the flow distribution from binding kinetic effects by accounting for accurate internal geometry of MC device. Moreover, the CFD model was applied to predict the binding behavior for different geometric device such as axial and radial flow chromatography. However, the comparison between the two devices was not discussed due to the very different scales.

This chapter is aimed to study the effects of axial and radial flow MC devices using both experimental and theoretical approach. The axial flow and radial flow devices are compared using three different commercialized strong anion ion-exchange MC sizes; two devices having the same diameter and two with the same bed height. The theoretical study is investigated using a CFD model to predict non-ideal flow distribution and the breakthrough curves. The breakthrough curves are performed using an inert tracer as acetone and an adsorbed protein as bovine serum albumin (BSA) solution, respectively, for a non-binding and a binding condition. According to the breakthrough prediction under a binding condition, the CFD model and the mass transport equations are resolved by coupling with the different binding kinetics models such as the Langmuir isotherm, bi-Langmuir isotherm and spreading models. Moreover, the CFD model is further studied at the different operating flow rates and BSA loading concentrations. Finally, the influence of flow configurations, scales of MC devices on flow distribution, binding behavior and breakthrough curve characteristics is discussed.

3.3 Theory

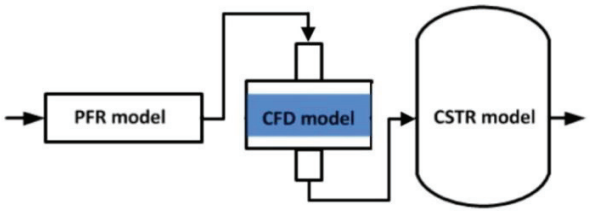

Fig. 3.1 CFD model configuration using a serial connection of a PFR model and CSTR model at inlet and outlet of the MC device, respectively.

The MC modeling could be established using a serial connection of CSTR and PFR model before an inlet of MC device to take dispersion and void volume of MC device and its external system into account [19]. Recently, the CFD model has been used to the MC device to precisely describe the velocity profiles of fluid inside the MC device with a connection of a PFR and CSTR model, respectively, at the inlet and outlet of the MC device as illustrated in Fig. 3.1 [29,30]. The flow through the MC device is influenced by internal geometry of a MC device and porous membrane properties. Thus, the mass transport phenomenon could be described by incorporating the velocity profile simulated from the CFD model. In this study, the numerical simulations were divided into three steps. Firstly, the Navier-Stoke and Brinkman equations were applied to simulate the velocity and pressure drop in a stationary state. The Reynolds number within the membrane is verified below than 10, in which the laminar flow condition can be applied. In the second step, the simulation of the breakthrough curve under non-binding condition was executed using convection-diffusion equations coupled with the CSTR and PFR model. Finally, the different binding kinetic models such as Langmuir isotherm, bi-Langmuir isotherm and spreading model were investigated to predict the BSA breakthrough curve under binding condition.

3.3.1 CFD model

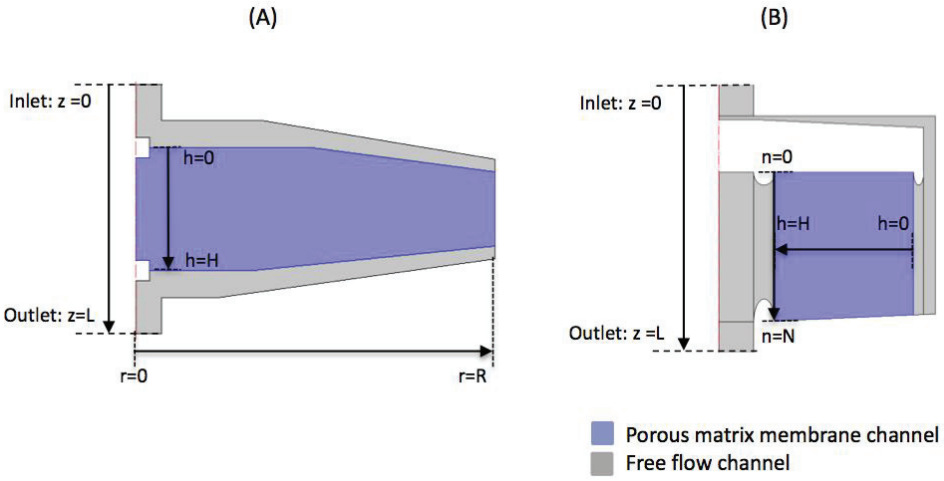

Fig. 3.2 Reconstructed geometry on Comsol software's interface of (A) Sartobind Q75 and (B) Sartobind Nano1mL assuming axial symmetry for both devices. The schematic representation is

composed of free flow channels and porous matrix membrane channels.

The internal geometry of the Sartobind Q75 (axial flow) and Sartobind Nano3mL (radial flow) devices in longitudinal section was reconstructed on Comsol Multiphysics 4.4 software and shown in Fig. 3.2. In the free channels of the MC capsule, the flow velocity (u) and the pressure (P) through the MC device were described using the Navier-Stokes equations at a steady state with negligible force (F=0) as given in Eq.1 and Eq.2:

$$\rho(u.\nabla u) = \nabla.\left[-PI + \mu\left(\nabla u + (\nabla u)^T\right) - \frac{2}{3}\mu(\nabla.u)I\right] \quad \text{Eq.1}$$

$$\nabla.u = 0 \quad \text{Eq.2}$$

where ρ and μ are density and viscosity of the mobile phase, respectively.

In the porous membrane bed, the porous media flow was governed by the Brinkman equations given in Eq.3 and Eq.4:

$$\rho(v.\nabla v) = \nabla.\left[-PI + \mu(\nabla v + (\nabla v)^T) - \frac{2}{3}\mu(\nabla.v)I\right] - \frac{\mu}{\kappa}v \quad \text{Eq. 3}$$

$$\nabla.v = 0 \quad \text{Eq. 4}$$

with v interstitial velocity (u/ε), I identity matrix, κ membrane permeability and ε membrane porosity. Continuity was applied between the fluid velocity and pressure in the free flow and the porous membrane channel. The difference corresponds to the stress adsorbed by the rigid porous matrix, which was implicated in the formulations of the Navier-Stokes and Brinkman equations.

Parabolic velocity (as a function of inlet radial position (r_{in}) divided by the inlet radius (R_{in})) and vanishing viscous stress were used as boundary conditions, respectively, at the inlet (z=0) and outlet (z=L) of the MC device (Eq.5-Eq.6).

$$Inlet \quad z = 0; \quad u = 2(1 - \frac{r_{in}^{\ 2}}{R_{in}^{\ 2}})u_{average} \quad \text{Eq.5}$$

$$Outlet \quad z = L; \quad \mu(\nabla u + (\nabla u))^T = 0 \quad \text{Eq.6}$$

3.3.2 Breakthrough curve simulation

The solute transport was modeled by the traditional diffusion-convection equations in the free channels as described in Eq.7:

$$\frac{\partial c}{\partial t} = \nabla.(D_a \nabla c - u.c) \quad \text{Eq.7}$$

where D_a is an axial diffusion coefficient determined from the correlation of Polson [17], the protein solution was assumed to be infinite. Here, u is the fluid velocity derived from the Navier-

Stokes equations. In the porous membrane regions, the binding kinetic model ($\frac{\partial q}{\partial t}$) was added to describe the protein binding behavior on the membrane support as shown in Eq.8:

$$\frac{\partial c}{\partial t} = \nabla.(D_a \nabla c - u.c) - \frac{(1-\varepsilon)}{\varepsilon}\frac{\partial q}{\partial t} \qquad \text{Eq. 8}$$

Adequate boundary conditions were described to resolve the PDEs. Combination of PFR and CSTR model are applied as illustrated in Fig. 3.1. At the entrance of the device, the inlet concentration is given in Eq.9, where τ_{PFR} is the residence time of the PFR model. At the device outlet (z=L), we assumed negligible dispersion combined with the dynamic concentration measured in the CSTR as shown in Eq. 10, where $\bar{c}$ is the average concentration at the device outlet and $\tau_{CSTR}$is the CSTR residence time. τ_{PFR} and τ_{CSTR} were determined from experiments using non-binding tracer as acetone solution. The simulated breakthrough curve was plotted against time using the average concentration, c_{out} at the outlet of MC device. At the beginning of the process, the mobile phase is free of protein; therefore the initial concentration of proteins is set to zero.

$$Inlet \quad z = 0 \quad ; \quad c = \begin{cases} 0 & t < \tau_{PFR} \\ c_0 & t \geq \tau_{PFR} \end{cases} \qquad \text{Eq.9}$$

$$Outlet \; z = L \quad ; \quad \nabla c = 0$$

$$\frac{\partial c_{out}}{\partial t} = \frac{\bar{c} - c_{out}}{\tau_{CSTR}} \qquad \text{Eq.10}$$

3.3.3 Binding kinetics model

Appropriate kinetic model describing binding of protein is required for solution of Eq. 8-10. Three different binding kinetic models such as the Langmuir model, the bi-Langmuir model and the spreading model as described by many authors [25,31] are compared with respect of their ability to describe the binding of the protein on the ion exchange membrane. The Langmuir reversible rate model is the simplest and most widely used to establish a protein bind kinetic model in dynamic state (Eq.11).

$$\frac{\partial q}{\partial t} = k_a c(q_m - q) - k_d q \qquad \text{Eq. 11}$$

It assumes energetic homogeneity of the adsorption sites without steric effects. Occupation of binding site by an adsorbed protein molecule is supposed not to affect adsorption of newly adsorbed molecules onto other sites. This occurs when the binding site density is so low and the average distance between adjacent sites is larger than the diameter of the adsorbed molecule. The single-component interaction with one type of binding site for solute molecules do not interact with each other [3]. In this model, k_a is the forward adsorption rate constant, k_d the

reverse rate constant and q_m the maximum binding capacity of membrane matrix.

At equilibrium of steady-state ($\frac{\partial q}{\partial t} = 0$), the rate constant can be lumped into a constant $b = \frac{k_a}{k_d}$.

The bi-Langmuir kinetic model (Eq.12) is based on the similar analogy of Langmuir model, but offering two energetically distinct types of independent binding sites as given in Eq.12-1,2 and 3.

$$\frac{\partial q}{\partial t} = \frac{\partial q_1}{\partial t} + \frac{\partial q_2}{\partial t} \qquad \text{Eq. 12-1}$$

$$\frac{\partial q_1}{\partial t} = k_{a1} c(q_{m1} - q_1) - k_{d1} q_1 \qquad \text{Eq. 12-2}$$

$$\frac{\partial q_2}{\partial t} = k_{a2} c(q_{m2} - q_2) - k_{d2} q_2 \qquad \text{Eq. 12-3}$$

Parameters, q_{m1} k_{a1} and k_{d1} represent the binding parameters associated with the high energy binding site 1, and parameters on the binding site 2, q_{m2} , k_{a2} and k_{d2} are associated with the lower-energy binding site 2 [25].

Unlike the Langmuir models, the spreading model allowed the reorientation or conformation of proteins in the adsorption layer. For the case of two adsorbed protein, states 1 and 2 are considered. The following spreading models are described in Eq.13:

$$\frac{\partial q}{\partial t} = \frac{\partial q_1}{\partial t} + \frac{\partial q_2}{\partial t} \qquad \text{Eq. 13-1}$$

$$\frac{\partial q_1}{\partial t} = (k_{a1} c - k_{12} q_1)(q_{m1} - q_1 - \beta q_2) - k_{d1} q_1 + k_{21} q_2 \qquad \text{Eq. 13-2}$$

$$\frac{\partial q_2}{\partial t} = (k_{a2} c + k_{12} q_1)(q_{m1} - q_1 - \beta q_2) - (k_{21} - k_{d2}) q_2 \qquad \text{Eq. 13-3}$$

where q_1 and q_2 are the concentration of bound protein in states 1 and 2, respectively, β is the ratio of the membrane surface area occupied by binding site 2 relative to that on the site 1, k_{12} and k_{21} are the exchange rate between binding sites 1 and 2 and vice versa, respectively, and q_{m1} is the saturation capacity of adsorbed proteins in state 1. To simplify this model, we assumed that the protein from the bulk cannot adsorb directly to state 2, therefore $k_{a2}=k_{d2}=0$.

3.4 Materials and methods

3.4.1 Experimental materials and methods

MC devices from Sartorius Stedim Biotech GmbH (Germany) were performed under frontal analysis to achieve breakthrough curve. They contain the same membrane characteristic; a stabilized reinforced cellulose matrix with quaternary ammonium group to functionalize as a strong anion exchanger. Sartobind Q15, Q75 and Q100 are considered as the axial flow devices and contain different membrane layer numbers and thus bed heights. The diameters of Sartobind Q15 and Q75 are identical at 25.00 mm, but the bed height of Sartobind Q75 (4.00 mm) is greater than Sartobind Q15 (0.80 mm). They contained respectively 15 and 3 layers of membrane. Sartobind Q100 has the largest diameter of the membrane disc at 50.00 mm. For the radial flow devices, Sartobind Nano1mL, Nano3mL and Mini containing different membrane wound volumes were studied. Nano1mL and Nano3mL have the different bed heights, which are 4.00 and 8.00 mm, respectively, whereas Nano1mL and Mini have the same bed height, but difference in the cylindrical height that the one of Sartobind Mini is at 30.00 mm [32]. The full characteristics and dimensions of all MC device used in this study can be found in the previous paper [33].

The experiments were conducted to observe the breakthrough curves under a binding condition using BSA lyophilized powder with the purity ≥ 98.00% (MP Biomedical France), which was dissolved in 10 mM potassium phosphate buffer pH 7.0. Phosphate buffer solution pH 7.0 was prepared by adjusting good portion of volume between K_2HPO_4 and KH_2PO_4 (Sigma Aldrich, France) and subsequently filtered through a 0.45 µm hydrophobic membrane filter with a 0.45 µm pore size (Millipore, France). Afterward, the bound protein was collected using 1.00 M NaCl diluted in the buffer solution, bound BSA was therefore eluted due to the increasing ion strength effect. In addition, 5.00 $\%_{vol}$ acetone solution diluted in the buffer solution was prepared as an inert tracer to observe the system dispersion and the void volume. All experiments were performed under the AktaPrime-Plus chromatography system (GE Healthcare Life Sciences, France) with a UV-280nm absorbance and conductivity online measurement. The membrane was cleaned and regenerated following the instructions from Sartorius, that 1.00 M NaOH was circulated through MC device for one hour with the flow rate of one bed volume $(BV)min^{-1}$, followed by the buffer and elution buffer for 10 minutes of each solutions at 10.0 $BVmin^{-1}$ [34]. All other reagents used in this study were obtained from Sigma Aldrich (France).

To obtain the accurate internal geometry and dimension of each MC device, the magnetic resonance imaging (MRI) visualization was applied using the 4.7 tesla Bruker Biospec MRI device with the 156/100/S Magnex SGRAD gradient set and the coil receiver was the Rapid Biomedical Quadrature. The MRI visualization examples of the internal geometry of Sartobind Q75 and Nano1mL were shown in Fig. 3.3, which show the porous membrane bed and void volume channel in the devices.

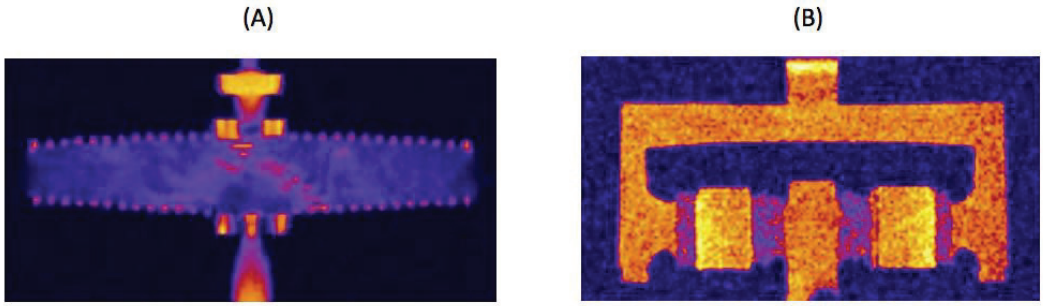

Fig. 3.3 Internal geometry of (A) the axial flow Sartobind Q75 device and (B) the radial flow Sartobind Nano1mL device elucidated by MRI visaulization technique.

3.4.2 Numerical methods

Entire system of coupled partial differential equations (PDEs) to simulate the breakthrough curves of membrane chromatography devices was implemented by Comsol Multiphysics 4.4 using a finite element method (FEM) as discretization method. In this work, the MC internal device geometry was measured by MRI device and reconstructed on Comsol Multiphysics 4.4 geometry interface assuming axial symmetry for the MC devices. This assumption allows computing explicitly the mathematic models only to a half of MC capsule into 2D longitudinal section employing cylindrical coordinate system (r,ϕ,z), which reduces simulation time requirement.

The CFD model was executed initially to simulate velocity and pressure profiles using Navier-Stokes and Brinkman's equation in a stationary state. In the study of Tatárová [35], the common type of membrane was investigated to measure the porosity and also the permeability. Using the same membrane type and buffer solution condition, the porosity of 0.78 and the permeability of 10^{-13} m^2 were applied in this study. Next, the dynamic breakthrough curves were computed using a time-dependent state for both non-binding and binding condition. To capture the non-ideal flow in MC devices, the velocity profiles were integrated and explicitly taken into account. The dynamic breakthrough curves under the binding condition were predicted by executing simultaneously two PDE systems; the diffusion-convection equations and the binding kinetic model. Binding kinetic model parameters were obtained by minimizing the sum of square deviation between simulated result and experimental data under 2.00 $mgmL^{-1}$ of a BSA loading concentration and 5.0 $mLmin^{-1}$ of a flow rate. An optimization method employed was SNOPT algorithm, which is based on a gradient-based optimization technique enhancing optimal solutions to a very general class of optimization problems.

3.5 Result and discussion

3.5.1 Flow distribution and pressure drops

The simulated velocity field and pressure drop was obtained using CFD model in the stationary state at the feed flow rate (Q) of 5.0 mLmin^{-1}. The CFD velocity of the Sartobind Q100 device was compared with the Nano3mL device because of their close membrane areas of 100 and 110 cm^2, respectively. The velocity fields of these two devices were illustrated in Fig. 3.4. The flow distribution was non-ideal in the free-flow channels before and after membrane stack in the Q100 devices as observed in Fig. 3.4-A. In the Nano3mL device, the non-ideal flow distribution was observed in the porous membrane region due to the high velocity reflected from narrower outlet channel (Fig. 3.4-B).

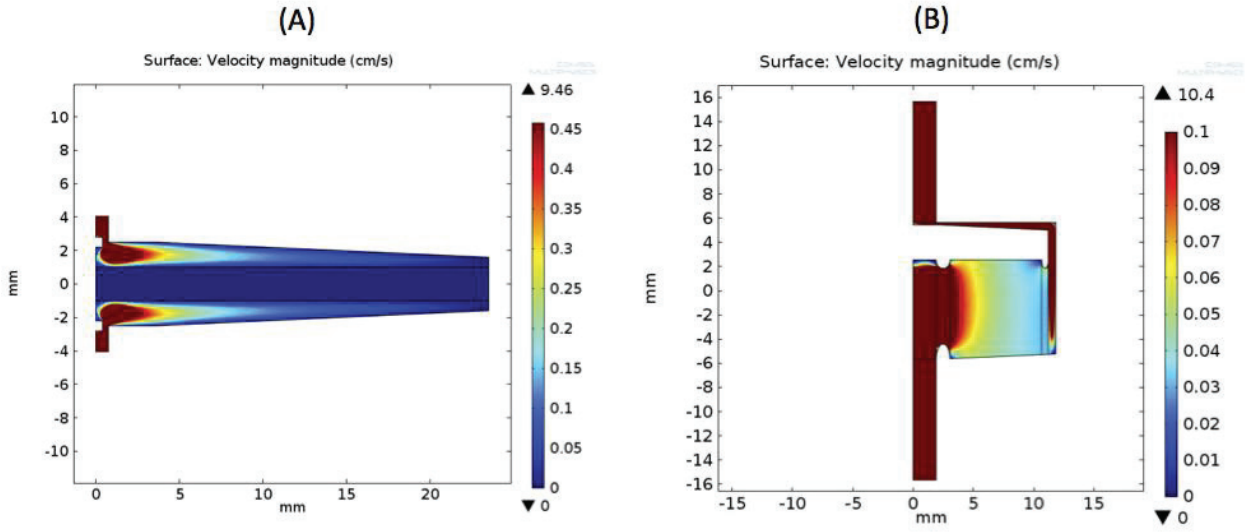

Fig. 3.4 Simulated velocity profiles using the CFD model at 5.0 mLmin^{-1} with (A) the axial flow Sartobind Q100 device and (B) the radial flow Sartobind Nano3mL.

The average velocities in the porous membrane regions of the different MC devices were estimated and given in Table 3.1. Using the axial flow devices, the average velocities were relatively low from 5.87x10^{-3} to 0.0231 cms^{-1}, which were depended principally on the membrane diameter. The radial flow capsules could conduct higher velocities between 0.00635 and 0.0539 cms^{-1}, depended on the cylindrical length. It can be concluded that a larger frontal area of membrane decreased significantly a velocity such as increasing membrane diameter and increasing spiral wound height (N), respectively, on the Sartobind Q100 and Mini devices.

Additionally, pressures drops for all MC devices were calculated at 5.0 mLmin^{-1} in Table 3.1. Low pressures drop between 800 and 9050 Pa was obtained using the axial flow capsules due to the identical flow direction between the inlet and outlet of these devices. Higher pressure drops were observed using the radial flow devices because the flow is perpendicularly directed to the inlet and outlet. The increasing membrane bed height leads to the important increase in pressure drop as observed for Sartobind Q75. It is worth noting that a lower pressure drop on Sartobind Nano3mL could be maintained along with higher linear velocity, which proved a good promise of the radial flow device.

With this result, it could be assumed that the radial flow device is more favorable to carry higher velocity compared to the axial flow devices at the same membrane surface area. The large scale of the radial flow devices could be obtained with a high velocity ($u=Q/\pi ND$) combining a shorter vertical length (N) with a larger cylindrical diameter (D), while the large volume of axial flow devices has to rely upon increasing the diameter, which leads to the decreased velocity ($u=Q/\frac{\pi}{4}D^2$). In addition, increasing linear velocity could be achieved by reducing the free-flow channel path as in Sartobind Nano3mL. This offers also optimized void volume, which permits economical buffer solution consumption used in a purification process.

Table 3.1 Average velocity and pressure drops estimated by CFD model in the porous membrane zone for each MC devices with the flow rate at 5.0 $mLmin^{-1}$.

MC devices	**Axial flow devices**			**Radial flow devices**		
	Sartobind Q15	Sartobind Q75	Sartobind Q100	Sartobind Nano1mL	Sartobind Nano3mL	Sartobind Mini
Average velocity in porous membrane zone (cms^{-1})	0.0210	0.0231	0.00587	0.0420	0.0539	0.00635
Pressure drop (Pa)	$1.84x10^3$	$9.05x10^3$	806	$3.36x10^4$	$2.95x10^4$	$5.95x10^3$

3.5.2 Simulated Breakthrough curves under non-binding condition

The predicted breakthrough curve under a non-binding condition at 5.00 $mLmin^{-1}$ using acetone solution at 5.0%$_{vol.}$ was compared to the experimental data as shown in Fig. 3.5. The optimized model parameter values of τ_{PRF} and τ_{CSTR} of the different MC devices were given in Table 3.2. We observed that the values of τ_{PRF} correspond to the dead volume of the external system; Aktaprime-plus, which was around 4-5 mL. The CFD model could match closely to the experimental results of the axial flow (Fig. 3.5-A) and radial flow devices (Fig. 3.5-B). From the previous study, flow distribution and MC design efficiency can be analyzed from experimental breakthrough curves under non-binding condition [23,36]; however they displayed almost the same breakthrough characteristics with identical sharpness. Moreover, the breakthrough curves may occur early or later depending adequately on volume of membrane devices and their external system. This method provides therefore a drawback that could not give enough information to analyze clearly the flow distribution. More complex mathematical model as CFD model should be a fair approach to verify the influence of axial and radial flow chromatography.

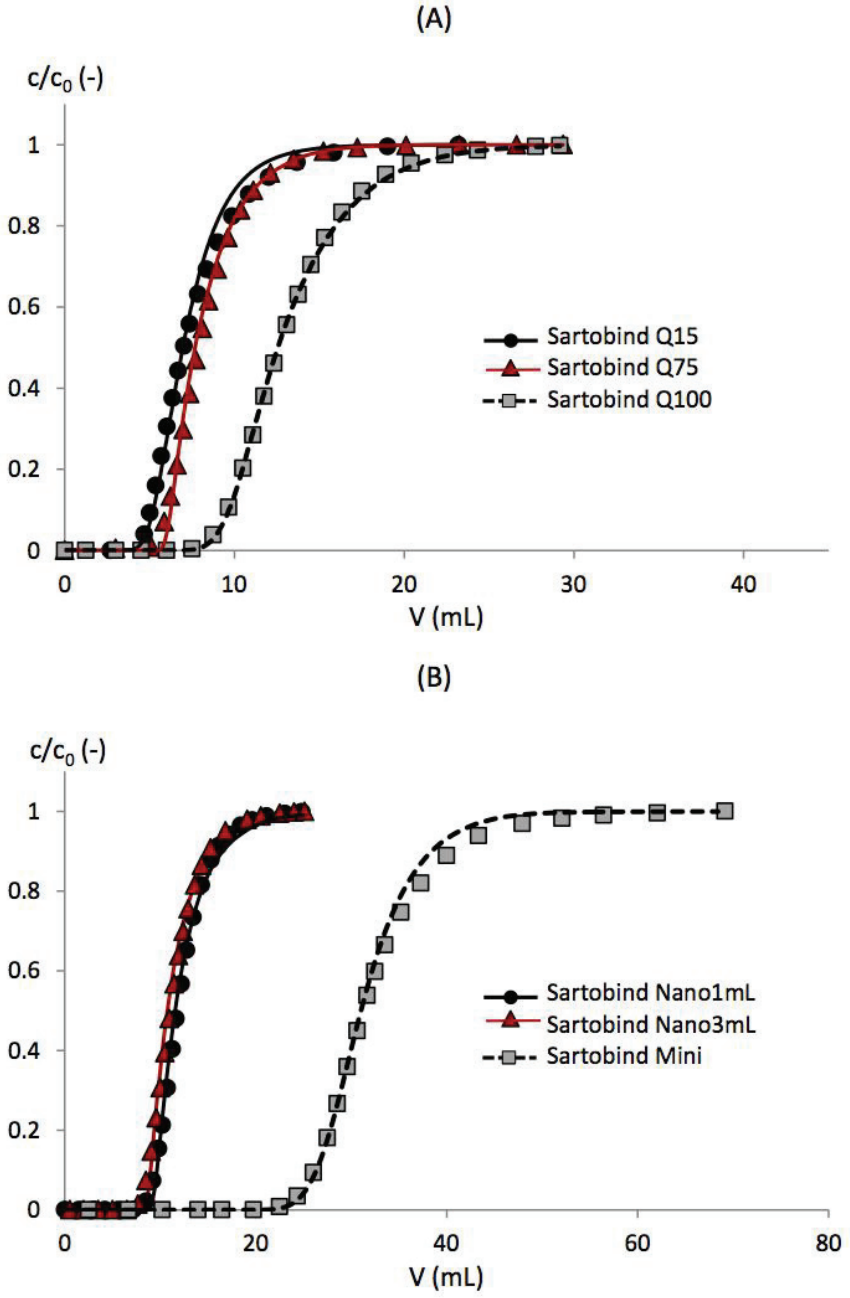

Fig. 3.5 Predicted and experimental breakthrough curves under a non-binding condition using $5\%_{vol}$. of acetone solution for (A) the axial flow devices and (B) the radial flow devices at 5.0 $mLmin^{-1}$. For eache curve, the line represents CFD model result and the point marks are experimental data.

Table 3.2 Optimized model parameter to predict the breakthrough curves under non-bining for the difference MC devices at 5.0 $mLmin^{-1}$ using $5_{\%vol.}$ acetone solution.

MC devices		τ_{PFR} (mL)	τ_{CSTR} (mL)
Axial flow devices	Sartobind Q15	4.596	2.518
	Sartobind Q75	4.901	2.428
	Sartobind Q100	5.346	4.523
Radial flow devices	Sartobind Nano1mL	5.766	1.095
	Sartobind Nano3mL	5.266	3.095
	Sartobind Mini	6.714	5.850

3.5.3 Simulated breakthrough curves under binding condition

CFD model was simulated using different binding kinetic models to predict dynamic breakthrough curves under a binding condition. The model parameters were estimated by fitting the experimental data and the ones obtaining from the CFD model with the Sartobind Q75 device at a flow rate of 5.0 $mLmin^{-1}$ and BSA loading concentration of 2.00 $mgmL^{-1}$. The values of binding kinetic parameters were shown in Table 3.3 with the values of objective function. The best fitting breakthrough curve results were shown in Fig. 3.6, the simple Langmuir isotherm model matched the experimental breakthrough curve upto 70% of breakthrough and failed to predict the observed tailing before membrane saturation. More complex binding models such as bi-Langmuir isotherm and Spreading model were shown to improve this error [25,28]. Predicted breakthrough curves using CFD model along with bi-Langmuir isotherm and spreading model matched closely the experiment data and improve accuracy by vanishing error of tailing prediction. The best result was obtained using the bi-Langmuir binding kinetic model, which leads to the lowest objective function. This implied inhomogeneous binding site of MC, including non-uniform membrane porosity, membrane thickness, and ligand grafting, thus at the model with at least two different binding sites like bi-Langmuir was required to predict the BSA binding behavior on MC. Moreover, the already adsorbed proteins during a certain loading step could reduce the accessibility of the binding sites, the slower binding rate near the saturation was therefore observed.

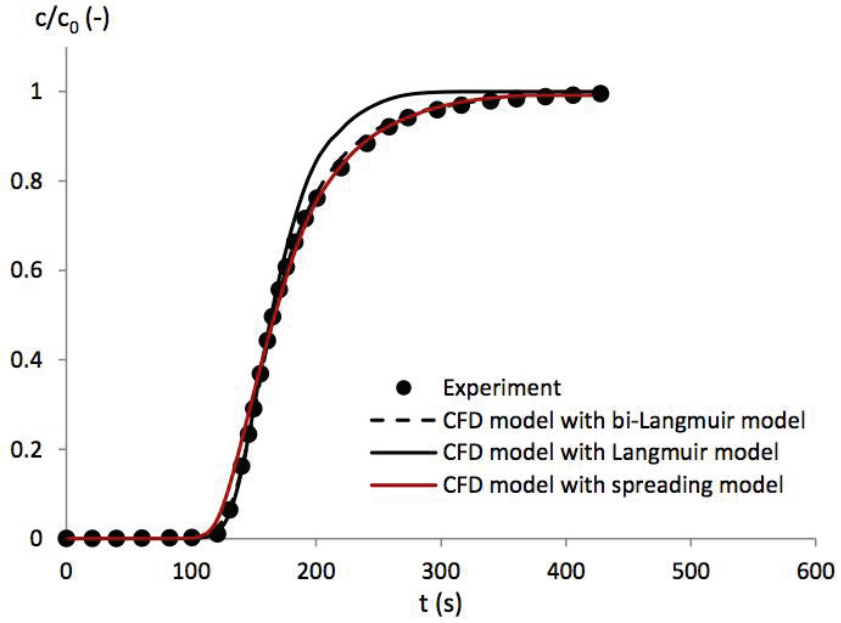

Fig. 3.6 Comparison between the experimental and simulated BSA breakthrough curves under binding condition using different binding kinetic models; Langmuir isotherm, bi-Langmuir isotherm and spreading models for the Sartobind Q75 device at a flow rate of 5.0 mLmin^{-1} and a BSA loading concentration of 2.00 mgmL^{-1}.

Table 3.3 Optimized parameter values of the different binding kinetic model by fitting the CFD result to the experimental BSA breakthrough curves under a binding condition with Sartobind Q75 at a flow rate of 5.0 mLmin^{-1} and a BSA initial concentration of 2.00 mgmL^{-1}.

Binding kinetic models	**Optimized model parameters**	**Sum of square deviation**
Langmuir isotherm model	k_a = 0.043 mLmg^{-1}s^{-1} k_d = 7.49x10^{-5} s^{-1} q_m=223.81 mgmL^{-1}	6.849
Bi-Langmuir isotherm model	k_{a1} = 0.0498 mLmg^{-1}s^{-1} k_{d1} =6.74x10^{-5} 1/s q_{m1} = 172.718 mgmL^{-1} k_{a2} = 0.0062 mLmg^{-1}s^{-1} k_{d2} =7.49x10^{-6} s^{-1} q_{m2} = 74.022 mgmL^{-1}	0.0276
Spreading model	k_{a1} = 0.0607 mLmg^{-1}s^{-1} k_{d1} =6.741x10^{-5} s^{-1} q_m = 246.74 mgmL^{-1} k_{12} = 0.1488 mLmg^{-1}s^{-1} k_{21} = 0.0372 mLmg^{-1}s^{-1} β=1.62	0.0376

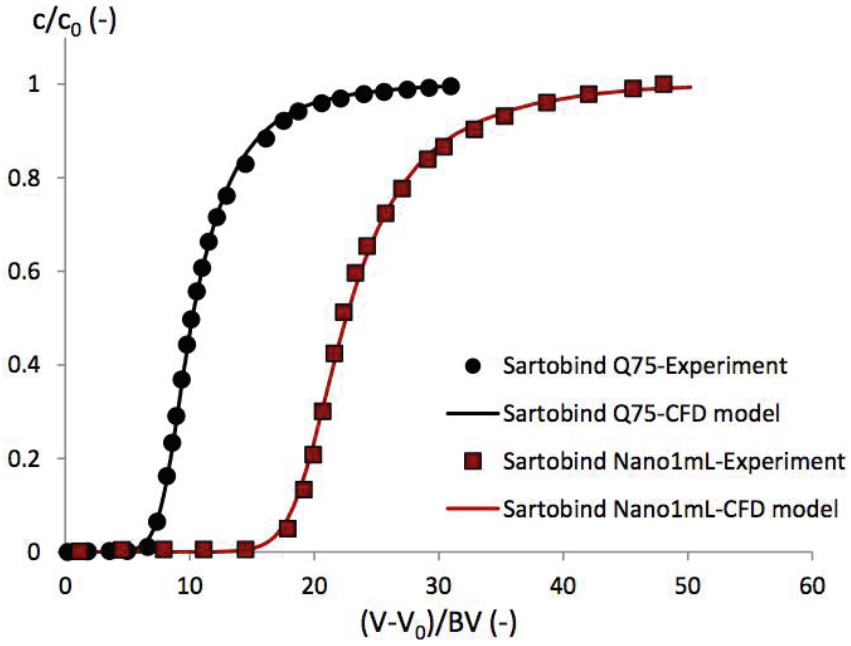

Fig. 3.7 Simulated and experimental BSA breakthrough curves under binding condition for the Sartobind Q75 and Sartobind Nano1mL devices using the identical values of bi-Langmuir isotherm model parameters at of 5.0 mLmin^{-1} of flow rate and 2.00 mgmin^{-1} of BSA loading concentration.

Verifying scalability of the CFD model to predict different size and geometry of MC capsule is essential to validate model performance and robustness. The CFD model was carried out with the different MC devices using the bi-Langmuir model. At the same operating condition, the predicted breakthrough curve on the radial flow device was investigated and compared to the experimental data keeping the same bi-Langmuir parameter values, which were estimated from the axial flow Sartobind Q75 device. The same kinetic parameters obtained were therefore used to simulate the Sartobind Nano1mL device; the results from predicted breakthrough curve using CFD model and experimental data were compared in Fig. 3.7. No difference of the BSA binding characteristics between axial and radial devices may be concluded. When the accurate internal geometry and hydrodynamics were taken into account, the breakthrough curves could be predicted precisely for both axial and radial flow devices. This illustrates the ability of CFD model to predict the breakthrough data in an alternative geometry by including the binding geometry parameter values estimated from the traditional geometry. The influence of MC device geometry on the breakthrough curves under binding condition could be investigated by comparing the breakthrough curves of Sartobind Q75 and Nano1mL (Fig. 3.7), both of them have the same bed height (H) at 4.0 mm. The radial flow Nano1mL device shows higher BSA binding capacity as the breakthrough curve happened later. From the previous paper, the dynamic binding capacity at 10% breakthrough ($DBC_{10\%}$) per BV for Nano1mL was about 30 mgmL^{-1}, while it reduced to 20 mgmL^{-1} for Q75 [33]. Therefore, the radial flow devices could be more preferential with higher binding capacity than the axial flow devices with the same bed height.

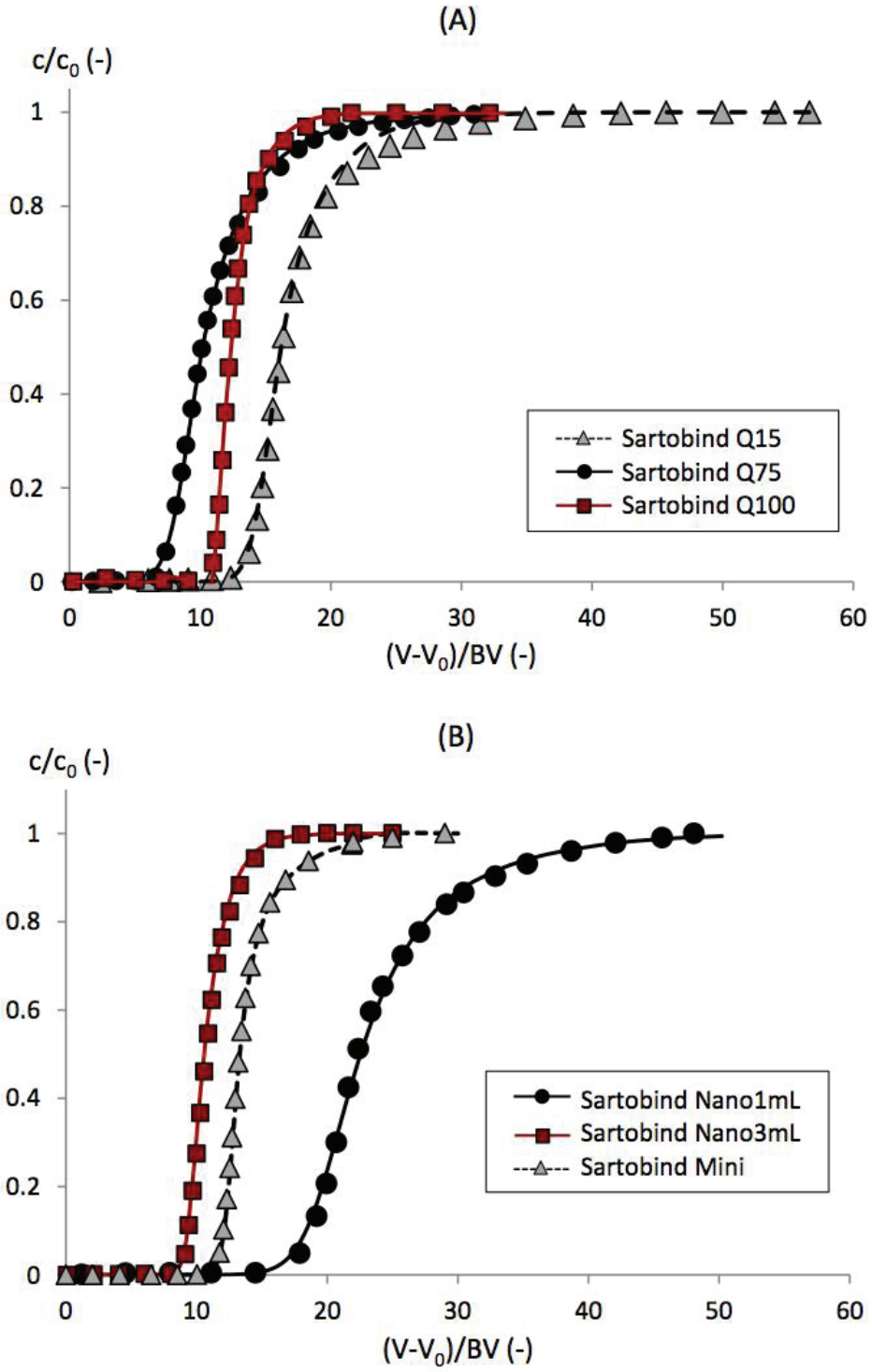

Fig. 3.8 Predicted and experimental BSA breakthrough curves using CFD model along with the bi-Langmuir isotherm model for the different scales of (A) the axial flow devices and (B) the radial flow devices at a flow rate of 5.0 $mLmin^{-1}$ and a BSA loading concentration of 2.00 $mgmL^{-1}$.

The CFD model followed closely the experimental breakthrough curves for all scales of the axial and radial flow devices as displayed in Fig. 3.8, the breakthrough curves were compared by plotting c/c_0 as a function of the loading volume (V) corrected by the void volume (V_0) divided by BV. An increase in bed height (H) from 1.4 mm (Sartobind Q15) to 4.0 mm (Sartobind Q75) for axial flow devices and from 4.0 mm (Sartobind Nano1mL) to 8.0 mm (Sartobind Nano3mL) for radial flow devices decrease the BSA binding capacity per BV, as the breakthrough curves for Sartobind Q75 and Nano3mL appeared earlier compared to the other axial flow and radial flow devices, respectively. The smallest BV devices as the Sartobind Q15 and Nano1mL provided the most significant BSA binding capacity as their breakthrough curves occurred later. The limitation of increasing bed height on MC scaling-up have been previously reported [15,17,45-46]. A larger surface area could provide the same binding capacity per BV, therefore, the axial flow device can be scaled up in diameter (increasing R), while the radial flow devices is scaled up vertically (increasing N). The negative effect of increasing bed height could be captured using CFD model that the simulation results match very well to the experimental data.

3.5.4 Breakthrough curves simulation at different operating conditions

The objectives here were to expand the CFD model along with the bi-Langmuir isotherm model for the different operating conditions. The study was investigated the breakthrough curves under a binding condition at the flow rates at 5.0, 10.0, 20.0 and 30.0 $mLmin^{-1}$ for Sartobind Nano1mL, when the BSA loading concentration was at 2 $mgmL^{-1}$. The study of Shiosaki et al. [16] and Francis et al. [25] observed that q_m increased with the increasing flow rate in the low flow rate operational regime for ovalbumin adsorption on ion exchange MC. Françis et al. [25] showed the breakthrough curve prediction using the zonal rate model along with bi-Langmuir model that $q_{m,1}$ and $q_{m,2}$ were estimated at different values to match the experiment result at different flow rates.

In this study, the experimental part from the previous paper has proved that there was no flow rate effect on the binding capacity of BSA for the Sartobind devices [33], this means the same amount of BSA was bound on the membrane in shorter time with the increasing flow rate. Here, we supposed that the biding rate constant was increased with the higher flow rates, which allowed us to adjust the values of k_a and k_d at the different flow rates as given in Eq. 14 and 15, respectively.

$$k_{a,f} = k_{a,s}\frac{Q_f}{Q_s} \quad \text{Eq. 13}$$

$$k_{d,f} = k_{d,s}\frac{Q_f}{Q_s} \quad \text{Eq. 14}$$

where $k_{a,s}$, $k_{d,s}$ and Q_s are the optimized parameters at the standard flow rate using the flow rate of 5.00 $mLmin^{-1}$ in this study and $k_{a,f}$, $k_{d,f}$ and Q_f are the linear adjusted parameters at the different flow rate. The values of $q_{m,1}$ and $q_{m,2}$ for bi-Langmuir model were constant for all operating flow rates.

In Fig. 3. 9(A), the breakthrough curve at the higher flow rate reached faster to the membrane saturation without any effects on the binding behavior. Again, this confirms the main advantage of MC to carry out at a high flow rate with a significant binding capacity. Fig. 3. 9(A)

illustrates the good agreement between the CFD simulation (line) and experimental (point marks) breakthrough curves for all flow rates of 5.0, 10.0, 20.0 and 30.0 $mLmin^{-1}$ with the Sartobind Nano1mL device. The CFD method offers therefore a fast breakthrough curves prediction with the simple parameter estimation. However, we realized that the adsorption isotherm parameters, k_a and k_d cannot be changed against flow rates according to the Langmuir isotherm model. Here, the values of the constant of Langmuir model like b, which is the ratio of k_a to k_d, were still identical at the different flow rates, which correspond to the Langmuir isotherm principle. Currently, the CFD model is developing to avoid the adjustment of the sorption rate constants.

In addition, the influence of BSA loading concentrations on the breakthrough curves was investigated at 2.0, 4.0 and 8.0 $mgmL^{-1}$ with a flow rate of 10 $mLmin^{-1}$. As observed previously, the breakthrough curve shape was unaffected by the loading concentration [33]. However, the BSA binding capacity was increased with the higher feed concentration. Therefore, the breakthrough curves plotted against the loading volume (V) corrected by the void volume (V_0) appeared earlier and reached faster to the saturation membrane using the higher loading concentration as illustrated in Fig. 3. 9(B). The CFD model coupled with the bi-Langmuir model was able to reproduce the experimental breakthrough curves at different BSA loading concentrations. The kinetic parameters of bi-Langmuir used are the one shown in Table 3.3 without any adjustment. Again, this confirms the performance of CFD model to predict binding behavior for MC at the different operating conditions.

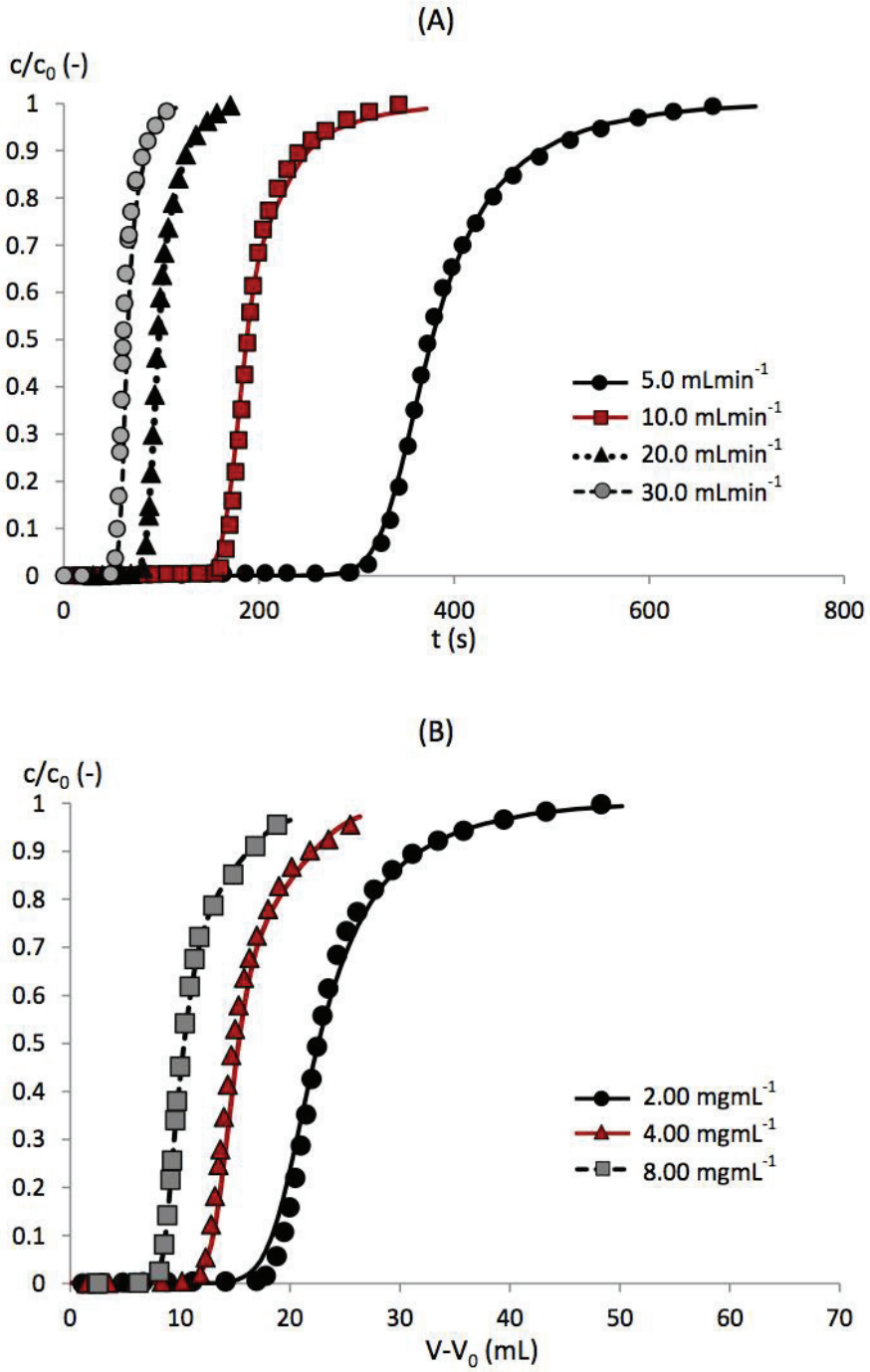

Fig. 3. 9 Predicted and experimental BSA breakthrough curves under binding condition for the Sartobind Nano1mL device under (A) the different operating flow rates, when a BSA loading concentration is at 2.00 $mgmL^{-1}$ and (B) the different BSA loading concentrations, when a flow rate is at 10.0 $mLmin^{-1}$. For each curves, the line is CFD model with bi-Langmuir isotherm model and the mark points are experimental data.

3.5.5 In-bed breakthrough curve simulation

In-bed breakthrough curves were observed using the CFD model along with bi-Langmuir model at the different positions in membrane bed to verify the origin of band-broadening and decreasing binding capacity with the higher bed height. The CFD model was simulated at a flow rate of 5.0 $mLmin^{-1}$ and a BSA feed concentration of 2.00 $mgmL^{-1}$ for the high bed height devices; the Sartobind Q75 (H=4.00mm) and Sartobind Nano3mL (H=8mm) devices. The in-bed breakthrough curves were plotted as a function of axial or radial position and time. Moreover, the predicted velocity at the same operating condition was investigated at the different membrane positions.

Using the axial flow Sartobind Q75 devices, the bed height (h) influence was studied at the radius of membrane (r) at 5.00 mm. In Fig. 3.10-A, the delay of in-bed breakthrough positions was observed with the increasing bed height (h), because there was a transition of solute transport time to reach to the different positions of h. However, the breakthrough curve shape was sharp and increased vertically at the membrane frontal surface, h=0. This was similar to the ideal PFR model. The effect of increasing bed height was observed on more dispersed and broader breakthrough curves. The explanation of the breakthrough shape change with the increasing bed height could be from the inhomogeneous binding sites as the bi-Langmuir model used and the non-uniform flow at the different bed height position as shown in Fig. 3.10- C.

Furthermore, the effect of membrane diameter (d) was examined, when h=2.00 mm. With the fluid distributor of Sartobind Q75, the solute fluid was forced to distribute radially all over the membrane surface and reach rapidly to the outer surface (increasing r). Therefore, we observed that the fluid reached faster to the outer surface with higher velocity at r=10.00 mm as the breakthrough curve occurred earlier (Fig. 3.10-B), whereas the breakthrough curves occurred later at the center region of membrane (r=0 mm). These results correspond to the velocity profile along with the radial positions as shown in Fig. 3.10- D. The decreasing velocity was found at the center of membrane (r=0 mm) and it increased with the increasing r. However, the breakthrough curve shape was almost identical all over the membrane diameter. We observed a change in breakthrough curve shape at the center (r=0.00-1.00 mm) and outer surface (r=5.00-10.00 mm) of membrane, where the velocity change was observed at this area.

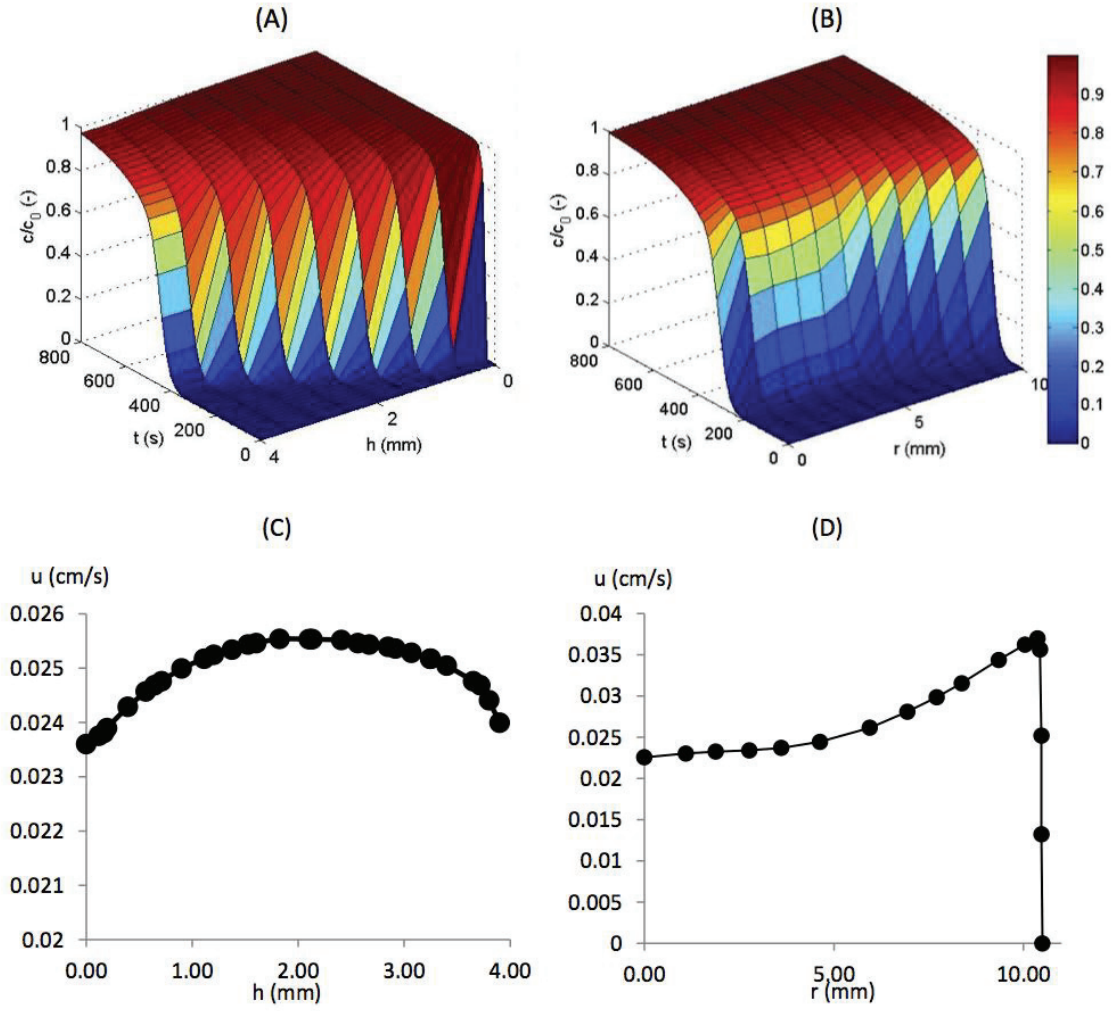

Fig. 3.10 Simulated BSA breakthrough curves under a binding condition for the axial flow Sartobind Q75 device with a flow rate of 5.00 mLmin^{-1} and a BSA loading concentration of 2.00 mgmL^{-1} at (A) the different bed heights, when the radius of membrane (r) is at 5.00 mm and (B) the different r, when h=2.00 mm. The predicted velocity (u) using CFD model at 5.00 mLmin^{-1} in the function of (C) u=f(h), when r=5.00 mm and (D) u=f(r), when h=2.00 mm.

Using the radial flow Sartobind Nano3mL device, the bed height (h) effects were studied at the cylindrical wound height (n) of 4.00 mm. The similar effects to the Sartobind Q75 were observed on the delay breakthrough curve positions (Fig. 3.11-A). The increasing band-broadening of breakthrough curve with the increasing bed height (h) was found on the radial flow device. However, the bed height effects on the broad breakthrough curves were less significant and the breakthrough curve for Sartobind Nano3mL at r=8.00mm reached more rapidly to the saturation compared to the Sartobind Q75 at r=4.00mm.

The velocity profile was plotted along with h in Fig. 3.11-C. The increasing velocity at higher h was found due to the narrow channel at the outlet of radial flow device. Moreover, the breakthrough curves along with the vertical positions (n) were studied at h=4.00. It was observed that the shapes and positions of the breakthrough curves were almost identical for all of n. There was a little change and delay of the breakthrough curves at the upper (n=0.00-1.00 mm) and lower part (n=6.00-8.00 mm) of the spiral wound. This was a consequence of the turbulence effect near the walls of device as the velocity was rapidly decreased to zero at these points. However, the velocity profile along with n positions was uniform around 0.07 cms^{-1} as displayed in Fig. 3.11-C. Therefore, the radial flow device has potential to distribute more uniform flow all over the membrane frontal surface compared with the axial flow device. The negative bed height effect on the binding capacity and broaden breakthrough curves was less important, which offer high performance at large scale applications for the radial flow devices.

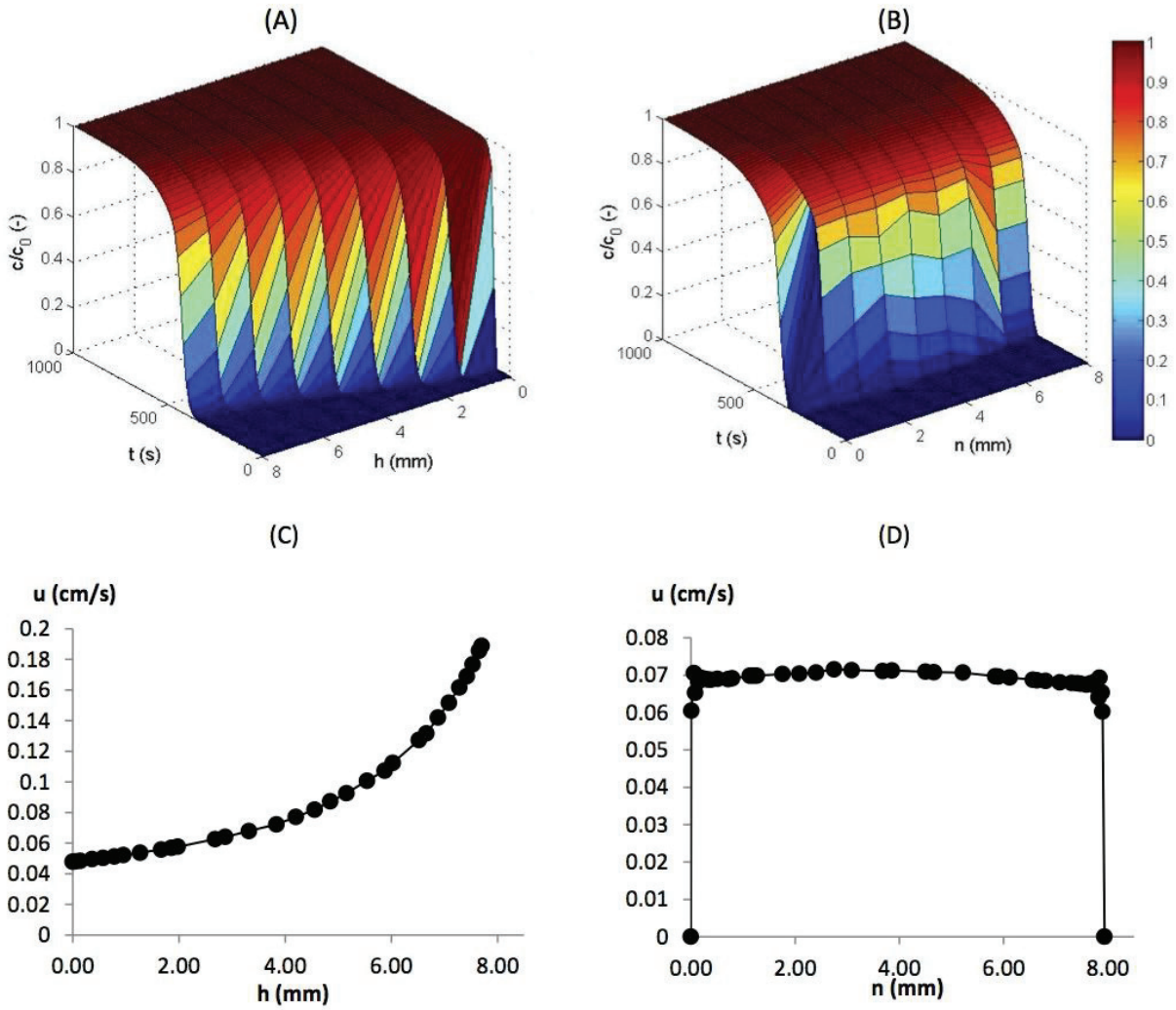

Fig. 3.11 Simulated BSA breakthrough curves under binding condition for the radial flow Sartobind Nano3mL device with a flow rate of 5.00 mLmin^{-1} and a BSA loading concentration of 2.00 mgmL^{-1} at the different bed heights (A), when the height of spiral wound , n is at 4.00 mm and the different n (B), when h=4.00 mm. The calculated velocity, u using CFD model at 5.00 mLmin^{-1} in the function of u=f(h) (C), when n=4.00 mm and u=f(n) (D), when h=4.00 mm.

3.6 Conclusion

In this work, the MC device and geometry was fully investigated using the theoretical and experimental approaches. We demonstrated that the CFD model is a powerful numerical approach to predict the flow distribution, BSA binding capacity and breakthrough curves. The breakthrough curve under a non-binding condition could be predicted using the CFD model for both axial flow and radial flow MC, which has been proved as a good promising tool to provide fundamental knowledge about hydrodynamics for the MC devices. In addition, the CFD simulation along with the bi-Langmuir model offered the accurate BSA breakthrough curve prediction under a binding condition, which indicated the inhomogeneous binding sites of the MC. Using the same bi-Langmuir parameters determined from the traditional geometric device, the breakthrough curves could be precisely predicted for the alternative radial flow devices. This means there is no difference on binding adsorption mechanism due to the same membrane used for both devices. The different breakthrough curve of the axial and radial flow devices was only from the different flow configuration. The employment of CFD model, which accounted for the flow configuration, improved the accuracy of the breakthrough curve prediction without any other adjustment of the model parameters. The transfer of the same bi-Langmuir model parameter values across the different scales and flow configurations have been illustrated. In addition, the binding behavior at different operating conditions; flow rates and BSA loading concentration could be rapidly predicted. This illustrates the good numerical approach to obtain the fast preliminary study for the separation process optimization and MC device design.

Finally, the band-broadening of the breakthrough curves for MC devices was a result from the increasing bed height for both axial and radial flow devices. The inhomogeneous binding sites of MC and the non-uniform flow distribution could explain the negative effect of the increasing bed height. Therefore, the scaling-up of MC devices has a limitation of the increasing bed height, whereas the increasing in membrane diameter for the axial flow devices and in spiral wound height for the radial flow devices could be achieved without the decreasing binding capacity. The increasing pressure drop was significantly observed with the increasing bed height. However, the negative effects of increasing bed height on the radial flow devices were less pronounced due to more uniform flow distribution compared to the axial flow devices. Therefore, the radial flow offer more preferential on the large scale applications as a short bed height can combine with the large surface area, whereas the significant velocity could be maintained employing the short spiral wound with the larger cylindrical diameter. The scaling-up of axial flow devices has a main limitation, which has to rely on the increase in diameter and the velocity becomes lower. With the simple production, the axial flow devices are then preferred at laboratory scales.

3.7 References

[1] J. Thommes, M.-R. Kula, Membrane chromatography - an integrative concept in the downstream processing of proteins, Biotechnol. Prog. 11 (1995) 357–367. doi:10.1021/bp00034a001.

[2] R. Ghosh, Protein separation using membrane chromatography: opportunities and challenges, Journal of Chromatography A. 952 (2002) 13–27. doi:10.1016/S0021-9673(02)00057-2.

[3] C. Charcosset, Membrane processes in biotechnology: An overview, Biotechnology Advances. 24 (2006) 482–492. doi:10.1016/j.biotechadv.2006.03.002.

[4] V. Orr, L. Zhong, M. Moo-Young, C.P. Chou, Recent advances in bioprocessing application of membrane chromatography, Biotechnol. Adv. 31 (2013) 450–465. doi:10.1016/j.biotechadv.2013.01.007.

[5] S. Huang, S. Roy, K. Hou, G. Tsao, Scaling-up of affinity-chromatography by radial-flow cartridges, Biotechnol. Prog. 4 (1988) 159–165. doi:10.1002/btpr.5420040306.

[6] V. Saxena, M. Dunn, Solving Scale–Up: Radial Flow Chromatography, Nat Biotech. 7 (1989) 250–255. doi:10.1038/nbt0389-250.

[7] L. Lane, M.L. Koscielny, P.R. Levison, D.W. Toome, E.T. Butts, Chromatography of hen egg-white proteins on anion-exchange cellulose at high flow rates using a radial flow column, Bioseparation. 1 (1990) 141–147.

[8] A. Jungbauer, F. Unterluggauer, K. Uhl, A. Buchacher, F. Steindl, D. Pettauer, et al., Scaleup of monoclonal antibody purification using radial streaming ion exchange chromatography, Biotechnol. Bioeng. 32 (1988) 326–333. doi:10.1002/bit.260320309.

[9] M. Puthirasigamany, M. Wirges, T. Zeiner, Membrane chromatography for the purification of laccase from the supernatant of Pleurotus sapidus, Biochem. Eng. J. 70 (2013) 180–187. doi:10.1016/j.bej.2012.11.003.

[10] D. Josić, J. Reusch, K. Löster, O. Baum, W. Reutter, High-performance membrane chromatography of serum and plasma membrane proteins, J. Chromatogr. A. 590 (1992) 59–76. doi:10.1016/0021-9673(92)87006-T.

[11] K.-G. Briefs, M.-R. Kula, Fast protein chromatography on analytical and preparative scale using modified microporous membranes, Chem. Eng. Sci. 47 (1992) 141–149. doi:10.1016/0009-2509(92)80208-T.

[12] R. Ghosh, T. Wong, Effect of module design on the efficiency of membrane chromatographic separation processes, J. Membr. Sci. 281 (2006) 532–540. doi:10.1016/j.memsci.2006.04.023.

[13] S.-Y. Suen, Y.-C. Liu, C.-S. Chang, Exploiting immobilized metal affinity membranes for the isolation or purification of therapeutically relevant species, J. Chromatogr. B. 797 (2003) 305–319. doi:10.1016/S1570-0232(03)00490-2.

[14] S.-Y. Suen, M.R. Etzel, A mathematical analysis of affinity membrane bioseparations, Chem. Eng. Sci. 47 (1992) 1355–1364. doi:10.1016/0009-2509(92)80281-G.

[15] K.H. Gebauer, J. Thömmes, M.R. Kula, Breakthrough performance of high-capacity membrane adsorbers in protein chromatography, Chem. Eng. Sci. 52 (1997) 405–419. doi:10.1016/S0009-2509(96)00426-5.

[16] A. Shiosaki, M. Goto, T. Hirose, Frontal analysis of protein adsorption on a membrane adsorber, J. Chromatogr. A. 679 (1994) 1–9. doi:10.1016/0021-9673(94)80306-4.

[17] C. Frerick, P. Kreis, A. Górak, A. Tappe, D. Melzner, Simulation of a human serum albumin

downstream process incorporating ion-exchange membrane adsorbers, Chem. Eng. Process. 47 (2008) 1128–1138. doi:10.1016/j.cep.2007.07.013.
[18] H. Yang, M.R. Etzel, Evaluation of three kinetic equations in models of protein purification using ion-exchange membranes, Ind. Eng. Chem. Res. 42 (2003) 890–896. doi:10.1021/ie020561u.
[19] C. Boi, S. Dimartino, G.C. Sarti, Modelling and simulation of affinity membrane adsorption, J Chromatogr A. 1162 (2007) 24–33. doi:10.1016/j.chroma.2007.02.008.
[20] S. Dimartino, C. Boi, G.C. Sarti, A validated model for the simulation of protein purification through affinity membrane chromatography, J. Chromatogr. A. 1218 (2011) 1677–1690. doi:10.1016/j.chroma.2010.11.056.
[21] S. Dimartino, C. Boi, G.C. Sarti, Influence of protein adsorption kinetics on breakthrough broadening in membrane affinity chromatography, J. Chromatogr. A. 1218 (2011) 3966–3972. doi:10.1016/j.chroma.2011.04.062.
[22] S. Dimartino, C. Boi, G.C. Sarti, A validated model for the simulation of protein purification through affinity membrane chromatography, Journal of Chromatography A. 1218 (2011) 1677–1690. doi:10.1016/j.chroma.2010.11.056.
[23] S. Schneiderman, H. Varadaraju, L. Zhang, H. Fong, T.J. Menkhaus, Mathematical model using non-uniform flow distribution for dynamic protein breakthrough with membrane adsorption media, J. Chromatogr. A. 1218 (2011) 9121–9127. doi:10.1016/j.chroma.2011.10.063.
[24] P. Francis, E. von Lieres, C.A. Haynes, Zonal rate model for stacked membrane chromatography. I: Characterizing solute dispersion under flow-through conditions, Biotechnol. Bioeng. 1218 (2011) 5071–5078. doi:10.1016/j.chroma.2011.05.017.
[25] P. Francis, E. von Lieres, C. Haynes, Zonal rate model for stacked membrane chromatography part II: characterizing ion-exchange membrane chromatography under protein retention conditions, Biotechnol. Bioeng. 109 (2012) 615–629. doi:10.1002/bit.24349.
[26] P. Ghosh, K. Vahedipour, M. Lin, J.H. Vogel, C.A. Haynes, E. von Lieres, Zonal rate model for axial and radial flow membrane chromatography. Part I: Knowledge transfer across operating conditions and scales, Biotechnol. Bioeng. 110 (2013) 1129–1141. doi:10.1002/bit.24771.
[27] P. Ghosh, M. Lin, J.H. Vogel, D. Choy, C. Haynes, E. von Lieres, Zonal rate model for axial and radial flow membrane chromatography, part II: Model-based scale-up, Biotechnol. Bioeng. 111 (2014) 1587–1594. doi:10.1002/bit.25217.
[28] P. Ghosh, K. Vahedipour, M. Lin, J.H. Vogel, C. Haynes, E. von Lieres, Computational fluid dynamic simulation of axial and radial flow membrane chromatography: Mechanisms of non-ideality and validation of the zonal rate model, J. Chromatogr. A. 1305 (2013) 114–122. doi:10.1016/j.chroma.2013.07.004.
[29] P. Ghosh, K. Vahedipour, M. Leuthold, E. von Lieres, Model-based analysis and quantitative prediction of membrane chromatography: Extreme scale-up from 0.08 ml to 1200 ml, J. Chromatogr. A. 1332 (2014) 8–13. doi:10.1016/j.chroma.2014.01.047.
[30] P. Ghosh, K. Vahedipour, M. Lin, J.H. Vogel, C. Haynes, E. von Lieres, Computational fluid dynamic simulation of axial and radial flow membrane chromatography: Mechanisms of non-ideality and validation of the zonal rate model, Journal of Chromatography A. 1305 (2013) 114–122. doi:10.1016/j.chroma.2013.07.004.
[31] P. van Beijeren, P. Kreis, T. Zeiner, Development of a generic process model for membrane adsorption, Comput. Chem. Eng. 53 (2013) 86–101. doi:10.1016/j.compchemeng.2013.03.005.

[32] Membrane Chromatography-Sartobind characteristics, Available on. http://www.sartorius.com/en/products/laboratory/membrane-chromatography/ (accessed December 10, 2014).
[33] C. Teepakorn, K. Fiaty, C. Charcosset, Effect of geometry and scale for axial and radial flow membrane chromatography—Experimental study of bovin serum albumin adsorption, J. Chromatogr. A. 1403 (2015) 45–53. doi:10.1016/j.chroma.2015.05.023.
[34] Operating manual of Sartobind IEX SingleSep, Available on: http://www.sartorius.de/fileadmin/fm-dam/sartorius_media/FILE_EXPORT/Bioprocess-Solutions/Purification_Technologies/Membrane_Chromatography/Manuals/Manual_Sartobind_IEX_SingleSep_SL-6178-E.pdf. (accessed August 12, 2015).
[35] I. Tatárová, R. Fáber, R. Denoyel, M. Polakovic, Characterization of pore structure of a strong anion-exchange membrane adsorbent under different buffer and salt concentration conditions, J Chromatogr A. 1216 (2009) 941–947. doi:10.1016/j.chroma.2008.12.018.
[36] M.W. Phillips, Method for determining an effective peclet number for a membrane adsorber device, US7281410 B2, 2007.

(This page is intentionally left blank)

Chapter 4

OPTIMIZATION OF LACTOFERRIN AND BOVINE SERUM ALBUMIN SEPARATION USING ION-EXCHANGE MEMBRANE CHROMATOGRAPHY

(This page is intentionally left blank)

Chapter 4
OPTIMIZATION OF LACTOFERRIN AND BOVINE SERUM ALBUMIN SEPARATION USING ION-EXCHANGE MEMBRANE CHROMATOGRAPHY

4.1 Abstract

Lactoferrin (LF), which is a high value minor whey protein, has recently received extensive attention from research scientists and industry due to its multifunction and potential therapeutic applications. In this study, the separation of two similar-sized proteins: bovine serum albumin (BSA) and LF was investigated using strong cation and anion exchange membrane chromatography (MC). Single protein and BSA-LF mixture adsorption were performed on Sartobind Q75 and S75 at pH between the LF and BSA isoelectric points. Identical breakthrough curves were obtained for both single protein and binary protein mixture, which suggests that there is no protein adsorption competition at the binding sites. The process optimization was further studied to yield optimum buffer and operating conditions. The highest BSA flux per membrane area (728.00 $gm^{-2}h^{-1}$) was obtained using 100 mM phosphate buffer solution at pH 6.0 on the cation exchange membrane, whereas LF was bound to the membrane with the dynamic binding capacity at 10% breakthrough ($DBC_{10\%}$) of about 60 mg. On the anion exchange membrane, LF was collected in the effluent at the flux of 287.46 gm^{-2} h^{-1} using 5 mM phosphate buffer at pH 6.0, while BSA was retained on the membrane with $DBC_{10\%}$ equal to 60.96 mg. The combination effect between pH change and hydrophobic interaction improved the eluted protein mass for both anion and cation exchangers. Furthermore, the completed separation cycle was operated with the Sartobind S75 device with a short process time of 34.19 min and optimal LF productivity over 2628.84 $mgmL^{-1}$ h^{-1}. This study confirms the advantage of MC for the separation of biomolecules with similar molecular weight and different isoelectric points, such as BSA-LF mixture separation. This fast and effective protein separation method could be applied at an industry scale.

Keywords :

Membrane chromatography, Bovine serum albumin, Lactoferrin, Separation, Ion-exchange

4.2 Introduction

Lactoferrin (LF) is a metal-binding glycoprotein, which was discovered over 50 years ago as red protein in bovine milk. The isolation of this molecule from both human and bovine milk was first achieved using cation exchange chromatography on traditional resin-based column [1,2]. LF is a well-known multifunctional or multi-tasking protein. Many important roles such as immunoregulatory, anti-bacterial, anti-virus, anti-parasitic and anti-inflammatory activity have been reported [3–5]. The wound healing, which is a complex biological process can be promoted using this protein [6]. In addition, LF has been proved to function as an anti-infective agent and prevent the outbreak of infections. It makes this molecule and its derivatives very promising tools for health or nutritional applications [7]. LF is found in whey as a high value minor protein with bovine serum albumin (BSA) and immunoglobulins [8,9].

Membrane separation and chromatography are the most widely used methods for LF isolation from bovine milk and whey. Membrane separation processes provide key advantages for whey fractionation as they do not include adsorption and elution steps, and avoid costs for chromatographic material, buffers and effluent disposal. However, membrane filtration is usually not effective in separating similar size proteins, such as LF and BSA, and other whey proteins. Several authors have reported the separation of LF from other proteins and whey. For example, Nyström et al. [10] investigated the fractionation of several proteins with molecular weight between 15 kD and 80 kD. The best pH value for fractionation was such that one protein had its isoelectric point at this pH, and passed through the membrane, while the other one was held back in the retentate because of charge repulsion with the membrane. In particular, LF was purified at low pressures while BSA was totally retained. However, at higher pressures, the selectivity was low. Similarly, Almécija et al. [11] reported LF isolation from whey using a 300 kDa tubular ceramic membrane. The effect of pH on LF selectivity was investigated in a continuous diafiltration mode. The best resolution was achieved at pH 5 and 10, where LF was obtained in the permeate and in the retentate, respectively, with α-lactalbumin and β-lactoglobulin. Other strategies have been investigated to overcome the limitations associated with LF separation by membrane filtration. For example, Brisson et al. [12] used charged membranes and electrically-enhanced cross-flow microfiltration. The electrical field played an important effect on protein transmission. However, electrolytic reactions occurring at the electrodes/solution interface had a negative impact on the protein separation. Ndiaye et al. [13] evaluated the feasibility of separating LF from whey solution using electrodialysis with an ultrafiltration membrane of 500 kDa. The highest LF migration rate was obtained at pH 3.0 with a migration yield of 15%. However, the selectivity of the technique decreased in whey solution due to simultaneous migration of β-lactoglobulin and other whey proteins. Valiño et al. [9] investigated the separation of BSA and LF using charged ultrafiltration membranes. Using an unmodified neutral membrane at pH 5.0 (isoelectric point of BSA), LF was completely retained, and BSA passed in the permeate at a maximum flux of 30.31 g m^{-2} h^{-1}. By contrast, BSA was completely retained by the negatively charged membrane at pH 9.0 (isoelectric point of LF), and LF was recovered at a maximum flux of 1.07 g m^{-2} h^{-1}.

Conventional chromatography is the most widely used method for protein recovery and purification as it is a robust and efficient technique. Many studies have reported LF isolation using micro-sized resins as a stationary phase. Different chromatographic modes have been tested such as cation exchange [14–18], affinity [19] and hydrophobic interaction [20]. However, conventional chromatographic processes show several disadvantages, since large volumes and

high protein concentrations in whey may cause fouling of columns, long cycle times, large pressure drops and complicated process control [21,22]. Other stationary phases have therefore been tested as possible alternatives to resins such as mixed-matrix membranes (MMMs), monolithic columns, and chromatographic membranes.

MMMs are prepared by incorporating an adsorptive resin into a membrane polymer solution prior to membrane preparation [23]. The polymer/resin suspension is then cast as a flat sheet membrane or spun into a hollow fiber membrane. The MMM concept has been successfully applied to the preparation of anionic, cationic, anionic/cationic hybrid membranes for protein separation. MMM combines the properties of membrane techniques (easy scale-up, low pressure drop) with column chromatography (high binding capacity, high recovery) [23]. Several MMMs have been applied to the recovery of LF from whey. For example, Saufi and Fee [24] developed a cationic MMM for recovery of LF from bovine whey by embedding SP Sepharose^{TM} cation exchange resin into an ethylene vinyl alcohol polymer based membrane. The separation was operated in cross-flow mode and recycling both permeate and retentate into the feed, to minimize fouling and enhance LF binding capacity. The system resulted in a constant permeate flux equal to 100 L m^{-2} h^{-1} and a high LF recovery of 91%, with high purity. A disadvantage of MMM could be the negative effect of flow rate on separation. For example, Avramescu et al. [23] reported a lower separation factor of 30 between BSA and bovine hemoglobin using MMM, when the filtration flux per membrane area increased from 10 to 20 Lm^{-2} h^{-1}. This effect was due to the decrease of the efficiency of adsorptive sites with flow velocity.

Another development in chromatography is the use of macroporous monolith columns. A monolith is a single piece of highly porous material characterized by a highly interconnected network of channels with a diameter in the range of 10–4000 nm [25]. Therefore, mass transport in monoliths is mainly based on convection. The use of short monolithic columns enhances the speed of the separation process and reduces the backpressure, unspecific binding and product degradation, without reducing resolution. In addition, the lack of void volume eliminates the turbulent void flow that contributes to molecular shear in conventional resin columns. Some studies have reported the use of monolithic columns for LF and whey protein separation. For example, Noppe et al. [26] covalently coupled phage clones expressing a peptide with high binding affinity for LF to a macroporous poly(dimethylacrylamide) monolithic column. The large pore size of the macroporous monolith makes it possible to couple the long phages as ligands without any risk of blocking the pores. Using this affinity support, LF was purified from human skimmed milk with purity higher than 95%, in one step. In another application, Etzel and Bund [27] purified whey protein-dextran conjugates from a feed solution also containing un-reacted protein and dextran using either a cation exchange packed bed column or a tube monolith. Binding capacities were similar for both monolith and beaded column (4-6 $mgmL^{-1}$). However, the monolith was operated at a 48-fold higher flow rate, which gave a 42-fold higher productivity, at the expense of a somewhat lower conjugate purity.

Membrane chromatography (MC) is a well-established technique for protein purification [22,23,28]. It is based on the integration of membrane filtration and liquid chromatography into a single-step operation. The advantage of MC over conventional resin chromatography is mainly attributed to the shorter diffusion times, as the interactions between molecules and active sites in the membrane occur in convective through-pores rather than in stagnant fluid inside the pores of the adsorbent particles. Therefore, MC has the potential to operate both at high flow rates and for use of large biomolecules with small diffusivities, reducing biomolecules degradation and

denaturation. Low pressure drops associated with high flow rates, as compared to packed bed chromatography, reduce buffer usages [22]. Fractionation of whey proteins by MC has been reported in several studies. For example, LF and lactoperoxidase (LP) were isolated from sweet cheese whey using cation exchange MC in an axial flow configuration [21]. LF was eluted in a three-step elution process (0.1 M NaCl, 0.2M NaCl, 1M NaCl), which led to a LF fraction of about 95% purity. The cationic MC was then upscalable from 15 cm^2 to 4 m^2 scale with a recovery yield for LF of more than 90%. However, it was observed that when increasing the flow rate from 3 to 15 $mLmin^{-1}$, the binding capacity decreased from 0.6 to 0.3 $mgcm^{-2}$. Similarly, Chiu and Etzel [28] extracted LF and LP from whey using cation exchange MC devices with surface area of 100 cm^2 and 790 cm^2. The purification process was operated repeatedly with 12 cycles consisting of loading of whey, washing, stepwise elution and washing. Recovery was unaffected by scale-up and repeated cycling, and was 50.0% and 73.0% for LF and LP, respectively. For the complete fractionation of whey proteins in a two-step process, Voswinkel and Kulozik [29] used ion-exchange radial flow devices with improved fluid distribution (anion and cation exchanger Sartobind Nano and Sartobind 150-mL). First, β-lactoglobulin and BSA were bound to the anion exchanger at pH 7.0. Second, the permeate obtained in the first step was introduced into the cation exchanger at pH 4.8. LF, LP and immunoglobulin G bound while β-lactalbumin passed through the membrane. The scalability of the process was investigated with the radial flow column and 50-fold membrane area. At lab scale, 97% LF purity was obtained with a yield of 66%. However, at pilot scale, LF purity and yield decreased to 89% and 39%, respectively. The authors concluded that further investigations were needed to increase the LF yield in the cation exchanger step. Affinity MC has also been tested for LF purification from bovine whey and colostrum. For example, Wolman et al. [30] modified a hollow fiber polysulfone membrane by grafting a glycidyl methacrylate/dimethyl acrylamide copolymer and attaching the triazinic dye Red HE-3B as an affinity ligand. Using 1 mL membrane volume, LF purification from bovine colostrum was performed in one step at different flow rates. The binding capacity did not decrease with increasing flow rate.

Several mathematical models have been proposed to predict MC performance, including breakthrough curves, elution profiles, and the effect of various parameters. Most models consider convection, diffusion and adsorption kinetics, like Langmuir adsorption for affinity separation [31] and ion-exchange [32,33]. Several other kinetic mechanisms have been evaluated, such as steric hindrance [34], spreading equations [35] and bi-Langmuir adsorption [36]. To account for flow non-idealities, such as dispersion, mixing and dead volumes, a combination in series of an ideal continuously stirred tank reactor and an ideal plug flow reactor has been introduced [36]. Mathematical models were applied successfully to complex purifications, such as the separation of immunoglobulin G from complex mixtures using affinity MC [37].

Although many techniques have been developed to isolate LF, the separation of high-value minor proteins of similar molecular weights such as BSA, LF, and immunoglobulins remains a challenge. BSA is a 66.5 kDa protein with an isoelectric point near 4.7. LF is a 78.0 kDa protein with an isoelectric point around 8.7. Both proteins tend to prevent foam formation at their isoelectric points by reducing the surface tensions, which makes their separation even more difficult [9]. In this work, the separation of LF and BSA mixture is carried out using strong anion and cation exchange MC. The influence of operating and buffer conditions on protein mixture separation is studied with Sartobind S75 and Q75 devices (Sartorius Stedim Biotech GmbH, Germany). The breakthrough curve, dynamic binding capacity at 10% breakthrough ($DBC_{10\%}$), selectivity and productivity of the BSA-LF mixture separation are measured at various

experimental conditions. The results obtained are discussed to obtain an optimum separation between BSA and LF.

4.3 Materials and methods

4.3.1 Materials

Sartobind S75 and Q75 MC devices are strong cation and anion exchangers, respectively, provided by Sartorius Stedim Biotech GmbH (Goettingen, Germany). The devices contain 75 cm^2 of stabilized reinforced cellulose membrane in a stack of 15 membrane discs. The flow configuration is dead-end geometry, in which the flow goes from top through the membrane stack to the outlet. The membrane bed volume (BV) of these Sartobind devices is 2.1 mL, with the diameter of the membrane of 25.0 mm, 4.0 mm bed height and 1.30 mL dead volume [38]. Functionalized sulfonic acid and quaternary ammonium groups are covalently bound to the membrane in the strong cation and anion exchangers, respectively.

BSA lyophilized powder with purity ≥ 96.00% was purchased from Sigma Aldrich (France). Purified bovine LF lyophilized powder (≥ 93.00% of purity) was kindly provided by Erie Europe (France). Potassium phosphate buffer solutions at desired concentrations and pH values were prepared by adjusting volumes of K_2HPO_4 and KH_2PO_4 solutions and subsequently filtered through a hydrophobic membrane filter with a 0.45-µm pore size (Millipore, France). Sodium phosphate buffer solutions were prepared by mixing Na_2HPO_4 (Fluka, France) and NaOH solutions. Citrate buffer 100 mM pH 3.0 was obtained by mixing adequately citric acid and sodium citrate dehydrate (Fluka, France) solutions. Ultrapurified water from a Milli-Q system (Millipore, France) was used in this work for solution preparation. For HPLC buffers, trifluoroacetic acid (TFA) and acetonitrile were obtained from Sigma-Aldrich (France). All other reagents are from Sigma-Aldrich (France).

Proteins were diluted into phosphate buffers by slowly stirring to prevent any foam formation. The diluted proteins were then stored overnight in the refrigerator until any foam had naturally disappeared [9]. Afterward, the protein solution was filtered through a 0.22 µm polyethersulfone hydrophilic Millex-GP filter unit (Millipore, France) to remove any fine particles. All experiments were carried out on an Aktaprime-plus (GE Healthcare, France) chromatography system with a UV-280 detector. The system was controlled by the PrimeView 5.0 software (GE Healthcare, France).

4.3.2 Protein analysis

The concentrations of LF and BSA solutions were measured by spectrophotometry at 280 nm using the UV detector of the Aktaprime-plus system. For each single protein, a standard curve was determined by plotting the absorbance versus concentration for a range of known solutions. From these standard curves, BSA and LF calibration constants were determined. To check the method of concentration measurement for BSA-LF mixture solutions by spectrophotometry, reversed-phase high performance liquid chromatography (RP-HPLC) was used according to the method of Voswinkel and Kulozik [39]. A Zorbax Eclipse XDB-C18 5 µm column was connected to

an Agilent 1200 HPLC system with a G1315D diode array detector (Agilent Technologies, France). Eluent A contained 0.1% (v/v) TFA dissolved in water and eluent B was a mixture of 0.0555% (v/v) TFA, 80% (v/v) acetonitrile and 20% (v/v) water, the flow rate was 1.0 mLmin^{-1} and temperature was 40°C. Peak detection was at 226 nm for both proteins. Protein concentration was determined by peak integration of each eluted fraction.

A typical 280 nm UV absorbance curve obtained for BSA and LF mixture adsorption on a Sartobind Q75 device shows two separate breakthrough curves (Fig. 4.1A) the first one corresponds to the non-binding LF, which would be more positively charged and does not bind to the ligands at the membrane surface. The second breakthrough curve corresponds to the binding BSA, which is negatively charged and is retained to the opposite charges on membrane. Consequently, the UV absorbance curve has been used to obtain LF and BSA breakthrough curves using Eq.1 and Eq.2, where A is the measured absorbance, $A_{1,0}$ is the UV absorbance corresponding to the loading concentration of the protein not adsorbed onto the membrane, K_i the absorbance calibration constant of protein i (LF or BSA) and c_i is the concentration of protein i.

To verify this method, RP-HPLC was used to measure LF and BSA concentrations in samples taken at various times during the loading step of the LF-BSA mixture (Fig. 4.1B). LF and BSA concentrations were measured in triplicate. The protein breakthrough curves using the UV-absorbance curves compared well to breakthrough curves obtained from RP-HPLC measurements. In the next, we choose the UV absorbance curve method to determine breakthrough curves during protein mixture adsorption.

$$when\ A < A_{1,0};\ c_1 = \frac{A}{K_1}\ and\ c_2 = 0 \qquad \text{Eq.1}$$

$$when\ A \geq A_{1,0};\ c_1 = \frac{A_{1,0}}{K_1}\ and\ c_2 = \frac{A - A_{1,0}}{K_2} \qquad \text{Eq.2}$$

Furthermore, the zeta potential of 1.00 mgmL^{-1} LF and BSA in 100 mM phosphate buffer at different pH was determined using a Zetasizer Nano-series (Malvern Instruments, Malvern France). All the measurements were performed at least three times and the data were expressed as the mean ± standard deviation (S.D.). The zeta potential was calculated from the electrophoretic mobility by the Helmholtz-Smoluchowski equation [40].

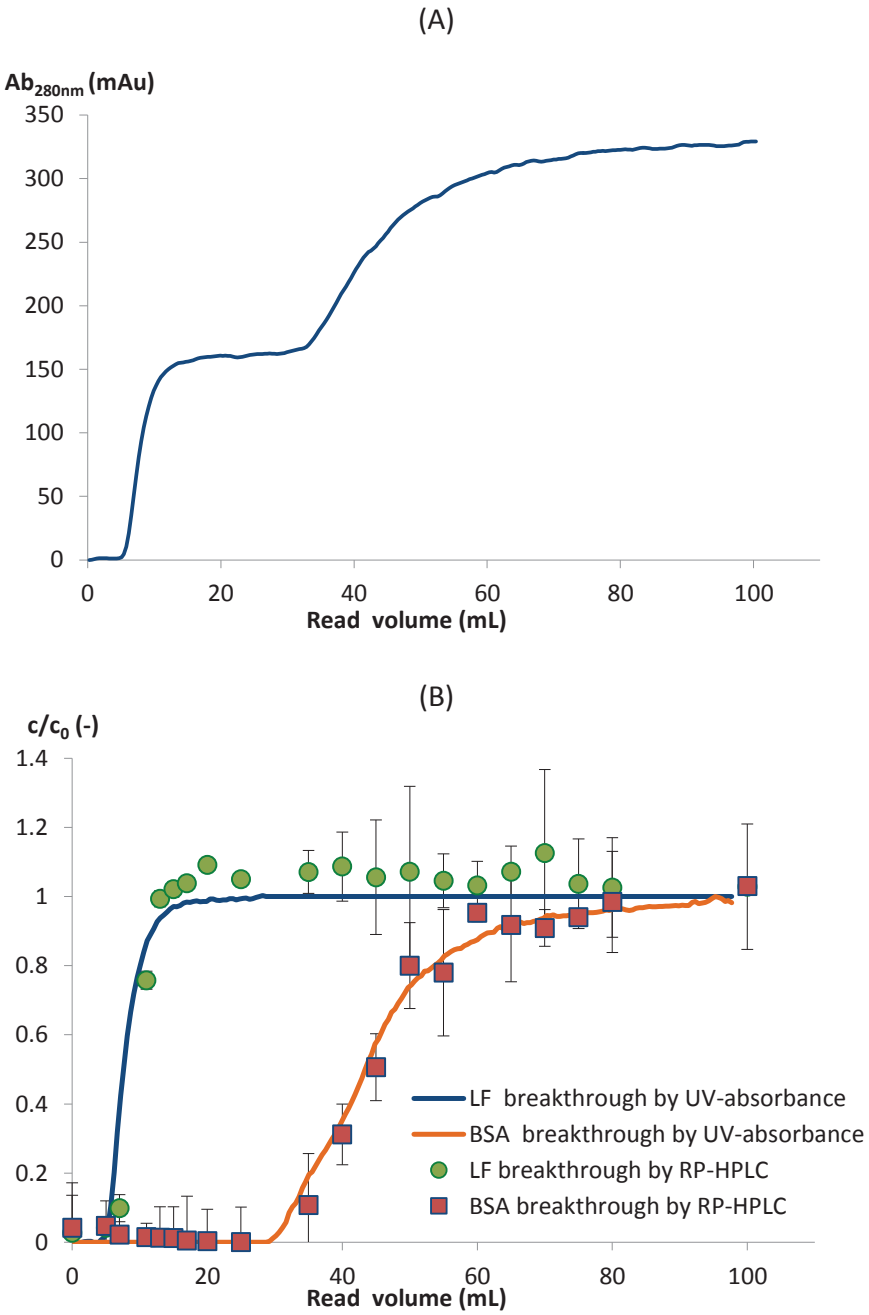

Fig. 4.1 (A) Protein mixture concentrations monitored by UV absorbance at a wavelength of 280 nm during the BSA-LF mixture separation using Sartobind Q75 at pH 6. 0 and a flow rate of 2.5 $BVmin^{-1}$. (B) LF and BSA breakthrough curves measured by UV absorbance compared to the ones obtained by RP-HPLC.

4.3.3 Process characteristics

System dispersion curves were measured by loading a phosphate buffer containing 5.00% (v/v) acetone as an inert tracer. The flow rate was 12.0 BVmin^{-1}. The absorbance was read at 280 nm. This non-binding experiment using acetone solution was used to determine the dead volume (V_0) of the Sartobind S75 or Q75 device connected to the Aktaprime-plus system, when the breakthrough concentration increased to 10.0% of acetone initial concentration. Using this method, V_0 was found to equal 6.06 mL.

BSA and LF breakthrough curves were measured at different buffer and operating conditions using Sartobind S75 and Q75 devices. In most MC applications, the separation process is stopped when the molecule to be purified starts to appear in the effluent, usually when the concentration reaches 10% of its initial value (c/c_0= 0.10). Therefore, several parameters were determined at 10 % breakthrough. The effuent volume ($V_{ef,10\%}$) was the volume read at 10% breakthrough ($V_{10\%}$) minus the dead volume of the Sartobind device and external system (V_0) as shown in Eq.3. $V_{ef,10\%}$ represents the volume of protein(s) solution that has be loaded until 10% breakthrough occurs.

$$V_{ef,10\%} = V_{10\%} - V_0 \qquad \text{Eq. 3}$$

The dynamic binding capacity at 10% breakthrough ($DBC_{10\%}$) per unit of Sartobind device was calculated using Eq.4, where c is the protein (LF or BSA) concentration in the effluent, c_0 is the protein (LF or BSA) loading concentration, $V_{10\%}$ is the read volume of BSA or LF solution at c/c_0= 0.10.

$$DBC_{10\%} = \int_0^{V_{10\%}} (c_0 - c)dV - c_0V_0 \qquad \text{Eq. 4}$$

Protein (LF or BSA) concentrations in the effluent at 10% breakthrough (c_{ef}) were determined by numerical integration of the breakthrough curve as indicated in Eq.5. The selectivity, which is one important parameter in the separation process, was determined using Eq. 6 and Eq. 7 for the cation and anion exchangers, respectively, where $c_{0,LF}$ and $c_{0,BSA}$ are the loading protein concentrations, respectively of LF and BSA.

$$c_{ef} = \frac{\int_0^{V_{10\%}} cdV - c_0V_0}{V_{10\%}} \qquad \text{Eq.5}$$

$$\alpha_{BSA/LF} = \frac{c_{ef,BSA}/c_{0,BSA}}{c_{ef,LF}/c_{0,LF}} \qquad \text{Eq. 6}$$

$$\alpha_{LF/BSA} = \frac{c_{ef,LF}/c_{0,LF}}{c_{ef,BSA}/c_{0,BSA}} \qquad \text{Eq. 7}$$

4.3.4 Single protein adsorption and BSA-LF mixture separation

BSA and LF concentrations in bovine milk are reported to depend on several factors like the lactation period, and are usually between 0.02 and 0.2 mgmL-^{1} for LF and between 0.2 and 2.6 mgmL^{-1} for BSA [41–43]. Whey protein concentrate is greater than 70% by weight, obtained by ultrafiltration in association with diafiltration [44]. The initial protein concentration of the BSA-

LF binary mixture in this work (2.00 $mgmL^{-1}$ and 1.00 $mgmL^{-1}$, respectively for BSA and LF) referred to conditions that have been previously used [9]. Those conditions simulated the concentrations found in the production of whey concentrate [45]. The influence of the different initial concentrations of proteins was investigated using the initial concentrations of BSA from 1.00 to 4.00 $mgmL^{-1}$ and LF from 0.50 to 2.00 $mgmL^{-1}$. Moreover, single protein adsorption experiments were operated at both LF and BSA loading concentration of 1.00 $mgmL^{-1}$ to keep the same concentration for both proteins.

For the Sartobind Q75 device, the pH effect was investigated at a reduced ionic strength using 20 mM phosphate buffers. BSA and LF concentrations were monitored by reading the UV-absorbance at 280 nm. All experiments of single protein adsorption were operated at 12.0 $BVmin^{-1}$.

Afterward, BSA-LF separation was performed by loading BSA-LF mixture solutions at 2/1 of BSA/LF initial concentrations. The loading solution was prepared by mixing the same volume of 2.00 $mgmL^{-1}$ BSA solution and 1.00 $mgmL^{-1}$ LF solution. The loading step was stopped when the loaded volume was 150.0 mL, which ensures that the protein amount is enough to reach 100% breakthrough. The effect of buffer ionic strength, flow rate and protein initial concentration on the BSA-LF mixture separation performance was investigated.

4.3.5 Elution step

The impact of the different eluents on BSA and LF eluted amount was investigated for both cation and anion exchangers devices. A BSA-LF solution at initial concentration of 2/1 was loaded at 24.0 $BVmin^{-1}$until $V_{ef,10\%}$. The elution buffer (20.0 mL) was then injected at a flow rate of 6.0 $BVmin^{-1}$. The amount eluted (BSA or LF) was determined by numerical integration of the elution peak. For both devices, the effect of the ionic strength of the elution buffer was tested (1.00 M and 2.00 M NaCl in phosphate buffer).

In addition, the effect of pH and hydrophobic interaction by adding ethylene glycol were evaluated. For the cation exchange device, 50 mM sodium phosphate buffer was used at two different pH 11.0 or 12.0 above the isoelectric point of LF. An additional elution buffer was tested by adding 25.00% ethylene glycol in 50 mM sodium phosphate buffer at pH 12.0. For the anion exchange device, the elution buffer was 100 mM citrate buffer pH 3.0 (below the isoelectric point of BSA). An additional elution buffer was tested by adding 25.00% ethylene glycol diluted in 100 mM citrate buffer, pH 3.0. Finally, the effect of flow rate on the eluted protein amount was investigated for the best elution buffer found.

4.3.6 LF-BSA separation cycles on cation exchange membrane

LF-BSA fractionation cycles on Sartobind S75 were operated with the optimal loading buffer, operating and elution conditions. The separation was composed of six steps: (1) equilibration of the MC device using the phosphate buffer for a volume V_{eq}= 20 mL, (2) loading of the BSA-LF mixture solution until 10% breakthrough of LF, i.e. for the optimized volume $V_{ef,10\%}$; (3) first washing with phosphate buffer (V_{w1} = 20 mL), (4) protein elution (V_{elu} =20 mL), (5) second washing with phosphate buffer (V_{w2} = 20 mL), and (6) membrane regeneration with phosphate buffer (V_{re}= 120 mL). The different steps where performed at various flow rates: Q_{ef} for the

loading and washing steps, Q_{elu} (elution step), and Q_{re} (regeneration step). The process separation was repeated over three cycles.

The membrane regeneration step was performed using the method described in the Sartobind user's guide. 1 M NaOH was loaded to the MC device at Q_{re}=1 BVmin^{-1} for 60.0 BV, followed by 1 M NaCl eluent and phosphate buffer for 10 BV of each solutions. The equilibrium, loading and all washing steps were operated at Q_{ef}=24.0 BVmin^{-1}. The flow rate during the elution step was decreased to Q_{elu}=1.0 BVmin^{-1}. For each process, the total process time (t_p) was defined by Eq. 8 and the productivity of the chromatographic process was calculated using Eq.9 [30].

$$t_p = \frac{V_{eq} + V_{ef,10\%} + V_{w1} + V_{w2}}{Q_{ef}} + \frac{V_{elu}}{Q_{elu}} + \frac{V_{re}}{Q_{re}} \quad \text{Eq.8}$$

$$Productivity = Eluted\ protein\ mass \times t_p^{-1} \times BV^{-1} \quad \text{Eq.9}$$

4.4 Results and discussion

4.4.1 Cation exchange membrane

- **Influence of buffer conditions**

Using the Sartobind S75 device, single protein adsorption experiments were performed by loading protein (BSA or LF) solution at different buffer pH values between the isoelectric point of BSA and LF. The effect of pH on the single protein adsorption was therefore examined at pH 6.0, 7.0 and 8.0. For all experiments, the flow rate was set at 12.0 BVmin^{-1}.

As shown in Fig. 4.1, BSA did not bind on the cation exchange membrane because BSA possessed more negative charges than LF at these pH (between 6 and 9); therefore, LF adsorbed preferentially to the membrane. The higher LF binding capacity was obtained at pH 6.0, as LF was less negatively charged (zeta potential of -2.36 mV in 100 mM phosphate buffer) as compared to pH 7.0 and 8.0 (-4.97 and -6.60 mV, respectively). The isoelectric point of BSA being close to 4.7, the zeta potential of BSA was negative at pH between 6.0 and 9.0, and decreased when increasing pH. Moreover, the isoelectric point of LF being given as close to 8.7, it could be foreseen that the zeta potential of this protein would be positive at pH 6.0 and 7.0, which is not the case. In a recent study, Valiño et al. [46] measured various parameters related to BSA and LF, including zeta potential, for a large range of experimental conditions, such as electrolyte type, ionic strength, and protein concentration. The authors observed that the zeta potential decreased with increasing electrolyte concentration. At ionic strength of 0.1 M, from pH 6 to 10, both BSA and LF had negative zeta potential value, which corresponds to our zeta potential data.

The highest $V_{ef,10\%}$ (60.63 mL) was obtained at pH 6.0 with $DBC_{10\%}$ equal to 60.17 mg of LF per unit of Sartobind device. This corresponds to an increase of LF $DBC_{10\%}$ over 46% and 97%, compared to data at pH 7.0 and 8.0, respectively. pH in the range 6-7 have been previously selected for the isolation of LF from whey. For example, Plate et al. [21] treated sweet cheese whey at pH of 6.2 using a cation exchange MC device Sartobind S75.

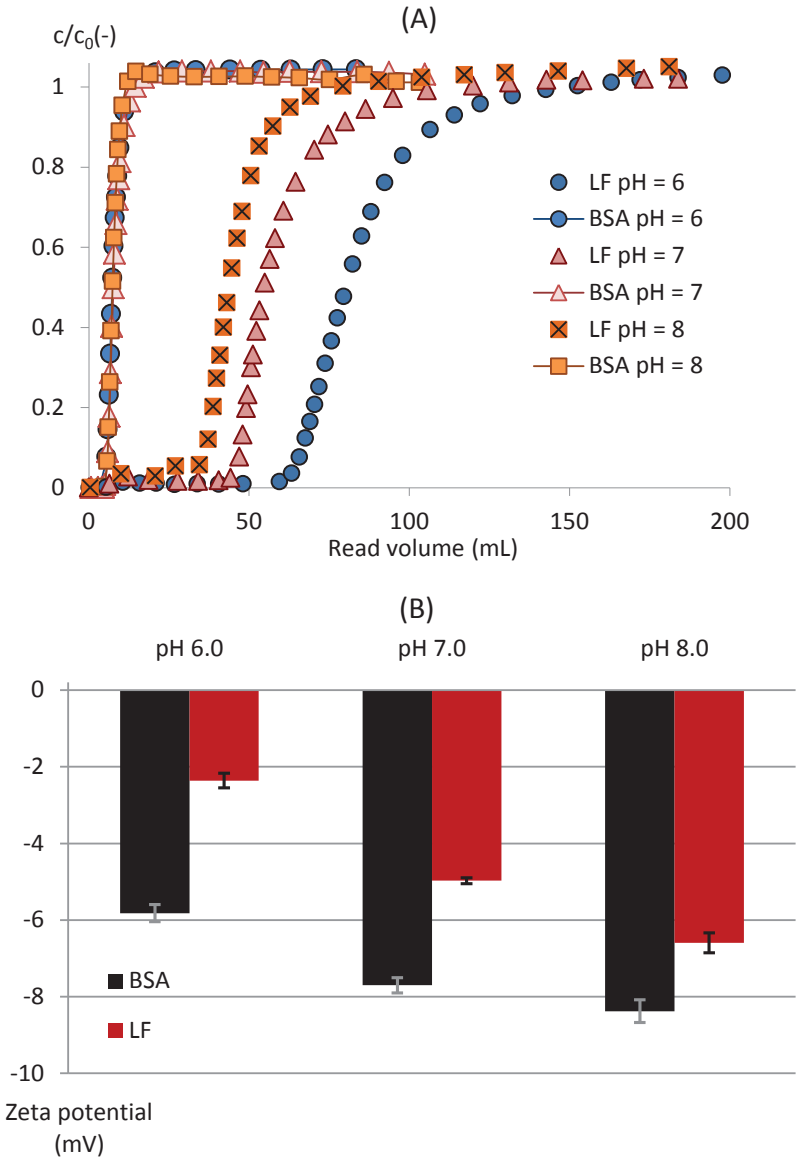

Fig. 4.2 (A) pH influence on breakthrough curves of single BSA and LF solutions on Sartobind S75 in 100 mM phosphate buffer at flow rate of 12.0 $BVmin^{-1}$, loading BSA concentration of 1.0 $mgmL^{-1}$ and loading LF concentration 1.0 $mgmL^{-1}$. (B) Zeta potential of BSA and LF at different buffer pH of 6.0, 7.0 and 8.0, at concentration of 1.0 $mgmL^{-1}$ in 100 mM phosphate buffer.

In addition, the breakthrough curves of single protein (BSA or LF) solutions and binary BSA-LF mixtures was compared at pH 6.0 (Fig. 4.3). LF breakthrough curves were found identical for both the single and binary protein mixture. In addition, the BSA breakthrough curve of the BSA solution and BSA/LF mixture were identical to the breakthrough curve of the non-binding solute acetone. This confirms that BSA passed through the membrane stack without binding. At this pH, only LF binds to the negatively charged ligands of the cation exchange membrane and there is no competition between BSA and LF adsorption at the binding sites.

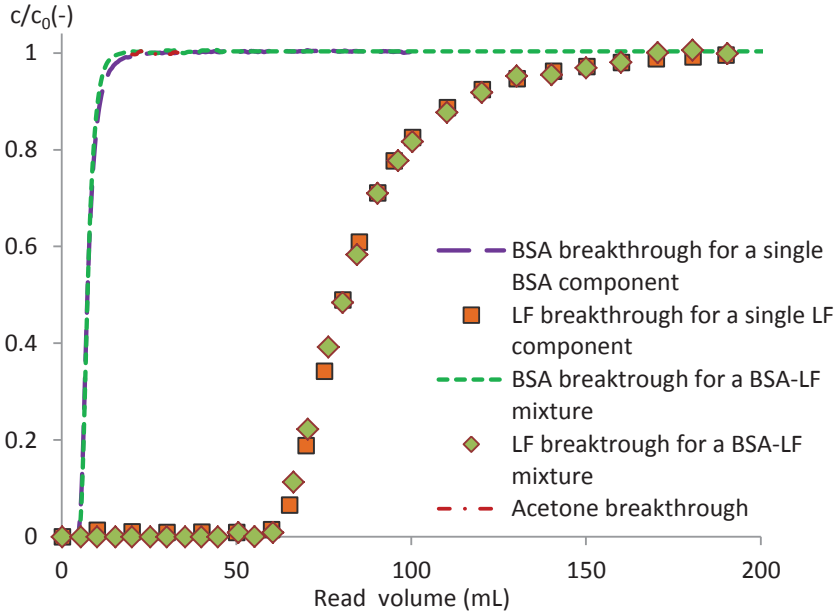

Fig. 4.3 Comparison between breakthrough curves of (1) single protein (LF and BSA) solutions at loading concentration of 1.00 $mgmL^{-1}$, (2) BSA-LF mixture at BSA-LF loading ratio of 2:1 and (3) 5.00%(v/v) acetone solution as an inert tracer. Sartobind S75 device, 100 mM phosphate buffer, pH 6.0 and flow rate 12.0 $BVmin^{-1}$.

The influence of ionic strength was studied by setting the phosphate buffer concentrations at 10, 100 and 200 mM at pH 6.0 (Fig. 4.4(A)). The highest LF binding capacity was obtained at 100 mM, compared to the binding capacity at 10 and 200 mM phosphate buffers. In addition, it was observed that the LF breakthrough curve was sharper at the highest phosphate concentration 200 mM compared to 10 mM. Several phosphate buffer concentrations were then tested from 40 to 125 mM ((Fig. 4.4(B)). The LF binding capacity increased slightly with the increasing phosphate concentrations until 100 mM. A decrease of LF binding capacity was then observed at 125 mM. The phosphate buffer concentrations of 40 and 125 mM provided very similar LF breakthrough curves, with slightly lower LF binding capacity than at 100 mM.

The effect of buffer ionic strength could be explained as follows. Before loading the protein solution onto the ion-exchange membrane, charge sites on proteins and sulfonic acid groups of the membrane are equilibrated by buffer counter-ions. During LF adsorption, these buffer ions are released and may prevent further adsorption by ionic strength increase or pH

change. To avoid these negative effects, an increase in buffer concentration can stabilize the pH and improve therefore protein binding. This effect was observed in our study for buffer concentration from 40 mM to 100 mM. However, the buffer ionic strength should not be too high, because the potassium ions could then compete for the same binding sites with LF as observed at buffer concentration of 125 mM and 200 mM.

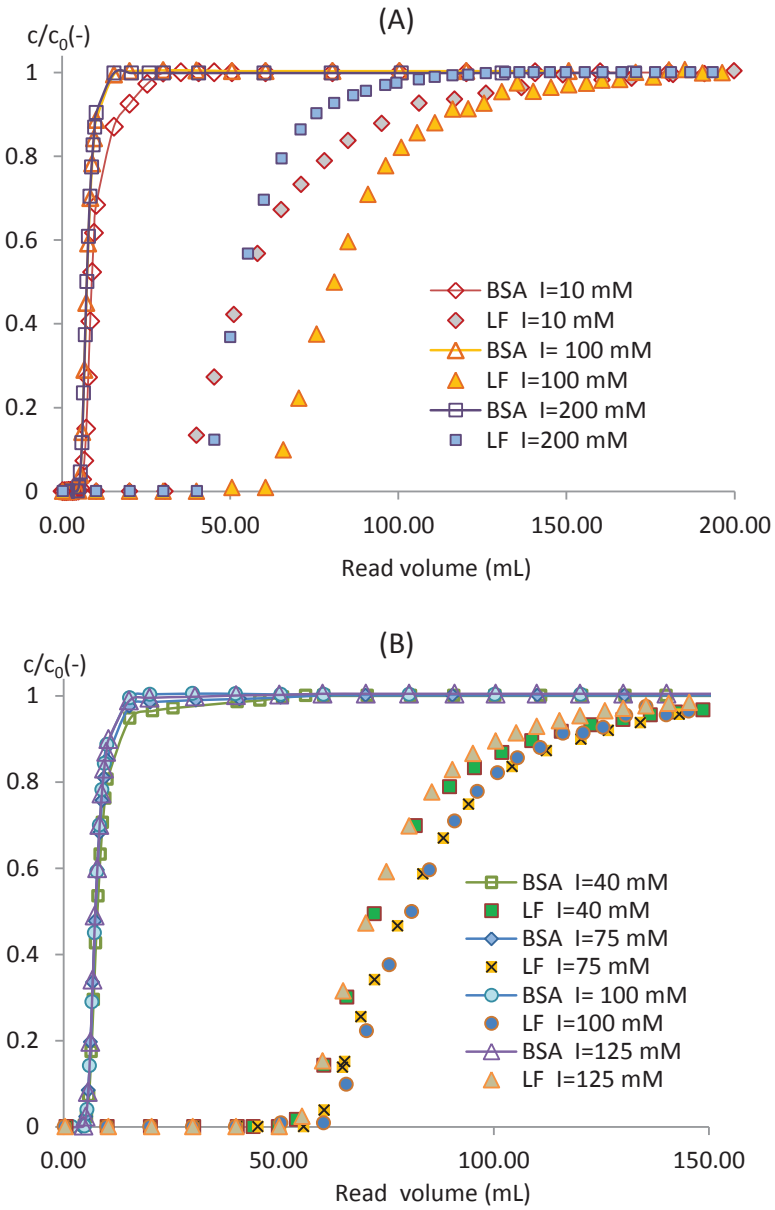

Fig. 4.4 Influence of ionic strength at pH 6.0 on breakthrough curves of BSA-LF mixture using Sartobind S75 at 12.0 $BVmin^{-1}$ and BSA-LF initial concentrations of 2/1.

(A) Phosphate concentrations at 10, 100 and 200 mM.

(B) Phosphate concentrations between 40 mM and 125 mM.

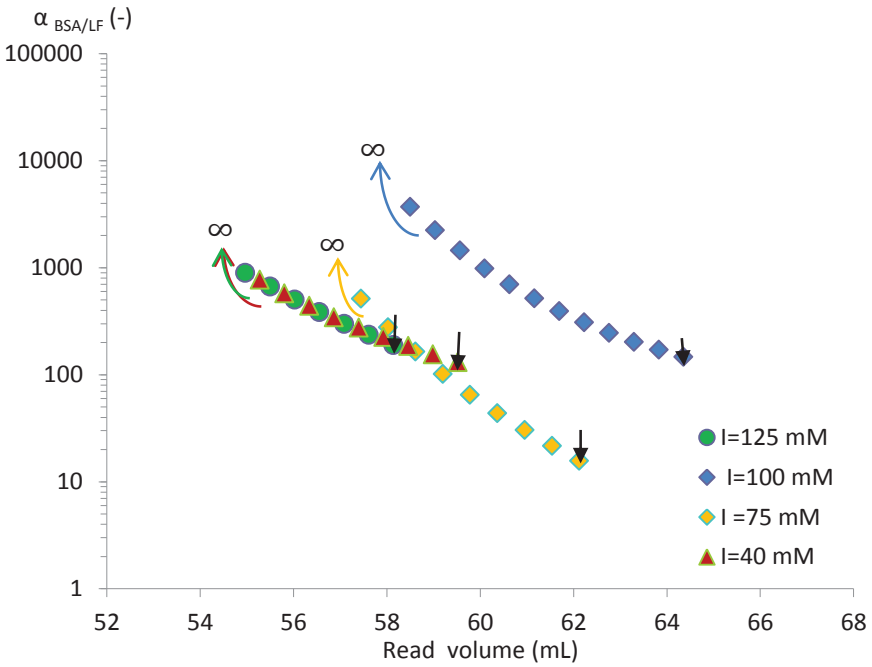

Fig. 4.5 Selectivity of the BSA and LF mixture separation ($\alpha_{BSA/LF}$) at different ionic strength values on Sartobind S75 with a flow rate of 12.0 $BVmin^{-1}$ and BSA/LF initial concentrations of 2/1. For each curve, the seletivity tends to infinity at the beginning due to the zero content of LF in the effluent , the arrows

(↓) correspond to 10% LF breakthrough.

The selectivity of the BSA/LF mixture separation, $\alpha_{BSA/LF}$, was determined using Eq. 6 and plotted versus the effluent volume until 10% LF breakthrough (Fig. 4.5). LF was first completely bound to the membrane while BSA passed through the membrane in the effluent. Therefore, $\alpha_{BSA/LF}$ was at first infinite due to the zero content of LF in the effluent. After breakthrough, the selectivity $\alpha_{BSA/LF}$ decreased sharply as LF started to pass in the effluent. At 10% LF breakthrough, the highest selectivity $\alpha_{BSA/LF}$ (147.02) was obtained at 100 mM phosphate buffer with $V_{ef,10\%}$ around 62 mL and $DBC_{10\%}$ at 61.46 mg per device. Therefore, in the range of conditions tested, the optimum buffer conditions for the BSA-LF mixture separation by cation exchange MC were selected to be pH 6.0 and phosphate buffer concentration of 100 mM. The amounts of bound LF at $DBC_{10\%}$ are specified in Table 4. 1, showing the important effect of buffer condition on MC separation.

Table 4. 1 LF and BSA $DBC_{10\%}$, using Sartobind S75 and Q75 devices, respectively, at an initial BSA/LF concentrations of 2/1 and a flow rate of 12.0 $BVmin^{-1}$,[A] except for the experiments at different pH, which were performed by loading single LF and BSA solutions at initial concentrations of 1.00 $mgmL^{-1}$ for both proteins.

Sartobind S75	pH^A at I=100 mM			Ionic strength (mM) at pH 6.0					
	6.0	7.0	8.0	10	40	75	100	125	200
LF $DBC_{10\%}$ (mg)	60.17	41.04	30.48	38.96	53.12	57.96	59.96	52.82	38.97

Sartobind Q75	pH^A at I=20 mM			pH^A at I=100 mM			Ionic strength (mM) at pH 6.0				
	6.0	7.0	8.0	6.0	7.0	8.0	5	10	20	40	60
BSA $DBC_{10\%}$ (mg)	37.22	35.30	28.10	5.48	0.76	5.36	61.13	48.44	37.54	29.56	23.42

- **Influence of operating conditions**

The influence of flow rate on BSA-LF fractionation was investigated at 12.0, 18.0 and 24.0 $BVmin^{-1}$ (Fig. 4.6), which correspond respectively to superficial velocities of 5.13, 7.70 and 10.27 $cmmin^{-1}$. Optimum pH and phosphate buffer concentration were used, respectively 6.0 and 100 mM. The BSA flux, $\alpha_{BSA/LF}$ at 10% LF breakthrough and LF $DBC_{10\%}$ are given in Table 4.2. For the different flow rates, breakthrough curves overlapped; LF breakthrough happened around 60.0 mL, which corresponds to LF $DBC_{10\%}$ per BV of 28.50 $mgmL^{-1}$. This data was higher than the data reported by Sartorius of 25.00 $mgmL^{-1}$ of membrane BV (for lysozyme adsorption in 10 mM potassium phosphate buffer at pH 7.0).

Similarly, van Beijeren et al.[47] observed almost no effect of flow rate in the range 15.0 to 20.0 $mLmin^{-1}$ on breakthrough curves by using the cation exchanger Sartobind S75 at pH 4.5. Moreover, the selectivity, $\alpha_{BSA/LF}$ at 10% LF breakthrough stayed in the same range between 89.97 and 147.02 at the different flow rates. This confirms one major advantage of MC, which can be operated at high flow rate without any decrease in binding capacity and separation performance. BSA flux is calculated from the total membrane area contained in the Sartobind device that is 75 cm^2. Effluent fluxes per membrane area were achieved of 200.0, 304.0 and 400.0 L $m^{-2}h^{-1}$ for flow rates at 12.0, 18.0 and 24.0 $BVmin^{-1}$, respectively. In a recent study, Valiño et al. [9] used a charged ultrafiltration membrane to separate BSA-LF mixture at a maximum flux per membrane area of 77.73 L $m^{-2}h^{-1}$ with an infinite selectivity. When operated at 24.0 $BVmin^{-1}$, the Sartobind S75 device in our study could therefore provide a five-fold higher

flux compared to the charged ultrafiltration membrane used by Valiño et al. [9].

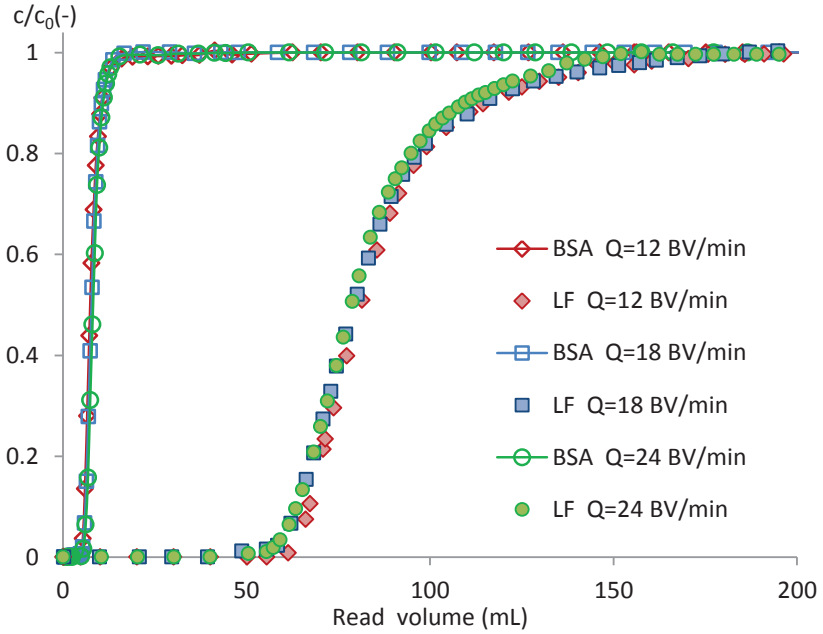

Fig. 4.6 Flow rate effects on the BSA-LF mixture breakthrough curves on Sartobind S75 in 100 mM phosphate buffer pH 6.0 and BSA/LF initial concentration of 2/1.

Table 4.2 BSA flux per membrane area, selectivity at 10% breakthrough and LF $DBC_{10\%}$ at different flow rates using Sartobind S75 with 100 mM phosphate buffer pH 6.0.

Sartobind S75			
Flow rate ($BVmin^{-1}$)	12.0	18.0	24.0
BSA flux ($gm^{-2}h^{-1}$)	370.00	544.16	728.00
Selectivity, $\alpha_{BSA/LF}$ at 10% breakthrough	147.02	89.97	123.23
LF $DBC_{10\%}$ (mg)	61.22	57.63	60.67

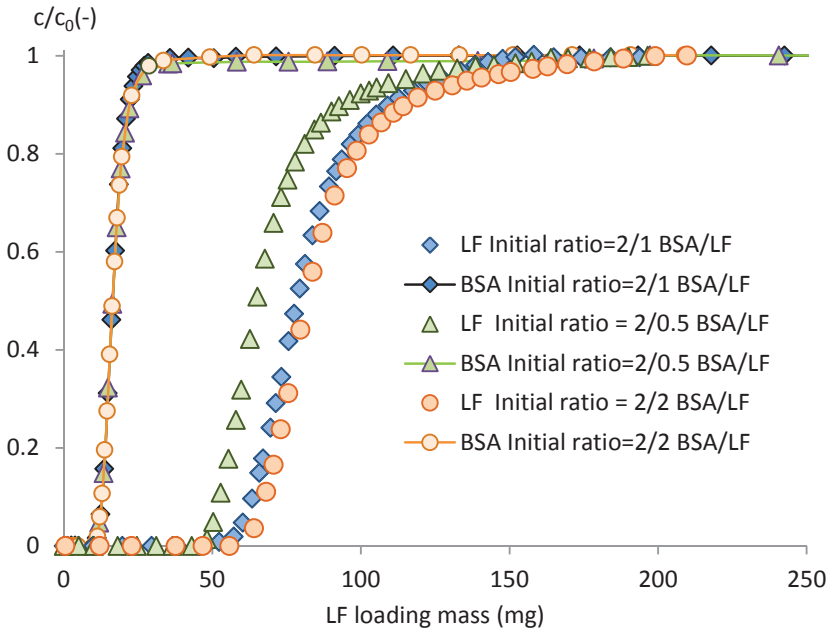

Fig. 4.7 Loading concentration effect on the BSA-LF mixture breakthrough curves at BSA/LF initial concentrations of 2/1, 2/0.5 and 2/2 on Sartobind S75 in 100 mM phosphate buffer with pH 6.0 at 24.0 $BVmin^{-1}$.

The influence of BSA/LF initial concentration was studied at 2/0.5, 2/1, and 2/2 by plotting the breakthrough curves versus LF loading mass (Fig. 4.7). For all initial concentrations, the breakthrough curves had the same shape, although breakthrough occurred slightly earlier at the concentration of 2/0.5. At the highest LF concentration (2/2), the process was faster and 10% LF breakthrough occurred after 40 s, compared to 76.15 s and 127.08 s, for the BSA/LF concentrations of 2/1 and 2/0.5, respectively. Therefore, loading of high protein concentration solution could be preferable to obtain a fast fractionation process. In a previous study, Valiño et al. [9] reported the loss in the separation selectivity at the BSA/LF concentrations of 2/1 compared to 4/1. This was suggested to be a consequence from the interaction between BSA and LF by forming stoichiometric complexes at the BSA/LF concentrations of 2/1, whose presence might modify the average size and the BSA flux. In our study, no effect of BSA/LF concentrations was observed and the selectivity remained infinite until breakthrough occurred, at the different BSA/LF concentrations.

4.4.2 Anion exchange membrane

- **Influence of buffer conditions**

Unlike the cation exchange device, the anion exchange device retains BSA molecules at pH between the isoelectric point of BSA and LF. BSA, being negatively charged, binds to the positively charged ligands of the anion exchange membrane; while LF, being less negatively charged, is collected in the effluent. Using the Sartobind Q75 device, the effect of the buffer pH values at 6.0, 7.0 and 8.0 on single protein adsorption performance was investigated (Fig. 4.8-A).

The buffers were first prepared using 100 mM phosphate. A low BSA binding capacity was obtained at all pH values because of the competition between salt ions and BSA for the binding sites. The highest $V_{ef,10\%}$ was obtained at pH 6.0 (about 3.00 mL). Using a lower ionic strength phosphate buffer (20 mM), the BSA binding capacity increased (Fig. 4.8-B).

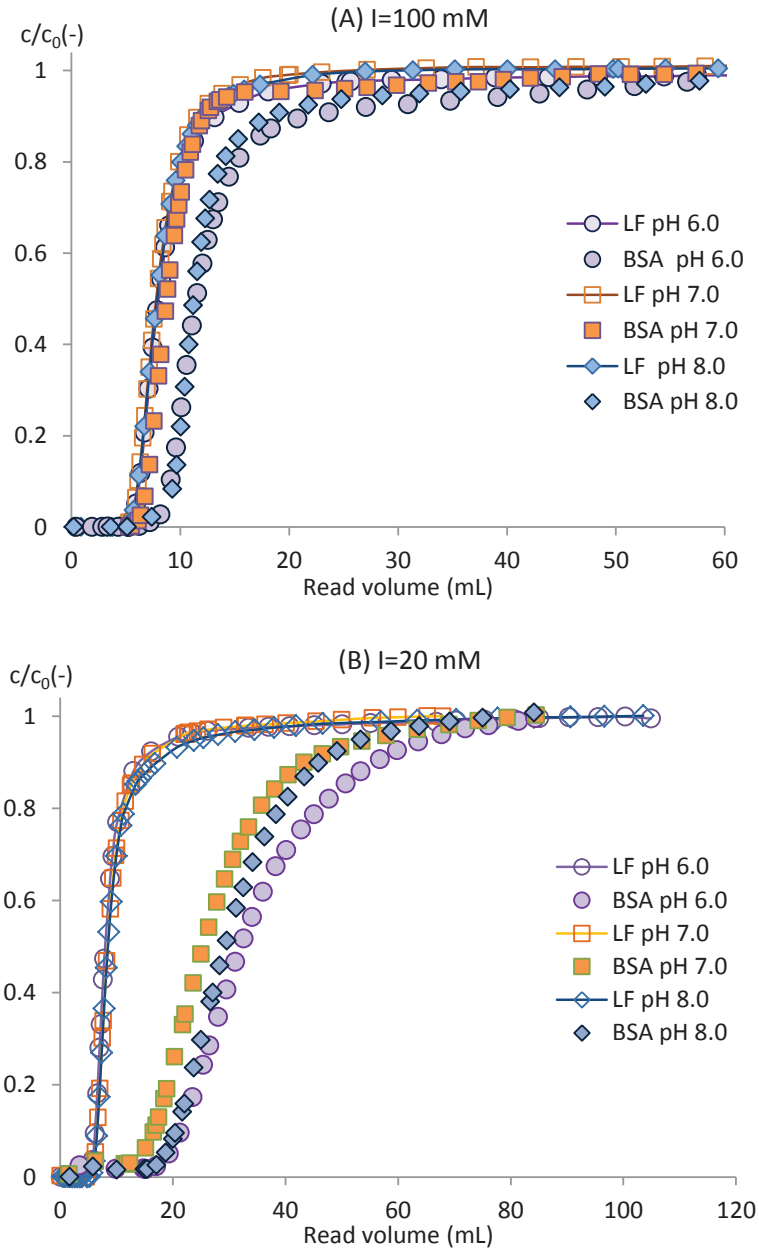

Fig. 4.8 pH influence on the single BSA and LF breakthrough curves on Sartobind Q75 at 12.0 $BVmin^{-1}$, 1.00 $mgmL^{-1}$ LF solution and 1.00 $mgmL^{-1}$ BSA solution. (A) 100 mM phosphate buffer. (B) 20 mM phosphate buffer.

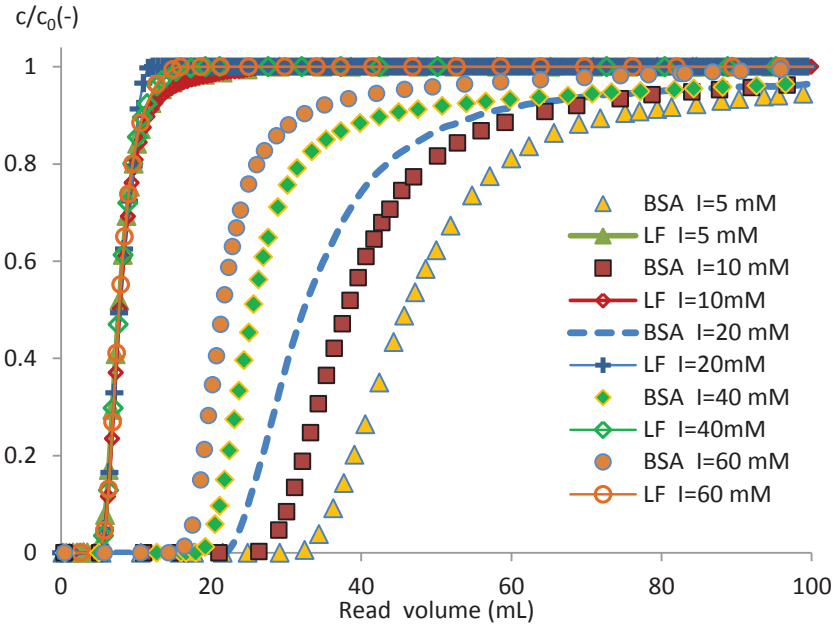

Fig. 4.9 Ionic strength effect between 5 mM and 60 mM phosphate buffer on the BSA-LF breakthrough curves at pH 6.0 and 12.0 $BVmin^{-1}$ on Sartobind Q75 with a BSA/LF initial concentration of 2/1.

To investigate further the effect of ionic strength, the phosphate buffer concentration was varied from 5 to 60 mM at pH 6.0 (Fig. 4.9). At lower buffer concentration, breakthrough occurred later and the BSA binding capacity increased. Similar shapes were obtained before 10 % breakthrough, although breakthrough curves became more delayed after 10 % breakthrough. Therefore, the lowest phosphate buffer concentration of 5 mM at pH 6.0 was retained for BSA/LF fractionation, providing the highest $V_{ef,10\%}$ at 30.67 mL with $DBC_{10\%}$ at 61.46 mg per device. Van Beijeren et al. [47] also reported a strong impact of ionic strength of acetate buffer on BSA adsorption behavior with a Sartobind Q device. The dynamic binding capacity decreased with increasing salt concentration due to the increased binding competition between phosphate ions and BSA for the quaternary ammonium functional groups, which has a strong interaction with the phosphate ions [48]. Moreover, strong complexes between BSA molecules and phosphate ions could be formed, which would reduce the BSA binding capacity on the anion exchange membrane [49]. The values of BSA $DBC_{10\%}$ are given in Table 4. 1 for every buffer condition.

4.4.2.2 Influence of operating conditions

Using the cation exchange device Sartobind Q75, BSA-LF separation was performed at different flow rates of 12.0, 18.0 and 24.0 $BVmin^{-1}$ (Fig. 4.10). At the different flow rates, BSA and LF breakthrough curves overlapped. This confirms that MC can be operated at high flow rates without any decrease in binding capacity and selectivity. Similar results are usually reported for BSA binding to Sartobind Q devices (for example van Beijeren et al. [47]). The highest flow rate of 24.0 $BVmin^{-1}$ was then retained for further experiments, because of the fast BSA-LF fractionation process with high separation performance. The process performances are summarized in Table 4.3. The LF flux per membrane area increased from 140.62 to 287.46 $Lm^{-2}h^{-1}$, for flow rates of 12.0 and 24.0 $BVmin^{-1}$, respectively. The selectivity of the LF/BSA mixture separation or $\alpha_{LF/BSA}$, was determined using Eq. 7 and found to in the range 69.94 to 76.05 at the various flow rates. The $DBC_{10\%}$ of BSA was unaffected by the flow rate and stayed constant about 61 mg.

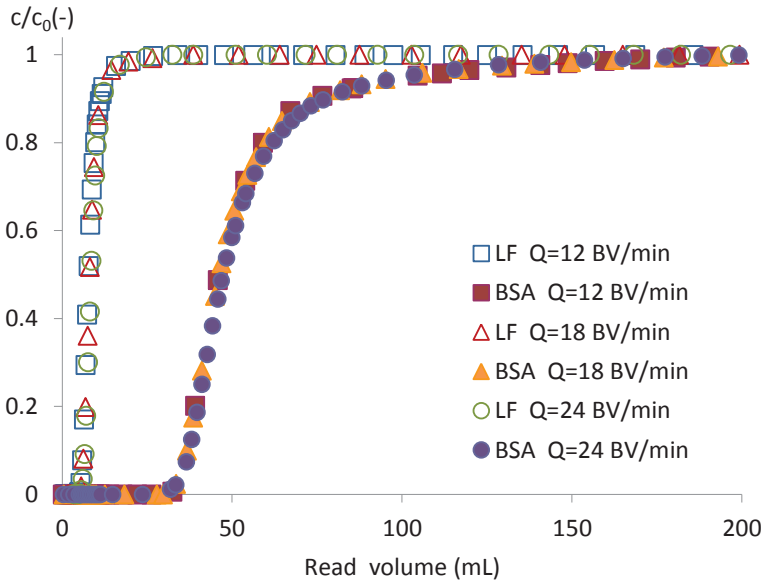

Fig. 4.10 Influence of flow rates at pH 6.0 on BSA-LF mixture breakthrough curves in 5 mM phosphate buffer with a BSA/LF loading concentrations of 2/1 on Sartobind Q75.

Table 4.3 LF flux per membrane area, selectivity at 10% breakthrough and BSA $DBC_{10\%}$ at different flow rates using Sartobind Q75 with 5 mM phosphate buffer pH 6.0.

Sartobind Q75 MC device			
Flow rate ($BVmin^{-1}$)	12.0	18.0	24.0
LF flux ($gm^{-2}\ h^{-1}$)	140.62	224.33	287.46
Selectivity, $\alpha_{LF/BSA}$ at 10% breakthrough	70.51	69.94	76.05
BSA $DBC_{10\%}$ (mg)	61.46	61.26	60.17

The effect of BSA-LF initial concentrations was investigated at 2/0.5, 2/1 and 4/1 by plotting the breakthrough curves versus BSA loading mass (Fig. 4.11). At BSA/LF concentrations of 2/0.5 and 2/1, the BSA breakthrough shape and position were unaffected. When the BSA concentration was increased two-fold from 2.00 to 4.00 $mgmL^{-1}$, the BSA binding capacity increased as the BSA breakthrough curve occurred later. The BSA breakthrough shape was not affected by the concentration change.

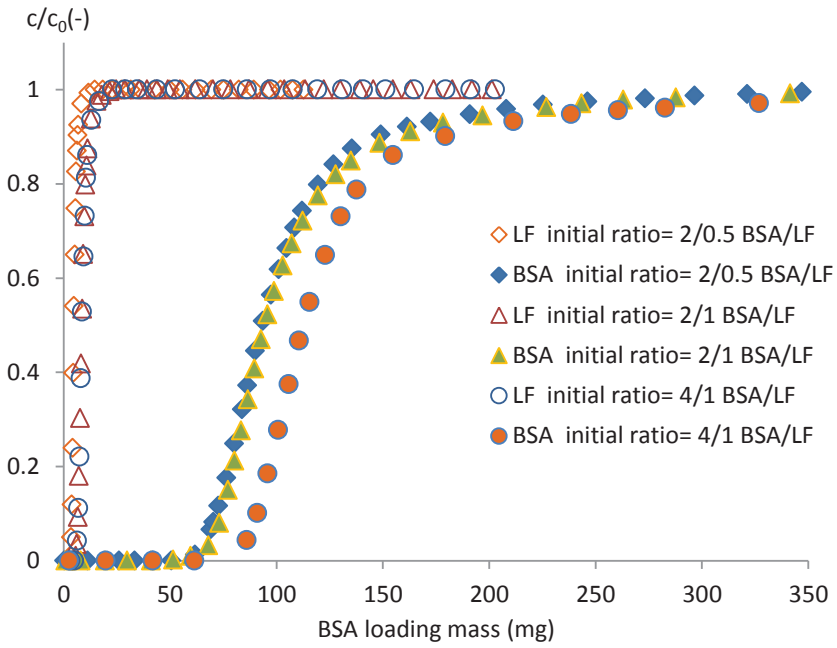

Fig. 4.11 Concentration effect on the BSA-LF mixture breakthrough curves in 5 mM phosphate buffer with pH 6.0 at the flow rate of 24.0 $BVmin^{-1}$ on Sartobind Q75. The loading BSA-LF concentrations were investigated at 2/0.5, 2/1 and 4/1.

4.4.3 Elution step

Eluent selection was investigated for LF from the cation exchange membrane and BSA from the anion exchange membrane (Table 4.4). All elution experiments were performed at a flow rate of 6.0 $BVmin^{-1}$. The optimized loading volume, $V_{ef,10\%}$, was 62.0 and 31.0 mL for Sartobind S75 and Q75 devices, respectively. With the cation exchange membrane, the ionic concentrations of 1.00 and 2.00 M NaCl in phosphate buffer pH 6.0 gave relatively low LF eluted amount. A slightly higher LF recovery was observed using phosphate buffer at pH 12.0. However, LF was not eluted using phosphate buffer pH 11.0. The addition of 25.00% ethylene glycol in phosphate buffer pH 12.0 gave the highest LF recovery (around 70.0 %). This may be due to the contribution of ionic and hydrophobic interaction in LF desorption, as previously showed by Wolman et al. [30] for LF desorption from dye-membranes. With the anion exchange membrane, the eluted amount of BSA was higher with the citrate eluent pH 3.0, compared to 1.00 and 2.00 M NaCl in phosphate buffer pH 6.0. Similarly to the cation exchange device, the simultaneous effect of pH change and hydrophobic interaction gave the highest BSA recovery (over 72.00%) by adding 25.00% ethylene glycol in citrate buffer pH 3.0.

Table 4.4 LF and BSA desorption using different eluents on Sartobind S75 and Q75, respectively. The elution step was operated at 6 $BVmin^{-1}$ with the eluent volume of 20 mL.

	Eluents	$DBC_{10\%}$ of LF (mg)	Eluted LF mass (mg)	Eluted LF / total loading (%)
Sartobind S75	1.00 M NaCl in phosphate buffer pH 6.0	59.44	25.99	40.61
	2.00 M NaCl in phosphate buffer pH 6.0	60.48	29.51	46.11
	Phosphate buffer pH 11.0	59.75	0.00	0.00
	Phosphate buffer pH 12.0	60.18	35.02	54.72
	25.00% ethylene glycol in phosphate buffer pH 12.0	59.60	44.76	69.94
	Eluents	$DBC_{10\%}$ of BSA (mg)	Eluted BSA mass (mg)	Eluted BSA / total loading (%)
Sartobind Q75	1.00 M NaCl in phosphate buffer pH 6.0	60.14	23.64	36.94
	2.00 M NaCl in phosphate buffer pH 6.0	61.39	25.17	39.33
	Citrate buffer pH 3.0	61.64	30.84	48.19
	25.00% ethylene glycol in citrate buffer pH 3.0	60.86	46.49	72.64

Finally, the effect of the flow rate was investigated at 6.0, 3.0 and 1.0 $BVmin^{-1}$. For the cation exchange device, the elution buffer was 25% ethylene glycol in phosphate buffer pH 12.0 and for the anion exchange device 25.00% ethylene glycol in citrate buffer pH 3.0. For both anion and cation exchange membranes, the eluted amount of protein increased with the decreasing flow rate (Table 4.5), as previously reported [30]. At the flow rate of 1.0 $BVmin^{-1}$, the protein recovery was about 81% and 93% for the cation and anion exchange devices, respectively. Therefore, a high flow rate during the loading step and a lower flow rate during the elution step were proposed for BSA-LF mixture separation to ensure a fast process and a high protein recovery.

Table 4.5 Flow rate effect on LF and BSA eluted mass on Sartobind S75 and Q75 ,respectively, using the eluent with hydrophobic and pH change effect.

	Flow rate ($BVmin^{-1}$)	6.0	3.0	1.0
Eluted LF on Sartobind S75 using 25% ethylene glycol in phosphate buffer pH 12.0	$DBC_{10\%}$ of LF (mg)	59.34	59.57	60.29
	Eluted LF mass (mg)	42.87	47.10	52.43
	Eluted LF/ total loading (%)	69.14	75.97	81.92
Eluted BSA on Sartobind Q75 using 25% ethylene glycol in citrate buffer pH 3.0	$DBC_{10\%}$ of BSA (mg)	60.86	62.60	62.72
	Eluted BSA mass (mg)	46.49	54.62	58.92
	Eluted BSA/total loading (%)	72.64	87.25	93.95

4.4.4 BSA-LF mixture separation cycles on cation exchange

Using the Sartobind S75 cation exchanger, different separation processes were tested (Table 4.6 Process time and LF productivity of different BSA-LF separation processes using Sartobind S75 devices.Table 4.6). The first process was operated at the same flow rate of 6.0 $BVmin^{-1}$ for the equilibrium, loading, washing and elution steps, according to Sartobind user's guide. This process led to almost the same process time as the process with optimized flow rate at each steps (24 $BVmin^{-1}$ for the loading and washing steps and 1 $BVmin^{-1}$ for the elution step). In addition, the LF productivity using 6.0 $BVmin^{-1}$ of flow rate at all steps was 936.20 $mgmL^{-1}$ h^{-1}, whereas, using different flow rates, a higher LF productivity was obtained equal to 1143.07 $mgmL^{-1}$ h^{-1}. This higher productivity was due to the higher LF eluted mass at the slowest elution flow rate.

However, for both methods, the processing time (around 78.50 min) was mainly attributed due to the slow regeneration step (1.0 $BVmin^{-1}$). Therefore, the BSA-LF mixture separation was further tested at the increased flow rate of 3.0 $BVmin^{-1}$ for the regeneration step. The separation was performed over 3 cycles, with very good repeatability (Fig. 4.12). The process time was significantly shortened to 34.19 min with an improved LF productivity of 2628.84 $mgmL^{-1}$ h^{-1}. In our study, the productivity was much higher than the one obtained by Wolman et al. [30] using triazinic dye HE-3B-HF-II membranes for LF purification from bovine whey (252.9 $mgmL^{-1}$ h^{-1} at combined flow rates). However, the results are difficult to compare as the LF concentration used in our study was much higher (70 folds), as well as the loaded mass of LF.

Table 4.6 Process time and LF productivity of different BSA-LF separation processes using Sartobind S75 devices.

Process conditions	Process time (min)	Productivity (mg(of LF) mL^{-1} h^{-1})
6 $BVmin^{-1}$ for all steps, except the regeneration step at 1 $BVmin^{-1}$	78.50	936.20
Different flow rates with the regeneration step at 1 $BVmin^{-1}$	78.63	1143.07
Different flow rates with the regeneration step at 3 $BVmin^{-1}$	34.19	2628.84

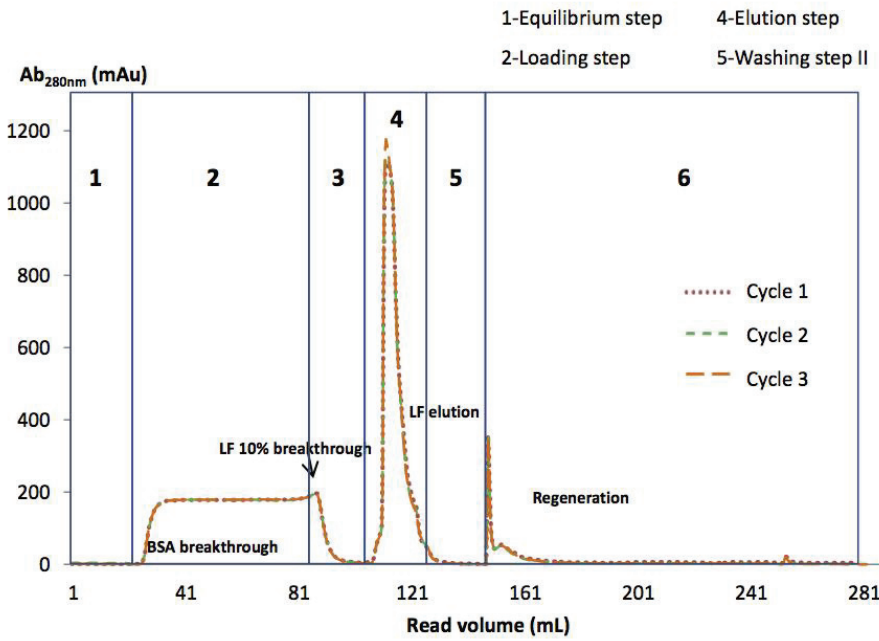

Fig. 4.12 BSA-LF mixture separation over three repeated cycles with the cation exchange MC Sartobind S75 at 24.0 $BVmin^{-1}$ for the loading and washing steps, 1.0 $BVmin^{-1}$ for the elution step and 3.0 $BVmin^{-1}$ for the regeneration step. The initial concentrations of BSA/LF were 2/1.

4.5 Conclusion

Using MC at pH between the isoelectric point of BSA and LF, separation between these two proteins was found very effective. Using the cation exchange membrane, LF was totally retained until breakthrough occurred; the higher selectivity being obtained at a strong ionic strength of 100 mM and buffer pH 6.0, with LF $DBC_{10\%}$ about 60 mg per device. At these conditions, BSA passed through the membrane and in the effluent at the optimal flux per membrane area of 728.00 $gh^{-1}m^{-2}$. Using the anion exchange membrane, an opposite effect was observed. Optimal BSA adsorption was obtained at mild ionic strength of 5 mM and pH 6.0, with BSA $DBC_{10\%}$ of 62.98 mg per device, while LF passed through the membrane at the optimal flux of 287.46 gm^{-2} h^{-1}.

The selectivity of LF and BSA with both anion and cation exchange membranes were independent of flow rate (between 12.0 and 24.0 $BVmin^{-1}$). This confirms the advantage of MC which can be used at high flow rate without any loss of selectivity. In addition, the selectivity did not decrease with increasing concentration of loaded LF, and even more, the binding capacity at 10 % breakthrough increased. These results suggest that high loaded concentrations can also be used.

To optimize the LF eluted mass on the cation exchange device, 25% ethylene glycol in phosphate buffer pH 12.0 was applied at the reduced flow rate of 1 $BVmin^{-1}$. At these conditions, LF recovery was around 80.0%. Similarly to the cation exchange membrane, the anion exchange membrane was tested with 25% ethylene glycol in citrate buffer pH 3.0 as the eluent, which led to the highest BSA recovery about 94.0% at the lowest flow rate of 1.0 $BVmin^{-1}$. Furthermore, the BSA-LF separation procedure using different flow rates (25.0 $BVmin^{-1}$ for the loading and washing steps and 1 $BVmin^{-1}$ for the elution step) led to a fast process and high protein recovery. Process time was shortened and productivity increased by 2-fold by changing the flow rate during the regeneration step to 3.0 $BVmin^{-1}$.

Overall, our results suggest that MC can be a very effective technique for BSA-LF mixture separation and could be applied at industrial scale. The technique could be applied also successfully to the separation of other proteins of similar size and different isoelectric points. However, for industrial applications such as whey treatment, lowering the price of the available MC devices would remain undoubtedly a major challenge.

4.6 References

[1] M.L. Groves, The isolation of a red protein from milk, J. Am. Chem. Soc. 82 (1960) 3345–3350. doi:10.1021/ja01498a029.

[2] B. Johanson, Isolation of an iron-containing red protein from human milk., Acta Chemica Scandinavica. 14 (1960) 510–12.

[3] J.K. Actor, S.-A. Hwang, M.L. Kruzel, Lactoferrin as a natural immune modulator, Curr Pharm Des. 15 (2009) 1956–1973.

[4] A.C.M. van Hooijdonk, K.D. Kussendrager, J.M. Steijns, In vivo antimicrobial and antiviral activity of components in bovine milk and colostrum involved in non-specific defence, British Journal of Nutrition. 84 (2000) 127–134. doi:10.1017/S000711450000235X.

[5] M. Marchetti, C. Longhi, M.P. Conte, S. Pisani, P. Valenti, L. Seganti, Lactoferrin inhibits herpes simplex virus type 1 adsorption to Vero cells, Antiviral Res. 29 (1996) 221–231.

[6] Y. Takayama, Lactoferrin and its role in wound healing, Springer Science & Business Media, 2011.

[7] T.W. Hutchens, B. Lönnerdal, eds., Lactoferrin: Interactions and biological functions, 1997 edition, Humana Press, Totowa, N.J, 1997.

[8] M.M.H. El-Sayed, H.A. Chase, Trends in whey protein fractionation, Biotechnol Lett. 33 (2011) 1501–1511. doi:10.1007/s10529-011-0594-8.

[9] V. Valiño, M.F. San Román, R. Ibañez, I. Ortiz, Improved separation of bovine serum albumin and lactoferrin mixtures using charged ultrafiltration membranes, Separation and Purification Technology. 125 (2014) 163–169. doi:10.1016/j.seppur.2014.01.023.

[10] M. Nyström, P. Aimar, S. Luque, M. Kulovaara, S. Metsämuuronen, Fractionation of model proteins using their physiochemical properties, Colloids and Surfaces A: Physicochemical and Engineering Aspects. 138 (1998) 185–205. doi:10.1016/S0927-7757(96)03892-7.

[11] M.C. Almécija, R. Ibáñez, A. Guadix, E.M. Guadix, Influence of pH in the recovery of lactoferrin from whey with ceramic membranes, Desalination. 200 (2006) 475–476. doi:10.1016/j.desal.2006.03.401.

[12] G. Brisson, M. Britten, Y. Pouliot, Electrically-enhanced crossflow microfiltration for separation of lactoferrin from whey protein mixtures, Journal of Membrane Science. 297 (2007) 206–216. doi:10.1016/j.memsci.2007.03.046.

[13] N. Ndiaye, Y. Pouliot, L. Saucier, L. Beaulieu, L. Bazinet, Electroseparation of bovine lactoferrin from model and whey solutions, Separation and Purification Technology. 74 (2010) 93–99. doi:10.1016/j.seppur.2010.05.011.

[14] S. Okonogi, M. Tomita, T. Tomimura, Y. Tamura, T. Mizota, Process for producing bovine lactoferrin in high purity, Google Patents, 1988. http://www.google.com/patents/US4791193.

[15] S. Yoshida, Ye-Xiuyun, Isolation of lactoperoxidase and lactoferrins from bovine milk acid whey by carboxymethyl cation exchange chromatography, Journal of Dairy Science. 74 (1991) 1439–1444. doi:10.3168/jds.S0022-0302(91)78301-X.

[16] R. Hahn, P.M. Schulz, C. Schaupp, A. Jungbauer, Bovine whey fractionation based on cation-exchange chromatography, Journal of Chromatography A. 795 (1998) 277–287.

doi:10.1016/S0021-9673(97)01030-3.
[17] C.J. Fee, A. Chand, Capture of lactoferrin and lactoperoxidase from raw whole milk by cation exchange chromatography, Separation and Purification Technology. 48 (2006) 143–149. doi:10.1016/j.seppur.2005.07.011.
[18] Y. Liang, X. Wang, M. Wu, W. Zhu, Simultaneous isolation of lactoferrin and lactoperoxidase from bovine colostrum by SPEC 70 SLS cation exchange resin, Int J Environ Res Public Health. 8 (2011) 3764–3776. doi:10.3390/ijerph8093764.
[19] B. Lönnerdal, J. Carlsson, J. Porath, Isolation of lactoferrin from human milk by metal-chelate affinity chromatography, FEBS Letters. 75 (1977) 89–92. doi:10.1016/0014-5793(77)80059-8.
[20] M.J. Santos, J.A. Teixeira, L.R. Rodrigues, Fractionation and recovery of whey proteins by hydrophobic interaction chromatography, Journal of Chromatography B. 879 (2011) 475–479. doi:10.1016/j.jchromb.2011.01.003.
[21] K. Plate, S. Beutel, H. Buchholz, W. Demmer, S. Fischer-Frühholz, O. Reif, et al., Isolation of bovine lactoferrin, lactoperoxidase and enzymatically prepared lactoferricin from proteolytic digestion of bovine lactoferrin using adsorptive membrane chromatography, Journal of Chromatography A. 1117 (2006) 81–86. doi:10.1016/j.chroma.2006.03.090.
[22] V. Orr, L. Zhong, M. Moo-Young, C.P. Chou, Recent advances in bioprocessing application of membrane chromatography, Biotechnology Advances. 31 (2013) 450–465. doi:10.1016/j.biotechadv.2013.01.007.
[23] M.-E. Avramescu, Z. Borneman, M. Wessling, Dynamic behavior of adsorber membranes for protein recovery, Biotechnol. Bioeng. 84 (2003) 564–572. doi:10.1002/bit.10807.
[24] S.M. Saufi, C.J. Fee, Recovery of lactoferrin from whey using cross-flow cation exchange mixed matrix membrane chromatography, Separation and Purification Technology. 77 (2011) 68–75. doi:10.1016/j.seppur.2010.11.021.
[25] R. Ghosh, Protein separation using membrane chromatography: opportunities and challenges, Journal of Chromatography A. 952 (2002) 13–27. doi:10.1016/S0021-9673(02)00057-2.
[26] W. Noppe, F.M. Plieva, I.Y. Galaev, K. Vanhoorelbeke, B. Mattiasson, H. Deckmyn, Immobilised peptide displaying phages as affinity ligands: Purification of lactoferrin from defatted milk, Journal of Chromatography A. 1101 (2006) 79–85. doi:10.1016/j.chroma.2005.09.064.
[27] M.R. Etzel, T. Bund, Monoliths for the purification of whey protein–dextran conjugates, Journal of Chromatography A. 1218 (2011) 2445–2450. doi:10.1016/j.chroma.2011.01.025.
[28] C.K. Chiu, M.R. Etzel, Fractionation of lactoperoxidase and lactoferrin from bovine whey using a cation exchange membrane, J. Food Sci. 62 (1997) 996–1000. doi:10.1111/j.1365-2621.1997.tb15023.x.
[29] L. Voswinkel, U. Kulozik, Fractionation of all major and minor whey proteins with radial flow membrane adsorption chromatography at lab and pilot scale, International Dairy Journal. 39 (2014) 209–214. doi:10.1016/j.idairyj.2014.06.012.
[30] F.J. Wolman, D.G. Maglio, M. Grasselli, O. Cascone, One-step lactoferrin purification from bovine whey and colostrum by affinity membrane chromatography, Journal of Membrane Science. 288 (2007) 132–138. doi:10.1016/j.memsci.2006.11.011.
[31] S.-Y. Suen, M.R. Etzel, A mathematical analysis of affinity membrane bioseparations,

Chemical Engineering Science. 47 (1992) 1355–1364. doi:10.1016/0009-2509(92)80281-G.
[32] A. Shiosaki, M. Goto, T. Hirose, Frontal analysis of protein adsorption on a membrane adsorber, Journal of Chromatography A. 679 (1994) 1–9. doi:10.1016/0021-9673(94)80306-4.
[33] K.H. Gebauer, J. Thömmes, M.R. Kula, Breakthrough performance of high-capacity membrane adsorbers in protein chromatography, Chemical Engineering Science. 52 (1997) 405–419. doi:10.1016/S0009-2509(96)00426-5.
[34] C. Frerick, P. Kreis, A. Górak, A. Tappe, D. Melzner, Simulation of a human serum albumin downstream process incorporating ion-exchange membrane adsorbers, Chemical Engineering and Processing: Process Intensification. 47 (2008) 1128–1138. doi:10.1016/j.cep.2007.07.013.
[35] H. Yang, M.R. Etzel, Evaluation of three kinetic equations in models of protein purification using ion-exchange membranes, Ind. Eng. Chem. Res. 42 (2003) 890–896. doi:10.1021/ie020561u.
[36] C. Boi, S. Dimartino, G.C. Sarti, Modelling and simulation of affinity membrane adsorption, Journal of Chromatography A. 1162 (2007) 24–33. doi:10.1016/j.chroma.2007.02.008.
[37] S. Dimartino, C. Boi, G.C. Sarti, A validated model for the simulation of protein purification through affinity membrane chromatography, Journal of Chromatography A. 1218 (2011) 1677–1690. doi:10.1016/j.chroma.2010.11.056.
[38] Sartobind® Q 75 93IEXQ42DB-12--V - Sartorius AG, (n.d.). http://www.sartorius.com/en/product/product-detail/93iexq42db-12-v/ (accessed December 10, 2014).
[39] L. Voswinkel, U. Kulozik, Fractionation of whey proteins by means of membrane adsorption chromatography, Procedia Food Science. 1 (2011) 900–907. doi:10.1016/j.profoo.2011.09.136.
[40] M.-S. Chun, S.-Y. Lee, S.-M. Yang, Estimation of zeta potential by electrokinetic analysis of ionic fluid flows through a divergent microchannel, Journal of Colloid and Interface Science. 266 (2003) 120–126. doi:10.1016/S0021-9797(03)00576-9.
[41] L. Sánchez, P. Aranda, Md. Pérez, M. Calvo, Concentration of Lactoferrin and Transferrin throughout Lactation in Cow's Colostrum and Milk, Biological Chemistry Hoppe-Seyler. 369 (1988) 1005–1008.
[42] R.J. Harmon, F.L. Schanbacher, L.C. Ferguson, K.L. Smith, Concentration of lactoferrin in milk of normal lactating cows and changes occurring during mastitis, Am. J. Vet. Res. 36 (1975) 1001–1007.
[43] J.M. Steijns, A.C.M. van Hooijdonk, Occurrence, structure, biochemical properties and technological characteristics of lactoferrin, British Journal of Nutrition. 84 (2000) 11–17. doi:10.1017/S0007114500002191.
[44] C. Baldasso, T.C. Barros, I.C. Tessaro, Concentration and purification of whey proteins by ultrafiltration, Desalination. 278 (2011) 381–386. doi:10.1016/j.desal.2011.05.055.
[45] K.W.K. Yee, D.E. Wiley, J. Bao, Whey protein concentrate production by continuous ultrafiltration: Operability under constant operating conditions, Journal of Membrane Science. 290 (2007) 125–137. doi:10.1016/j.memsci.2006.12.026.
[46] V. Valiño, M.F. San Román, R. Ibáñez, J.M. Benito, I. Escudero, I. Ortiz, Accurate determination of key surface properties that determine the efficient separation of bovine

milk BSA and LF proteins, Separation and Purification Technology. 135 (2014) 145–157. doi:10.1016/j.seppur.2014.07.051.

[47] P. van Beijeren, P. Kreis, T. Zeiner, Ion exchange membrane adsorption of bovine serum albumin—Impact of operating and buffer conditions on breakthrough curves, Journal of Membrane Science. 415–416 (2012) 568–576. doi:10.1016/j.memsci.2012.05.051.

[48] C. Teepakorn, K. Fiaty, C. Charcosset, Effect of geometry and scale for axial and radial flow membrane chromatography—Experimental study of bovin serum albumin adsorption, Journal of Chromatography A. 1403 (2015) 45–53. doi:10.1016/j.chroma.2015.05.023.

[49] I.M. Klotz, J.M. Urquhart, The binding of organic ions by proteins. Buffer effects, J. Phys. Chem. 53 (1949) 100–114. doi:10.1021/j150466a008.

Chapter 5

COMPARISON OF MEMBRANE CHROMATOGRAPHY AND MONOLITH CHROMATOGRAPHY FOR LACTOFERRIN AND BOVINE SERUM ALBUMIN SEPARATION

(This page is intentionally left blank)

Chapter 5
COMPARISON OF MEMBRANE CHROMATOGRAPHY AND MONOLITH CHROMATOGRAPHY FOR LACTOFERRIN AND BOVINE SERUM ALBUMIN SEPARATION

5.1 Abstract

These last decades, membranes and monoliths have been increasingly used as stationary phases for chromatographic process. Their fast mass transfer is mainly based on convection, which leads to reduced diffusion usually observed in resins. Nevertheless, poor flow distribution leading to inefficient binding remains a major challenge for the development of both membrane and monolith devices. Moreover, the comparison of membranes and monoliths for biomolecule separation has been very little investigated. In this paper, the separation of two proteins, BSA and LF, with similar size but different isoelectric point, was investigated using strong cation exchange membranes at pH 6.00 and monoliths packed in the same housing, as well as commercialized devices. Using membranes in the CIM housing, higher binding capacities, sharper breakthrough curves, as well as sharper and more symmetric elution peaks were obtained. The monolith and commercialized membrane device showed lower LF binding capacity, and broadened and non-symmetric elution peaks. The CFD model confirmed that poor flow distribution inside the devices led to low binding capacities. Moreover, for the membrane, a bi-Langmuir isotherm was needed to predict the tailing breakthrough curve near saturation, whereas a Langmuir isotherm was adequate for the modeling of monoliths, which did not show this tailing effect.

Keywords :

Membrane chromatography, Monolith chromatography, Bovine serum albumin (BSA), Lactoferrin (LF), Separation

5.2 Introduction

Downstream processes in the biopharmaceutical and biotechnological industries usually rely on multiple chromatographic steps, with micro-sized resins in a packed-bed column as the stationary phase. The resins have diameter between 100 and 500 µm, and generally provide an efficient chromatographic technique with high binding capacity [1,2]. However, the method is rather slow and represents a major cost in biomolecules production, as the transport of solute molecules to the binding sites inside resins pores is limited by intra-particle diffusion. The pressure drop over the column is high even at low flow rates and increases during processing due to bed consolidation and column blinding [3]. Decrease in binding capacity and throughput are also observed using large biomolecules and highly concentrated feed-stocks [4,5]. Furthermore, the scaling-up of a resin-based column remains a challenge, as significant medium compression and increasing pressure drops are observed with increasing bed height [6]. Consequently, several other innovative stationary phases, including monoliths and membranes, have been developed in the last few decades as possible alternatives to classical chromatographic supports

Membrane chromatography is based on the integration of membrane filtration and liquid chromatography into a single-step operation [3,7,8]. The main advantage of the method is attributed to short diffusion times, as the interactions between molecules and active sites in the membrane occur in convective through-pores rather than in stagnant fluid inside the resin pores. Therefore, membrane chromatography has the potential to operate at high flow rates and low pressure drops, to purify large biomolecules with small diffusivities, to reduce biomolecules degradation and denaturation, and buffer usages [3,8,9]. Another interesting feature of these membrane devices for biopharmaceutical industries is their single-use ability, as the elimination of cleaning and regeneration steps reduces the contamination risk and manufacturing costs. Several membrane materials have been tested as chromatographic supports: inorganic-organic (e.g. an alkoxysilane coated on glass fiber and alumina membranes [10]) and organic materials (i.e. cellulose and its derivatives, nylon, polyethersulfone, polypropylene, polyvinylidene, etc. [5, 10]). Most membrane chromatography devices, especially for ion-exchange, are made from regenerated cellulose [10]. Several devices have also been tested including axial, radial and tangential flow devices. Axial flow devices containing stacked membrane disks are commonly used at laboratory scale and are commercialized with different membrane volumes. Radial flow membrane chromatography, reported first in the late 1980's [11], are preferred for large scale applications due to easiest scaling-up. Nowadays, several radial flow membrane chromatography devices are commercialized with large bed volumes up to 1-5 L. Tangential flow device is another possible alternative for industrial applications and could reduce membrane fouling [12]. Recently, Madadkar et al. [13] presented a novel configuration using stacked membrane sheets with lateral fed, to obtain a more uniform flow distribution, and therefore higher resolution of elution peaks.

Monoliths are single pieces of porous material characterized by a highly interconnected network of channels with diameters in the range of 10–4000 nm [7,14,15]. The major benefit of monolithic supports for chromatography is similar to the one of membranes. The mobile phase is forced to flow through the large pores; as a consequence, mass transport is mainly based on

convection, and high flow rates can be obtained without negative effect on separation performance. Due to the large pore size and short bed of monolith supports, the separation time can be decreased, as well as the pressure drop compared to traditional resin columns [15–18]. In addition, monolithic columns offer high resolution fractionation and have been increasingly employed for analytical and chip-based separation [24]. This high resolution separation results from the absence of void volume in the monolithic column, which reduces eddy dispersion and turbulent void flow [14,18–20]. Monoliths have been produced using a large range of materials, including polymethacrylate, polyacrylate, polyacrylamide, polystyrene, cellulose and silica [7,17,21]. Most monoliths for chromatography are made from polymethacrylate [17,21]. They are available in two main geometries: disk shape (diameter>length) and rod shape (length>diameter) for laboratory scale [22]. For both geometries, scaling-up remains an issue as mechanical instability and inhomogeneity in the monolith are observed with increasing diameter. Monolithic rods can be scaled up by increasing their length; however, the increasing pressure drop becomes a major problem [21]. Similarly to membrane devices, monolithic tubes have been introduced for large-scale separation unit with radial flow [21]. To prepare a monolith tube of desired thickness, several cylinders of appropriate dimensions are polymerized and inserted one into another [21]. A subsequent second-step polymerization can be performed to fill the void between the cylinders when required. The same authors [23] prepared tubular monolithic columns up to 8000 mL, having high resolution separation and significant productivity.

Several models of membrane and monolith chromatography have been proposed to predict and characterize flow distribution and binding performance. In case of monolith chromatography, Meyers and Liapis [24] estimated the intraparticle interstitial velocity and pore diffusivity of solute molecules within the monolith, by using a model, called “pore network model”, which combined the effects of steric hindrance at the entrance of the pores and frictional resistance within the pores, as well as the effects of pore size, porous network connectivity, ligand size, solute molecule size and fractional saturation of ligands. The results obtained showed that the pore connectivity played a key role in solute molecule transport. Both interstitial velocity and effective pore diffusivity increased significantly with pore connectivity. The value of the pore diffusivity in the pores was further used to simulate the dynamic adsorption behavior of bovine serum albumin (BSA) in a monolith column [25]. Mathematical modeling determined by the Langmuir equilibrium isotherm, mass transfer resistances, and axial dispersion was proposed by Hahn et al. [26] to investigate mass transfer properties of a CIM monolith ion-exchanger. The model predicted accurately lysozyme, BSA and IgG breakthrough curves at different flow rates. The same authors used their model to simulate breakthrough curves for disk and tube geometries, assuming axial flow in case of the tube geometry [27]. However, a large difference was found between predicted results and experimental data. Sanchez et al. [28] proposed a similar modeling of affinity chromatography using an agarose-coated monolith support, to characterize the adsorption and elution behavior of asparaginase on the monolithic support.

Mathematical modeling of membrane chromatography has been extensively studied. Most models consider a convection-diffusion equation and a Langmuir type equation to describe binding kinetics for affinity [29] and ion-exchange separation [30,31]. Several other kinetic

equations have been tested, derived from the steric mass action model [32], steric hindrance and spreading equations [33] and bi-Langmuir model [34]. However, flow distribution in membrane chromatography devices leads to discontinuous flow and dead volume with side-effects like asymmetric and tailing breakthrough curves. To account for flow non-idealities, several methods have been proposed such as introducing a polynomial equation for flow boundary condition at the membrane inlet [35] or using a combination in series of an ideal continuously stirred tank reactor (CSTR) and an ideal plug flow reactor (PFR) [34]. This mathematical model was then applied successfully to complex purifications, such as separation of immunoglobulin G from complex mixtures using affinity membrane chromatography [36]. Moreover, Von Lieres et al. [37] introduced a similar model called "zonal rate model" (ZRM), using a network of CSTRs to represent different zones of the module, that were considered homogeneous with respect to flow velocity. An additional PFR was connected in series with the CSTR network in order to account for time lags. The model predicted the breakthrough curves under non-binding and binding conditions for ion-exchange chromatography [38,39]. Moreover, the ZRM was extended to predict the binding behavior of both axial and radial flow chromatography devices [40] and the scaling-up from a 5 mL axial flow device to a 140 mL radial flow device [41]. Recently, computational fluid dynamics (CFD) was applied to small-scale axial and large-scale radial flow chromatography modeling [42]. The CFD model was used to predict the hydrodynamics and the breakthrough curves under non-binding and binding conditions using the device geometry and membrane properties.

Despite numerous studies on membrane and monolith chromatography, the comparison of their separation performance has been little studied. To our knowledge, only Gagnon et al. [43] compared the performance of membrane and monolith anion exchangers for removal of DNA from IgG solutions. The authors showed that breakthrough curves using membrane devices were broadened and happened earlier; in addition, the binding capacities were lower than the ones obtained with the monolith device. The lowest performance of the membrane was explained by the non-ideal flow distribution in the membrane device: turbulent mixing occurs between membrane layers and elsewhere within the housing; on the contrary, this does not happen in monoliths which have a very limited void volume. Turbulent mixing in the void volume (eddy dispersion) is a major cause of band spreading in chromatographic separation. However, the housings containing membrane and monolith were different, which could lead to an erroneous comparison.

In this work, the separation of two similar size proteins, BSA and lactoferrin (LF), is studied using monolith and membrane supports, both being strong cation exchangers. Although many techniques have been developed to isolate LF, the separation of high-value minor proteins of similar molecular weights such as BSA and LF remains a challenge [44,45]. BSA is a 66.5 kDa protein with an isoelectric point near 4.7; LF is a 78.0 kDa protein with an isoelectric point around 8.7. In our former study [51], we showed that using membrane chromatography at pH between the isoelectric point of BSA and LF, the separation between these two proteins was very effective. Using the cation exchange membrane, LF was totally retained until breakthrough occurred; the higher selectivity being obtained at a strong ionic strength of 100 mM and buffer pH 6.0. At these conditions, BSA passed totally through the membrane and in the effluent.

To compare monolith and membrane chromatography for LF and BSA separation, we used membranes stacks and monolith discs with identical bed height placed into the same housing (CIM housing, BIA Separations, Slovenia). The effect of membrane and monolith support on flow distribution, binding behavior and elution peaks were measured. In addition, scaling-up of membrane and monolithic supports was investigated by increasing the bed height. Performances of membranes packed in the CIM housing and commercial chromatographic membrane devices are also compared. In addition, for both membrane and monolith media, a CFD model is developed and used to predict flow distribution and breakthrough curves. Finally, the comparison between membrane and monolith media for BSA-LF separation was discussed from both experimental and CFD model results.

5.3 Theory

5.3.1 CFD model

The performance of a chromatographic device is highly dependent on its geometry and to the related fluid distribution. To simulate transport and other phenomena within complex geometries, CFD is a powerful tool. In CFD, partial differential equations (PDEs) with initial and boundary conditions are solved using numerical methods. In the CFD modeling of a chromatographic device [42, 52], the stationary phase (membrane or monolith) is assumed homogeneous, and the internal volume is divided in two different regions: void and porous. The hold-up volumes before and after the membrane stack or monolith constitutes the void regions.

The CFD model was solved in two steps [42, 52]. In the first step, the velocity field and pressure profile were calculated at steady-state assuming an incompressible flow. The Reynolds number within the membrane and monolith device is below 10, in which the laminar flow condition can be applied. The Navier-Stokes equations without external forces were solved in the void regions as described in Eq.1-a and Eq.1-b:

$$\rho(u.\nabla u) = \nabla.\left[-PI + \mu\left(\nabla u + (\nabla u)^T\right) - \frac{2}{3}\mu(\nabla.u)I\right] \quad \text{Eq.1-a}$$

$$\nabla.u = 0 \quad \text{Eq.1-b}$$

where u is the fluid velocity, P the pressure, ρ the density and μ the dynamic viscosity. The density and dynamic viscosity are those of water at 20°C.

The velocity field and pressure profile in the porous region were calculated using Brinkman's equation:

$$\rho(v.\nabla v) = \nabla.\left[-PI + \mu(\nabla v + (\nabla v)^T) - \frac{2}{3}\mu(\nabla.v)I\right] - \frac{\mu}{\kappa}v \quad \text{Eq.2-a}$$

$$\nabla.v = 0 \quad \text{Eq.2-b}$$

where ε is the porosity, κ the permeability and v the interstitial velocity given by u/ε. The porosity and permeability of the Sartobind membrane were, respectively, 0.78 and 1.00×10^{-13} m^2

[42,46], while the monolith had a lower porosity and permeability, 0.60 and 1.11×10^{-14} m^2, respectively [47]. At the inner boundaries within the chromatographic devices, no-slip conditions were applied. A given velocity was specified as the boundary condition at the inlet (z=0) of the chromatographic device, and vanishing viscous stress was used at the outlet (z=L).

In the second step, time-dependent concentration profiles were computed by solving the transport equations using the velocity field calculated previously. The transport of BSA and LF was described by classical diffusion-convection equations in the void and porous (Eq.3 and Eq.4, respectively). In these equations, i=1 and 2 denote BSA, and LF, respectively.

$$\frac{\partial c_i}{\partial t} = \nabla.(D_{a,i} \nabla c_i - u.c_i) \quad i = 1, 2 \qquad \text{Eq.3}$$

$$\frac{\partial c_i}{\partial t} = \nabla.(D_{a,i} \nabla c_i - u.c_i) - \frac{(1-\varepsilon)}{\varepsilon} \frac{\partial q_i}{\partial t} \quad i = 1, 2 \qquad \text{Eq.4}$$

where c_i and q_i are the solute concentration in the mobile and stationary phases, respectively. Within the porous region, the binding rate was $\frac{\partial q_i}{\partial t}$ for the i specie. At t=0, the initial concentration $c_{0,i}$ were set to zero.

It is usually admitted that axial dispersion within the membrane stack or monolith makes a negligible contribution to the total system dispersion. D_a was therefore set to the diffusion coefficients of the proteins in water. Here, $D_{a,i}$ was determined using Polson correlation as given in Eq.5, considering infinite dilution of the protein [32]:

$$D_{a,i} = K_{prot} M_{w,i}^{-1/3} \qquad \text{Eq.5}$$

where K_{prot} is approximately 1.644×10^{-3} $g^{1/3}$ cm^2 $mol^{-1/3}$ min^{-1}, the molecular weight of BSA, $M_{w,1}$, and LF, $M_{w,2}$, are 66.5 and 78.0 kDa, respectively. The calculated diffusion coefficients are $1.092\ 10^{-7} \times m^2\ s^{-1}$ and 1.167×10^{-7} m^2 s^{-1} for BSA and LF, respectively.

Additional time-lag and dispersion due to the tubing and holdup volumes in the experimental set-up were described by a plug flow reactor (PFR) and continuous stirred tank reactor (CSTR) combination [34, 42]. At the inlet of the chromatographic device, the PFR model was applied to account for time lag due to external tubing, valves and pumps (Eq.6), whereas the CSTR model was connected at the outlet of device to take into account dispersion within the experimental set-up (Eq.7). This outlet boundary condition (z=L) was calculated from the average concentration, $\overline{c}_i$. The residence times in the PFR and CSTR models, τ_{PFR} and τ_{CSTR}, respectively, were then estimated by fitting the PFR and CSTR model to an experimental dispersion curve measured on the Aktaprime-plus system without any chromatography device. The average concentration after the CSTR model, $c_{out,i}$ was estimated at the outlet device of MC device and then plotted versus time as the predicted breakthrough curve.

$$Inlet \quad z = 0 \quad ; \quad c_i = \begin{cases} 0 & t < \tau_{PFR} \\ c_{0,i} & t \geq \tau_{PFR} \end{cases} \qquad \text{Eq.6}$$

$$Outlet \quad z = L \quad ; \quad \nabla c_i = 0 \qquad \text{Eq.7}$$

$$\frac{\partial c_{out,i}}{\partial t} = \frac{\bar{c}_i - c_{out,i}}{\tau_{CSTR}}$$

The CFD model was numerically solved using Comsol Multiphysics 4.4 software (Comsol, France). The internal geometry of the CIM housing and Sartobind S75 devices (

Fig. 5.1) were obtained by Magnetic Resonance Imaging (MRI) using a 4.7 T BioSpec (Bruker, France) with a magnetic Magnex field gradient SGRAD 156/100/S and a quadrature coil (Rapid Biomedical, Germany) used for excitation and signal detection. The device geometry was then reconstructed in Comsol Multiphysics assuming rotational symmetry (Fig. 5.2). The CFD simulations were performed using cylindrical coordinates, in a 2D section of half of the device, to reduce simulation time and computational system requirement.

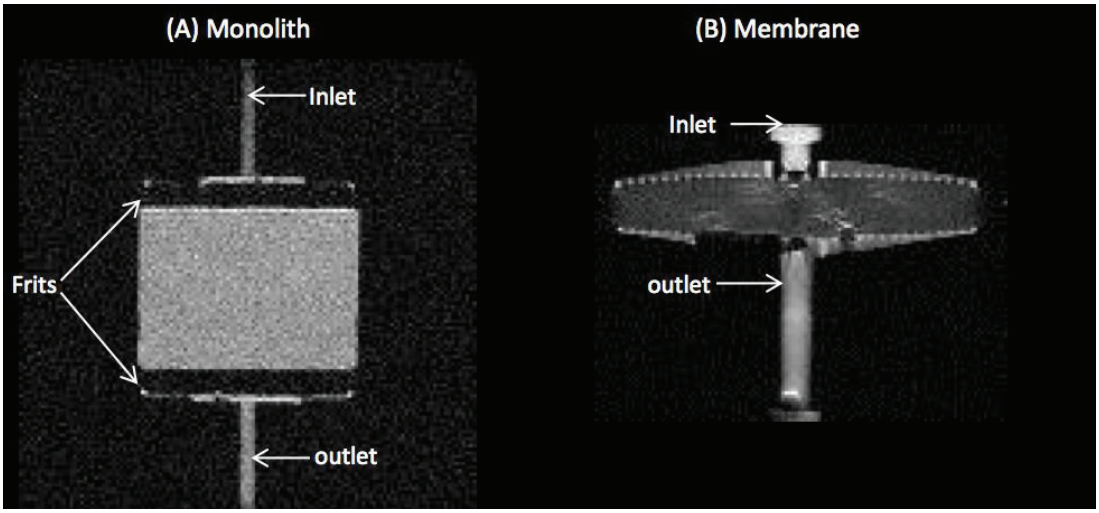

Fig. 5.1 Visualization by MRI of the chromatographic devices: (A) CIM housing containing 3 discs of monolith (H=9.0 mm), (B) Sartobind S75 device containing 15 membranes (H=4.0 mm).

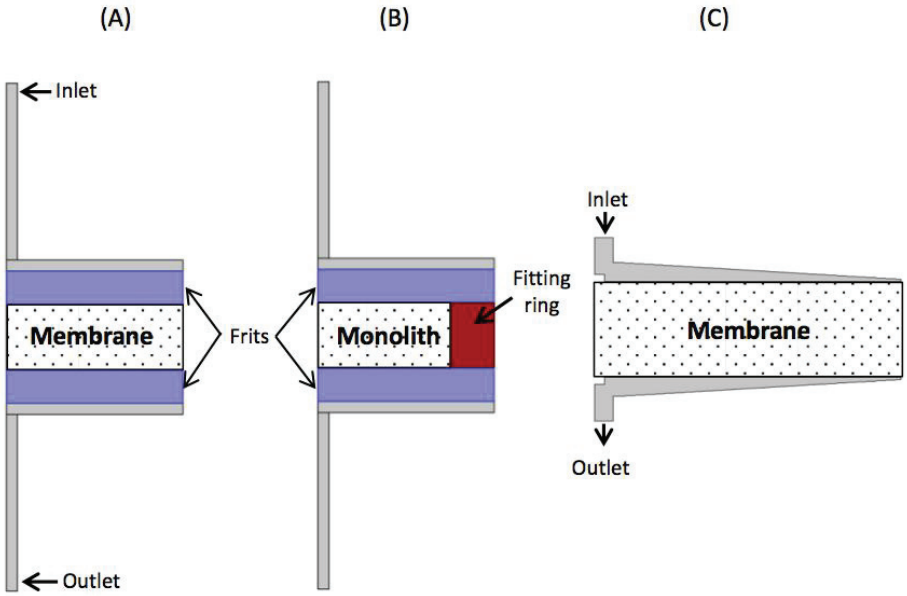

Fig. 5.2 Geometry of the various devices for the CFD simulations: (A) CIM housing containg 11 membrane discs (H= 3.0 mm), (B) CIM housing containg 1 monolith (H= 3.0 mm), and (C) Sartobind S75 device.

5.3.2 Binding kinetic models

At pH between the isoelectric point of BSA (4.6) and LF (8.6), we assume that there is no BSA adsorption on the cation exchange media due to the both positive charge of BSA molecules and stationary phase. The binding rate of BSA, $\frac{\partial q_1}{\partial t}$ is thus set to zero, whereas the binding rate of LF, $\frac{\partial q_2}{\partial t}$, can be given by different binding kinetic models.

The Langmuir model assumes one type of biding sites without steric effects (Eq.8). In this model, $k_{a,2}$ is the forward adsorption rate constant, $k_{d,2}$ the reverse rate constant and $q_{m,2}$ the maximum binding capacity of the media.

$$\frac{\partial q_2}{\partial t} = k_{a,2} c_2 (q_{m,2} - q_2) - k_{d,2} q_2 \qquad \text{Eq. 8}$$

The bi-Langmuir model considers two distinct types of independent binding sites, with different biding energies and kinetics (Eq.9). Parameters $q_{m,2a}$ $k_{a,2a}$ and $k_{d,2a}$ are associated to the higher energy binding sites a, and parameters $q_{m,2b}$, $k_{a,2b}$ and $k_{d,2b}$ to the lower energy binding sites b.

$$\frac{\partial q_2}{\partial t} = \frac{\partial q_{2a}}{\partial t} + \frac{\partial q_{2b}}{\partial t}$$ Eq. 9-a

$$\frac{\partial q_{2a}}{\partial t} = k_{a,2a} c_2 (q_{m,2a} - q_{2a}) - k_{d,2a} q_{2a}$$ Eq. 9-b

$$\frac{\partial q_{2b}}{\partial t} = k_{a,2b} c_2 (q_{m,2b} - q_{2b}) - k_{d,2b} q_{2b}$$ Eq. 9-c

The parameters of the kinetic models (Langmuir and bi-Langmuir) were obtained by minimizing the sum of squared deviations between simulated results and experimental data of LF breakthrough curves using the SNOPT (Sparse Nonlinear OPTimizer) algorithm.

5.4 Materials and methods

5.4.1 Chromatographic media and devices

Monolithic discs and membrane flat-sheet stacks were compared at the same bed height using the same CIM housing from BIA Separations (Ljubljana, Slovenia). The characteristics of the different chromatographic media and devices used in this work are summarized in Table 5.1 . The internal diameter of the CIM housing is 16.00 mm and the bed height can be increased up to 12.00 mm. The CIM housing allows efficient flow distribution and optimized void volume; moreover, it makes the column packing and unpacking simple.

Strong cation exchange CIM monolithics from BIA Separations (Ljubljana, Slovenia) were selected as the monolith supports. These poly(glycidyl methacrylate-co-ethylene dimethacrylate) monoliths are highly interconnected polymeric networks of nuclei, agglomerated into globules, further agglomerated into clusters [47]. CIM monoliths (12.00 mm diameter, H=3.00 mm) are surrounded by a nonporous fitting ring, which prevents chipping of the edges and/or breaking when exposed to the maximal flow rate. The pore diameter of the monolithic is 1.35 µm for the CIM disc and 2.10 µm for the CIM multus device (data given by the manufacturer); the porosity is around 0.60 for CIM discs [47]. For strong cation exchanger monoliths, sulfonyl groups are coated on the internal surfaces. In the first experiments, a CIM disc (H=3.00 mm, BV=0.34 mL) was inserted into the CIM housing; then, H was increased by inserting 3 CIM discs (H=9.0 mm and BV=1.02 mL). A CIMmultus device with radial flow (BIA Separations) was also investigated (BV=1.00 mL).

Table 5.1 Caracteristics of the different devices of strong cation exchange chromatography.

Ion exchange chromatography device	Membrane H=3.0 mm	Membrane H=9.0 mm	Sartobind S75	Monolith H=3.0 mm	Monolith H=9.0 mm	CIMmultus
Support matrix	Stabilized reinforced cellulose			Poly(glycidyl methacrylate-co-ethylene dimethacrylate)		
Average pore diameter (µm)	3.0-5.0			1.35 (CIM disc)		2.1 (CIMmultus)
Porosity (-)	0.78[46]			0.60 (CIM disc) [47]		
Permeability (m^2)	10^{-13} [42]			1.11×10^{-14} [47]		
Functionalized group	Sulfonic acid			Sulfonyl group		
Housing	CIM housing	CIM housing	Already packed	CIM housing	CIM housing	Already packed
Bed height H (mm)	3.00	9.00	4.00	3.00	9.00	5.95
Diameter D_m (mm)	16.00	16.00	25.00	12.00 *(16.0 with the fitting ring)	12.00 *(16.0 with the fitting ring)	Outer:18.60mm Inner:6.70mm Tube length:4.20 mm
Number of discs	11	33	15	1	3	-
Bed volume BV (mL)	0.6	1.8	2.1	0.34	1.02	1

Strong cation exchange membranes Sartobind S (Sartorius Stedim Biotech GmbH, Goettingen, Germany) were used as the membrane chromatographic media. Sartobind S membranes are formed by a macroporous support based on reinforced cross-linked cellulose containing a hydrogel layer on the macroporous walls [46]. The membrane pore diameter is in the range 3.0-5.0 µm, the membrane thickness 275 µm (data provided by the manufacturer) and the porosity around 0.78 [46]. Sulfonic acid groups for cation exchange are bound covalently to the internal surface of the membrane. To fit the CIM housing, an A4 sheet of membrane was cut into discs of 16.00 mm diameter. First, 11 membrane discs were placed into the CIM housing (H=3.00 mm and BV=0.60 mL). The membrane stack was then increased by packing 33 membrane discs into the housing (H=9.00 mm and BV=1.80 mL). The performance of a commercialized membrane device Sartobind S75, with 15 discs (BV=2.1 mL), was also tested for comparison.

5.4.2 Protein solutions

BSA-LF solutions were prepared at a BSA-LF concentration ratio of 2/1 by mixing the same volume of 2.00 $mgmL^{-1}$ BSA solution and 1.00 $mgmL^{-1}$ LF solution. Before use, the protein mixtures were filtered through a 0.22 µm polyethersulfone hydrophilic Millex-GP filter unit (Millipore, France) to remove any fine particles. The BSA lyophilized powder with purity ≥ 96.00% was obtained from Sigma Aldrich (France). Purified bovine LF lyophilized powder (≥ 93.00% of purity) was generously offered by Erie Europe (France). 100 mM potassium phosphate buffer solutions at pH 6.0 were prepared by adjusting volumes of K_2HPO_4 and KH_2PO_4 solutions (Sigma Aldrich, France) and subsequently filtered through a hydrophobic membrane filter with a 0.45 µm pore size (Millipore, France). Concentrations of LF and BSA solutions were measured by spectrophotometry at 280 nm using the UV detector of the Aktaprime-plus system (GE Healthcare, France). For BSA–LF mixture solutions, concentrations of LF and BSA were determined using the two separate breakthrough curves of BSA and LF, as previously detailed in the chapter 4 using ion exchange chromatography membrane devices [48].

5.4.3 BSA-LF mixture separation

All experiments were performed using an Aktaprime-plus system with a UV-280 detector (GE Healthcare, France). Data acquisition was monitored online using the Primeview 5.0 software (GE Healthcare, France). The Aktaprime-plus pump controls the flow rate in the range 0.1 to 50.0 $mLmin^{-1}$, the maximum operating pressure being 1.10 MPa. The separation was composed of the following different steps: equilibrium, protein loading, washing and elution steps. All separation steps were operated at a constant flow rate of 12.0 $BVmin^{-1}$. Bound LF was recovered using a phosphate buffer saline solution with 2.00 M NaCl.

The BSA-LF separation cycles were performed in triplicate without regeneration between each cycle. After three complete cycles, the stationary phase was cleaned and regenerated using 1.00 M NaOH at 1.0 $BVmin^{-1}$ for 1 h, followed by 10.0 BV of the elution and phosphate buffers, during 10 min for each solution. The dynamic binding capacity of LF at 10% breakthrough ($DBC_{10\%}$) was determined using the method previously described [49]. Values were reported per

BV of stationary phase, and were the average ± standard deviation of 3 independent measurements. The void volume (V_0) of each chromatographic device connected to the external system (i.e. tube, pump, UV cell, etc.) was measured by loading 5% of acetone in phosphate buffer; V_0 was then read at 10% of the loading concentration.

5.4.4 LF adsorption isotherms

LF adsorption isotherms were obtained with the membrane and monolithic media in the CIM housing using the Aktaprime-plus system at a low flow rate of 1.0 $BVmin^{-1}$ for 24 h. For both membrane and monolith media, the bed heights H=3.00 and 9.00 mm were investigated, as well as the Sartobind S75 device. LF adsorption was performed at different initial concentrations from 0.10 to 4.00 $mgmL^{-1}$. 50 mL of LF solution was circulated through the chromatographic device. During the experiment, the loading solution in the flask was slowly stirred using a magnetic bar. The recorded absorbance 280-UV on the Aktaprime-plus system was checked to be stable after 24 h. The LF concentration adsorbed onto the chromatographic media (q_e) was determined as the difference of LF concentrations in the flask between the beginning of the experiment and after 24 h, multiplied by the volume of LF solution, divided by the volume of chromatographic media.

At equilibrium, the instantaneous adsorption rate in the stationary phase is zero ($\frac{\partial q}{\partial t} = 0$), thus the Langmuir isotherm is given by Eq.10, where $q_{m,2}$ is the maximum binding capacity of the stationary phase and b is the ratio of the forward adsorption rate constant, $k_{a,2}$ to the reverse rate constant, $k_{d,2}$. These two model parameters, $q_{m,2}$ and b, were estimated using a nonlinear least-squares solver on Matlab R2013a.

$$q_e = \frac{q_{m,2} b c_e}{1 + b c_e} \qquad \text{Eq. 10}$$

5.5 Results and discussion

5.5.1 LF adsorption isotherms

LF adsorption isotherms were measured for the membranes and monoliths in the CIM housing, and for the Sartobind S75 device. For each device, the bound LF concentration at equilibrium (q_e) was plotted against the free LF concentration (c_e) Fig. 5.3. The data were fitted to the Langmuir isotherm (Eq. 10), with $q_{m,2}$, the maximum LF binding capacity per volume of chromatographic media, and b, the equilibrium binding constant (Table 5.2).

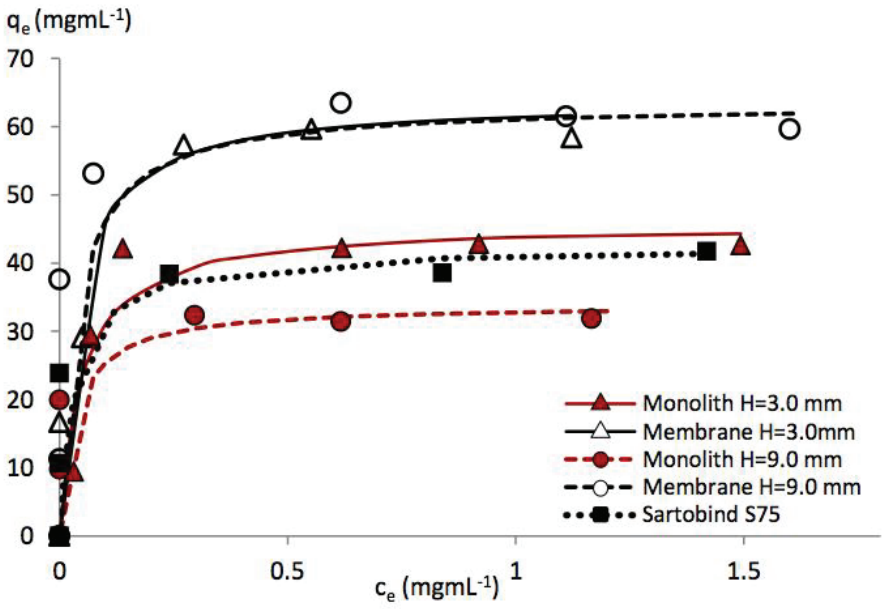

Fig. 5.3 LF static binding capacity using the membrane and monolith in the CIM housing at H=3.0 and 9.0 mm, and the Sartobind S75 device. The experimental data (dots) were fitted to Langmuir isotherms (lines). The Langmuir parameters are given in Table 5.2.

The highest LF maximum binding capacity, $q_{m,2}$, about 63 mgmL^{-1}, was obtained using the Sartobind membranes in the CIM housing, with no significant effect of bed height (H= 3.00 and 9.00 mm). Using the Sartobind S75 device, the value of $q_{m,2}$ decreased to 42.3 mgmL^{-1}. The effect of the device geometry in membrane chromatography is well known and has been highlighted by several authors [e.g. [13,49,50]. Increasing bed height of commercial membrane chromatography devices, with either axial flow or radial flow, has been reported to decrease the dynamic binding capacity [49,51]. This effect was not observed for the chromatographic membranes housed in the CIM column. In this configuration, the membranes are used in a very efficient manner, probably because the protein solution can flow at the edges of the membrane discs, which is not possible in the Sartobind housing. The CFD simulations will be used in a following section to calculate the velocity profile in the membrane and monolith.

The maximum LF binding capacity of the monolith with H=3.00 mm (45.7 mgmL^{-1}) was lower than the one obtained with the membrane with the same bed height. Moreover, for the monolith with H= 9.00 mm, a decrease in $q_{m,2}$ (33.9 mgmL^{-1}) was observed. This decrease in maximum LF binding capacity with increasing bed height could be due to non-ideal flow distribution at the inlet of the monolith, due to the difference in diameter between the inlet frit and monolith. This effect will be discussed also from CFD results.

Table 5.2 Langmuir model parameters, determined by least-squares regression of LF static adsorption data; and parameters of Langmuir and bi-Langmuir models for monolith and membrane, respectively, obtained by fitting the CFD model to LF binding breakthrough curves using 100 mM phosphate buffer pH 6.00 at a BSA/LF initial concentration of 2/1.

Model parameters	LF static adsorption		LF dynamic breakthrough				
	$q_{m,2}$ ($mgmL^{-1}$)	b ($mLmg^{-1}$)	Flow rate ($BVmin^{-1}$)	$q_{m,2}$ ($mgmL^{-1}$)	b ($mLmg^{-1}$)	$k_{a,2}$ ($mLmg^{-1}s^{-1}$)	$k_{d,2}$ (s^{-1})
Membrane H=3.0 mm	63.63	25.03	12.0	$q_{m,2a}$ = 40.82 $q_{m,2b}$ = 17.49	b_a= 24.90 b_b= 26.18	$k_{a,2a}$=0.14 $k_{a,2b}$=0.018	$k_{d,2a}$=0.0056 $k_{d,2b}$=0.00069
Membrane H=9.0 mm	63.33	26.81	12.0				
Sartobind S75	42.36	29.12	12.0	$q_{m,2a}$ = 27.67 $q_{m,2b}$ = 11.86			
Monolith H=3.0 mm	45.77	28.66	12.0	39.34	29.84	1.25	0.042
Monolith H=9.0 mm	33.89	29.66	0.4	33.58			

5.5.2 BSA-LF mixture separation

BSA-LF mixture separation was performed at different flow rates (12.0, 18.0 and 24.0 $BVmin^{-1}$) using monolith and membrane in the CIM housing (H=3.00 mm) and the Sartobind S75 device (H=4.00 mm). The average operating pressure was measured during the loading step (Fig. 5.4). The operating pressures were slightly higher using the monolith in the CIM housing compared to the membranes. This could be due to the membrane larger pore size, 3.00-5.00 µm, and higher porosity, 0.78 [46], compared to the values of the monolith, which are respectively given as 1.35 µm and 0.60 [47]. In addition, the Sartobind S75 device required slightly higher operating pressures than the membrane in the CIM housing, which may be due to its higher bed height (4 mm) compared to the membranes stacked in the CIM housing (3 mm).

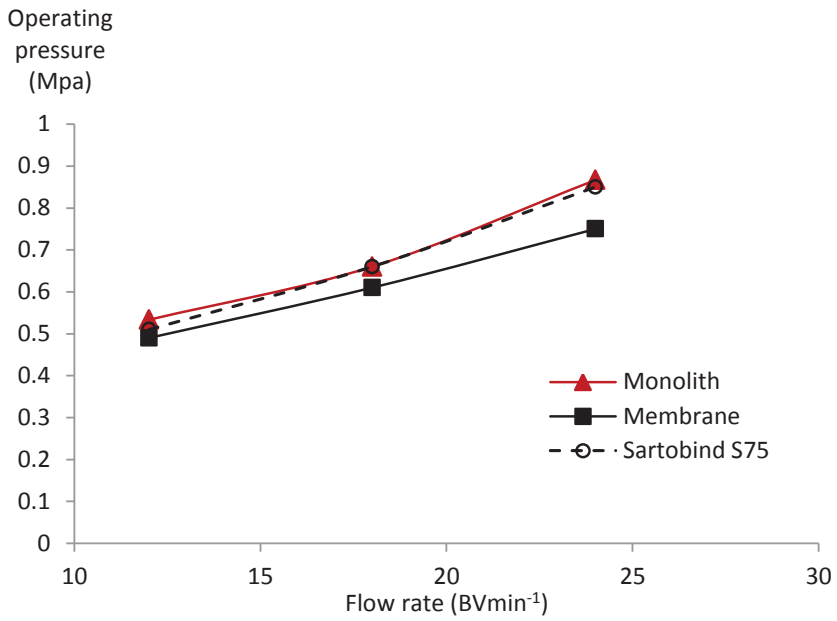

Fig. 5.4 Average operating pressures during the BSA-LF mixture loading step at flow rates of 12.0, 18.0 and 24.0 $BVmin^{-1}$ using the monolith (H=3.00 mm), membrane (H=3.00 mm) in the CIM housing and Sartobind S75 device (H=4.00 mm).

The BSA-LF separation cycles are displayed in Fig. 5.5A for the monolith and in Fig. 5.5B for the membrane housed in the CIM column (H=3 mm). The loading step was operated at pH 6.00, i.e. between the isoelectric point of BSA (4.7) and LF (8.7). At this pH, BSA possesses more negative charges than LF and thus flows in the effluent without binding, while LF being more positively charged is bound to the cation exchanger membrane or monolith [48]. Two separate breakthrough curves were obtained during BSA-LF mixture separation at pH 6.00. At the beginning of the loading step, the breakthrough curve was BSA, whereas LF was fully retained on the membrane or monolith. Afterward, the membrane or monolith reached saturation, and LF breakthrough curve started. At the end of the loading step, washing was performed until the adsorbance decreased to zero. Finally, the elution buffer using higher ionic strength was used to recover bound LF. The separation cycle was repeated for at least three cycles without any

regeneration step for both monolith and membrane. No major differences were observed between the three cycles, which indicates good repeatability of membranes and monoliths. However, regular cleaning and regeneration is strongly recommended to reduce risk of fouling and contamination.

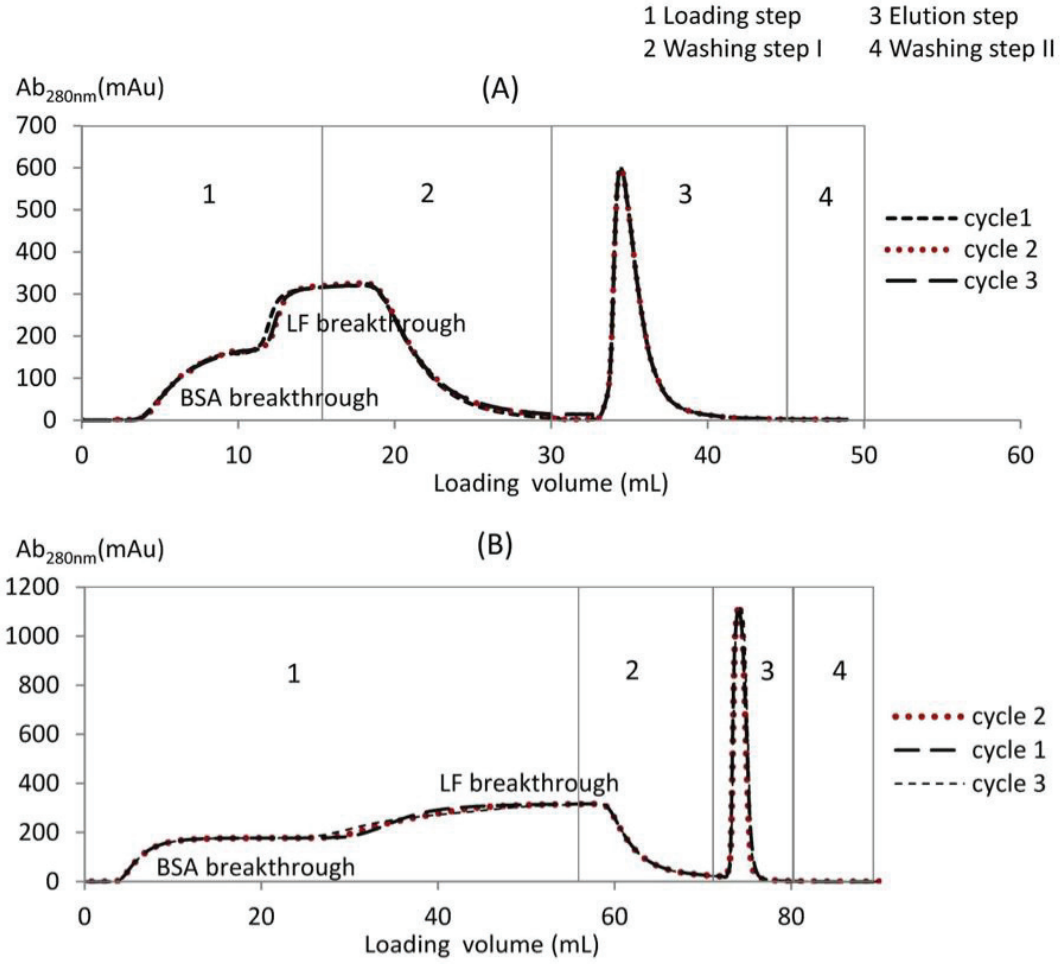

Fig. 5.5 Three repeated cycles of BSA-LF mixture separation using for loading 100 mM phosphate buffer at pH 6.00 at a BSA-LF initial ratio of 2/1 and a flow rate of 12 $BVmin^{-1}$ for (A) monolithic disc H=3.00 mm and (B) membrane stack H=3.00 mm in the CIM housing.

Furthermore, the BSA-LF separation was performed at different flow rates (12.0, 18.0 and 24.0 $BVmin^{-1}$). For each flowrate, the binding capacity of LF was calculated at 10% breakthrough ($DBC_{10\%}$) and reported in Table 5.3. The highest $DBC_{10\%}$ of LF per BV (about 42 $mgmL^{-1}$) was obtained using the membrane support in the CIM housing (H=3.00 mm), while the Sartbobind S75 device gave lower LF $DBC_{10\%}$ around 28 $mgmL^{-1}$. The lowest binding capacity was found using the monolith in the CIM housing with LF $DBC_{10\%}$ around 24 $mgmL^{-1}$ (43% of the value of the binding capacity of the membrane in the same housing). In addition, there was no significant effect of the flow rate (between 18.0 and 24.0 $BVmin^{-1}$) for all devices, as LF $DBC_{10\%}$ were almost identical at the different operating flow rates. This confirms the advantage of membrane and

monolith chromatography, for which mass transport is mainly convective, and therefore higher flow rates can be used without any loss in binding capacity. Increase in productivity is possible by increasing the operating flow rate with both membrane and monolith chromatography as usually reported [e.g. 2, 20, 22].

Table 5.3 $DBC_{10\%}$ of LF per BV using membrane and monolith supports at a BSA-LF loading ratio of 2/1 diluted in 100 mM phosphate buffer at pH 6.0 and the flow rates of 12.0, 18.0 and 24.0 $BVmin^{-1}$.

Flow rate ($BVmin^{-1}$)		**12.0**	**18.0**	**24.0**
LF $DBC_{10\%}$ per BV of chromatographic support ($mgmL^{-1}$)	Monolith H=3.0 mm	24.74±0.43	24.50±0.02	24.29±0.25
	Membrane H=3.0 mm	43.80±0.81	42.25±2.12	41.84±2.25
	Sartobind S75	29.15±0.38	27.44±0.14	28.89±0.47

5.5.3 Non-binding breakthrough curves

As mentioned earlier, BSA is not retained by the cation exchange membrane or monolith, therefore it may be used as a tracer for non-binding experiments. Experimental BSA breakthrough curves are plotted as a function of loading volume (V) for the membrane and monolithic with H=3.00 mm (Fig. 5.6A). For both media, BSA breakthrough curves were similar until around 70% breakthrough. Afterward, the BSA breakthrough curve of the membrane was more dispersed and 100% breakthrough was reached after a higher loading volume (15.46 mL), whereas a lower volume (10.52 mL) was required for the monolith. Using the Sartobind S75 device, the BSA breakthrough curve was significantly different from the one of the membrane in the CIM housing. Breakthrough happened later, due to the larger void volume inside the device, and the breakthrough curve was more dispersed.

The CFD model was combined in series to PFR and CSTR to account for the void volume and dispersion of the external system (Aktaprime-plus system, tubes, etc). To first estimate τ_{PFR} and τ_{CSTR}, an experiment was conducted by loading a BSA solution in the Aktaprime-plus system and tubes, with no chromatographic device. The flow rate was 7.10 $mLmin^{-1}$ and the BSA initial concentration 2.00 $mgmL^{-1}$. The BSA dispersion curve is shown in Fig. 5.6B. τ_{PFR} and τ_{CSTR} were estimated by least-squares regression on Matlab to fit the BSA dispersion curve. The volumes, V_{PFR} and V_{CSTR}, 3.66 and 1.61 mL, respectively, were obtained by multiplying the optimized residence time (τ_{PFR} and τ_{CSTR}) by the flow rate. These two parameters were then introduced in the CFD model to simulate the BSA breakthrough curve under non-binding condition for the different chromatographic devices. As shown in Fig. 5.6A, the experimental data and the CFD results were in a good agreement.

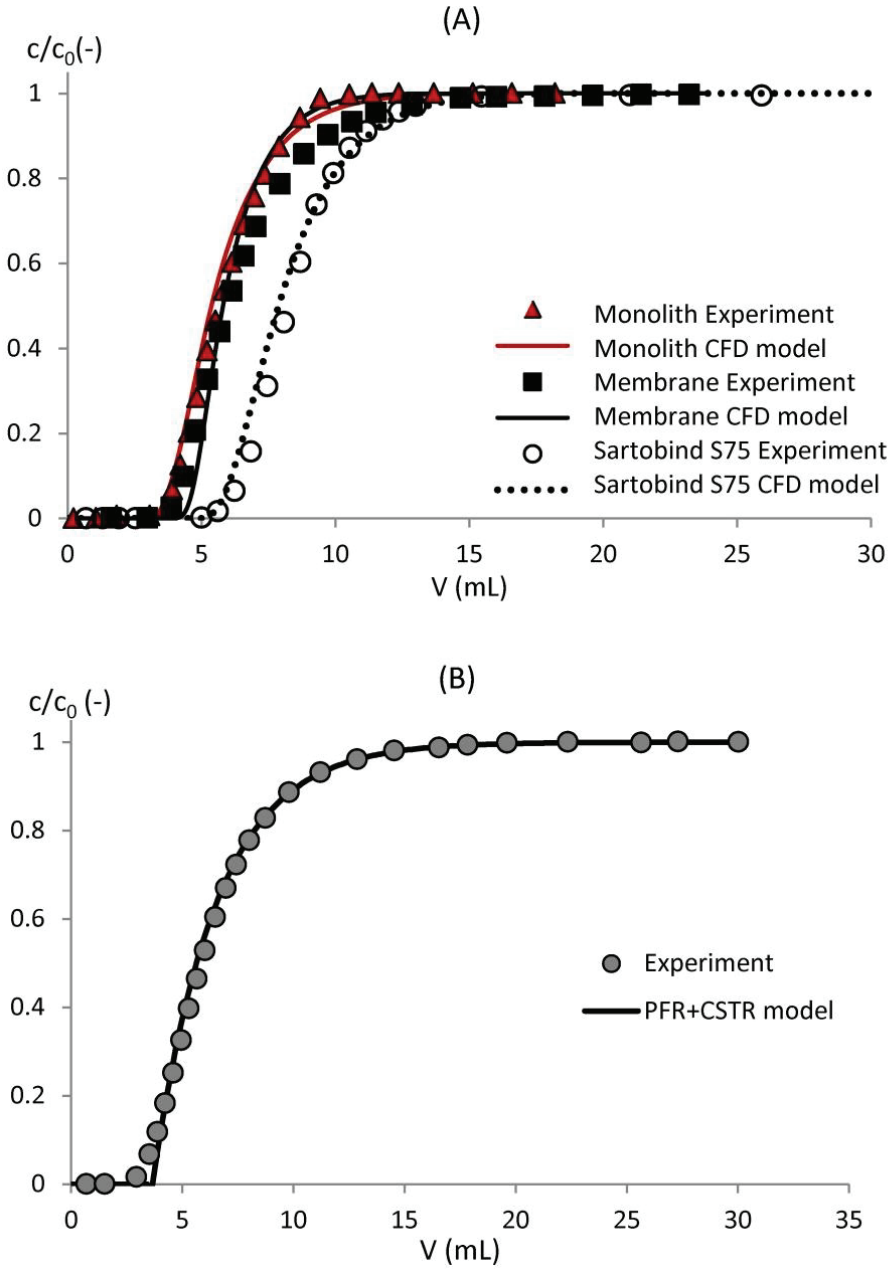

Fig. 5.6 (A) Comparison between experimental non-binding breakthrough curves of BSA obtained with the membrane (H=3.00 mm), monolith (H=3.00 mm) in the CIM housing, the Sartobind S75 device and simulation using the combinaison of CFD, PFR and CSTR models. The experimental breakthrough curves were obtained using 100 mM phosphate buffer pH 6.00 at the BSA/LF initial concentration of 2/1 and flow rate of 12.0 $BVmin^{-1}$. The parameters V_{PFR} and V_{CSTR} were estimated from (B) the experimental BSA dispersion curve of the external system (Aktaprime-plus and tubes) at flow rate of 7.10 $mLmin^{-1}$ and BSA initial concentration of 2.00 $mgmL^{-1}$ and a model using PFR and CSTR in series. The model parameters, V_{PFR} and V_{CSTR}, were estimated as 3.66 mL and 1.61 mL, respectively.

5.5.4 Flow distribution and BSA concentration profiles

The CFD model was solved to estimate the velocity field within the membrane and monolith when housed in the CIM column, and the Sartobind S75 device. For the three devices, the same flow rate of 12 $BVmin^{-1}$ was applied. The velocity profiles are displayed in Fig. 5.7A1, A2, and A3. The membrane in the CIM housing showed constant velocity, as the frit before and after the membrane stack distributes homogenously the flow. The average velocity in the membrane was 0.057 cms^{-1}. On the contrary, lower velocities and turbulences were observed at the peripheral region of the monolithic disc due to the change in diameter between the frit and the monolith. The average velocity within the monolith was in the same range than in the membrane (around 0.056-0.058 cms^{-1}). Within the Sartobind S75 device, the flow is radially distributed to the membrane surface due to the large void volume before the membrane. A higher average velocity within the membrane stack was obtained (0.085 cms^{-1}) due to the higher volumetric flow rate applied (12 $BVmin^{-1}$= 25.2 $mLmin^{-1}$).

The CFD model was then used to estimate the BSA concentration profiles. As seen previously, BSA does not bind to the cation exchanger media and can be used as a tracer. The variation in BSA concentration divided by the BSA initial concentration ($c_1/c_{0,1}$) is shown for the different devices in Fig. 5.7B and Fig. 5.7C, when $c_1/c_{0,1}$reaches 0.10 and 0.50 at the outlet of the devices, respectively. The loading ratio of BSA-LF mixture was 2/1. For the the membrane within the CIM colum, the BSA concentration was slightly lower at the peripheric region of membrane at $c_1/c_{0,1}$ of 0.10 (Fig. 5.7B1). When $c_1/c_{0,1}$ reached 0.50 (Fig. 5.7C1), BSA was distributed in the whole membrane bed at a concentration equal to its initial value. For the monolith, the BSA concentration was significantly lower at the peripheric region of the monolith, near the fitting ring, as displayed in Fig. 5.7B2. At $c_1/c_{0,1}$ = 0.50 (Fig. 5.7C2), lower concentration in BSA were still found at the peripheral region of the monolith. It may be then suggested that the pack of membrane discs in the CIM column gave more uniform BSA solute transport, while the fitting ring of the monolith creates difficul to reach regions. Despite this result, it should not be advisable to remove the fitting ring whose function is to avoid the fragile monolith to be cracked or broken.

Furthermore, the CFD model was used to estimate the BSA concentration within the membrane in the Sartobind Q75 device. At $c_1/c_{0,1}$ = 0.10 (Fig. 5.7C2), the BSA concentration profile was almost parabolic, with a very low BSA concentration at the peripherical region of the membrane. When $c_1/c_{0,1}$ = 0.50, (Fig. 5.7C3), the variation of BSA concentration versus radius was still parabolic and a low BSA concentration was still observed at the periperical region.

Membrane H=3.00 mm

(A1) Velocity field (cm/s)

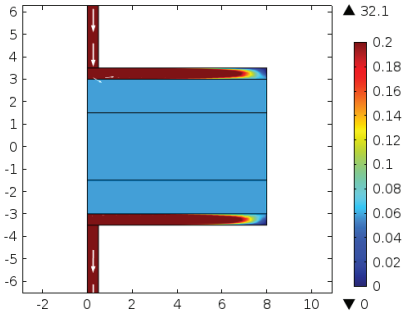

(B1) Dimensionless BSA $c_1/c_{0,1}$ profile ,when $c_1/c_{0,1}$ =0.10 at z=L, t=36 s.

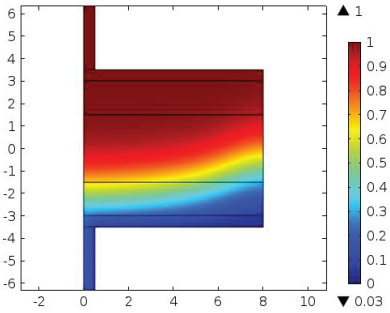

(C1) Dimensionless BSA $c_1/c_{0,1}$ profile, when $c_1/c_{0,1}$ =0.10 at z=L, t=41 s.

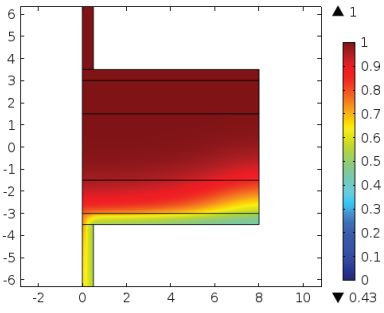

Monolith H=3.00 mm

(A2) Velocity field (cm/s)

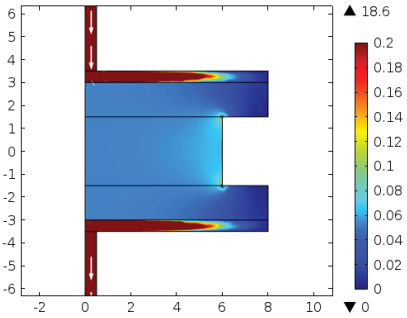

(B2) Dimensionless BSA $c_1/c_{0,1}$ profile, when $c_1/c_{0,1}$ =0.10 at z=L, t=37 s.

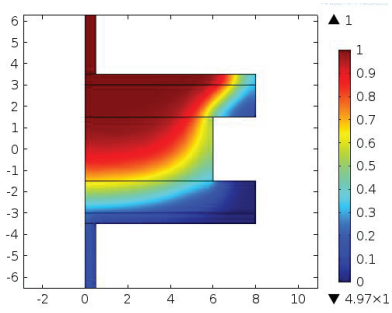

(C2) Dimensionless BSA $c_1/c_{0,1}$ profile, when $c_1/c_{0,1}$ =0.10 at z=L, t=41 s.

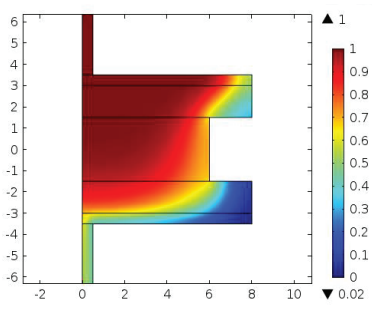

Sartobind S75

(A3) Velocity field (cm/s)

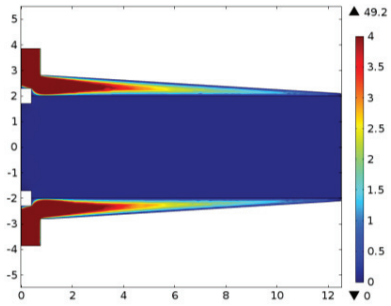

(B3) Dimensionless BSA $c_1/c_{0,1}$ profile, when $c_1/c_{0,1}$ =0.10 at z=L, t=11 s.

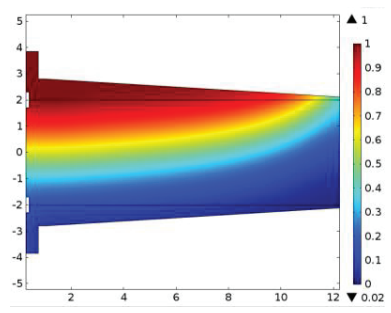

(C3) Dimensionless BSA $c_1/c_{0,1}$ profile, when $c_1/c_{0,1}$ =0.10 at z=L, t=14 s.

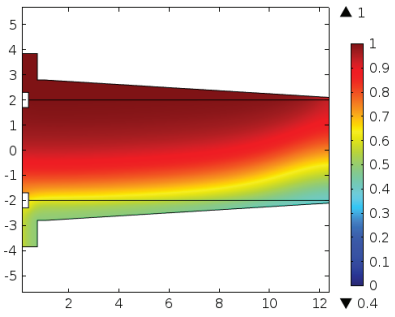

Fig. 5.7 Simulated velocity profiles (A1,A2,A3), dimensionless non-binding BSA profiles, when $c_1/c_{0,1}$=0.10 (B1,B2,B3) and when $c_1/c_{0,1}$=0.50 (C1,C2,C3) at the outlet of the devices (z=L), for the membranes and monolith at the feed flow rate of 12 BVmin^{-1} and the initial BSA-LF mixture concentration ratio of 2/1.

Consequently, the simulation results presented here suggest that the Sartobind device, which has void volumes before and after the membrane stack lacks of efficient flow distribution and shows inhomogenous BSA transport within the membrane. However, it may be highlighted that the geometry used in the simulations, although obtained from MRI images of the Sartobind device, and thus close to the reality, is a simplified picture of the real device, as the inlet and outlet distributors consist of circular and radial line channels. It can then be foreseen that a 3D simulation, which would take into account these channels, would predict better flow and non-binding solute distribution in the Sartobind S75 device.

As the permeability and porosity of the monolith and membranes are slightly different, it was checked that these data did not influence the simulation results. To do so, the CFD model was used to simulate the velocity and BSA concentration in a monolith without fitting ring. The velocity and BSA concentration profiles within the monolith and membrane were then very similar (data not shown) due to the indentical geometry of both systems and their similar permeability and porosity data. This highlights the important effect of the housing configuration and flow pattern to explain the difference in velocity and BSA concentration profiles when the monolith is housed in the CIM column compared to the membrane.

5.5.5 LF binding breakthrough curves

As seen previously, BSA does not bind on the cation exchange membrane or monolith because BSA possesses more negative charges than LF at pH 6; therefore, LF adsorbs preferentially. In Fig. 5.8(A), LF breakthrough curves were plotted against the loading volume corrected by void volume (V_0) and divided by BV, for the membrane and monolith with H=3.00 mm in the CIM housing, and the Sartobind device. The same parameters were used during the loading steps: flow rate 12.0 $BVmin^{-1}$ and initial BSA-LF ratio of 2/1. The data for breakthrough at 10%, $DBC_{10\%}$, are reported in Table 5.3.

For the monolith, the breakthrough curve appeared early due to its lower LF binding capacity (24.74 ± 0.43 $mgmL^{-1}$). The breakthrough curve was very sharp and reached rapidly 100% breakthrough, which indicates very efficient binding. For the membrane housed in the CIM housing, the LF breakthrough curve happened later and $DBC_{10\%}$ was higher (43.80 ± 0.81 $mgmL^{-1}$). A more dispersed breakthrough curve was observed due to the tailing effect near 100% breakthrough. This suggests slower kinetics between LF and the binding sites near saturation of membrane.

Van Beijeren et al. [53] highlighted that the presence of a grafted polymer layer in the ion exchange Sartobind membranes, in which a high degree of multilayering takes place, reduces the accessibility of the binding sites and/or introduces a diffusive transport limitation. The amount of proteins that breakthrough at a certain point depends primarily on the amount of already adsorbed proteins, as the binding of proteins reduces the accessibility of the binding sites. This phenomena seems to occur in a lesser extent within the functionalized poly(glycidyl methacrylate-co-ethylene dimethacrylate) monolith, although such behavior has also been reported [27]. Another explanation from Orr et al. [8] was that non-uniform membrane porosity, membrane thickness, and ligand grafting can lead to variable flow resistance and binding kinetics within the membrane matrix.

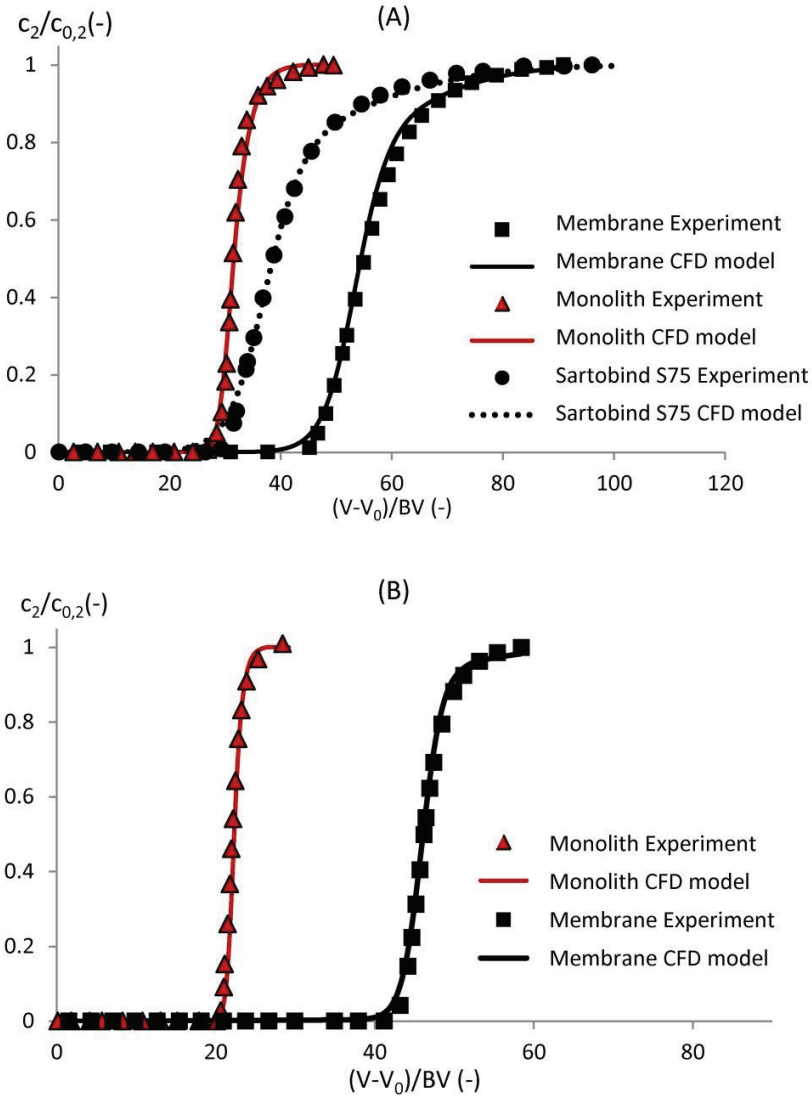

Fig. 5.8 Simulated and experimental LF binding breakthrough curves for (A) the membrane, the monolith with H=3.00 mm in the CIM housing and the Sartobind S75 device, and (B) the membrane and the monolith with H=9.00 mm. The simulated breakthrough curves were plotted using the binding kinetic parameters given in Table 5.2. The experimental data were obtained using 100 mM phosphate buffer pH 6.00 at a BSA/LF initial concentrations of 2/1 and flow rate of 12.0 $BVmin^{-1}$, except for the monolith with H=9.00 mm for which the flow rate was 0.40 $BVmin^{-1}$.

Using the Sartobind S75 device, the LF breakthrough occurred early with a lowest value for $DBC_{10\%}$ of 29.15 ± 0.38 $mgmL^{-1}$, and the dispersion and tailing effects were more significant than observed for the membrane in the CIM housing. These results suggest again the major role plays by the membrane module design on membrane binding capacity [13]. The optimized flow distribution in the CIM housing improved the performance of the membrane.

The model was solved to predict the LF binding breakthrough curves. The binding kinetic

parameters were determined by fitting the calculated breakthrough curve to the experimental LF breakthrough curve obtained using 100 mM phosphate buffer pH 6.00, BSA/LF initial concentrations of 2/1 and flow rate of 12 $BVmin^{-1}$. The optimized model parameters for the different devices are reported in Table 5.2. As shown in Fig. 5.8(A), the breakthrough curve for the monolith could be accurately predicted using the Langmuir isotherm model, which assumes binding sites with identical kinetic. The bi-Langmuir model was needed to describe the tailing effect of membrane adsorption near 100% breakthrough for the membrane in the CIM housing and for the Sartobind S75 device, as previously emphasized for affinity membrane chromatography [53]. This may correspond to the phenomena pointed out by van Beijeren et al. [52] and Orr et al. [8]; at high protein loadings, already bound proteins reduces the accessibility of the binding sites, and therefore may induce a change in the binding kinetic parameters. Moreover, non-uniform pore and grafting ligand density could provide two energetically types of independent binding sites within the membrane.

Using the membrane in the CIM housing, the highest $q_{m,2}$ (58.31 $mgmL^{-1}$) was obtained (equal to the sum of $q_{m,2a}$ and $q_{m,2b}$) whereas lower $q_{m,2}$ were obtained for the monolith and Sartobind S75 device, 39.34 and 39.53 $mgmL^{-1}$, respectively. The same result was obtained from the LF isotherm experiment, where the highest $q_{m,2}$ was obtained for the membrane in the CIM housing. Within the Sartobind device, some regions of the membrane and therefore some binding sites are more difficult to reach than within the membrane in the CIM housing. Moreover, the $q_{m,2}$ values obtained from the CFD model were lowest than the ones measured from the isotherm experiments. It appears again that the efficiency of flow distribution has a major effect on $q_{m,2}$ values. It is worth noting that the values of $k_{a,2}$ and $k_{d,2}$ were identical for the membrane in the CIM housing and in the Sartobind device (Table 5.2), as the membrane and membrane ligand are identical.

5.5.6 Effect of bed height

The membrane and monolith in the CIM column with both H=9 mm were first investigated at 12.00 $BVmin^{-1}$ and a loading BSA-LF ratio of 2/1. However, using the monolith, this high flow rate could not be operated due to the over pressure on the Aktaprime-plus system (>1.10 MPa). Therefore, the flow rate was reduced to 0.4 $BVmin^{-1}$. For both media, the LF $DBC_{10\%}$ values were calculated from experimental breakthrough curves and compared to values from other devices in Fig. 5.9.

By increasing the monolith bed height, a decrease in LF $DBC_{10\%}$ was observed. The $DBC_{10\%}$ per BV was 19.80 $mgmL^{-1}$ for the monolith with H=9.00 mm, instead of 24 $mgmL^{-1}$ for H=3.00 mm. The monolith radial flow device CIMmultus gave an intermediate LF binding capacity (around 22 $mgmL^{-1}$), which may be due in part to its intermediate bed height (H=4.20 mm). On the contrary, for the two membranes in the CIM housing (H=3 mm and 9 mm), no effect of bed height was observed, both binding capacities being around 43 $mgmL^{-1}$. In our previous study [49], by comparing Sartobind devices with increasing bed height, a decrease in binding capacity was obtained. When packed in the CIM column, this effect was not observed, which may suggest an improved flow distribution. This may be due to the absence of O-ring between membrane sheets, and therefore to the ability of the flow to pass at the peripheral region of the membrane discs.

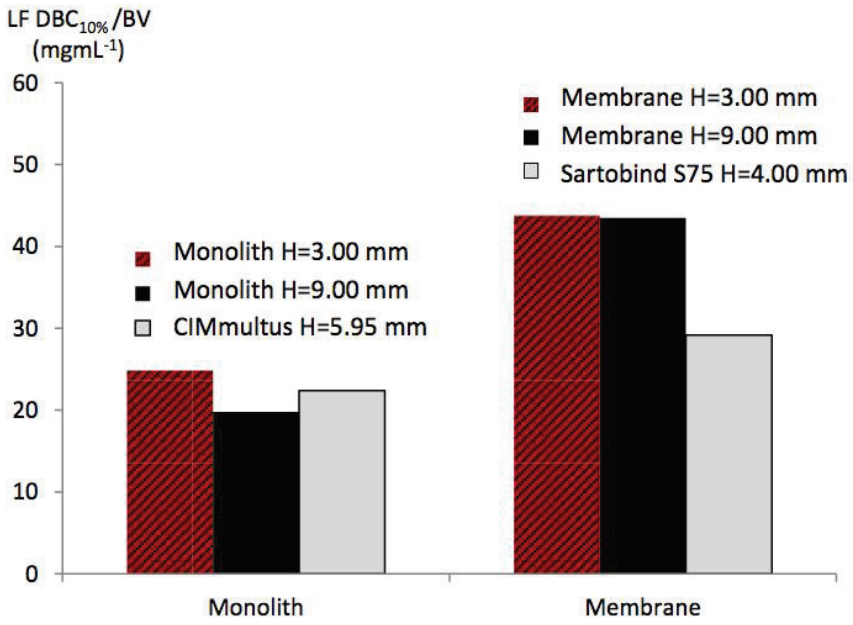

Fig. 5.9 Comparison of LF $DBC_{10\%}$ per BV for the different chromatographic monoliths and membranes. The experiments were performed using 100 mM phosphate buffer at pH 6.0 at the initial BSA/LF ratio of 2/1. The operating flow rate was 12 $BVmin^{-1}$, except for the monolith H=9 mm, which was 0.4 $BVmin^{-1}$.

The velocity profile was simulated for H=9 mm (data not shown). Like for the bed height H=3 mm, the velocity was found uniform within the membrane. The flow is distributed uniformly within the membrane thanks to the frits before and after the membrane stack. Moreover, the membrane and frit diameters being the same, it creates uniform flow within the membrane, contrary to the monolith. The model was applied to simulate the LF breakthrough curves obtained with the membrane in the CIM housing with H= 9.00 mm (Fig. 5.8B, Table 5.2). Using the same bi-Langmuir parameter values than those obtained for the membrane with H=3 mm, the LF breakthrough curve was predicted accurately. The same fitting parameters could be used probably because there was no change in binding properties between H=3 mm and H=9 mm. As for the 3 mm bed height membrane, the optimized $q_{m,2}$ from the CFD model ($q_{m,2a}$+$q_{m,2b}$) was lower than the $q_{m,2}$ data obtained from the LF static adsorption experiment.

The decrease in the monolith binding capacity with increasing bed height may be explained by the non-uniform flow inside the CIM housing due to the diameter change between the frit and monolith section. Indeed, the simulated velocity profile for the highest monolith bed height (H=9 mm) shows larger regions with non-uniform flow, than the monolith with bed height 3mm (data not shown). These peripheral regions of the monolithic disc could be not easily reached by the LF molecules. This effect could lead to the decrease in LF binding capacity with increasing bed height. For the simulation of the LF breakthrough curves using the monolith with H=9 mm Fig. 5.8B, Table 5.2), a change in q_m value was necessary to fit the experimental LF breakthrough curve. The optimized q_m for the monolith having H=9.00 mm was decreased to 33.58 $mgmL^{-1}$ compared to 39.34 $mgmL^{-1}$ at H=3.00 mm. Besides, $k_{a,2}$ and $k_{d,2}$ data were not affected by the bed height, and therefore by the uneven flow distribution for H=9 mm. Thus, the

values of $k_{a,2}$ and $k_{d,2}$ seems to be dependent mainly on the media structure and ligands properties, rather than the flow distribution.

5.5.7 Elution peaks

After loading a BSA/LF solution at initial BSA-LF ratio of 2/1, the LF bound to the membrane or monolith was eluted using a phosphate buffer containing 2 M NaCl at a flow rate of 12 $BVmin^{-1}$. Fig. 5.10 shows the elution peaks for the Sartobind device, membrane and monolith with H=3.00 mm in the CIM column. The eluted mass, peak width at half-height, asymmetric ratio, and tailing factor obtained are shown in Table 5.4. The asymmetry ratio was calculated at 10% of the peak height whereas the tailing factor was measured for the 5% of the peak height [13,54].

The highest LF eluted mass (32.58 $mg.mL^{-1}$) was obtained for the membrane in the CIM housing. In addition, the elution peak was then sharper and more symmetrical. The lower the values of the asymmetry ratio (2.10), tailing factor (1.08) and peak width at half-height (1.32) indicate that the flow distribution was significantly superior compared to flow distribution in the Sartobind device and in the monolith. The Sartobind S75 device gave the lowest eluted mass (14.05 $mgmL^{-1}$), whereas higher asymmetrical ratio and tailing factor were obtained, respectively 3.61 and 3.12. Using the monolith, the LF eluted mass was lower (19.33 $mgmL^{-1}$), the elution peak became also more asymmetrical with an asymmetric ratio of 3.37. The tailing effect was also increased with a tailing factor of 1.35. Finally, a larger peak width at half-height of 1.65 was obtained, which is also indicative of flow mal-distribution.

Overall, these results were consistent with the adsorption isotherms, breakthrough experiments and CFD results discussed earlier. The membranes in the CIM housing show the best flow distribution, and therefore the best LF binding capacity during loading and LF recovery during elution.

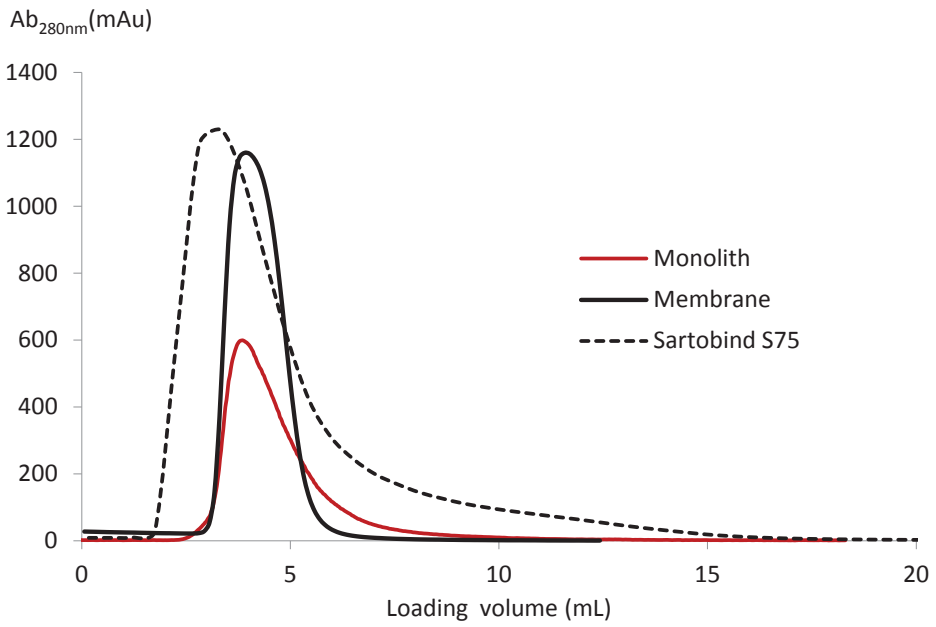

Fig. 5.10 LF elution peaks using for elution 2 M NaCl in phosphate buffer for the membrane, monolith with H= 3.00 mm in the CIM housing and the Sartobind S75 device at a flow rate of 12.0 $BVmin^{-1}$.

Table 5.4 LF Characteristics of elution peaks using membrane and monolith. LF Loading using 2 M NaCl in phosphate buffer solution at 12.0 $BVmin^{-1}$.

	Monolith H=3.00 mm	**Membrane H=3.00 mm**	**Sartobind S75**
LF eluted mass/BV ($mgmL^{-1}$)	19.33	32.58	14.05
Asymmetry ratio	3.37	2.10	3.61
Tailing factor	1.35	1.08	3.12
Peak width at half-height (mL)	1.65	1.32	2.64

5.6 Conclusion

In this paper, we compared the performance of monolith and membrane chromatography, both based on convective mass transport, for the separation of two similar size proteins, BSA and LF. The strong cation exchange membrane and monolith showed very good selectivity at pH=6.00 as LF was bound onto the binding sites, whereas BSA passed in the effluent. For both membrane and monolith, the separation cycles were repeated three times without cleaning and regeneration between each cycle. High productivities were obtained without any decrease in LF binding capacity.

A CFD model was developed to predict breakthrough curves of BSA and LF under non-binding and binding conditions, respectively, as well velocity and BSA concentration distribution within the membrane and monolith. As BSA does not bind onto the cation exchange supports, it can be used as an inert tracer to analyze mass transport. Using the model, a uniform BSA distribution was calculated within the membrane when housed in the CIM column, while lower accessibility was observed at the peripheral region of the monolith disc due to the change in diameter between the frit and the monolith. An uneven distribution of BSA was also calculated within the Sartobind S75 device, with low BSA concentration at the peripheral region of the membrane.

LF binding was characterized using both dynamic and isotherm adsorption experiments. The highest binding capacity of LF per support volume was obtained using the membrane housed in the CIM column, while the monolith and the commercialized Sartobind S75 device gave lower LF binding capacities, may be due to less efficient mass transport and non-accessible regions within both devices. LF breakthrough curves were predicted for the monolith using the CFD model and a Langmuir isotherm, while a bi-Langmuir isotherm, which assumes two different types of binding sites, was needed for the membrane in order to simulate slow binding kinetic near saturation. This tailing effect could be explained by steric interaction between already bound LF and available binding sites, which reduced their accessibility and thus binding kinetic. Moreover, the non-uniform membrane pore size and ligand density could be another reason, to explain why the bi-Langmuir equation was needed for the membrane.

The scaling-up of membrane and monolith in the CIM column was carried out by increasing the bed height to 9.00 mm instead of 3 mm. A lower LF bind capacity per support volume was then measured for the monolith, while this negative effect was not observed with the membrane. Concerning LF elution, the membrane in the CIM housing gave a sharper and more symmetric elution peak compared to the one measured for the monolith and commercial membrane device.

In conclusion, the efficiency of membrane and monolith chromatography was shown to be strongly dependent on flow distribution inside the housing. From this point of view, the CIM column, which uses porous frits before and after the ion exchange media, is suggested to be efficient.

5.7 References

[1] K.H. Gebauer, J. Thömmes, M.-R. Kula, Plasma protein fractionation with advanced membrane adsorbents, Biotechnol. Bioeng. 54 (1997) 181–189. doi:10.1002/(SICI)1097-0290(19970420)54:2<181::AID-BIT9>3.0.CO;2-H.

[2] A.K. Pabby, S.S.H. Rizvi, A.M.S. Requena, Handbook of membrane separations: chemical, pharmaceutical, food, and biotechnological applications, second edition, CRC Press, 2015.

[3] R. Ghosh, Protein separation using membrane chromatography: opportunities and challenges, J. Chromatogr. A. 952 (2002) 13–27. doi:10.1016/S0021-9673(02)00057-2.

[4] A.K. Hunter, G. Carta, Protein adsorption on novel acrylamido-based polymeric ion-exchangers: IV. Effects of protein size on adsorption capacity and rate, J. Chromatogr. A. 971 (2002) 105–116. doi:10.1016/S0021-9673(02)01027-0.

[5] A. Jungbauer, R. Hahn, Polymethacrylate monoliths for preparative and industrial separation of biomolecular assemblies, J. Chromatogr. A. 1184 (2008) 62–79. doi:10.1016/j.chroma.2007.12.087.

[6] J.J. Stickel, A. Fotopoulos, Pressure-flow relationships for packed beds of compressible chromatography media at laboratory and production scale, Biotechnol. Progr. 17 (2001) 744–751. doi:10.1021/bp010060o.

[7] C. Charcosset, Membrane processes in biotechnology and pharmaceutics, Elsevier, 2012.

[8] V. Orr, L. Zhong, M. Moo-Young, C.P. Chou, Recent advances in bioprocessing application of membrane chromatography, Biotechnol. Adv. 31 (2013) 450–465. doi:10.1016/j.biotechadv.2013.01.007.

[9] J. Thömmes, M.-R. Kula, Membrane chromatography - an integrative concept in the downstream processing of proteins, Biotechnol. Progress. 11 (1995) 357–367. doi:10.1021/bp00034a001.

[10] C.-S. Chang, H.-S. Ni, S.-Y. Suen, W.-C. Tseng, H.-C. Chiu, C.P. Chou, Preparation of inorganic–organic anion-exchange membranes and their application in plasmid DNA and RNA separation, J. Membr. Sci. 311 (2008) 336–348. doi:10.1016/j.memsci.2007.12.034.

[11] S. Huang, S. Roy, K. Hou, G. Tsao, Scaling-up of affinity-chromatography by radial-flow cartridges, Biotechnol. Prog. 4 (1988) 159–165. doi:10.1002/btpr.5420040306.

[12] V. Orr, J. Scharer, M. Moo-Young, C.H. Honeyman, D. Fenner, L. Crossley, et al., Simultaneous clarification of Escherichia coli culture and purification of extracellularly produced penicillin G acylase using tangential flow filtration and anion-exchange membrane chromatography (TFF-AEMC), J. Chromatogr. B. 900 (2012) 71–78. doi:10.1016/j.jchromb.2012.05.039.

[13] P. Madadkar, Q. Wu, R. Ghosh, A laterally-fed membrane chromatography module, J. Membr. Sci. 487 (2015) 173–179. doi:10.1016/j.memsci.2015.03.056.

[14] D. Josic, A. Buchacher, A. Jungbauer, Monoliths as stationary phases for separation of proteins and polynucleotides and enzymatic conversion, J. Chromatogr. B. 752 (2001) 191–205. doi:10.1016/S0378-4347(00)00499-0.

[15] A. Strancar, A. Podgornik, M. Barut, R. Necina, Short monolithic columns as stationary phases for biochromatography, Modern advances in chromatography, Springer Berlin Heidelberg, 2002: pp. 49–85.

[16] F. Svec, J.M.J. Fréchet, Modified poly(glycidyl metharylate-co-ethylene dimethacrylate)

continuous rod columns for preparative-scale ion-exchange chromatography of proteins, J. Chromatogr. A. 702 (1995) 89–95. doi:10.1016/0021-9673(94)01021-6.
[17] A. Jungbauer, R. Hahn, Monoliths for fast bioseparation and bioconversion and their applications in biotechnology, J. Sep. Sci. 27 (2004) 767–778. doi:10.1002/jssc.200401812.
[18] P. Gagnon, Technology trends in antibody purification, J. Chromatogr. A. 1221 (2012) 57–70. doi:10.1016/j.chroma.2011.10.034.
[19] S.M. Cramer, M.A. Holstein, Downstream bioprocessing: recent advances and future promise, Curr. Opin. Chem. Eng. 1 (2011) 27–37. doi:10.1016/j.coche.2011.08.008.
[20] K. Hormann, T. Müllner, S. Bruns, A. Höltzel, U. Tallarek, Morphology and separation efficiency of a new generation of analytical silica monoliths, J. Chromatogr. A. 1222 (2012) 46–58. doi:10.1016/j.chroma.2011.12.008.
[21] A. Podgornik, M. Barut, A. Strancar, D. Josić, T. Koloini, Construction of large-volume monolithic columns, Anal. Chem. 72 (2000) 5693–5699.
[22] A. Podgornik, A. Strancar, Convective Interaction Media (CIM)--short layer monolithic chromatographic stationary phases, Biotechnol. Annu. Rev. 11 (2005) 281–333. doi:10.1016/S1387-2656(05)11009-6.
[23] A. Podgornik, J. Jancar, M. Merhar, S. Kozamernik, D. Glover, K. Cucek, et al., Large-scale methacrylate monolithic columns: design and properties, J. Biochem. Biophys. Methods. 60 (2004) 179–189. doi:10.1016/j.jbbm.2004.01.002.
[24] J.J. Meyers, A.I. Liapis, Network modeling of the convective flow and diffusion of molecules adsorbing in monoliths and in porous particles packed in a chromatographic column, J. Chromatogr. A. 852 (1999) 3–23. doi:10.1016/S0021-9673(99)00443-4.
[25] A.I. Liapis, J.J. Meyers, O.K. Crosser, Modeling and simulation of the dynamic behavior of monoliths: Effects of pore structure from pore network model analysis and comparison with columns packed with porous spherical particles, J. Chromatogr. A. 865 (1999) 13–25. doi:10.1016/S0021-9673(99)01031-6.
[26] R. Hahn, M. Panzer, E. Hansen, J. Mollerup, A. Jungbauer, Mass transfer properties of monoliths, Sep. Sci. Technol. 37 (2002) 1545–1565. doi:10.1081/SS-120002736.
[27] R. Hahn, A. Tscheliessnig, P. Bauerhansl, A. Jungbauer, Dispersion effects in preparative polymethacrylate monoliths operated in radial-flow columns, J. Biochem. Biophys. Methods. 70 (2007) 87–94. doi:10.1016/j.jbbm.2006.09.005.
[28] F.J.M. Sanchez, E.M. del Valle, M.A.G. Serrano, R.L. Cerro, Modeling of monolith-supported affinity chromatography, Biotechnol. Progress. 20 (2004) 811–817. doi:10.1021/bp034343n.
[29] S.-Y. Suen, M.R. Etzel, A mathematical analysis of affinity membrane bioseparations, Chem. Eng. Sci. 47 (1992) 1355–1364. doi:10.1016/0009-2509(92)80281-G.
[30] A. Shiosaki, M. Goto, T. Hirose, Frontal analysis of protein adsorption on a membrane adsorber, J. Chromatogr. A. 679 (1994) 1–9. doi:10.1016/0021-9673(94)80306-4.
[31] K.H. Gebauer, J. Thömmes, M.R. Kula, Breakthrough performance of high-capacity membrane adsorbers in protein chromatography, Chem. Eng. Sci. 52 (1997) 405–419. doi:10.1016/S0009-2509(96)00426-5.
[32] C. Frerick, P. Kreis, A. Górak, A. Tappe, D. Melzner, Simulation of a human serum albumin downstream process incorporating ion-exchange membrane adsorbers, Chem. Eng. Process. 47 (2008) 1128–1138. doi:10.1016/j.cep.2007.07.013.
[33] H. Yang, M.R. Etzel, Evaluation of three kinetic equations in models of protein purification using ion-exchange membranes, Ind. Eng. Chem. Res. 42 (2003) 890–896. doi:10.1021/ie020561u.

[34] C. Boi, S. Dimartino, G.C. Sarti, Modelling and simulation of affinity membrane adsorption, J. Chromatogr. A. 1162 (2007) 24–33. doi:10.1016/j.chroma.2007.02.008.
[35] S. Schneiderman, H. Varadaraju, L. Zhang, H. Fong, T.J. Menkhaus, Mathematical model using non-uniform flow distribution for dynamic protein breakthrough with membrane adsorption media, J. Chromatogr. A. 1218 (2011) 9121–9127. doi:10.1016/j.chroma.2011.10.063.
[36] S. Dimartino, C. Boi, G.C. Sarti, A validated model for the simulation of protein purification through affinity membrane chromatography, J. Chromatogr. A. 1218 (2011) 1677–1690. doi:10.1016/j.chroma.2010.11.056.
[37] E. von Lieres, J. Wang, M. Ulbricht, Model based quantification of internal flow distributions from breakthrough curves of flat sheet membrane chromatography modules, Chem. Eng. Technol. 33 (2010) 960–968. doi:10.1002/ceat.200900614.
[38] P. Francis, E. von Lieres, C.A. Haynes, Zonal rate model for stacked membrane chromatography. I: Characterizing solute dispersion under flow-through conditions, Biotechnol. Bioeng. 1218 (2011) 5071–5078. doi:10.1016/j.chroma.2011.05.017.
[39] P. Francis, E. von Lieres, C. Haynes, Zonal rate model for stacked membrane chromatography part II: characterizing ion-exchange membrane chromatography under protein retention conditions, Biotechnol. Bioeng. 109 (2012) 615–629. doi:10.1002/bit.24349.
[40] P. Ghosh, K. Vahedipour, M. Lin, J.H. Vogel, C.A. Haynes, E. von Lieres, Zonal rate model for axial and radial flow membrane chromatography. part I: knowledge transfer across operating conditions and scales, Biotechnol. Bioeng. 110 (2013) 1129–1141. doi:10.1002/bit.24771.
[41] P. Ghosh, M. Lin, J.H. Vogel, D. Choy, C. Haynes, E. von Lieres, Zonal rate model for axial and radial flow membrane chromatography, part II: model-based scale-up, Biotechnol. Bioeng. 111 (2014) 1587–1594. doi:10.1002/bit.25217.
[42] P. Ghosh, K. Vahedipour, M. Lin, J.H. Vogel, C. Haynes, E. von Lieres, Computational fluid dynamic simulation of axial and radial flow membrane chromatography: Mechanisms of non-ideality and validation of the zonal rate model, J. Chromatogr. A. 1305 (2013) 114–122. doi:10.1016/j.chroma.2013.07.004.
[43] P. Gagnon, G. Richieri, S. Zaidi, F. Aolin, A comparison of microparticulate, membrane, and monolithic anion exchangers for polishing applications in the purification of monoclonal antibodies. IBC International Conference and Exposition, October 1-4, Boston, MA, USA.
[44] C.K. Chiu, M.R. Etzel, Fractionation of lactoperoxidase and lactoferrin from bovine whey using a cation exchange membrane, J. Food Sci. 62 (1997) 996–1000. doi:10.1111/j.1365-2621.1997.tb15023.x.
[45] V. Valiño, M.F. San Román, R. Ibañez, I. Ortiz, Improved separation of bovine serum albumin and lactoferrin mixtures using charged ultrafiltration membranes, Sep. Purif. Technol. 125 (2014) 163–169. doi:10.1016/j.seppur.2014.01.023.
[46] I. Tatárová, R. Fáber, R. Denoyel, M. Polakovic, Characterization of pore structure of a strong anion-exchange membrane adsorbent under different buffer and salt concentration conditions, J Chromatogr A. 1216 (2009) 941–947. doi:10.1016/j.chroma.2008.12.018.
[47] I. Mihelič, A. Podgornik, T. Koloini, Temperature influence on the dynamic binding capacity of a monolithic ion-exchange column, J. Chromatogr. A. 987 (2003) 159–168. doi:10.1016/S0021-9673(02)01811-3.
[48] C. Teepakorn, K. Fiaty, C. Charcosset, Optimization of lactoferrin and bovine serum albumin separation using ion-exchange membrane chromatography, Sep. Purif. Technol. 151 (2015)

292–302. doi:10.1016/j.seppur.2015.07.046.
[49] C. Teepakorn, K. Fiaty, C. Charcosset, Effect of geometry and scale for axial and radial flow membrane chromatography—experimental study of bovine serum albumin adsorption, J. Chromatogr. A. 1403 (2015) 45–53. doi:10.1016/j.chroma.2015.05.023.
[50] S.E. Bower, S.R. Wickramasinghe, Elimination of non-uniform, extra-device flow effects in membrane adsorbers, J. Membr. Sci. 330 (2009) 379–387. doi:10.1016/j.memsci.2009.01.020.
[51] M. Puthirasigamany, P. van Beijeren, P. Kreis, CHROM2—A method to enhance the dynamic binding capacity, yield and productivity of a chromatographic column, J. Chromatogr. A. 1236 (2012) 139–147. doi:10.1016/j.chroma.2012.03.015.
[52] P. Ghosh, K. Vahedipour, M. Leuthold, E. von Lieres, Model-based analysis and quantitative prediction of membrane chromatography: extreme scale-up from 0.08 ml to 1200 ml, J. Chromatogr. A. 1332 (2014) 8–13. doi:10.1016/j.chroma.2014.01.047.
[53] P. van Beijeren, P. Kreis, T. Zeiner, Ion exchange membrane adsorption of bovine serum albumin—Impact of operating and buffer conditions on breakthrough curves, J. Membr. Sci. 415–416 (2012) 568–576. doi:10.1016/j.memsci.2012.05.051.
[54] S.C. Moldoveanu, V. David, Essentials in modern HPLC separations, Elsevier, Waltham, 2013.

(This page is intentionally left blank)

Chapter 6

CHARACTERIZATION OF HYDRODYNAMICS IN MEMBRANE CHROMAGRAPHY DEVICES USING NUCLEAR MAGNETIC RESONANCE AND COMPUTATIONAL FLUID DYNAMICS

(This page is intentionally left blank)

Chapter 6
CHARACTERIZATION OF HYDRODYNAMICS IN MEMBRANE CHROMAGRAPHY DEVICES USING NUCLEAR MAGNETIC RESONANCE AND COMPUTATIONAL FLUID DYNAMICS

6.1 Abstract

Membrane chromatography is increasingly used in downstream processes for biomolecule purification as a large range axial or radial flow commercial membranes. The design of these devices plays a major role on flow distribution and biomolecule binding. To better understand the hydrodynamic, the velocity field was experimentally measured using Magnetic Resonance Imaging (MRI) and calculated by CFD on reconstructed geometries obtained by MRI. The CFD model solved Navier-Stokes and Brinkman equations in the free and membrane regions, respectively. Two membrane chromatography devices were investigated: the axial flow device Sartobind Q75 and the radial flow device Sartobind Nano 1 mL (Sartorius, Germany). The velocity field was simulated and velocity data were plotted versus membrane height and length. For the axial flow device, the measured velocity was found higher at the periphery at all membrane bed heights, whereas the velocity was constant elsewhere within the membrane. These results suggest that the whole membrane housing has an effect on flow distribution, the inlet and outlet distributors as well as the peripheral walls of the module. In the radial flow device, a high decrease was observed along the membrane bed height, which could be due to the reduction of the diameter section at the module outlet. Measured and calculated velocities (either in 2D or 3D) were found in good agreement, which suggests that the 2D model was sufficient to predict accurately the velocity field. Overall, it can be concluded that MRI and CFD are powerful methods to better understand the hydrodynamic within these membrane devices.

Keywords :

Membrane chromatography (MC), Magnetic resonance imaging (MRI), Computational Fluid Dynamic (CFD), Velocimetry

6.2 Introduction

Membrane chromatography (MC) is an alternative technique to traditional resin chromatography. This purification method employs a microporous membrane with large pore size as a stationary phase. The major advantage of MC comes from its convective mass transport, which is not limited by diffusion like in resin columns. Using MC, faster binding than in traditional columns is obtained, resulting in a fast biomolecules purification and high productivities [1–3]. Furthermore, MC can be employed for single-use applications due to its simple and disposable format. This can significantly reduce capital costs of production facilities in biopharmaceutical manufacturing [4]. Nowadays, MC devices are mainly commercialized into two configurations, axial and radial flow. Axial flow devices consist of several stacked membrane discs contained in housing. The flow goes from top through the membrane bed to the outlet. Inside radial flow devices, the membrane is in the form of a spiral wound or rolled around a cylindrical core. The flow pattern is from the outside membrane cylinder to the inside core. For both MC devices, non-uniform flow distribution may limit performances by a decrease in binding capacity and poor resolution [5]. In order to improve MC performance, the understanding of the hydrodynamics within the void regions and the membrane is needed and can be obtained using mathematical modeling and non-invasive measurement [6].

Mathematical modeling of MC binding breakthrough curve can be obtained by solving transport and binding kinetic equations within the membrane region (e.g. Suen and Etzel [7], Shiosaki et al. [8], Gebauer et al.[9], Frerick et al. [10]). To match the experimental results, the real flow distribution has been taken into account. For this purpose, a continuously stirred tank reactor (CSTR) and a plug flow reactor (PFR) in series were used to describe dead volumes and dispersion in the MC device and the experimental set-up [11,12]. The velocity at the inlet of the MC module in the form of a polynomial equation was used to describe the non-symmetrical breakthrough curve shape [13]. Computational Fluid Dynamics (CFD) has been recently integrated into the MC model [14,15] to predict the flow field in the complex geometry of the MC device. CFD can provide data which are difficult to measure experimentally, such as velocity and pressure. However, CFD may require very large computational grid for complex geometry and moderate to high Reynold numbers [16], which may be computationally expensive and time consuming.

To visualize the flow distribution in the membrane devices, non-intrusive or/and quasi-non-intrusive observation methods can be used [6]. The optical techniques, which employ high magnification camera or microscope to obtain real-time imaging, have been extensively studied in many applications. Particle image velocimetry (PIV) is one of the optical technique that can be applied to determine the instantaneous velocity field in applications such as ultrafiltration in a plane Plexiglass module [17] and cylindrical rotating filtration [18]. In the PIV system, suitable tracer particles are injected into the flow field [6]. A short pulse laser system emits high power light beams to illuminate particles driven in the flow, which are digitally recorded using a high speed camera. The relative displacement of tracer particles within the flow is therefore determined. However, PIV and other optical methods are limited by instantaneous data acquisition and low resolution in the sub-micron range, as well as by the requirements for transparency and discrimination between particles. The velocity in the porous membrane thus cannot be measured. A non-optical method like magnetic resonance imaging (MRI) is characterized by a quite poor microscopic resolution (voxels size of the order of some 10µm) but

within these voxels, it allows the detection of brownian scale movements (in diffusion techniques) and even Angstrom scaled sub-brownian periodical movements (in elastography techniques). Numerous flow quantities can be measured by MRI including mean velocities, Reynolds stresses, and diffusion coefficients and tensors [16].

MRI, generally used for medical diagnostics, is an imaging technique for generating spatially resolved images inside an object utilizing the interaction between an applied magnetic field and a nucleus that possesses spin [19]. MRI has been reported in several studies of hydrodynamic characterization in membrane modules. Pangrle et al. [20,21] investigated the flow distribution in a hollow fiber membrane reactor and in a porous tube and shell module at different Reynold numbers in the laminar flow regime. The MRI technique used was a spin-echo "time of flight", which provided a 2-D image of a selected cross section based on spin-echo ^{1}H. Flow distribution in a hollow fiber bioreactor was also investigated by Hammer et al. [22] and Heath et al. [10]. In these studies, MRI was used to measure the convective leakage flow in the extracapillary space of the hollow fiber module. The measured velocities compared well with theoretical results obtained from a solution of Poisson's equation. The authors concluded that the combination of MRI measurements and mass transfer modeling is a powerful tool for process optimization and design of membrane devices. Yao et al. [24] mapped the flow distribution in a hollow fiber membrane module employing shell side feed. The results show channeling of flow in regions of low membrane fiber packing density, which may significantly influence filtration efficiency. To improve MRI performance at higher flow rates, the use of flow compensated imaging gradients was found essential.

Flow distribution in complex geometries can also be characterized by MRI. For example, Mallubhotla et al. [25] investigated centrifugally induced (Dean) vortices generated to reduce concentration polarization and fouling in membrane devices. The measurements were made in a curved tube at different flow rates and ratio of the tube radius to that of curvature. Theoretical velocities obtained from Navier-Stokes and continuity equations agreed well with the experimental velocities obtained by MRI. Multiphase flow in a porous media can also be investigated by RMN. For example, Agranovski et al. [26] characterized gas-liquid flow distribution in a bubbling filter device designed for particulate and gaseous pollutants removal. Moreover, complex phenomenon such as biofouling in nanofiltration and reverse osmosis devices were investigated using MRI [27]. For example, MRI provided a non-invasive quantitative measurement of membrane biofouling and its impact on hydrodynamics and mass transport. The method led to the optimization of the chemical cleaning strategy of a biofouled reverse osmosis membrane [28]. Recently, low field MRI was used to characterize flow distribution in membrane distillation modules with four different configurations of randomly-packed, spacer-knitted, curly and semi-curly fibers [29]. Low-field MRI at 0.3 T (corresponding to a 1H resonance frequency of 12.7 MHz) was chosen due to its simpler operational procedures and lower cost. The effect of the membrane distillation module design configuration was discussed in terms of flow distribution and permeation flux.

Despite many applications of MRI for studying hydrodynamics in membrane devices, MRI measurement within the membrane is still challenging due to the small pore volumes, in which there is not much fluid to create a measurable signal. In addition, velocities within the porous membrane are generally slow and can require long scan times [16]. However, determination of flow distribution within the membrane is of great interest, especially for MC, to improve module design and process performance. To our knowledge, characterization of flow distribution in MC

devices using MRI has never been carried out. In this work, flow distribution is investigated for strong ion exchange Sartobind MC devices (Sartorius, Germany) in an axial and a radial flow configurations. The velocity fields measured by MRI are compared to values obtained by CFD, based on the resolution of Navier-Stokes and Brinkman's equations for a reconstructed geometry of the Sartobind MC devices in 2D and 3D dimensions. The flow measurement by MRI is obtained using a 4.7 T BioSpec MRI device (Bruker, France) with ^{1}H resonance frequency of 200 MHz. The effect of the MC device geometry on flow distribution is discussed, while the advantages and limits of both flow visualization methods are evaluated.

6.3 Theory

6.3.1 Basic principle of MRI

In presence of a magnetic field B_0, the intrinsic magnetic moment (spin) of hydrogens protons acquires a precessing movement around the magnetic field axis. The pulsation of the precession is given by $\omega=\gamma B_0$ where γ is called the magnetogyric ratio of the given nucleus (in Hz/T). In spite of the fact that a very large number of spins are involved, the resulting macroscopic magnetization is very small due to the fact that the difference between the spins of positive and negative values given by Boltzman's law is very small. That explains why MRI is not a sensitive method. It also explains why, at thermal equilibrium, the only non-null component of the macroscopic magnetization is along the magnetic field applied [16].

To observe an MRI signal, an oscillatory resonant magnetic pulse (RF-Pulse) is applied along a direction perpendicular to the static magnetic field (B_0). This RF-Pulse is applied by an excitation coil. The purpose of this pulse is to tilt the macroscopic magnetization (M_0) from its equilibrium state along the B_0 axis (arbitrarily called the z-axis, which is identical to the z direction of the CFD simulation) to create an observable macroscopic transverse magnetization. When the RF-Pulse is stopped, the precessing of M_0 can be recorded by the same coil or by specific ones. The basic properties of the signal are its intensity (related to the density of proton ρ in the observed media), its duration (the parameters named T_2 and T_2* reflects times during which the vectorial sum of all the small magnetization is non negligible) and the T_1 parameter which corresponds to the characteristic time needed by the system to lose its energy and reach back the equilibrium state along the z-axis. The principle of an MRI imaging experiment is to break the spatial isotropy of the static magnetic field, using magnetic field gradients which can be applied along the three spatial dimensions. These gradients can be used to encode spatial information in the phase and frequency of the signal acquired. A judicious choice of alternating RF-Pulses and gradients allows acquiring and reconstructing images exhibiting the MRI properties of the sample studied. The proton density parameters, T_1 and T_2 are commonly studied but a vast panel of other properties can be measured. Among them is the velocity of the spins within the media.

Using MRI, the main way to access molecular displacement is to add velocity encoding gradients into a classical MRI experiment considering the addition of a magnetic gradient of duration τ and of intensity G_x (T/m) applied arbitrarily along the x direction. This gradient is then followed by a gradient of same duration and intensity $-G_x$. A straightforward calculation of the phase accumulated after the application of the two gradients leads to Eq. 1, where φ_v is the

phase accumulated by spins travelling at speed v_x along the x direction:

$$\varphi_v = \gamma G_x v_x \tau^2 \qquad \text{Eq.1}$$

where γ being a constant. This simple equation is very useful to explain the advantages and drawbacks of the technique. To measure small velocities, strong gradients have to be used (a preclinical hardware is usually limited to gradients strength below 1 T/m) or/and a long τ (but τ must still be shorter than the duration of the macroscopic MRI signal which is usually around 100 ms). The phase is defined modulo 2π and thus a maximum speed has to be estimated first to prevent phase wrap in the images or an unwrapping algorithm has to be used afterward.

All these technical considerations led us to choose for our experiments a Gradient Echo MRI sequence of type Fast Low-Angle Shot (FLASH) [30] coupled to a four points velocity vector estimation [31]. FLASH sequences are well suited for 2D and 3D MRI microscopy and provides a good signal/noise ratio per units of time. The four points velocity vector estimation module added to the FLASH is inherently designed to remove spurious phase artefacts and minimize the acquisition time needed.

6.3.2 Computational fluid dynamics

Computation fluid dynamics (CFD) is based on the solution of the fundamental conservation laws of mass, momentum and energy in a set of partial differential equations (PDEs). The set of PDEs, coupled to initial and boundary conditions, is solved by numerical methods and discretization techniques of the domains such as the finite volume method, finite element method, finite difference method, etc. In this study, the internal geometry of the MC device is divided into two regions: free and porous as illustrated in Fig. 6.2. The porous membrane is assumed to be homogenous. Both regions are discretized using the finite element method. The fluid flow in the free region was obtained by solving the Navier-Stokes equations (Eq.1 and 2) assuming negligible external force (F=0):

$$\rho(u.\nabla u) = \nabla.\left[-PI + \mu\left(\nabla u + (\nabla u)^T\right) - \frac{2}{3}\mu(\nabla.u)I\right] \qquad \text{Eq.2}$$

$$\nabla.u = 0 \qquad \text{Eq.3}$$

where u is the fluid velocity, I the identity matrix, P the pressure, ρ the density and μ the dynamic viscosity. The density and dynamic viscosity are those of water at 20°C.

In the porous membrane region, the flow is governed by the Brinkman equations (Eq. 4-5), where the membrane properties are the porosity, ε, and the permeability, κ, respectively equal to 0.78 and 1.00×10^{-13} m^2 [42,46]. Continuity was enforced between the fluid velocity and pressure in the free flow and the porous membrane channel. The difference corresponded to the stress adsorbed by the rigid porous matrix, which was a consequence implicit in the formulations of the Navier-Stokes and Brinkman equations.

$$\rho(v.\nabla v) = \nabla.\left[-PI + \mu(\nabla v + (\nabla v)^T) - \frac{2}{3}\mu(\nabla.v)I\right] - \frac{\mu}{\kappa}v \quad \text{Eq. 4}$$

$$\nabla.v = 0 \quad \text{Eq.5}$$

At the inner boundaries within the MC device, no-slip conditions were applied, while a parabolic velocity profile at the inlet and vanishing viscous stress at the outlet of the device were used as boundary conditions (Eq.6-7):

$$Inlet\ ; \quad u = 2(1 - \frac{r^2}{R^2})u_{av} \quad \text{Eq.6}$$

$$Outlet\ ; \quad \mu(\nabla u + (\nabla u))^T = 0 \quad \text{Eq.7}$$

where R and u_{av} are the radius of the tube at the inlet of the device and the average velocity at the inlet, respectively. r is the radial coordinate. The inlet and outlet positions for each MC devices were described as displayed in Fig. 6.2. In addition, the continuity of velocity and pressure was enforced between the free and the porous region. The resulted discontinuous stress was assumed to do not cause any movement of the membrane.

6.4 Materials and methods

6.4.1 Chromatographic membrane and devices

Sartobind MC devices (Sartorius Stedim Biotech GmbH, Goettingen, Germany) contain a stabilized reinforced cellulose membrane with a thickness of 275 µm and pore size around 3 - 5 µm. Functionalized quaternary ammonium (Q) groups are bound covalently to the grafted polymer layer. The Sartobind Q75 device is an axial flow device with a diameter of 25.0 mm and bed height of 4.0 mm. Stacked membrane discs are housed in a complex geometry with flow distributors at the inlet and outlet. The Sartobind Nano 3mL is a radial flow device was with a bed height of 8 mm.

6.4.2 MRI experiments

The MRI experiments were conducted using a Biospec preclinical MRI system (Bruker, France) with field strength of 4.7 T coupled to a set of Magnex 3D magnetic field gradient SGRAD 156/100/S with a maximum gradient strength of 250 mT/m. Depending of the emission and reception coils used, an inner diameter up to 72 mm was usable. To maximize the Signal to noise ratio, a 39 mm diameter RAPID Biomedical (Germany) quadrature coil was used for excitation and signal detection.

Using MRI, two sets of experiments were conducted. First, the 3D internal geometry of

both MC devices was measured employing a high resolution 2D gradient echo technique (FLASH) encoding technique. A high resolution image of the Sartobind Q75 geometry was obtained over a field of view (FOV) of 32x32x20 mm on a 256x256x64 voxels matrix along the read (x), phase (y) and slice (z) axis, respectively. The spatial resolution was then 125x125x313 µm. The internal geometry of Sartobind Nano 1mL device was similarly acquired in 2D with a FOV of 41.2x41x20.6 mm on a 192x192x96 voxels matrix. The isotropic resolution was 215x215x215 µm.

The velocity fields were then measured within both MC devices using 4 points velocity estimation technique. In the experiments, the flow rate was set to 10.0 $mL.min^{-1}$ on an Äktaprime-Plus chromatography system (GE Healthcare Life Sciences, France). The flow value was calibrated using a 1.00 mm diameter tube at different flow rates from 0 to 0.50 $mL.min^{-1}$. The maximum velocity was set to 2.00 $cm.s^{-1}$. The flow encoding was acquired along the three directions. For the Sartobind Q75 device, the acquisition of the velocity was obtained in 3D, over a FOV of 27.0x27.0x15.0 mm on a 128x128x16 pixels matrix. The velocity image resolution was then 211x211x938 µm. Besides the FOV and resolution, the basic parameters of the FLOW encoding sequence were: echo time TE=8 ms, repetition time TR=32 ms, flip angle α =60°, acquisition bandwidth Bw=25 kHz, maximum velocity encoded 2.00 cm/s. For the Sartobind Nano1mL, the velocity image was acquired using the same technique in 2D longitudinal and cross sections with the resolution over 230x230µm. The 2D image was obtained in a slice with a thickness of 1.5mm and 1.3mm, respectively, for the longitudinal and cross sections. For the longitudinal section, the MRI parameters were set using TE/TR=7/30ms, α =30°, Bw= 101kHz and the maximum velocity of 2cm/s. To obtain the cross section of Nano1mL, TE/TR of 9/30.6ms, α =30°, Bw =30kHz and the maximum velocity at 1cm/s were applied.

MRI images were visualized and analyzed using the Fiji software (NIH, USA) and Matlab 2013a (Mathworks, USA). The flow encoding was done along the three directions using the 4 steps method. A T_1 relaxation agent at 0.08% w/w using Dotarem© solution (Guerbet, France) was added to the flowing fluid to increase the MRI signal. For velocity measurements, depending on the signal level, an acquisition averaging process of 4 to 12 times was used leading to an acquisition time ranging from 20 min to 1 h.

6.4.3 CFD simulations

To simulate the velocity profiles, the system of PDEs was solved with Comsol Multiphysics 4.4 software. PDEs were spatially discretized using the finite element method using a mesh of triangles in 2D or tetrahedra in 3D [33]. The minimum mesh size used was $6.73x10^{-7}$ m and the maximum $3.36x10^{-4}$ m. The internal geometry of the MC device was measured by MRI and reconstructed on Comsol Multiphysics 4.4 assuming rotational symmetry around the z-axis. This assumption allows the CFD model to be transformed into cylindrical coordinates, which reduces the model to 2D.

6.5 Results and discussion

6.5.1 Geometry of the axial flow device

The axial and radial flow modules were both imaged by MRI. The axial flow device was observed along a longitudinal section (Fig. 6.1-A1) and a cross-section just above the membrane surface (Fig. 6.1-A2). In this device, the fluid enters at the top, is distributed by the inlet distributor, passes through the membrane stack, and is then collected by the outlet distributor before emerging at the outlet of the device. Both inlet and outlet distributors consist of 8 radial channels and several circular channels. In the inlet distributor, the fluid is conducted to the peripheral region of membrane by the radial channels and distributed through all the membrane section by the circular channels. The fluid takes an inverse path in the outlet distributor. The complex geometry of the inlet distributor is clearly seen on Fig. 6.1-A2. Such distributors are commonly found in syringe type filters. Fig. 6.1-A1 also shows that the membrane height is slightly lower at the peripheral region of the capsule than in the center.

From the images obtained by MRI, the internal geometry of the axial flow device was reconstructed on Comsol Multiphysics. Two model geometries were drawn. The first one in 3D took into account the radial and circular channels of the inlet and outlet distributors. As the geometry was the same between two of the 8 radial channels, only one-eighth sector of the device was drawn (Fig. 6.2(A)). However, this complex 3D geometry with many details led to long calculation time and high computational memory. Therefore, a second model was drawn in 2D, assuming radial symmetry and free regions before and after the membrane stacks (Fig. 6.2(B)).

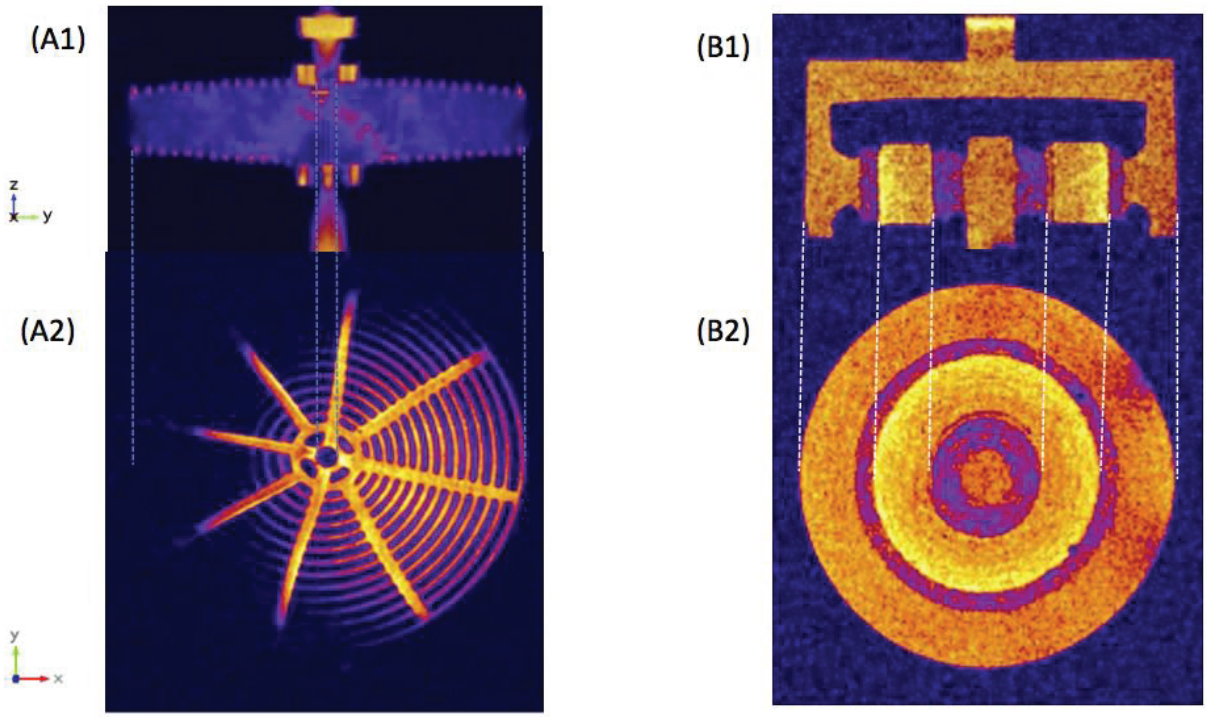

Fig. 6.1 MRI scan for the axial flow device; Sartobind Q75 in longitudinal (A1) and axial cross

sectional (A2). For the radial flow device; Sartobind Nano1mL, the MRI was scanned in the similar cross sections displayed at B1 and B2, respectively.

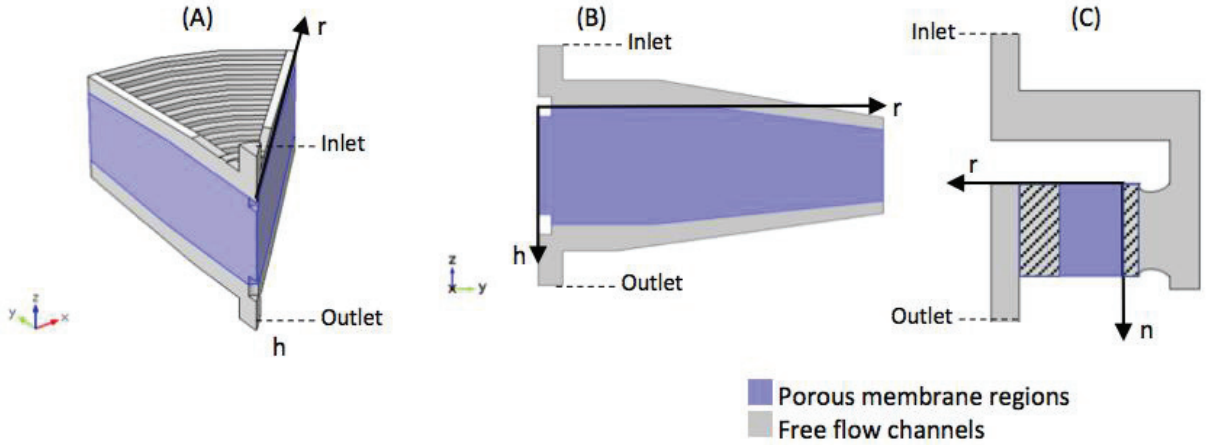

Fig. 6.2 Reconstructed geometry on the Comsol's interface for the 3D simulation of the Sartobind Q75 device (A) and the 2D axissymetric simulation of the Sartobind Q75 (B) and Sartobind Nano1mL (C) devices.

6.5.2 Flow distribution in the axial flow device

The velocity field within the axial flow device was measured by MRI velocimetry and calculated by CFD in 2D and 3D. The fluid flow rate was set to 10.0 $mLmin^{-1}$ for MRI measurements and CFD simulations. The average velocity in the whole membrane region were found very similar and equal to 0.0473, 0.0422, 0.0432 cms^{-1} from the 3D CFD, 2D CFD and MRI velocimetry measurement, respectively.

The velocity fields obtained from 3D CFD, 2D CFD and MRI velocimetry are shown in cross-sections and longitudinal sections in Fig. 6.3 and Fig. 6.4, respectively. In both sections, good agreement were obtained between measured and simulated velocities, as well as between velocities calculated in 2D or 3D. The MRI cross section in Fig. 6.3(C) shows that the velocity was higher near the peripheral wall. This phenomenon was also observed in 2D and 3D simulations. In an attempt to explain the higher velocity at the peripheral wall, simulations of velocity profiles were done in 2D and 3D assuming a constant membrane height (data not shown). In this case, the simulations predicted a constant velocity versus the membrane radius. It is then suggested that the higher velocity measured and calculated near the peripheral well may be due to the small decrease of membrane height in the capsule. The sealing of the top and bottom parts during the capsule production could also increase the loss of membrane height at the periphery. In addition, the 3D simulation, which took into account the flow distributors, was not able to predict the increasing velocity at the peripheral wall when assuming a constant membrane height (data not shown). Overall, it is suggested that the flow distributors are important features of the membrane housing; however, the whole design of the capsule, including its periphery, has also an important effect on the flow distribution. The longitudinal section of the velocity field is shown in

Fig. 6.4. Again, a good agreement was obtained between measured and simulated velocities. On the three pictures (Figure 4A, 4B, 4C), higher velocities were observed at the inlet and outlet of the capsule. The velocities obtained in 2D and 3D were again very close.

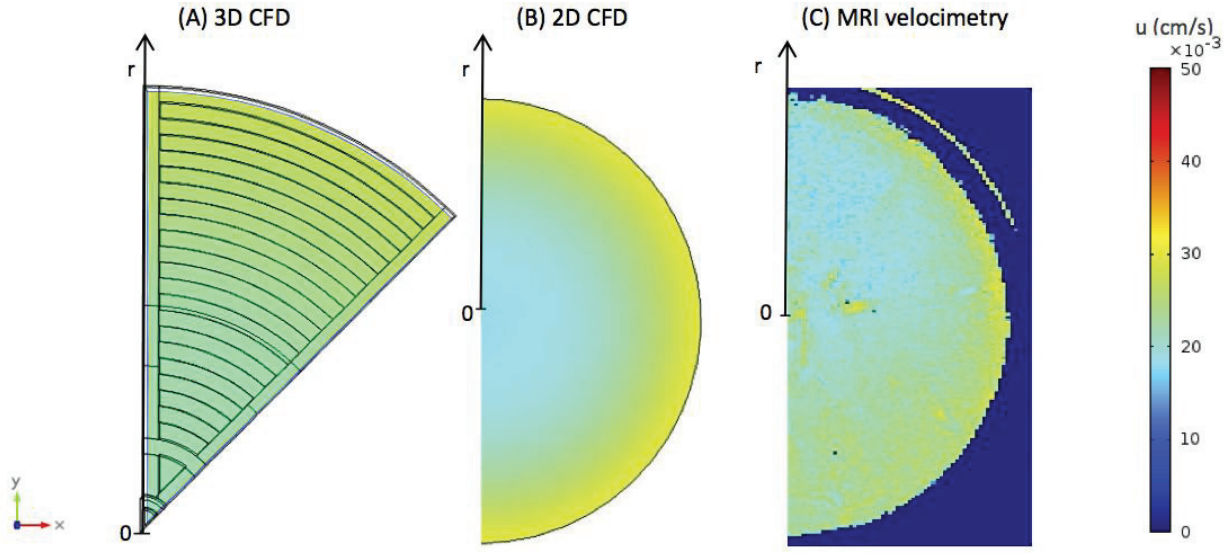

Fig. 6.3 Velocity field in a cross section of the Sartobind Q75 device obtained by 3D CFD simulation (A), 2D CFD simulation (B) and MRI velocimetry (C) at 10 mLmin^{-1} with a 100 mM phosphate buffer solution. The cross section is taken at the membrane bed height; h=2.00 mm.

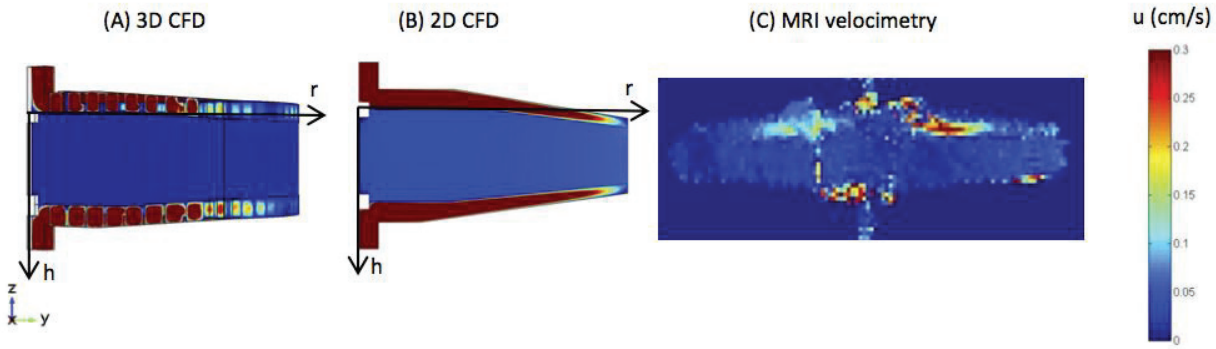

Fig. 6.4 Velocity filed in a longitudinal section of the Sartobind Q75 device obtained by 3D CFD simulation (A), 2D CFD simulation (B) and MRI velocimetry (C) at 10 mLmin^{-1} with a 100 mM phosphate buffer solution.

To have a closer look at the results, the measured and simulated velocities were plotted versus the membrane radius (r) and membrane height (h) in Fig. 6.5 and Fig. 6.6, respectively. In Fig. 6.5, the velocity as function of h was calculated for r=1.00, 5.00, 8.00 and 10.00 mm and compared to measured velocities. The predicted velocity using 2D and 3D CFD were in good agreement with the measured velocity data obtained by MRI velocimetry. From Fig. 6.5, a slight difference between velocities obtained in 2D and 3D can be seen: the 3D CFD gave slightly higher velocities near the center of the module, similar velocities at r=8.00 mm, and lower velocities near the edge of membrane, when r=10.00 mm, compared to velocities calculated with in 2D.

In Fig. 6.6, the velocity is plotted against the membrane radius at different membrane height (h=0.50, 1.50, 2.50 and 3.50 mm). As previously mentioned, the velocity increased versus r, the higher data being obtained near the peripheral region (this effect being more pronounced from r>5.00 mm) using all three methods. Again, this indicates the importance of the housing design: the inlet and outlet distributors contribute to flow distribution as well as the peripheral region of the axial flow device. A good agreement was also observed between simulated and measured velocities, and a small difference between velocities calculated in 2D and 3D.

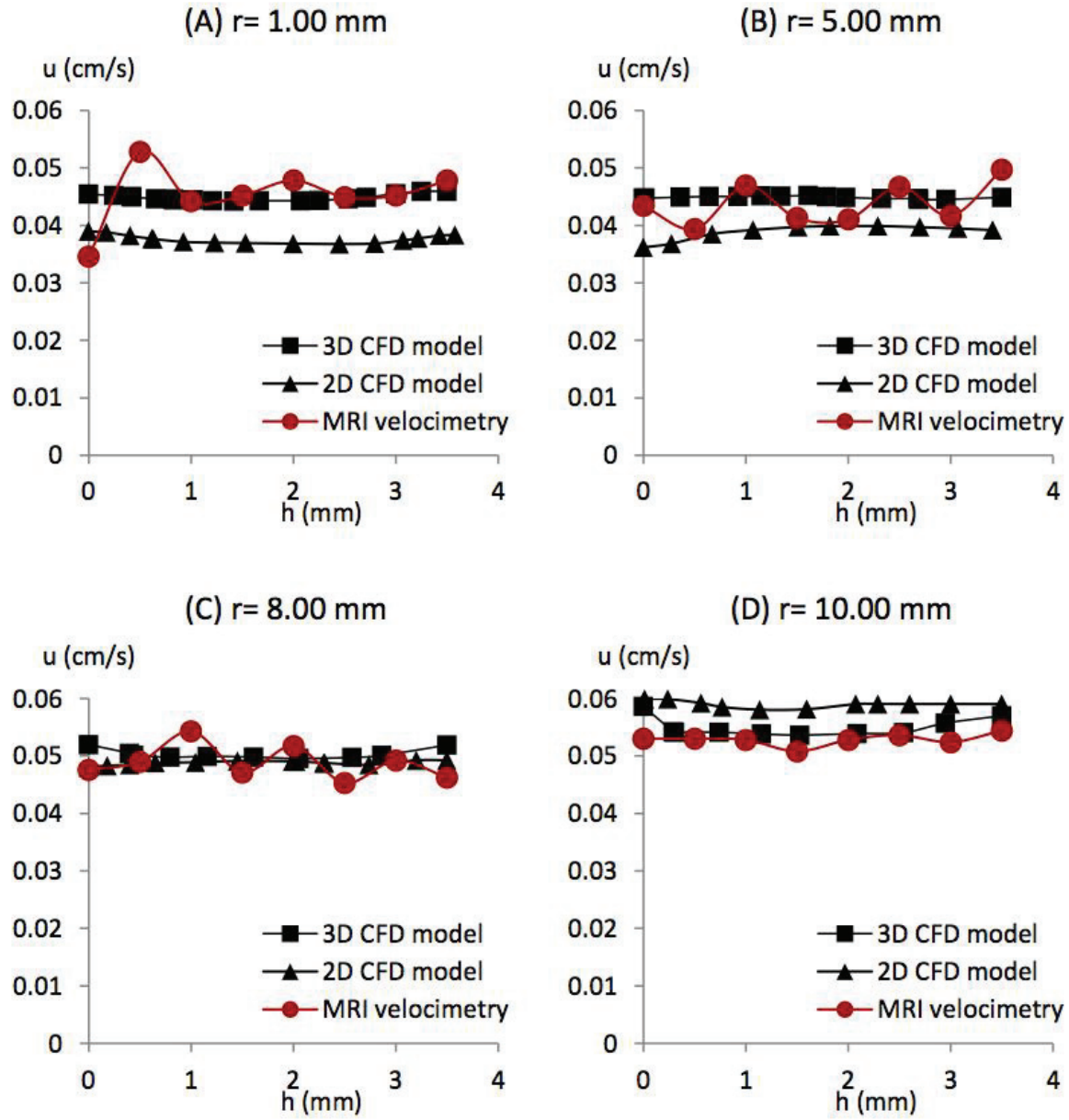

Fig. 6.5 Comparison of the velocity profiles as function of the membrane bed height (h) of the Sartobind Q75 device at the different radius positions (r) of 1.00, 5.00, 8.00 and 10.00 mm using the 3D, 2D CFD simulations, exterimental MRI velocimetry at 10.0 $mLmin^{-1}$ with 100 mM phosphate buffer.

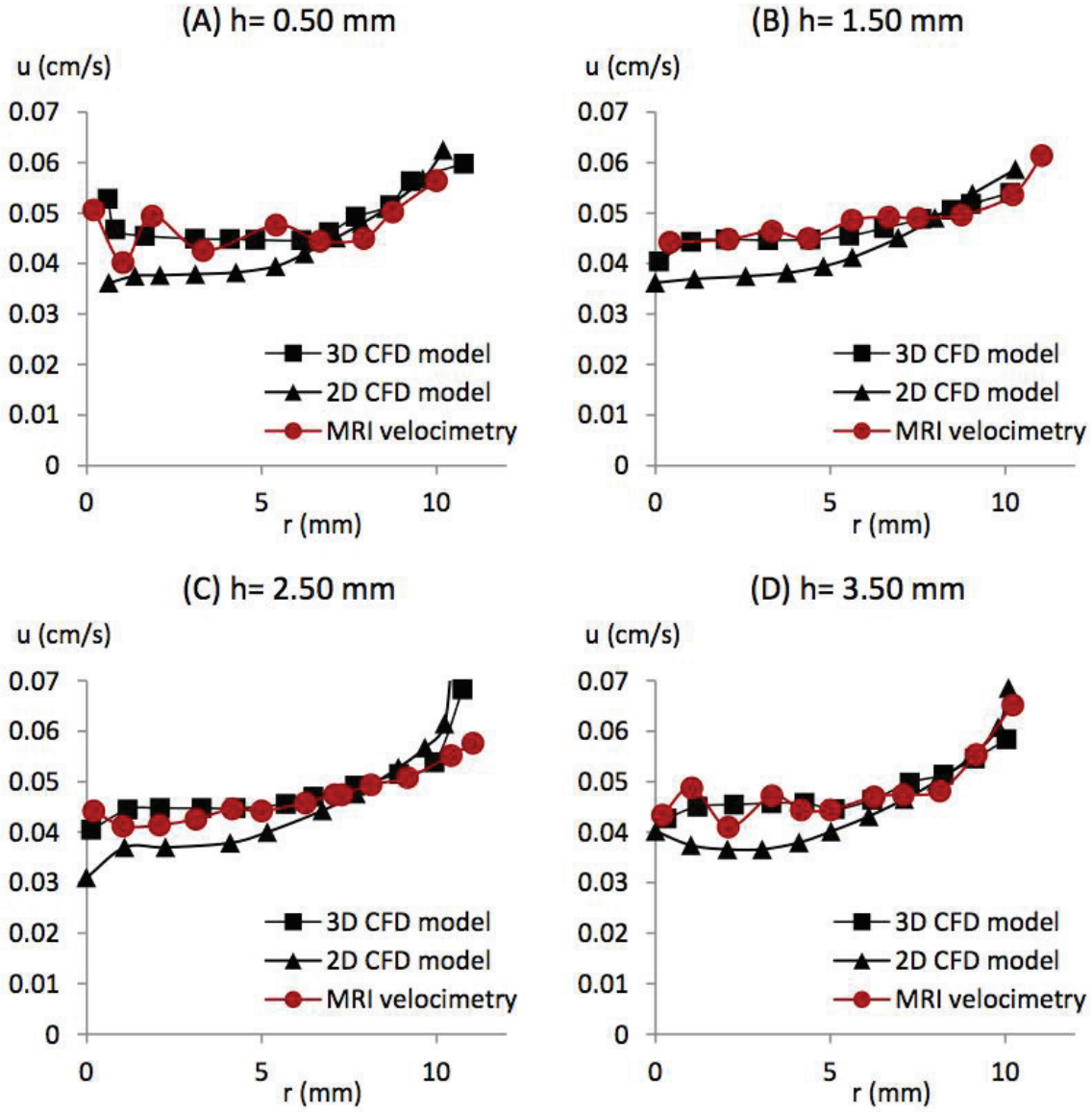

Fig. 6.6 Comparison of the velocity profiles as function of the membrane radius(r) of the Sartobind Q75 device at the different bed height positions (h) of 0.50, 1.50, 2.50 and 3.50 mm using the 3D, 2D CFD simulations, exterimental MRI velocimetry at 10.0 $mLmin^{-1}$ with 100 mM phosphate buffer.

6.5.3 Geometry of the radial flow device

Two sections of the radial flow device were obtained by MRI: a longitudinal section (Fig. 6.1-B1) and a cross-section at the membrane level (Fig. 6.1-B2). Inside the radial flow device, the membrane is rolled around a cylindrical core. The fluid flows from the top of the capsule to the outlet walls. The flow pattern is then from outside of the cylinder through the membrane bed to the inside core of the cylinder, and finally through the capsule outlet. Before and after the membrane, two different regions appeared on the longitudinal section (Fig. 6.1-B1). They correspond to fibrous materials placed on both sided of the membrane. They also appear in the cross-section (Fig. 6.1-B2).

The internal structure of the radial flow device was reconstructed on Comsol Multiphysics (Fig. 6.2-C). The internal structure was drawn in 2D thanks to the rotational symmetry of the capsule. The characteristics of the fibrous material (porosity and permeability) were unknown. For the simulations, these data were first assumed to be the same as those of the membrane.

6.5.4 Flow distribution in radial flow MC

The velocity field calculated by CFD was compared to the MRI velocimetry data in longitudinal and cross sections as shown in Fig. 6.7 and Fig. 6.8, respectively. For the experiments and the simulations, the feed flow rate was set to 10.0 $mLmin^{-1}$. The measured and calculated average velocities within the membrane were found in very good agreement, respectively equal to 0.0841 cms^{-1} and 0.0846 cms^{-1}. In the longitudinal section, high velocities were observed at the device outlet on both simulated and MRI images (Fig. 6.7). The diameter section is shorter at the outlet of the capsule, leading to higher velocities. The same trend could be observed at the inlet of the capsule, although the image was less clear. The MRI measurement will be done again to check this effect. In the cross section taken at the membrane level, a good agreement was also obtained between calculated and measured velocities (Fig. 6.8). In particular, the velocity in the cylinder core was in the same range for both simulation and MRI experiment. On the other hand, the two circular regions which appeared on the MRI image were not predicted by the simulation. They might correspond to the fibrous material found before and after the membrane which was assumed to have the same permeability and porosity than the membrane. In addition, these very dense fibrous regions might have less water molecules and therefore give a lower signal. In addition, some signal noise around the Nano1mL device was observed.

Next, the measured and calculated velocity fields were compared at different positions along the membrane length (n) and bed height (h). The velocity was plotted against the bed height (h) at n=1.00, 2.00, 4.00 and 6.00 mm (Fig. 6. 9). A good agreement was found between experimental and simulated velocities. Mainly, it was observed that the velocity increased with the bed height. This could be explained by the narrower section at the outlet of the radial flow device which leads to higher velocities. At different values of h, the velocity was constant versus n (Fig. 6.10). The increase in velocity which was observed near the periphery of the axial flow capsule was not observed here. This suggests a more uniform velocity in the membrane section perpendicular to the flow direction for the radial flow device. However, for this device, a much larger decrease in velocity was observed in the flow direction.

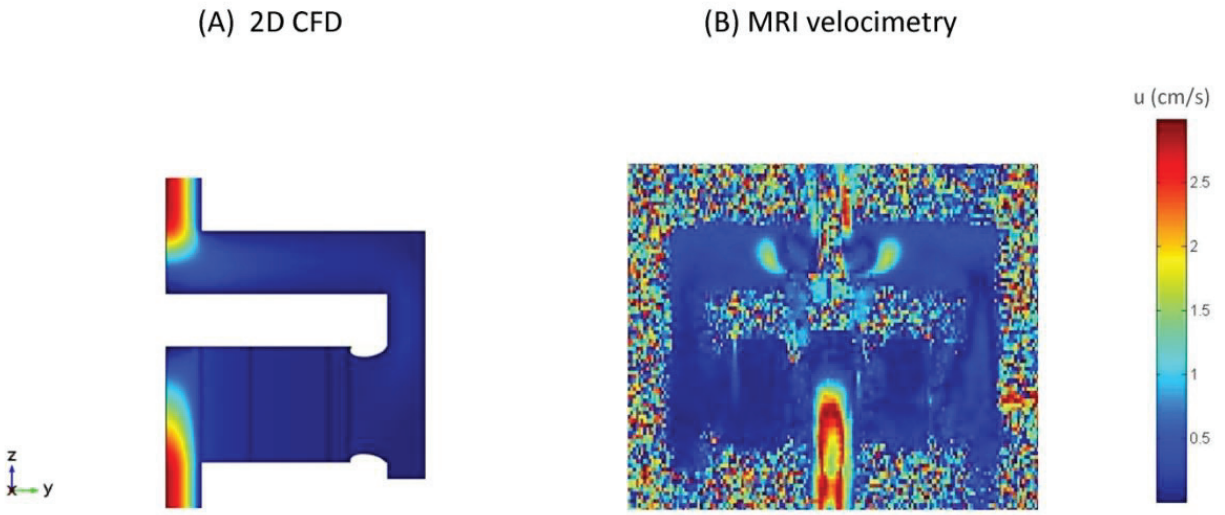

Fig. 6.7 Velocity fileds for the longitudinal cross section of the Sartobind Nano1mL device using the 2D axissymmetric CFD simulation (A) and MRI velocimetry (B) at 10 mLmin^{-1} with a 100 mM phosphate buffer solution.

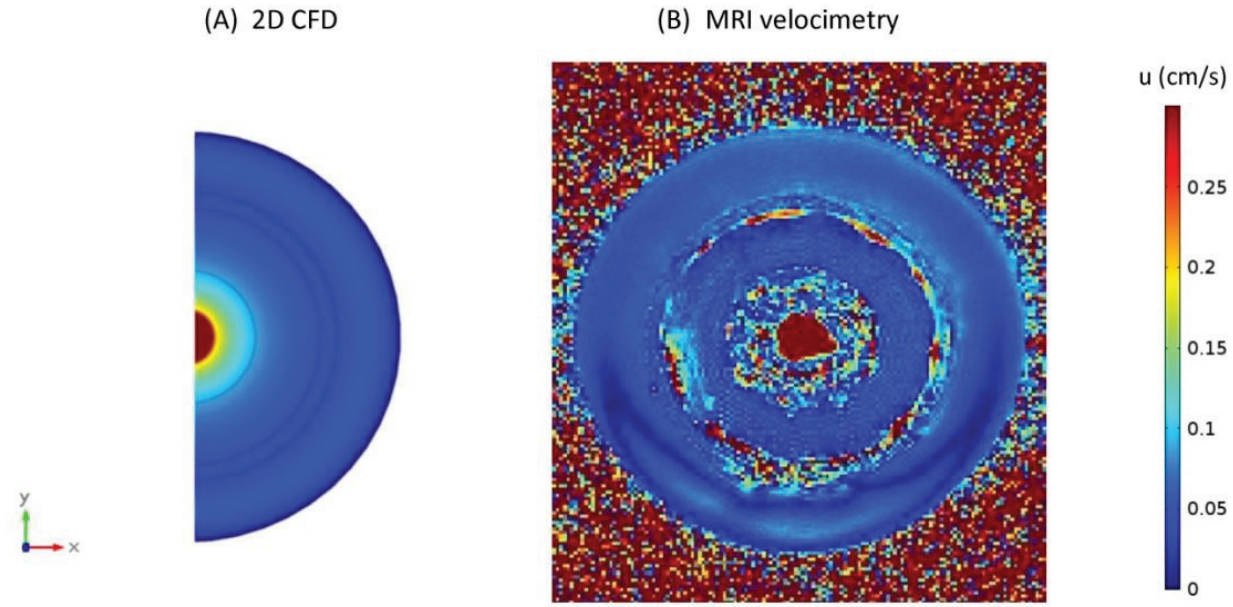

Fig. 6.8 Velocity fileds for the axial cross section of the Sartobind Nano1mL device using the 2D axissymmetric CFD simulation (A) and MRI velocimetry (B) at 10 mLmin^{-1} with a 100 mM phosphate buffer solution.

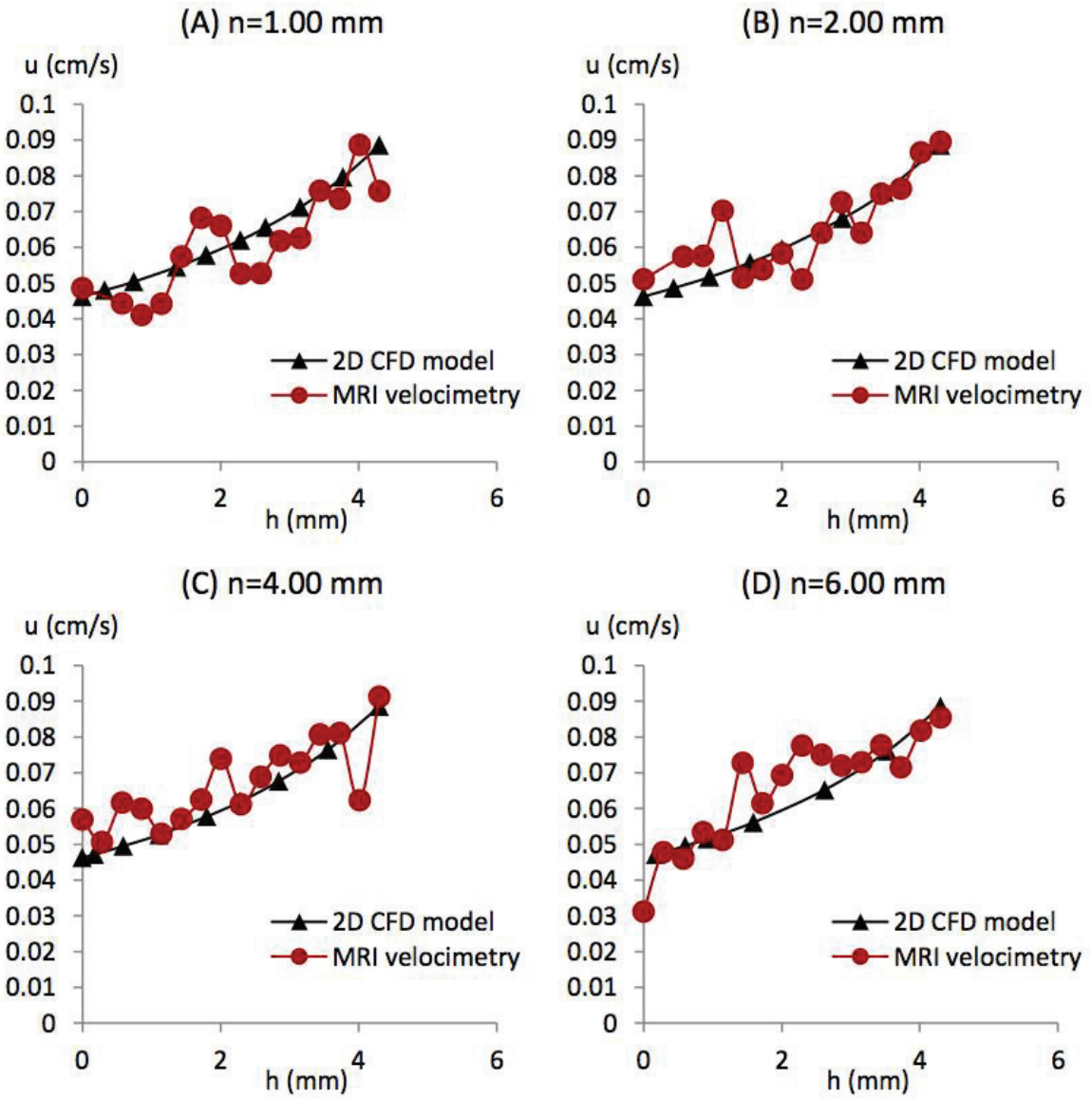

Fig. 6. 9 Velocity profiles as function of the bed hieght (h) of the Sartobind Nano1mL device at the different positions of the cylindrical length (n) of 1.00, 2.00, 4.00 and 6.00 mm using the 2D CFD simulation and exterimental MRI velocimetry at 10.0 $mLmin^{-1}$ with 100 mM phosphate buffer.

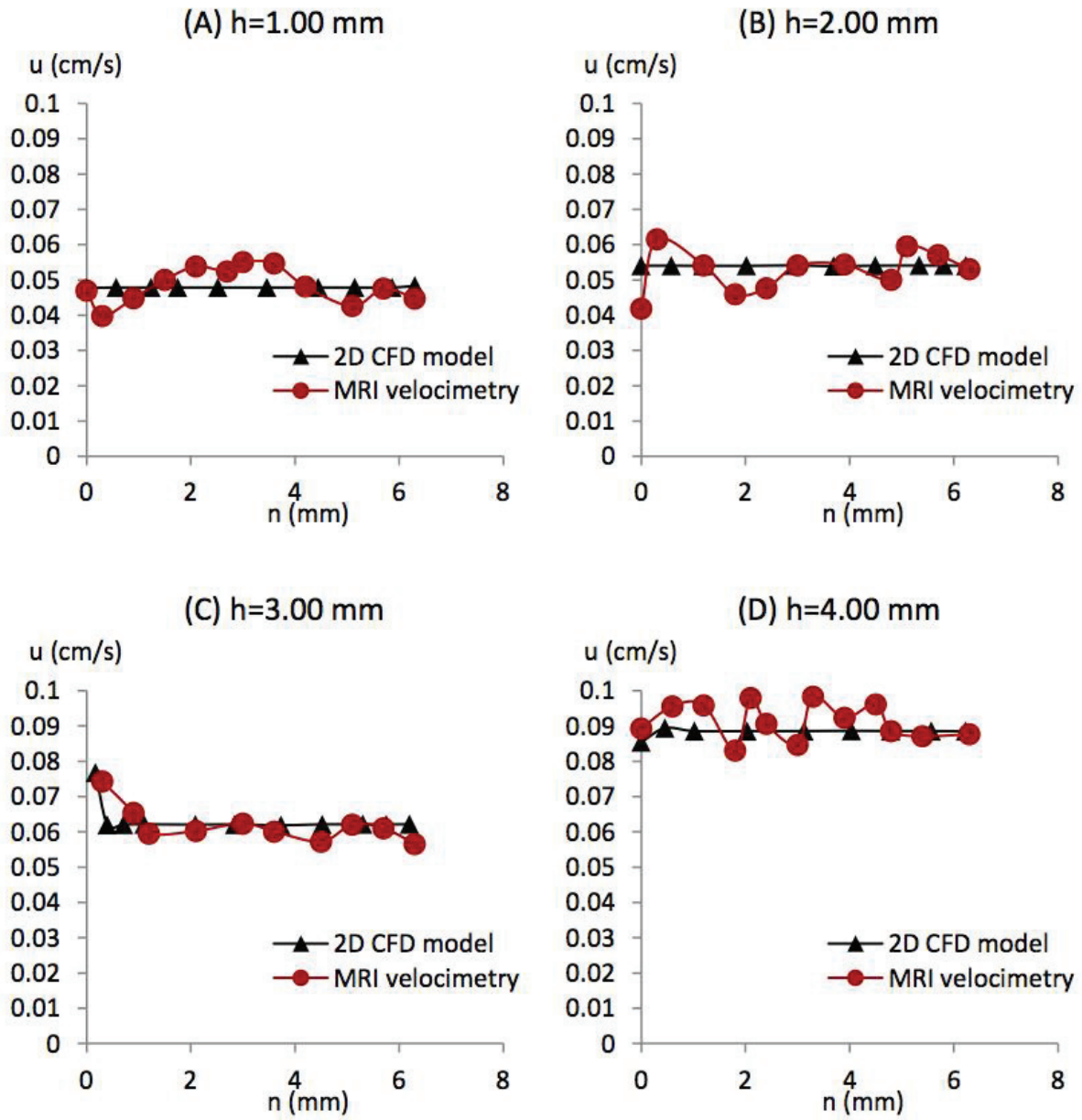

Fig. 6.10 Velocity profiles as function of the cylindrical length (n) of the Sartobind Nano1mL device at the different positions of the bed hieght (h) of 1.00, 2.00, 3.00 and 4.00 mm using the 2D CFD simulation and exterimental MRI velocimetry at 10.0 $mLmin^{-1}$ with 100 mM phosphate buffer.

6.6 Conclusion

The CFD velocity profiles within the axial and radial flow devices were compared to the measured MRI data with good agreement. Both techniques have shown limits and advantages. CFD simulation of flow within complex geometries remains a challenge due to the very large computational grid requirement and long calculation time. MRI velocimetry is a powerful method to obtain flow distribution in complex and opaque media. However, this technique is restricted to object with limited size or field of view and long acquisition times. In addition, the scanning and encoding sequences of the MRI technique require specialist support to realize the experiments and to obtain accurate data. In this study, MRI results were compared to 2D and 3D CFD simulation data. Thanks to the good agreement between the three velocity fields obtained, it was concluded that the 2D CFD simulation was sufficient for accurate velocity prediction. From this 2D model, other quantities could be calculated like the concentration field within the membrane by adding appropriate equations.

For both the axial and radial flow configurations, the membrane housing significantly affects the velocity field. Using the axial flow device, the velocity was found higher at the peripheral regions of the membrane stack; this can be explained by a small decrease in membrane thickness in this part of the device. It is expected that this specificity of the housing design would give efficient flow distribution for larger membrane device with higher membrane diameter. However, other phenomena could explain the increase in velocity at the edges, like fluid leakage and/or increasing flow rate at the end of the 8 radial channels. Using the radial flow device, an increase in velocity was observed as function of membrane bed height, which may be due to the narrow section at the outlet of the device. Finally, it is suggested that MRI and CFD methods can complement each other to validate experimental and simulated results obtained.

In order to fulfill the present results, some additional MRI experiments will be realized. For the axial flow device, the MRI velocimetry experiment repetitions are required to improve the quality of longitudinal section and to check the results of the cross section with a longer acquisition time. For the radial flow device, the MRI velocity in the fibrous regions of the cross sectional results did not contain enough information due to low water content in these regions. Longer MRI acquisition times will be thus necessary to obtain the better results. Next, some additional CFD simulations will also be done to simulate the velocity in the fibrous regions of the radial flow device, by changing the permeability and porosity data.

6.7 References

[1] R. Ghosh, Protein separation using membrane chromatography: opportunities and challenges, Journal of Chromatography A. 952 (2002) 13–27. doi:10.1016/S0021-9673(02)00057-2.

[2] C. Charcosset, Membrane Processes in Biotechnology and Pharmaceutics, Elsevier, 2012.

[3] C. Boi, Membrane adsorbers as purification tools for monoclonal antibody purification, J. Chromatogr. B Analyt. Technol. Biomed. Life Sci. 848 (2007) 19–27. doi:10.1016/j.jchromb.2006.08.044.

[4] Research and Markets: 9th Annual Report and Survey of Biopharmaceutical Manufacturing Capacity and Production, Reuters. (2012). http://www.reuters.com/article/2012/07/03/idUS126634+03-Jul-2012+BW20120703 (accessed October 10, 2014).

[5] P. Madadkar, Q. Wu, R. Ghosh, A laterally-fed membrane chromatography module, Journal of Membrane Science. 487 (2015) 173–179. doi:10.1016/j.memsci.2015.03.056.

[6] V. Chen, H. Li, A.G. Fane, Non-invasive observation of synthetic membrane processes – a review of methods, Journal of Membrane Science. 241 (2004) 23–44. doi:10.1016/j.memsci.2004.04.029.

[7] S.-Y. Suen, M.R. Etzel, A mathematical analysis of affinity membrane bioseparations, Chemical Engineering Science. 47 (1992) 1355–1364. doi:10.1016/0009-2509(92)80281-G.

[8] A. Shiosaki, M. Goto, T. Hirose, Frontal analysis of protein adsorption on a membrane adsorber, J. Chromatogr. A. 679 (1994) 1–9. doi:10.1016/0021-9673(94)80306-4.

[9] K.H. Gebauer, J. Thömmes, M.R. Kula, Breakthrough performance of high-capacity membrane adsorbers in protein chromatography, Chem. Eng. Sci. 52 (1997) 405–419. doi:10.1016/S0009-2509(96)00426-5.

[10] C. Frerick, P. Kreis, A. Górak, A. Tappe, D. Melzner, Simulation of a human serum albumin downstream process incorporating ion-exchange membrane adsorbers, Chem. Eng. Process. 47 (2008) 1128–1138. doi:10.1016/j.cep.2007.07.013.

[11] C. Boi, S. Dimartino, G.C. Sarti, Modelling and simulation of affinity membrane adsorption, Journal of Chromatography A. 1162 (2007) 24–33. doi:10.1016/j.chroma.2007.02.008.

[12] P. Francis, E. von Lieres, C.A. Haynes, Zonal rate model for stacked membrane chromatography. I: Characterizing solute dispersion under flow-through conditions, Biotechnol. Bioeng. 1218 (2011) 5071–5078. doi:10.1016/j.chroma.2011.05.017.

[13] S. Schneiderman, H. Varadaraju, L. Zhang, H. Fong, T.J. Menkhaus, Mathematical model using non-uniform flow distribution for dynamic protein breakthrough with membrane adsorption media, J. Chromatogr. A. 1218 (2011) 9121–9127. doi:10.1016/j.chroma.2011.10.063.

[14] P. Ghosh, K. Vahedipour, M. Lin, J.H. Vogel, C. Haynes, E. von Lieres, Computational fluid dynamic simulation of axial and radial flow membrane chromatography: Mechanisms of non-ideality and validation of the zonal rate model, Journal of Chromatography A. 1305 (2013) 114–122. doi:10.1016/j.chroma.2013.07.004.

[15] P. Ghosh, K. Vahedipour, M. Leuthold, E. von Lieres, Model-based analysis and quantitative prediction of membrane chromatography: Extreme scale-up from 0.08 ml to 1200 ml, J. Chromatogr. A. 1332 (2014) 8–13. doi:10.1016/j.chroma.2014.01.047.

[16] C.J. Elkins, M.T. Alley, Magnetic resonance velocimetry: applications of magnetic resonance

imaging in the measurement of fluid motion, Exp Fluids. 43 (2007) 823–858. doi:10.1007/s00348-007-0383-2.
[17] C. Gaucher, P. Legentilhomme, P. Jaouen, J. Comiti, J. Pruvost, Hydrodynamics study in a plane ultrafiltration module using an electrochemical method and particle image velocimetry visualization, Experiments in Fluids. 32 (2002) 283–293. doi:10.1007/s003480100317.
[18] S.T. Wereley, A. Akonur, R.M. Lueptow, Particle–fluid velocities and fouling in rotating filtration of a suspension, Journal of Membrane Science. 209 (2002) 469–484. doi:10.1016/S0376-7388(02)00365-4.
[19] L.F. Gladden, Nuclear magnetic resonance in chemical engineering: Principles and applications, Chemical Engineering Science. 49 (1994) 3339–3408. doi:10.1016/0009-2509(94)00129-4.
[20] B.J. Pangrle, E.G. Walsh, S. Moore, D. DiBiasio, Investigation of fluid flow patterns in a hollow fiber module using magnetic resonance velocity imaging, Biotechnol Tech. 3 (1989) 67–72. doi:10.1007/BF01876224.
[21] B.J. Pangrle, E.G. Walsh, S.C. Moore, D. DiBiasio, Magnetic resonance imaging of laminar flow in porous tube and shell systems, Chemical Engineering Science. 47 (1992) 517–526. doi:10.1016/0009-2509(92)80001-S.
[22] B.E. Hammer, C.A. Heath, S.D. Mirer, G. Belfort, Quantitative Flow Measurements in Bioreactors by Nuclear Magnetic Resonance Imaging, Nat Biotech. 8 (1990) 327–330. doi:10.1038/nbt0490-327.
[23] C.A. Heath, G. Belfort, B.E. Hammer, S.D. Mirer, J.M. Pimbley, Magnetic resonance imaging and modeling of flow in hollow-fiber bioreactors, AIChE J. 36 (1990) 547–558. doi:10.1002/aic.690360406.
[24] S. Yao, M. Costello, A.G. Fane, J.M. Pope, Non-invasive observation of flow profiles and polarisation layers in hollow fibre membrane filtration modules using NMR micro-imaging, Journal of Membrane Science. 99 (1995) 207–216. doi:10.1016/0376-7388(94)00219-O.
[25] H. Mallubhotla, G. Belfort, W.A. Edelstein, T.A. Early, Dean vortex stability using magnetic resonance flow imaging and numerical analysis, AIChE J. 47 (2001) 1126–1140. doi:10.1002/aic.690470519.
[26] I.E. Agranovski, R.D. Braddock, S. Crozier, A. Whittaker, S. Minty, T. Myojo, Study of wet porous filtration, Separation and Purification Technology. 30 (2003) 129–137. doi:10.1016/S1383-5866(02)00136-3.
[27] M.C.M. van Loosdrecht, L. Bereschenko, A. Radu, J.C. Kruithof, C. Picioreanu, M.L. Johns, et al., New approaches to characterizing and understanding biofouling of spiral wound membrane systems, Water Sci. Technol. 66 (2012) 88–94. doi:10.2166/wst.2012.096.
[28] S.A. Creber, J.S. Vrouwenvelder, M.C.M. van Loosdrecht, M.L. Johns, Chemical cleaning of biofouling in reverse osmosis membranes evaluated using magnetic resonance imaging, Journal of Membrane Science. 362 (2010) 202–210. doi:10.1016/j.memsci.2010.06.052.
[29] X. Yang, E.O. Fridjonsson, M.L. Johns, R. Wang, A.G. Fane, A non-invasive study of flow dynamics in membrane distillation hollow fiber modules using low-field nuclear magnetic resonance imaging (MRI), Journal of Membrane Science. 451 (2014) 46–54. doi:10.1016/j.memsci.2013.09.015.
[30] J. Frahm, A. Haase, D. Matthaei, Rapid NMR imaging of dynamic processes using the FLASII technique, Magn. Reson. Med. 3 (1986) 321–327. doi:10.1002/mrm.1910030217.
[31] M.A.B. Norbert J. Pelc, Encoding strategies for three-direction phase-contrast MR imaging of

flow. J Magn Reson Imaging, Journal of Magnetic Resonance Imaging : JMRI. 1 (1991) 405–13. doi:10.1002/jmri.1880010404.
[32] E.J.F. Dickinson, H. Ekström, E. Fontes, COMSOL Multiphysics®: Finite element software for electrochemical analysis. A mini-review, Electrochemistry Communications. 40 (2014) 71–74. doi:10.1016/j.elecom.2013.12.020.
[33] Simulation Optimization Software - Improve Your Engineering Designs, (n.d.). http://www.comsol.com/optimization-module#overview (accessed December 12, 2014).
[34] P. Ghosh, K. Vahedipour, M. Lin, J.H. Vogel, C. Haynes, E. von Lieres, Computational fluid dynamic simulation of axial and radial flow membrane chromatography: Mechanisms of non-ideality and validation of the zonal rate model, J. Chromatogr. A. 1305 (2013) 114–122. doi:10.1016/j.chroma.2013.07.004.

(This page is intentionally left blank)

CONCLUSION AND PERSPECTIVES

This PhD thesis focuses on membrane chromatography (MC) for biomolecules purification. Ion-exchange, being one of the most applied chromatographic modes (see Chapter 1), was selected to investigate MC performance for biomolecule separation using both experimental measurements and numerical simulations. The hydrodynamic and binding properties were studied in order to optimize the biomolecule separation and the MC device design. The conclusions and perspectives of this PhD thesis are summarized as followed.

In Chapter 2, three different scales of axial (Sartobind Q15, Q75 and Q100) and radial (Sartobind Nano 1 mL, Nano 3 mL, Mini) flow anion exchange MC devices (two of them having the same diameter, and two the same bed height) were experimental tested for bovine serum albumin (BSA) binding. The results obtained confirmed the advantage of MC, for which high flow rates can be operated without decreasing the dynamic binding capacity as usually observed using traditional resin columns. The flow rate is a significant factor for downstream purification, particularly in polishing steps, for which large volumes of diluted streams have to be treated. Operating at high flow rates can reduce significantly the operation cost of the process.

The comparison between axial flow and radial flow devices showed that lower pressure drops were obtained with axial flow devices than with radial flow devices at identical flow rates. When the membrane bed height was increased, a decrease in $DBC_{10\%}$ and DBC_{Total} was observed. Therefore, scaling-up by increasing the bed height should be avoided for both MC device configurations. This becomes a main limitation of axial flow devices, for which scaling-up relies upon increasing the bed height in order to maintain a high velocity. However, the packing and assemblies of the axial flow devices remains simple, which makes them more suitable at small laboratory scale. In addition, the radial flow devices can be scaled up by increasing the length of the radial flow column and not only the bed height. Radial flow devices can then be advised for large scale applications.

Chapter 3 is intended to develop a mathematical model using CFD for the prediction of hydrodynamics and breakthrough curves as obtained in Chapter 2. The internal geometry of the MC devices was visualized using MRI and reconstructed on Comsol Multiphysics software. The porous membrane was assumed to be one homogeneous region. The results showed that BSA binding breakthrough curves were predicted accurately by the CFD model with a bi-Langmuir equation. Using the same kinetic parameters, the BSA breakthrough curves were predicted at the different scales of the axial flow devices (Sartobind Q15 and Q100) and the radial flow devices (Sartobind Nano1mL, 3mL and Mini). This means there is no difference of binding adsorption mechanisms between the axial and radial flow devices due to the same type of functionalized group and membrane inside both devices. The difference in breakthrough curves between the axial and radial flow devices comes from the difference in flow pattern. Furthermore, the experimental breakthrough curves were broadened as a long time was needed to reach the BSA initial concentration. This tailing effect could be explained by the already adsorbed proteins, which reduced the accessibility of the binding sites or/and the non-uniform membrane porosity, membrane thickness, and ligand grafting impact. A binding model with two energetically levels of binding sites (bi-Langmuir model) was necessary to obtain an accurate

prediction of BSA breakthrough curves.

The CFD model gave much useful information, such as the breakthrough curves at different positions along the membrane bed height. Indeed, the breakthrough curves were found to be broadened with increasing bed height. This negative effect of bed height obtained from CFD simulations agreed with the experimental results obtained in Chapter 2. Non-uniform flow velocity along the bed height was found, which could be one of the reasons of this disadvantage of both axial and radial flow devices. A major challenge of MC device design is to optimize the flow distribution on the membrane surface and through the membrane height. Thus, the negative effect of the increasing membrane bed height could be avoided. Nowadays, many developments on MC device design have been reported. For example, a novel MC device with laterally fed was recently presented by Madadkar et al. as described in Chapter 1. -The CFD model could be further applied as a powerful tool to better understand the hydrodynamics in MC devices and thus improve their geometries.

In Chapter 4, the separation of a binary protein mixture of two similar size proteins (BSA and lactoferrin (LF)) was experimentally investigated using strong anion (Q) and cation (S) exchange MC devices. In milk, LF is a minor protein with several applications in nutritional and medical fields. At first, single protein and BSA-LF mixture binding were performed using Sartobind Q75 and S75 devices at pH between the LF and BSA isoelectric points. A good selectivity was observed with two distinct BSA and LF breakthrough curves. Identical breakthrough curves were obtained for a single protein solution and for the same protein contained in the binary mixture, which suggests that there is no competition between the two proteins at the binding sites. Next, the optimization of the entire BSA-LF separation was conducted. In particular, the different buffer (pH, ionic strength) and operating (flow rate, initial concentration ratio of BSA/LF) conditions were investigated to optimize the loading step. To improve the elution step, different interactions (pH change, increasing ionic strength and hydrophobic interaction) were tested at different operating flow rates. Operating the cleaning or regeneration steps at higher flow rates were shown to increase LF productivity. Consequently, high LF productivity and fast separation were obtained by combining different flow rates (high flow rate for the loading step, lower flow rate for the elution step).

This study confirms the potential of MC for the separation of proteins like LF. MC is an efficient process which could compete with other techniques at industry scale for biomolecule purification. However, several points remain to be clarified. First, the physical/chemical properties of LF and BSA were significantly affected by the type of buffer. In this study, a phosphate buffer was used and the interaction between phosphate and BSA was clearly observed at high phosphate concentration with a decrease in BSA binding capacity. Therefore, the effect of other buffer is another important point that should be further investigated. The optimized eluent found in this study had a high pH (12.0), which could modify the protein structure and its properties. The absence of protein denaturation is another interesting point to check. Other elution modes such as gradient elution with increasing eluent concentration versus time should also be tested as they could give a higher eluted amount of protein, compared to the isocratic mode used in this study. Moreover, for industrial applications such as whey treatment, lowering the price of the available MC devices would remain undoubtedly a major challenge. The development of low cost membranes and functionalized groups for MC is thus necessary.

In the last decades, membrane and monolith chromatography have appeared as two

alternative techniques to traditional chromatography, both being based on convective mass transport instead of internal diffusion. In Chapter 5, we compared membrane and monolith performance for the separation of BSA-LF mixture using the optimized operating conditions obtained in Chapter 4 with cation exchange MC devices. The membrane (Sartobind S, Sartorius) and monolith (CIM disks from BIA Separation, Slovenia) supports were placed in the same axial flow CIM housing in order to get rid of the effect of the housing. The CIM housing is designed to provide efficient flow distribution and optimized void volume. It uses porous frits to distribute the fluid over the chromatographic media. Other commercialized membrane (Sartobind S75) and monolith devices (CIMmultus) were compared. A higher LF binding capacity was obtained when the membrane was placed in the CIM housing, which suggests that the design was then more efficient. In addition, no effect of bed height was observed for this configuration. Lower LF binding capacities were obtained using the monolith in the CIM housing and the commercialized Sartobind S75 module. Besides, when eluting bound LF, a sharper and more symmetric elution peak was obtained using the membrane in the CIM housing.

The CFD model was further investigated to predict the LF breakthrough curves. For the monolith, the predicted results could match closely the experimental results when using a Langmuir isotherm, while a bi-Langmuir isotherm was required for the membrane to simulate the slow binding kinetic near saturation. The monolithic media is closer to an ideal adsorbent, with faster and steeper breakthrough curves, whereas the tailing effect of the membrane could be explained by steric interaction between already bound LF and available binding sites, which reduced their accessibility and thus binding kinetic. Moreover, the non-uniform membrane pore size and ligand density could be another reason, to explain why the bi-Langmuir equation was needed for the membrane.

Moreover, the solute concentration profiles inside the different devices were calculated using the CFD model. With the Sartobind S75 device and monolith column, some regions of the membrane or monolith were difficult to reach which could explain why lower LF binding capacities were obtained with these devices. Some regions of the monolith, and therefore some binding sites, were more difficult to reach due to non-ideal flow distribution at the inlet of the monolith device, because of the difference in diameter between the frits and monolith. Moreover, the solute concentration within the Sartobind S75 device was radially distributed due to the difference in inlet and membrane diameters, therefore the solute reached slowly to the peripheral region of the membrane.

In Chapter 6, the velocity field calculated using the CFD model was compared to the velocity measured using MRI velocimetry for both an axial and a radial flow device. Because of the complex internal geometry of the axial flow device (Sartobind Q75), MRI results were compared to 2D and 3D CFD simulation data. The flow inside the radial flow device (Sartobind Nano 1 mL) was also investigated. A good agreement between the three velocity fields was obtained. It was then concluded that the 2D CFD simulation using the simplified 2D geometry was sufficient for accurate velocity prediction. From this 2D model, other quantities could be further calculated for breakthrough curves prediction.

From these results, limitations and advantages of MRI velocimetry and CFD simulation for the characterization of hydrodynamics in MC devices are discussed. CFD is powerful simulation tool which requires the knowledge of the internal geometry of the MC device. A complex geometry requires long times to be reconstructed on the software's interface. Moreover, the CFD

simulation within complex geometries remains a challenge due to the very large computational grid requirement and long calculation time. The validation of CFD results is sometimes ambiguous and difficult. Although, CFD gives very useful information that are difficult to access from experiments (i.e. sheer stress, pressure field, local concentration, etc.). In parallel, MRI velocimetry is a powerful method to obtain flow distribution in complex and opaque media. MRI velocimetry can show some non-ideal properties of the MC devices (i.e. presence of bubbles, non-uniform stack, membrane compression, etc.), which are not predictable by the CFD model. However, this technique is restricted to object with limited size or field of view. In addition, the scanning and encoding sequences of the MRI technique require specialist support to realize the experiments and to obtain accurate data. Supplementary knowledge on the raw image data is necessary with the imaging software skill. Due to the small amount of fluid inside the porous membrane regions, long acquisition time are required to obtain images with good resolution. Overall, it can be concluded that MRI velocimetry and CFD modeling are complementarily to obtain an exact geometry further used in CFD and to an experimental velocity field which has to be to be in agreement with the calculated velocity field.

In the future, we plan to develop the CFD model to predict more complex purification such as those found in the biopharmaceutical industry, such as DNA and monoclonal antibody purification. It will be a challenge to predict the binding behavior of a mixture of several components on the binding sites of the MC device, as competitive adsorption will have to be taken into account. It will be also interesting to predict the entire separation process including the washing and elution steps using the CFD model. The modeling and experimental characterization of elution in different operating modes (i.e. isocratic and gradient elution) will have to be studied in details to improve the biomolecule separation efficiency. In addition, the biomolecule size has been reported previously to influence the binding behavior in MC, in particularly biomolecules of small size have been shown to give lower binding capacities. The influence of the biomolecule size in MC deserves to be studied using both experimental and modeling approaches. In particular, a mathematical model with additional physical-chemical interactions between biomolecules and the membrane support is needed in order to predict the effect of the molecular size.

APPENDICES

(This page is intentionally left blank)

List of figures

Chapter 1

INTRODUCTION AND THESIS BACKGROUND

Chapter 2

EFFECT OF GEOMETRY AND SCALE FOR AXIAL AND RADIAL FLOW MEMBRANE CHROMATOGRAPHY - EXPERIMENTAL STUDY OF BOVIN SERUM ALBUMIN (BSA) ADSORPTION

Chapter 5

COMPARISON OF MEMBRANE CHROMATOGRAPHY AND MONOLITH CHROMATOGRAPHY FOR LACTOFERRIN AND BOVINE SERUM ALBUMIN SEPARATION

Chapter 6

VALIDATION OF COMPUTATIONAL FLUID DYNAMICS MODEL FOR AXIAL AND RADIAL FLOW MEMBRANE CHROMAGRAPHY DEVICES USING NUCLEAR MAGNETIC RESONANCE

(This page is intentionally left blank)

List of tables

Chapter 5

COMPARISON OF MEMBRANE CHROMATOGRAPHY AND MONOLITH CHROMATOGRAPHY FOR LACTOFERRIN AND BOVINE SERUM ALBUMIN SEPARATION

Publications

(This page is intentionally left blank)

Publications

C. Teepakorn, C. Charcosset, K. Fiaty, **Adsorption de biomolécules par membrane échangeuse d'ions: Etude expérimentale et modélisation**, Comptes rendus chimie. Article submitted.

C. Teepakorn, K. Fiaty, C. Charcosset, **Optimization of lactoferrin and bovine serum albumin separation using ion-exchange membrane chromatography**, Separation and. Purification Technology. 151 (2015) 292–302.

C. Teepakorn, K. Fiaty, C. Charcosset, **Effect of geometry and scale for axial and radial flow membrane chromatography—Experimental study of bovin serum albumin adsorption**, Journal of Chromatography A. 1403 (2015) 45–53.

(This page is intentionally left blank)

Journal of Chromatography A, 1403 (2015) 45–53

Contents lists available at ScienceDirect

Journal of Chromatography A

journal homepage: www.elsevier.com/locate/chroma

Effect of geometry and scale for axial and radial flow membrane chromatography—Experimental study of bovin serum albumin adsorption

Chalore Teepakorn, Koffi Fiaty, Catherine Charcosset*

Laboratoire d'Automatique et de Génie des Procédés (LAGEP), Université Claude Bernard Lyon I, 43, bd du 11 Novembre 1918, Bâtiment CPE, 69622 Villeurbanne Cedex, France

ARTICLE INFO

Article history:
Received 19 March 2015
Received in revised form 12 May 2015
Accepted 12 May 2015
Available online 21 May 2015

Keywords:
Membrane chromatography
Breakthrough curve
Dynamic binding capacity
Axial flow chromatography
Radial flow chromatography

ABSTRACT

During the last 10 years, membrane chromatography (MC) has been increasingly reported for biomolecule purification at both small and large scales. Although, several axial and radial flow MC devices are commercialized, the effect of the device dimensions on the adsorption performance has not been fully investigated. In this study, axial and radial flow anion ion-exchange MC devices were used for bovine serum albumin (BSA) adsorption. For both axial and radial flow, three devices at different scales were compared, two having similar diameter and two similar bed height. The pressure drop and the flow distribution using acetone as a non-binding solute were measured, as well as BSA breakthrough curves at different flow rates and BSA loading concentrations. For all devices, it was observed that the flow rate had no effect on the breakthrough curve, which confirms the advantage of MC to be used at high flow rates. In addition, the BSA binding capacity increased with increasing BSA concentration, which suggests that it could be preferable to work with concentrated solutions rather than with very dilute solutions, when using buffer at high phosphate concentration. For both axial and radial flow, the bed height had a negative impact on the binding capacity, as the lowest binding capacities per membrane volume were obtained with the devices having the highest bed height. Radial flow MC has potential at large-scale applications, as a short bed thickness can be combined with a large inlet surface area.

1. Introduction

Membrane chromatography (MC) was introduced in the late 1980s as a novel chromatographic technique based on the integration of membrane filtration and liquid chromatography into a single-step operation [1]. From the beginning of the 1990s, MC has been extensively designed and evaluated in different geometries such flat sheet systems and stacks of membranes, hollow fibers, radial flow cartridges, and different interaction modes including affinity interaction, ion exchange, hydrophobic interaction, reversed-phase and multistage chromatography [2–5]. Nowadays, MC is being employed for the purification and polishing of a large range of biomolecular species, including purification of monoclonal antibodies, DNA, and virus capture. MC devices are commercially available from several suppliers, ranging from laboratory scale to process scale.

The benefit of MC over conventional resin chromatography is mainly attributed to the shorter diffusion times, as the interactions between molecules and active sites in the membrane occur in convective through-pores rather than in stagnant fluid inside the pores of the adsorbent particles. Therefore, MC has the potential to maintain high efficiencies both at high flow rates and for use of large biomolecules with small diffusivities, reducing biomolecules degradation and denaturation. Low pressure drop associated with high flow rate, as compared to packed bed chromatography, reduced buffer usages due to low void volume and scalability for process development are other key advantages of MC. In addition, MC devices can be used as single-use units to eliminate the requirement for cleaning and regeneration and to reduce contamination risk. It has been estimated that single-use techniques can reduce by up to 40% the capital costs of production facilities in the biopharmaceutical manufacturing. Its advantages have made MC to have the highest market growth among all commercial disposable devices, such as mixing systems and bioreactors, with an annual growth rate of nearly 27% between 2006 and 2012 [6].

MC devices are often characterized by the shape of their breakthrough curves. The breakthrough curve shape is governed by

* Corresponding author. Tel.: +33 4 72 43 18 34.
E-mail address: charcosset@lagep.univ-lyon1.fr (C. Charcosset).

http://dx.doi.org/10.1016/j.chroma.2015.05.023
0021-9673/

adsorption kinetics within the functionalized membrane and by fluid hydrodynamics in the hold-up volumes of the MC devices. Commercial MC devices are optimized such as to obtain breakthrough curves that are as sharp as possible, in order to minimize buffer consumption and to maximize the utilized membrane capacity. Significant developments in MC devices have been obtained by considering advanced materials [7,8], polymer grafting of the surface of the pore walls [9,10], fluid flow distribution and collection within the MC device [11,12], as well as optimized geometry [13,14].

The scaling up of MC devices has been reported in several studies. For example, Briefs and Kula [15] increased the membrane diameter from 90 mm to 142 mm of a stack of 96 membranes without any change in the anion exchange membrane capacity. Using devices having two different diameters of 15 and 25 mm, a good resolution was obtained compared to DEAE-Sephacel gel for pyruvate decarboxylase purification. Huang et al. [16] investigated the radial flow MC devices made from modified cellulose for trypsin removal. The trypsin binding capacity was found linearly related to the bed volume for 250, 800 and 3200 ml devices. Puthirasigamany et al. [17] measured the binding capacity of two Nano Sartobind Q devices with different bed volume: 1 ml and 3 ml. For the 3 ml device, the dynamic binding capacity per unit of membrane volume was found around 20% lower than the one obtained with the 1 ml device, although this result was not discussed. Ghosh et al. [14] used two MC devices with a scale-up factor of 15,000: an axial flow Sartobind Pico MC capsule with 0.08 ml bed volume and a radial flow Sartobind 1.2 l MC capsule. A simulation based on CFD and on the spreading binding model was developed for analyzing MC at the very small scale, and transferring the identified binding mechanism and parameters for predicting the performance of the very large scale device. These authors underlined that the introduction of appropriate flow distribution and binding mechanism for each device was necessary to obtain a good fit between modeling and experimental values.

The effect of membrane diameter and bed height of membrane absorbers has also been investigated by some authors. For example, Josić et al. [18] used anion exchange MC devices made from poly(glycidyl methacrylate) membranes for separations of standard proteins. The thickness of the membrane layers was between 1 and 7 mm and the disc diameter between 10 and 50 mm. The results obtained showed that with increasing thickness better separation was achieved. The separation obtained with a 10 mm diameter disc could also be achieved with a 50 mm diameter disc. Knudsen et al. [13] determined the breakthrough capacities of Sartobind cation-exchange membranes as a function of layer number, from 1 to 60. The continued rise in breakthrough capacity was explained by the inefficient flow distribution within the MC devices and/or the housing and the experimental system.

The comparison between axial and radial flow has been little studied using MC devices. For example, Ghosh et al. [14] used two MC devices: an axial flow Sartobind Pico MC capsule and a radial flow Sartobind 1.2 l MC capsule. However, due to the very different scales, the comparison between the two devices was difficult. On the contrary, comparison of radial flow over axial flow chromatography using traditional resin columns has been largely investigated (e.g. Besselink et al. [19], Tharakan [20]). A radial flow column typically consists of two concentric cylinders between which the resin bed is packed. The liquid is directed from outside inwards or vice versa, resulting in horizontal, radial flow. In a recent study, Besselink et al. [19] compared axial and radial flow affinity chromatography using columns packed with affinity resin to adsorb BSA. No difference in performance between the two columns was observed. The authors concluded that for small-scale processes, axial flow chromatography may be preferable, for resin volumes of at least several tens of litres, radial flow chromatography is probably the best choice. Unlike radial flow chromatography, axial flow chromatography has significant limitation of scaling up because high volumes can be obtained by varying only the membrane diameter, while the bed height is maintained constant. Higher scalability is obtained using radial flow geometry by increasing both column height and diameter [20].

In this work, the effect of axial and radial flow, membrane area, membrane diameter, and bed height on the MC device performance is investigated. Commercialized strong anion ion-exchange MC is used for bovine serum albumin (BSA) adsorption. For both axial and radial flow, three devices with different membrane area are tested, two having similar diameter, and two similar bed height. The flow distribution is first observed under a non-binding condition loading an acetone solution. BSA breakthrough curves are then compared at different flow rates and BSA loading concentrations. The dynamic binding capacity at 10% breakthrough is calculated and compared for the various devices. Finally, the effect of flow configuration, dimensions of MC devices on flow distribution and binding capacity is discussed.

2. Materials and methods

2.1. Materials

BSA lyophilized powder (≥98.00% purity) was purchased from MP Biomedical (France). BSA was dissolved in a phosphate buffer prepared from 100 mM solution of K_2HPO_4 and KH_2PO_4, adjusted to pH 7.0. The elution buffer was phosphate buffer saline (PBS), prepared by adding 1 M NaCl to the above buffer, and adjusted at pH 7.0. The washing and regeneration buffers were 1 M NaOH. Except BSA, all chemical reagents used in this study were purchased from Sigma Aldrich (France). Ultra-pure water was obtained using a Milli-Q system (Millipore, France). Prior to use, all buffer solutions were filtered through a hydrophobic membrane filter with a 0.45 μm pore size (Millipore, France). A 0.22 μm polyethersulfone hydrophilic Millex-GP filter unit (Millipore, France) was set-up before the MC device to remove fine particles from solutions during the experiments.

The experiments were carried out on the Äktaprime Plus chromatography system (GE Healthcare Life Sciences, France), which includes a system pump, a fraction collector, a pressure sensor, and monitors for UV and conductivity. Valves for buffer selection, sample injection, gradient formation, and flow diversion are integrated into the system.

2.2. Strong anion ion exchange MC

All MC devices were obtained from Sartorius Stedim Biotech GmbH (Goettingen, Germany). They contain a stabilized reinforced cellulose membrane with thickness 275 μm and pore size around 3–5 μm. Functionalized quaternary ammonium (Q) groups are bound covalently to a grafted polymer layer.

The characteristics of the MC devices provided by the manufacturer are summarized in Table 1. For each radial flow devices, the outer diameter and the cylindrical height were obtained from the nuclear magnetic resonance (NMR) technique. For both axial and radial flow, three different devices were investigated. The flow configuration is shown in Fig. 1. Axial flow devices are composed of several stacked membrane sheets in capsules. The flow goes from top through the membrane bed to the outlet. Inside radial flow devices, the membrane is in the form of spiral wound or rolled around a cylindrical core. The flow pattern is from outside of the membrane cylinder through the membrane bed to the inside core of the membrane cylinder. The superficial velocity was determined as the flow rate divided by the cross-sectional area of the bed, that

Table 1
Characteristics of the radial and axial flow MC devices.

	Axial flow MC			Radial flow MC		
	Sartobind Q15	Sartobind Q75	Sartobind Q100	Sartobind Nano 1 ml	Sartobind Nano 3 ml	Sartobind Mini
Ligand				$R\text{-}CH_2\text{-}N^+(CH_3)_3$		
Membrane bed volume (ml)	0.41	2.10	2.80	1.00	3.00	7.00
Void volume (ml)	1.00	1.30	4.20	5.00	4.00	20.0
Bed height H_B (mm)	0.8	4.0	1.4	4.0	8.0	4.0
Membrane bed diameter D_m (mm)	25.0	25.0	50.0	22.0[a]	26.0[a]	36.0[a]
Spiral wound height L (mm)	–	–	–	6.5[a]	8.0[a]	30.0[a]
Membrane area (cm^2)	15.0	75.0	100.0	36.4	110.0	250.0
Number of layers	3	15	5	–	–	–

[a] Dimensions obtained from the nuclear magnetic resonance (NMR) technique.

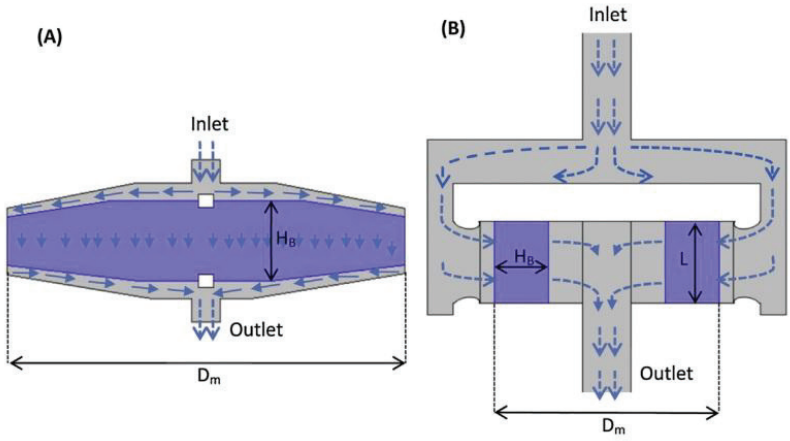

Fig. 1. Geometry and flow paths of: (A) axial flow MC (Sartobind Q 75), and (B) radial flow chromatography (Sartobind Nano 1 ml).

is to say $(\pi/4)D_m^2$ for the axial flow devices and πLD_m for the radial flow devices.

2.3. Breakthrough curves under non-binding conditions

The system dispersion curve was measured using a phosphate buffer containing 5.00 v.% acetone. Similarly to binding experiments, the non-binding breakthrough curves were monitored by reading the UV absorbance at 280 nm. A wash step was then performed using a 100 mM phosphate buffer at pH 7.0.

The non-binding breakthrough curves were fitted to **Eq. 1** to determine the Peclet number (*Pe*) using least squares regression [7,21]. In **Eq. 1**, c is the outlet effluent concentration, c_0 is the solute loading concentration, $V_{loading}$ is the volume of acetone solution loaded, and V_{50} is the loaded volume when $c/c_0 = 0.50$. The dimensionless number *Pe* is the ratio between the rate of convective flow (mean velocity, *u*, multiplied by bed height, *L*) and the rate of diffusive flow (axial dispersion, *D*).

$$\frac{c}{c_0} = \frac{1}{2}\left\{1 + erf\left(\frac{Pe^{1/2}(V_{loading} - V_{50})}{2(V_{loading}V_{50})^{1/2}}\right)\right\} \quad (1)$$

High *Pe* values are associated with uniform distribution of flow to the inlet surface of the MC device as well as uniform distribution of the binding site properties. Low *Pe* number values are associated with poor flow distribution, large flow dispersive characteristics of the MC devices, and/or large binding mechanism distribution [21].

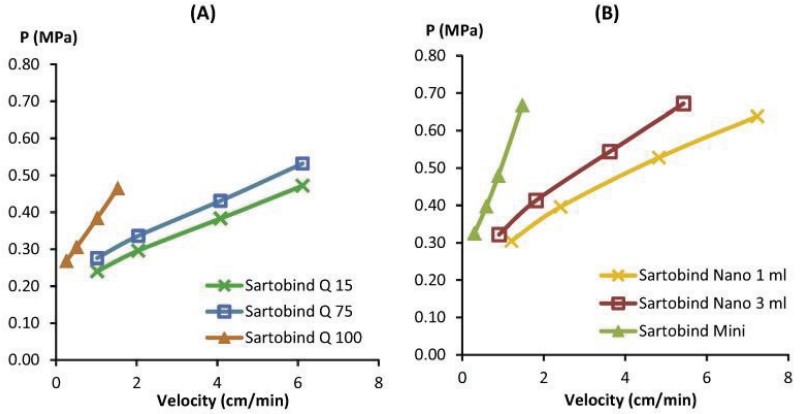

Fig. 2. Operational pressures at different superficial velocities for the different scales of: (A) axial flow devices and (B) radial flow devices.

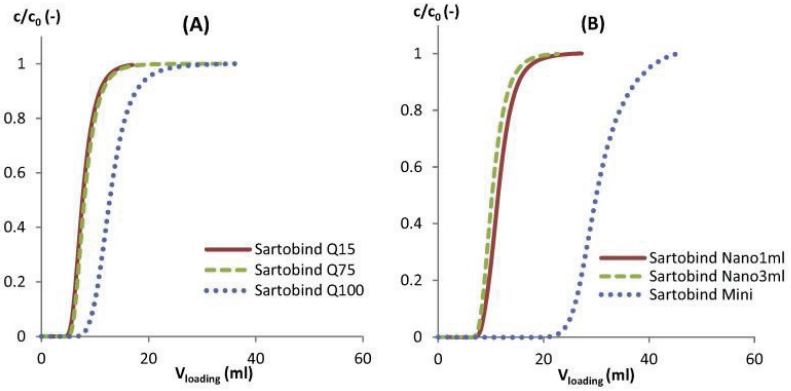

Fig. 3. Non-binding breakthrough curves: (A) axial flow devices and (B) radial flow devices at a flow rate of 10 ml/min and acetone loading concentration of 5 v.%.

Table 2
Peclet numbers, velocities and dead volumes of the MC devices and external system measured at the flow rate of 5 ml/min under a non-binding condition with 5 v.% of acetone. The dead volume, V_0, was obtained, when the breakthrough concentration reached to 10%.

Membrane chromatography modules	Axial flow module			Radial flow module		
	Sartobind Q 15	Sartobind Q 75	Sartobind Q 100	Sartobind Nano1 ml	Sartobind Nano3 ml	Sartobind Mini
Dead volume of MC device and external system-V_0 (ml)	5.94	6.25	9.75	8.88	8.25	25.28
Superficial velocity (cm/min)	1.02	1.02	0.25	1.20	0.90	0.15
Pe (–)	33	33	35	45	46	77

In addition to the determination of *Pe* numbers, the non-binding experiments were used to determine the dead volume of the experimental set-up and device, V_0, from the breakthrough at 10%.

2.4. Protein dynamic adsorption

BSA breakthrough curves were measured at different BSA concentrations (0.5, 2.0, 4.0 and 8.0 mg/ml) and flow rates (5.0, 10.0, 20.0, 30.0 ml/min). After the loading step, the membrane was washed using 1 M NaOH solution for 1 h at a flow rate of 1 bed volume (BV)/min, followed by the elution and phosphate buffers for 10 BV of each.

To compare the adsorption performance of the different MC devices, the dynamic binding capacity at 10% breakthrough ($DBC_{10\%}$) was calculated using **Eq. 2**, where c is the BSA outlet concentration, c_0 is the BSA loading concentration, $V_{10\%}$ is the loading volume of BSA solution when $c/c_0 = 0.10$ and V_0 is the dead volume of the MC device and external system. In addition, the dynamic binding capacity at total breakthrough (DBC_{Total}) was determined using **Eq. 3**.

$$DBC_{10\%} = \int_0^{V_{10\%}} (c_0 - c)\, dV_{loading} - c_0 V_0 \quad (2)$$

$$DBC_{Total} = \int_0^{V_{Total}} (c_0 - c)\, dV_{loading} - c_0 V_0 \quad (3)$$

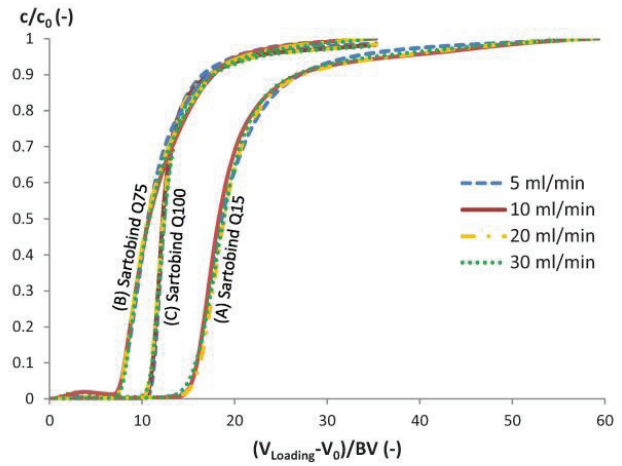

Fig. 4. BSA breakthrough curves of the axial flow devices: (A) Sartobind Q15, (B) Sartobind Q75, and (C) Sartobind Q100 at different flow rates 5, 10, 20 and 30 ml/min.

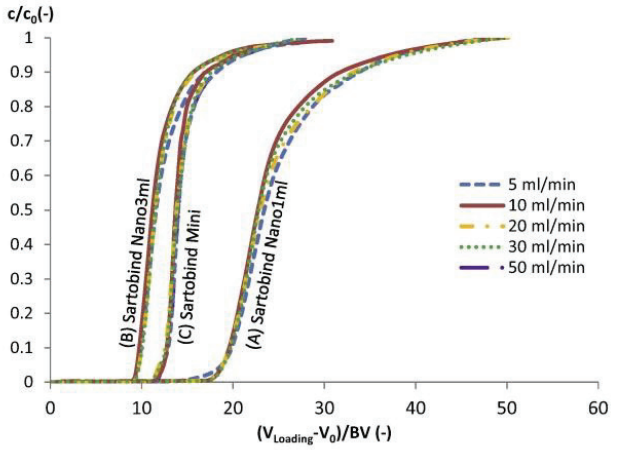

Fig. 5. Breakthrough curves of the radial flow devices; (A) Sartobind Nano 1 ml (B) Sartobind Nano 3 ml, and (C) Sartobind Mini at different flow rates 5, 10, 20, 30 and 50 ml/min.

3. Results and discussion

3.1. Operational pressure

Fig. 2 shows the operational pressure (P) as a function of superficial velocity for the different devices. The pressures were lower than 0.6 MPa and 0.7 MPa for axial flow and radial flow devices, respectively. This low pressure is a major advantage of MC and is due to the large membrane pore size around 3–5 μm. Both axial and radial flow devices show similar pressure values, as well as similar effect of velocity. For all devices, the operational pressure increased almost linearly with increasing superficial velocity, which has been also reported previously, e.g. with nylon-based microporous membranes from Pall of two different mean pore size 1.2 and 3 μm [15], radial flow cartridges made of modified cellulose [16] and Sartobind Q Nano 1 ml and 3 ml [17].

For axial flow devices, the effect of bed height can be seen by comparing the operational pressure obtained with the Sartobind Q75 device (bed height 4 mm) to the Q15 device (bed height 0.8 mm). Fig. 2 shows that the pressure was slightly higher with the Sartobind Q 75 device. In addition, much lower velocities were obtained with the Sartobind Q100 device due to its larger cross-section area.

For radial flow geometry, the increase in operational pressure with bed height can be seen with the Sartobind Nano 3 ml device (bed height 8 mm) compared to the Nano 1 ml devices (bed height 4 mm). The Sartobind Nano 1 ml and Nano 3 ml devices showed similar superficial velocity, due to similar cross-section area. Identically to the axial flow devices, the lowest velocities were obtained with the Sartobind Mini device, which has the largest cross-section area. However, similar operational pressures to the one of the Sartobind Nano 1 ml were obtained due to their identical bed height (4 mm).

3.2. Flow distribution analysis

For each device, the acetone breakthrough curve was measured under non-binding conditions. Fig. 3 shows that the acetone breakthrough curves obtained for both axial (Sartobind Q 15 and Q75) and both radial flow devices (Sartobind Nano 1 ml and 3 ml) were identical. For the two larger devices, Sartobind Q 100 and Mini, the breakthrough occurred later due to their larger void volumes.

Pe values were estimated from **Eq. 1** and summarized in Table 2. For axial flow devices, Pe values were almost identical, between 33 and 35. The radial flow devices led to higher Pe, between 45 and 77. As mentioned previously, higher Pe are preferred as they are associated with uniform distribution of flow to the inlet surface of the MC device as well as uniform distribution of the binding site properties. Phillips [21] stated that for higher Pe values, such as above 100, the breakthrough curve begins to approach ideality and breakthrough corresponds to the capacity of the device, i.e. high efficiency. Considering the Pe criteria, our results suggest that the

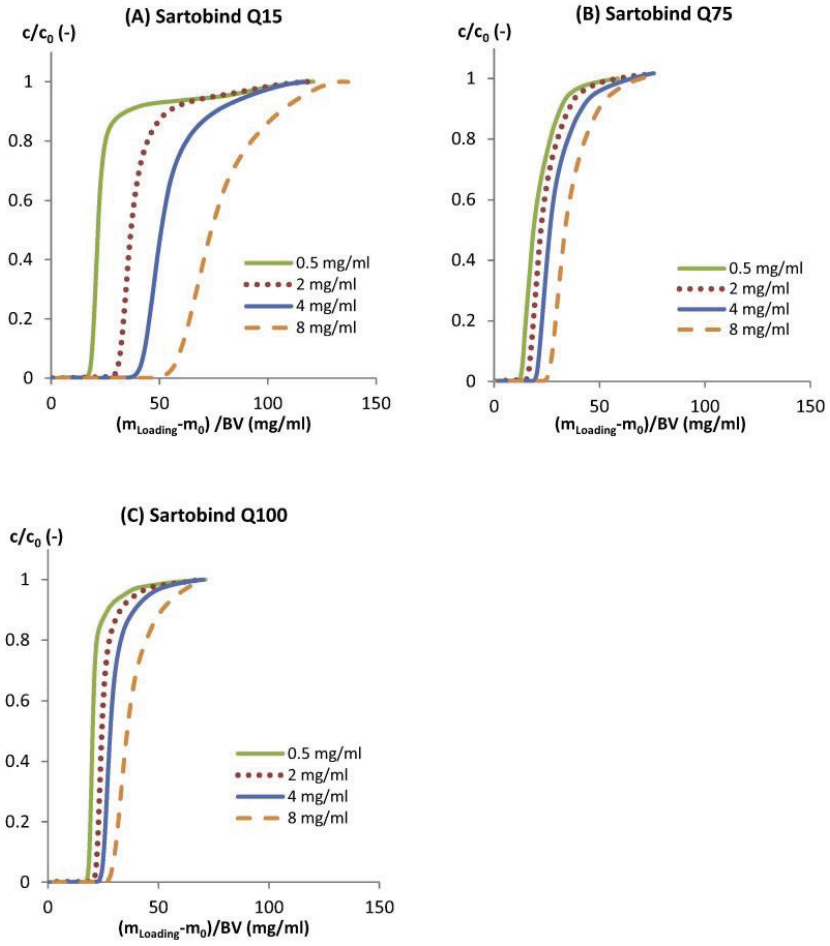

Fig. 6. Experimental breakthrough curves of the axial flow devices: (A) Sartobind Q 15, (B) Sartobind Q 75, and (C) Sartobind Q 100 under different BSA loading concentrations at 0.5, 2.0, 4.0 and 8.0 mg/ml.

radial flow devices are more efficient than the axial ones. *Pe* values of 102 and 88 were reported by Schneiderman et al. [7] when using MC devices Mustang S (Pall Corporation) and homemade nanofiber supports, respectively. Using commercial MC devices, Phillips [21] measured *Pe* numbers on the order of 20 and 100. Therefore, our *Pe* values were in the range of previously reported data for MC devices.

3.3. BSA breakthrough curves at different operating conditions

The obtained BSA breakthrough curves showed the same shape as usually observed (i.e. van Beijeren et al. [22], Puthirasigamany et al. [17]. The shape of the BSA breakthrough curves was not rectangular, as it would happen for an ideal adsorbent [22], but was initially steep and became gradually broader. One reason for such a behavior is usually admitted to be dispersion effects due to pore size and length distribution. Another reason could be the slow adsorption kinetic on the grafted polymer layers at the membrane surface. The amount of BSA that breakthrough at a certain point loaded depends on the amount of already adsorbed proteins. Thus, the adsorption of BSA seems to reduce the accessibility of the binding sites and increases mass transport limitations [22].

3.3.1. BSA adsorption at different flow rates

To observe the influence of flow rate on BSA breakthrough curves, dynamic adsorption experiments were performed at flow rate between 5.00 ml/min and 30.0 ml/min, except for the Sartobind Mini device for which the flow rate was set between 10.0 and 50.0 ml/min. The BSA loading concentration was maintained at 2.00 mg/ml. The experimental breakthrough curves obtained were plotted against the BSA loading volume minus the dead volume (V_0), divided by BV for the axial flow devices (Fig. 4) and the radial flow devices (Fig. 5). For both axial and radial flow devices, and even for the larger scales, the breakthrough curves were unaffected by flow rate from 5 to 30 ml/min (50 ml/min for the radial flow Mini device). This confirms that it is possible to obtain high throughput using MC without any flow rate effect. The absence of flow rate effect on the experimentally observed breakthrough curves has been reported previously, for MC devices (e.g. Knudsen et al. [13], van Beijeren et al. [22], Puthirasigamany et al. [17]). This phenomenon is generally explained by the absence of diffusive transport limitation.

The lowest residence time of the mobile phase in the void volume, which was measured loading acetone solution as an inert tracer, was obtained with the Sartobind Q 15 device at the flow rate of 30 ml/min and was equal to 2.00 s. This confirms the high rate of mass transport in MC devices in comparison to conventional resins, where residence times of several minutes are required to obtain sufficient dynamic binding capacities. The residence time of 2.00 s is slightly lower than that reported at 3.12 s by van Beijeren et al. [22] using a Sartobind Q75 device.

3.3.2. BSA adsorption at different BSA loading concentrations

The effect of BSA loading concentration on breakthrough curves was studied at 0.5, 2, 4 and 8 mg/ml BSA, except for the largest radial

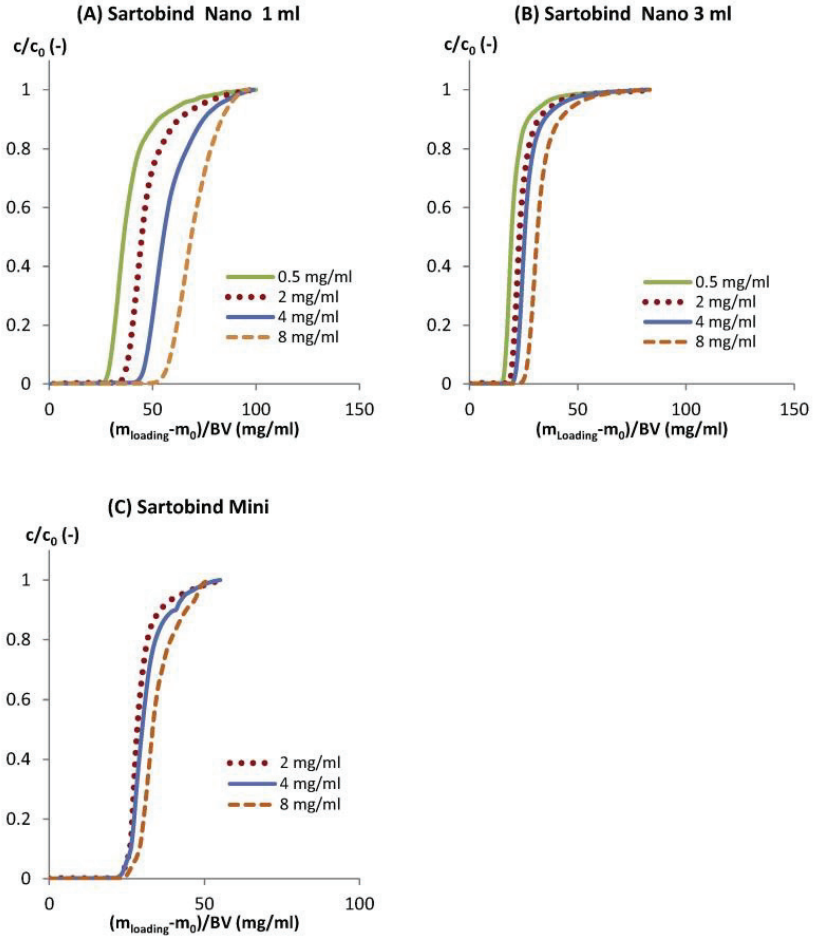

Fig. 7. Experimental breakthrough curves of the radial flow devices: (A) Sartobind Nano 1 ml, (B) Sartobind Nano 3 ml, and (C) Sartobind Mini under different BSA loading concentrations at 0.5, 2.0, 4.0 and 8.0 mg/ml.

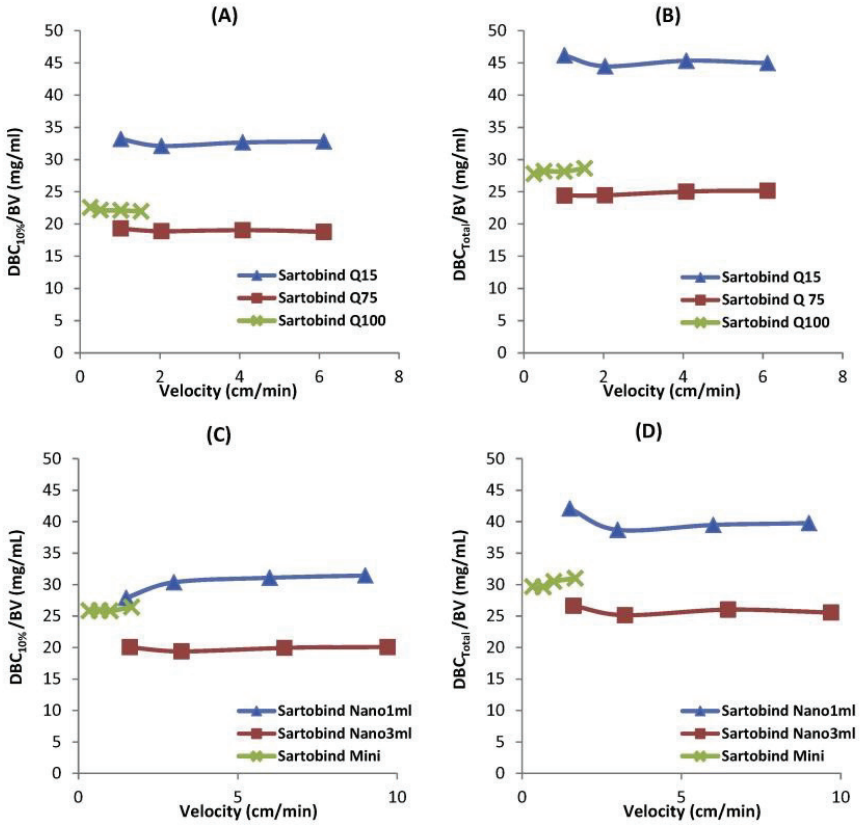

Fig. 8. Effect of flow rate for the axial flow devices: (A) dynamic binding capacity at 10% of breakthrough ($DBC_{10\%}$) per bed volume and (B) dynamic binding capacity at total breakthrough (DBC_{Total}) per bed volume. For the radial flow devices: (C) $DBC_{10\%}$/BV and (D) DBC_{Total}/BV. BSA loading concentration 2.0 mg/ml.

flow device (Sartobind Mini) for which the lower BSA concentration of 0.5 ml/min was not tested. The flow rate was maintained at 10 ml/min. The breakthrough curves were compared by plotting c/c_0 as a function of the loading mass of BSA corrected for the BSA mass loss in the void volume (m_0)/BV, i.e. the loading volume of BSA solution ($V_{loading}$) corrected by V_0, multiplied by the inlet concentration (c_0) and divided by BV.

Fig. 6 and Fig. 7 show the BSA breakthrough curves at different BSA feed concentrations, for the axial and radial flow devices, respectively. For both geometries, the shape of the breakthrough curves was unaffected by the feed concentration. However, for all devices, the breakthrough curves appeared earlier at lower loading concentrations. This effect was already observed, i.e. for the adsorption of BSA on a Sartobind Q device: below 1 mg/ml BSA feed concentration, breakthrough occurred earlier at low feed concentrations. The difference in dynamic capacity at different BSA concentrations may be due to the high amount of phosphate (100 mM) present. The strong anion exchanger is usually in the OH-form, and has a high preference for phosphate ions. With increasing BSA concentration, the preference for BSA over phosphate ions

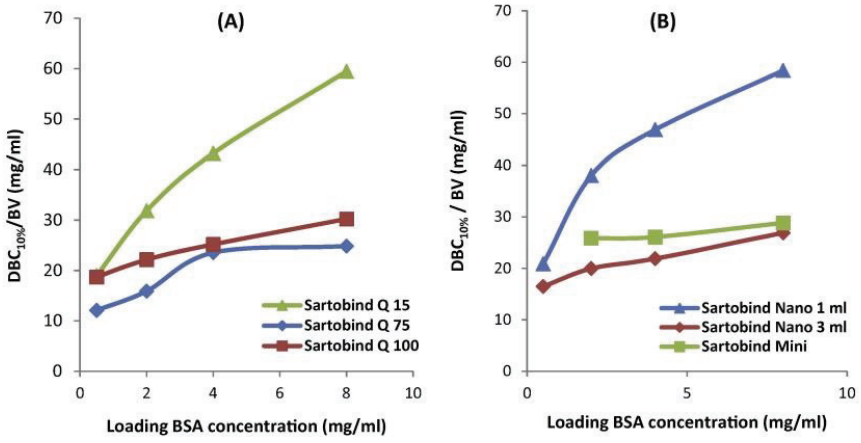

Fig. 9. Effect of BSA loading concentration for axial flow devices on the dynamic binding capacity at 10% of breakthrough ($DBC_{10\%}$) per bed volume for (A) axial flow MC and (B) radial flow MC. Flow rate 10 ml/min.

shifts resulting in a later breakthrough and higher dynamic capacity. Van Beijeren et al. [22] also reported an increasing in BSA binding capacity with increasing BSA loading concentration and decreasing the acetate buffer concentration.

3.4. Dynamic binding capacity

For each device, the dynamic binding capacities at 10% breakthrough ($DBC_{10\%}$) and at the end of the loading step (DBC_{Total}) were determined from the breakthrough curves obtained at different flow rates. $DBC_{10\%}$ and DBC_{Total} divided by the BV were plotted as a function of superficial velocity in Fig. 8. As mentioned previously, the BSA dynamic capacity remained almost constant as a function of flow rate for both axial and radial flow and for each scales.

For axial and radial flow devices, the highest capacities $DBC_{10\%}$ and DBC_{Total} were obtained for the devices with the lowest bed volume (respectively, Sartobind Q 15 and Nano 1 ml). In addition, for axial flow, the capacity of the Q 75 device (bed height 4 mm, bed volume 2.10 ml) was found lower than the Q 100 device (bed height 1.4 mm, bed volume 2.80 ml). A similar effect was observed with the radial flow devices, where the binding capacity of the Nano 3 ml device (bed height 8 mm, bed volume 3.00 ml) was lower than that of the Mini device (bed height 4 mm, bed volume 7 ml). This effect was already observed by Puthirasigamany et al. [17] for the 3 ml device, the BSA binding capacity per unit of membrane volume was found around 20% lower than the one obtained with the 1 ml device. Thus, the bed height appears as a main parameter for MC device design: an increase in bed height (from 1.4 to 4 mm for axial flow and from 4 to 8 mm for radial flow) decreases the binding capacity. This effect is probably due to the more difficult access of molecules to binding sites at the bottom of the thicker membrane.

Similar binding capacities were found with both axial and radial flow devices: around 40–45 mg/ml for the smallest Q 15 and Nano 1 ml device, and around 25 mg/ml for the two intermediate devices Q75 and Nano 3 ml. For the Sartobind Q 75 device, the observed binding capacity of for BSA at 10% breakthrough was 20 mg/ml, which increased to 25 mg/ml at the end of loading. The first value was very close to the one reported by Van Beijeren et al. [22] for the same MC device (19.1 mg/ml). Moreover, for the Nano 1 ml and 3 ml, the observed binding capacity of for BSA at 10% breakthrough was respectively equal to 31 and 20 mg/ml. These values are in agreement with the ones obtained by Puthirasigamany et al. [17], who found respectively around 32 and 25 mg/ml.

The dynamic binding capacity was also measured as a function of BSA loading concentration. Fig. 9 shows the concentration effect for the different axial and radial flow devices. For the smallest bed volume devices, Sartobind Q 15 and Nano 1 ml, the $DBC_{10\%}$ increased significantly with the BSA loading concentration. The $DBC_{10\%}$ at 0.5 mg/ml were 19 and 21 mg/ml for the Sartobind Q 15 and Nano 1 ml devices, respectively. At 8 mg/ml, these values increased to 59.4 and 58.4 mg/ml, corresponding to an increase in binding capacity of 213% and 178%, as the initial concentration increased. As previously explained, a higher BSA concentration in the phosphate buffer (100 mM) led to an increase in $DBC_{10\%}$/BV.

The binding capacity per BV was less important for the intermediate (Sartobind Q 75 and Nano 3 ml) and larger scale devices (Sartobind Q 100 and Mini). Moreover, the observed breakthrough curves at loading concentration between 0.5 and 8 mg/ml confirms the result obtained previously at a concentration of 2 mg/ml. At these various loading concentrations, the binding capacities were lowest with the Sartobind Q 75 and Nano 3 ml devices, due to their higher bed height, respectively 4 and 8 mm.

3.5. Scaling-up of MC devices

For both axial and radial flow, Fig. 10 demonstrates the $DBC_{10\%}$ values as a function of bed volume at different velocities. The $DBC_{10\%}$ values provided by the manufacturer were obtained with the Sartobind Q 15 device at 10 ml/min with BSA in 20 mM Tris/HCL and pH at 7.5. This value (12 mg/unit) compared well with the one obtained in the present study (13 mg/unit). The same result was obtained with the Nano 1 ml device. At the same experimental conditions, the values provided by the manufacturer (29 mg/unit) compared well with the one obtained in this study (30 mg/unit).

From Fig. 10, it can be seen that the experimental $DBC_{10\%}$ increased nonlinearly as a function of bed volume. Moreover, the difference between experimental and $DBC_{10\%}$ values provided by the manufacturer was larger with the axial flow devices than with the radial flow ones. This may be a consequence of a better flow distribution throughout the radial flow devices than the axial ones. This difference was also slightly higher for the two devices with the higher bed height (Sartobind Q 75 and Nano 3 ml). This may be due to the negative effect of bed height, as previously mentioned.

The radial flow column has potential at large-scale applications, as a short bed height can be combined with a large surface area. Therefore, the axial flow device is scaled up in diameter, while the radial flow device can be scaled up vertically. This allows for the large scale radial flow MC device to be easier to handle than the equivalent axial flow device. Similar conclusions were recently obtained with packed bed resins for the comparison between axial and radial flow chromatography [19]. An advantage of MC devices over resins column is that the height of the radial flow column may

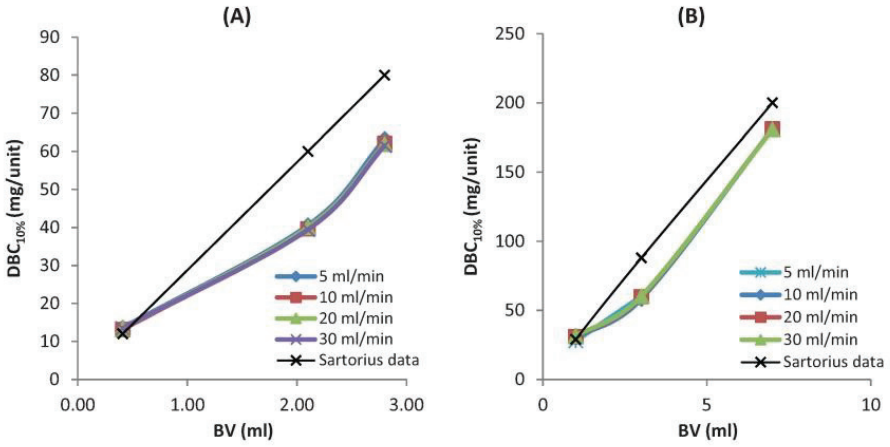

Fig. 10. Dynamic binding capacity at 10% of breakthrough as a function of bed volume for different MC device scales: (A) axial flow devices and (B) radial flow devices.

be not limited, contrary to resin packing which may limit the height of the radial flow column.

4. Conclusion

In this work, various axial and radial flow anion exchange devices have been selected for their different scales, membrane diameters and bed heights. For the different devices, BSA breakthrough curves were measured at various flow rates and BSA feed concentrations. It was observed that the BSA dynamic binding capacity at 10% and the total breakthrough capacity were independent upon flow rates for the two geometries at the different scales. This confirms the advantage of MC devices, for which high flow rates can be used without decreasing the dynamic binding capacity. In addition, the dynamic binding capacity increased at higher BSA concentration, which may be due to the competitive adsorption between phosphate ions, at the high concentration used, and BSA.

The axial flow MC devices showed slightly lower pressure drops than the radial flow MC devices at identical flow rates. Moreover, lower Peclet number values were obtained than for axial flow devices, which may be explained by the uneven flow distribution over the membrane surface. In addition, the device with the highest bed height (Sartobind Q75) showed the lowest dynamic binding capacity per membrane volume. This is a main limitation of axial flow devices, for which scaling-up has to rely upon increasing the diameter, which leads to lower velocities. However, the axial flow devices have the advantage to be simplest to produce; they are then preferred at small scale to radial flow devices.

With the radial flow devices, the pressure drop increased slightly with increasing bed height. In addition, slightly higher Peclet numbers were obtained, which may confirm reduced flow non-idealities compared to axial flow devices. As observed for axial flow devices, by increasing the bed height (Nano 3 ml device), the dynamic binding capacity decreased because of non-ideal flow distribution. However, the difference between experimental and theoretical BSA binding capacities, was slightly lower in case of radial flow devices. In addition, the radial flow devices can be scaled up by increasing the length of the radial flow column and not only the bed height. Radial flow devices are then preferred at industrial scales.

Acknowledgements

This work was supported by the Ministry of Science and Technology (MOST) of Thailand and Campus France with a doctoral scholarship for Chalore Teepakorn. The authors would like to thank Sartorius Stedim Biotech GmbH, especially Louis Villain, for providing MC modules.

References

[1] S. Brandt, R.A. Goffe, S.B. Kessler, J.L. O'Connor, S.E. Zale, Membrane-based affinity technology for commercial scale purifications, Nat. Biotech. 6 (1988) 779–782, http://dx.doi.org/10.1038/nbt0788-779

[2] C. Boi, Membrane adsorbers as purification tools for monoclonal antibody purification, J. Chromatogr. B 848 (2007) 19–27, http://dx.doi.org/10.1016/j.jchromb.2006.08.044

[3] C. Charcosset, Membrane Processes in Biotechnology and Pharmaceutics, Elsevier, 2012.

[4] V. Orr, L. Zhong, M. Moo-Young, C.P. Chou, Recent advances in bioprocessing application of membrane chromatography, Biotechnol. Adv. 31 (2013) 450–465, http://dx.doi.org/10.1016/j.biotechadv.2013.01.007

[5] J.X. Zhou, T. Tressel, Basic concepts in Q membrane chromatography for large-scale antibody production, Biotechnol. Progr. 22 (2006) 341–349, DOI 10.1021/bp050425v.

[6] Research and markets: 9th annual report and survey of biopharmaceutical manufacturing capacity and production, Reuters (2012). http://www.reuters.com/article/2012/07/03/idUS126634+03-Jul-2012+BW20120703 (accessed October 10, 2014).

[7] S. Schneiderman, H. Varadaraju, L. Zhang, H. Fong, T.J. Menkhaus, Mathematical model using non-uniform flow distribution for dynamic protein breakthrough with membrane adsorption media, J. Chromatogr. A 1218 (2011) 9121–9127, http://dx.doi.org/10.1016/j.chroma.2011.10.063

[8] C.-S. Chang, H.-S. Ni, S.-Y. Suen, W.-C. Tseng, H.-C. Chiu, C.P. Chou, Preparation of inorganic–organic anion-exchange membranes and their application in plasmid DNA and RNA separation, J. Membr. Sci. 311 (2008) 336–348, http://dx.doi.org/10.1016/j.memsci.2007.12.034

[9] T. Kawai, K. Saito, W. Lee, Protein binding to polymer brush, based on ion-exchange, hydrophobic, and affinity interactions, J. Chromatogr. B 790 (2003) 131–142, http://dx.doi.org/10.1016/S1570-0232(03)00090-4

[10] N. Singh, J. Wang, M. Ulbricht, S.R. Wickramasinghe, S.M. Husson, Surface-initiated atom transfer radical polymerization: a new method for preparation of polymeric membrane adsorbers, J. Membr. Sci. 309 (2008) 64–72, http://dx.doi.org/10.1016/j.memsci.2007.10.007

[11] R. Ghosh, T. Wong, Effect of module design on the efficiency of membrane chromatographic separation processes, J. Membr. Sci. 281 (2006) 532–540, http://dx.doi.org/10.1016/j.memsci.2006.04.023

[12] S.E. Bower, S.R. Wickramasinghe, Elimination of non-uniform, extra-device flow effects in membrane adsorbers, J. Membr. Sci. 330 (2009) 379–387, http://dx.doi.org/10.1016/j.memsci.2009.01.020

[13] H.L. Knudsen, R.L. Fahrner, Y. Xu, L.A. Norling, G.S. Blank, Membrane ion-exchange chromatography for process-scale antibody purification, J. Chromatogr. A 907 (2001) 145–154, http://dx.doi.org/10.1016/S0021-9673(00)01041-4

[14] P. Ghosh, K. Vahedipour, M. Leuthold, E. von Lieres, Model-based analysis and quantitative prediction of membrane chromatography: extreme scale-up from 0.08 ml to 1200 ml, J. Chromatogr. A 1332 (2014) 8–13, http://dx.doi.org/10.1016/j.chroma.2014.01.047

[15] K.-G. Briefs, M.-R. Kula, Fast protein chromatography on analytical and preparative scale using modified microporous membranes, Chem. Eng. Sci. 47 (1992) 141–149, http://dx.doi.org/10.1016/0009-2509(92)80208-T

[16] S.H. Huang, S. Roy, K.C. Hou, G.T. Tsao, Scaling-up of affinity chromatography by radial-flow cartridges, Biotechnol. Progr. 4 (1988) 159–165, http://dx.doi.org/10.1002/btpr.5420040306

[17] M. Puthirasigamany, M. Wirges, T. Zeiner, Membrane chromatography for the purification of laccase from the supernatant of Pleurotus sapidus, Biochem. Eng. J. 70 (2013) 180–187, http://dx.doi.org/10.1016/j.bej.2012.11.003

[18] D. Josić, J. Reusch, K. Löster, O. Baum, W. Reutter, High-performance membrane chromatography of serum and plasma membrane proteins, J. Chromatogr 590 (1992) 59–76, http://dx.doi.org/10.1016/0021-9673(92)87006-T

[19] T. Besselink, A. van der Padt, A.E.M. Janssen, R.M. Boom, Are axial and radial flow chromatography different? J. Chromatogr. A 1271 (2013) 105–114, http://dx.doi.org/10.1016/j.chroma.2012.11.027

[20] M.B.J. Tharakan, Ligand efficiency in axial and radial flow immunoaffinity chromatography of factor IX, J. Chromatogr. A 702 (1995) 191–196, http://dx.doi.org/10.1016/0021-9673(94)01141-Z

[21] M.W. Phillips, Method for determining an effective peclet number for a membrane adsorber device, US7281410 B2, 2007, http://www.google.com.ar/patents/US7281410 (accessed October 2, 2014).

[22] P. van Beijeren, P. Kreis, T. Zeiner, Ion exchange membrane adsorption of bovine serum albumin—Impact of operating and buffer conditions on breakthrough curves, J. Membr. Sci. 415–416 (2012) 568–576, http://dx.doi.org/10.1016/j.memsci.2012.05.051.

(This page is intentionally left blank)

Separation and Purification Technology 151 (2015) 292–302

Contents lists available at ScienceDirect

Separation and Purification Technology

journal homepage: www.elsevier.com/locate/seppur

Optimization of lactoferrin and bovine serum albumin separation using ion-exchange membrane chromatography

Chalore Teepakorn, Koffi Fiaty, Catherine Charcosset *

Laboratoire d'Automatique et de Génie des Procédés (LAGEP), Université Claude Bernard Lyon I, 43 bd du 11 Novembre 1918, Bâtiment CPE, 69622 Villeurbanne Cedex, France

ARTICLE INFO

Article history:
Received 28 April 2015
Received in revised form 16 July 2015
Accepted 19 July 2015
Available online 20 July 2015

Keywords:
Membrane chromatography
Bovine serum albumin
Lactoferrin
Separation
Ion-exchange

ABSTRACT

Lactoferrin (LF), which is a high value minor whey protein, has recently received extensive attention from research scientists and industry due to its multifunction and potential therapeutic applications. In this study, the separation of two similar-sized proteins: bovine serum albumin (BSA) and LF was investigated using strong cation and anion exchange membrane chromatography (MC). Single protein and BSA–LF mixture adsorption were performed on Sartobind Q75 and S75 at pH between the LF and BSA isoelectric points. Identical breakthrough curves were obtained for both single protein and binary protein mixture, which suggests that there is no protein adsorption competition at the binding sites. The process optimization was further studied to yield optimum buffer and operating conditions. The highest BSA flux per membrane area (728.00 $gm^{-2}\,h^{-1}$) was obtained using 100 mM phosphate buffer solution at pH 6.0 on the cation exchange membrane, whereas LF was bound to the membrane with the dynamic binding capacity at 10% breakthrough ($DBC_{10\%}$) of about 60 mg. On the anion exchange membrane, LF was collected in the effluent at the flux of 287.46 $gm^{-2}\,h^{-1}$ using 5 mM phosphate buffer at pH 6.0, while BSA was retained on the membrane with $DBC_{10\%}$ equal to 60.96 mg. The combination effect between pH change and hydrophobic interaction improved the eluted protein mass for both anion and cation exchangers. Furthermore, the completed separation cycle was operated with the Sartobind S75 device with a short process time of 34.19 min and optimal LF productivity over 2628.84 mg $mL^{-1}\,h^{-1}$. This study confirms the advantage of MC for the separation of biomolecules with similar molecular weight and different isoelectric points, such as BSA–LF mixture separation. This fast and effective protein separation method could be applied at an industry scale.

1. Introduction

Lactoferrin (LF) is a metal-binding glycoprotein, which was discovered over 50 years ago as red protein in bovine milk. The isolation of this molecule from both human and bovine milk was first achieved using cation exchange chromatography on traditional resin-based column [1,2]. LF is a well-known multifunctional or multi-tasking protein. Many important roles such as immunoregulatory, anti-bacterial, anti-virus, anti-parasitic and anti-inflammatory activity have been reported [3–5]. The wound healing, which is a complex biological process can be promoted using this protein [6]. In addition, LF has been proved to function as an anti-infective agent and prevent the outbreak of infections. It makes this molecule and its derivatives very promising tools for health or nutritional applications [7]. LF is found in whey as a high value minor protein with bovine serum albumin (BSA) and immunoglobulins [8,9].

Membrane separation and chromatography are the most widely used methods for LF isolation from bovine milk and whey. Membrane separation processes provide key advantages for whey fractionation as they do not include adsorption and elution steps, and avoid costs for chromatographic material, buffers and effluent disposal. However, membrane filtration is usually not effective in separating similar size proteins, such as LF and BSA, and other whey proteins. Several authors have reported the separation of LF from other proteins and whey. For example, Nyström et al. [10] investigated the fractionation of several proteins with molecular weight between 15 kD and 80 kD. The best pH value for fractionation was such that one protein had its isoelectric point at this pH, and passed through the membrane, while the other one was held back in the retentate because of charge repulsion with the membrane. In particular, LF was purified at low pressures while BSA was totally retained. However, at higher pressures, the selectivity was low. Similarly, Almécija et al. [11] reported LF isolation

* Corresponding author.
E-mail address: charcosset@lagep.univ-lyon1.fr (C. Charcosset).

http://dx.doi.org/10.1016/j.seppur.2015.07.046
1383-5866/

from whey using a 300 kDa tubular ceramic membrane. The effect of pH on LF selectivity was investigated in a continuous diafiltration mode. The best resolution was achieved at pH 5 and 10, where LF was obtained in the permeate and in the retentate, respectively, with α-lactalbumin and β-lactoglobulin. Other strategies have been investigated to overcome the limitations associated with LF separation by membrane filtration. For example, Brisson et al. [12] used charged membranes and electrically-enhanced cross-flow microfiltration. The electrical field played an important effect on protein transmission. However, electrolytic reactions occurring at the electrodes/solution interface had a negative impact on the protein separation. Ndiaye et al. [13] evaluated the feasibility of separating LF from whey solution using electrodialysis with an ultrafiltration membrane of 500 kDa. The highest LF migration rate was obtained at pH 3.0 with a migration yield of 15%. However, the selectivity of the technique decreased in whey solution due to simultaneous migration of β-lactoglobulin and other whey proteins. Valiño et al. [9] investigated the separation of BSA and LF using charged ultrafiltration membranes. Using an unmodified neutral membrane at pH 5.0 (isoelectric point of BSA), LF was completely retained, and BSA passed in the permeate at a maximum flux of 30.31 g m^{-2} h^{-1}. By contrast, BSA was completely retained by the negatively charged membrane at pH 9.0 (isoelectric point of LF), and LF was recovered at a maximum flux of 1.07 g m^{-2} h^{-1}.

Conventional chromatography is the most widely used method for protein recovery and purification as it is a robust and efficient technique. Many studies have reported LF isolation using micro-sized resins as a stationary phase. Different chromatographic modes have been tested such as cation exchange [14–18], affinity [19] and hydrophobic interaction [20]. However, conventional chromatographic processes show several disadvantages, since large volumes and high protein concentrations in whey may cause fouling of columns, long cycle times, large pressure drops and complicated process control [21,22]. Other stationary phases have therefore been tested as possible alternatives to resins such as mixed-matrix membranes (MMMs), monolithic columns, and chromatographic membranes.

MMMs are prepared by incorporating an adsorptive resin into a membrane polymer solution prior to membrane preparation [23]. The polymer/resin suspension is then cast as a flat sheet membrane or spun into a hollow fiber membrane. The MMM concept has been successfully applied to the preparation of anionic, cationic, anionic/cationic hybrid membranes for protein separation. MMM combines the properties of membrane techniques (easy scale-up, low pressure drop) with column chromatography (high binding capacity, high recovery) [23]. Several MMMs have been applied to the recovery of LF from whey. For example, Saufi and Fee [24] developed a cationic MMM for recovery of LF from bovine whey by embedding SP Sepharose™ cation exchange resin into an ethylene vinyl alcohol polymer based membrane. The separation was operated in cross-flow mode and recycling both permeate and retentate into the feed, to minimize fouling and enhance LF binding capacity. The system resulted in a constant permeate flux equal to 100 L m^{-2} h^{-1} and a high LF recovery of 91%, with high purity. A disadvantage of MMM could be the negative effect of flow rate on separation. For example, Avramescu et al. [23] reported a lower separation factor of 30 between BSA and bovine hemoglobin using MMM, when the filtration flux per membrane area increased from 10 to 20 L m^{-2} h^{-1}. This effect was due to the decrease of the efficiency of adsorptive sites with flow velocity.

Another development in chromatography is the use of macroporous monolith columns. A monolith is a single piece of highly porous material characterized by a highly interconnected network of channels with a diameter in the range of 10–4000 nm [25]. Therefore, mass transport in monoliths is mainly based on convection. The use of short monolithic columns enhances the speed of the separation process and reduces the backpressure, unspecific binding and product degradation, without reducing resolution. In addition, the lack of void volume eliminates the turbulent void flow that contributes to molecular shear in conventional resin columns. Some studies have reported the use of monolithic columns for LF and whey protein separation. For example, Noppe et al. [26] covalently coupled phage clones expressing a peptide with high binding affinity for LF to a macroporous poly(dimethylacrylamide) monolithic column. The large pore size of the macroporous monolith makes it possible to couple the long phages as ligands without any risk of blocking the pores. Using this affinity support, LF was purified from human skimmed milk with purity higher than 95%, in one step. In another application, Etzel and Bund [27] purified whey protein-dextran conjugates from a feed solution also containing un-reacted protein and dextran using either a cation exchange packed bed column or a tube monolith. Binding capacities were similar for both monolith and beaded column (4–6 mg mL^{-1}). However, the monolith was operated at a 48-fold higher flow rate, which gave a 42-fold higher productivity, at the expense of a somewhat lower conjugate purity.

Membrane chromatography (MC) is a well-established technique for protein purification [22,23,28]. It is based on the integration of membrane filtration and liquid chromatography into a single-step operation. The advantage of MC over conventional resin chromatography is mainly attributed to the shorter diffusion times, as the interactions between molecules and active sites in the membrane occur in convective through-pores rather than in stagnant fluid inside the pores of the adsorbent particles. Therefore, MC has the potential to operate both at high flow rates and for use of large biomolecules with small diffusivities, reducing biomolecules degradation and denaturation. Low pressure drops associated with high flow rates, as compared to packed bed chromatography, reduce buffer usages [22]. Fractionation of whey proteins by MC has been reported in several studies. For example, LF and lactoperoxidase (LP) were isolated from sweet cheese whey using cation exchange MC in an axial flow configuration [21]. LF was eluted in a three-step elution process (0.1 M NaCl, 0.2 M NaCl, 1 M NaCl), which led to a LF fraction of about 95% purity. The cationic MC was then upscalable from 15 cm^2 to 4 m^2 scale with a recovery yield for LF of more than 90%. However, it was observed that when increasing the flow rate from 3 to 15 mL min^{-1}, the binding capacity decreased from 0.6 to 0.3 mg cm^{-2}. Similarly, Chiu and Etzel [28] extracted LF and LP from whey using cation exchange MC devices with surface area of 100 cm^2 and 790 cm^2. The purification process was operated repeatedly with 12 cycles consisting of loading of whey, washing, stepwise elution and washing. Recovery was unaffected by scale-up and repeated cycling, and was 50.0% and 73.0% for LF and LP, respectively. For the complete fractionation of whey proteins in a two-step process, Voswinkel and Kulozik [29] used ion-exchange radial flow devices with improved fluid distribution (anion and cation exchanger Sartobind Nano and Sartobind 150-mL). First, β-lactoglobulin and BSA were bound to the anion exchanger at pH 7.0. Second, the permeate obtained in the first step was introduced into the cation exchanger at pH 4.8. LF, LP and immunoglobulin G bound while β-lactalbumin passed through the membrane. The scalability of the process was investigated with the radial flow column and 50-fold membrane area. At lab scale, 97% LF purity was obtained with a yield of 66%. However, at pilot scale, LF purity and yield decreased to 89% and 39%, respectively. The authors concluded that further investigations were needed to increase the LF yield in the cation exchanger step. Affinity MC has also been tested for LF purification from bovine whey and colostrum. For example, Wolman et al. [30] modified a hollow fiber polysulfone membrane by grafting a glycidyl methacrylate/dimethyl acrylamide copolymer and attaching the

triazinic dye Red HE-3B as an affinity ligand. Using 1 mL membrane volume, LF purification from bovine colostrum was performed in one step at different flow rates. The binding capacity did not decrease with increasing flow rate.

Several mathematical models have been proposed to predict MC performance, including breakthrough curves, elution profiles, and the effect of various parameters. Most models consider convection, diffusion and adsorption kinetics, like Langmuir adsorption for affinity separation [31] and ion-exchange [32,33]. Several other kinetic mechanisms have been evaluated, such as steric hindrance [34], spreading equations [35] and bi-Langmuir adsorption [36]. To account for flow non-idealities, such as dispersion, mixing and dead volumes, a combination in series of an ideal continuously stirred tank reactor and an ideal plug flow reactor has been introduced [36]. Mathematical models were applied successfully to complex purifications, such as the separation of immunoglobulin G from complex mixtures using affinity MC [37].

Although many techniques have been developed to isolate LF, the separation of high-value minor proteins of similar molecular weights such as BSA, LF, and immunoglobulins remains a challenge. BSA is a 66.5 kDa protein with an isoelectric point near 4.7. LF is a 78.0 kDa protein with an isoelectric point around 8.7. Both proteins tend to prevent foam formation at their isoelectric points by reducing the surface tensions, which makes their separation even more difficult [9]. In this work, the separation of LF and BSA mixture is carried out using strong anion and cation exchange MC. The influence of operating and buffer conditions on protein mixture separation is studied with Sartobind S75 and Q75 devices (Sartorius Stedim Biotech GmbH, Germany). The breakthrough curve, dynamic binding capacity at 10% breakthrough ($DBC_{10\%}$), selectivity and productivity of the BSA–LF mixture separation are measured at various experimental conditions. The results obtained are discussed to obtain an optimum separation between BSA and LF.

2. Materials and methods

2.1. Materials

Sartobind S75 and Q75 MC devices are strong cation and anion exchangers, respectively, provided by Sartorius Stedim Biotech GmbH (Goettingen, Germany). The devices contain 75 cm^2 of stabilized reinforced cellulose membrane in a stack of 15 membrane discs. The flow configuration is dead-end geometry, in which the flow goes from top through the membrane stack to the outlet. The membrane bed volume (BV) of these Sartobind devices is 2.1 mL, with the diameter of the membrane of 25.0 mm, 4.0 mm bed height and 1.30 mL dead volume [38]. Functionalized sulfonic acid and quaternary ammonium groups are covalently bound to the membrane in the strong cation and anion exchangers, respectively.

BSA lyophilized powder with purity ⩾96.00% was purchased from Sigma Aldrich (France). Purified bovine LF lyophilized powder (⩾93.00% of purity) was kindly provided by Erie Europe (France). Potassium phosphate buffer solutions at desired concentrations and pH values were prepared by adjusting volumes of K_2HPO_4 and KH_2PO_4 solutions and subsequently filtered through a hydrophobic membrane filter with a 0.45 μm pore size (Millipore, France). Sodium phosphate buffer solutions were prepared by mixing Na_2HPO_4 (Fluka, France) and NaOH solutions. Citrate buffer 100 mM pH 3.0 was obtained by mixing adequately citric acid and sodium citrate dehydrate (Fluka, France) solutions. Ultrapurified water from a Milli-Q system (Millipore, France) was used in this work for solution preparation. For HPLC buffers, trifluoroacetic acid (TFA) and acetonitrile were obtained from Sigma–Aldrich (France). All other reagents are from Sigma–Aldrich (France).

Proteins were diluted into phosphate buffers by slowly stirring to prevent any foam formation. The diluted proteins were then stored overnight in the refrigerator until any foam had naturally disappeared [9]. Afterward, the protein solution was filtered through a 0.22 μm polyethersulfone hydrophilic Millex-GP filter unit (Millipore, France) to remove any fine particles. All experiments were carried out on an Aktaprime-plus (GE Healthcare, France) chromatography system with a UV-280 detector. The system was controlled by the PrimeView 5.0 software (GE Healthcare, France).

2.2. Protein analysis

The concentrations of LF and BSA solutions were measured by spectrophotometry at 280 nm using the UV detector of the Aktaprime-plus system. For each single protein, a standard curve was determined by plotting the absorbance versus concentration for a range of known solutions. From these standard curves, BSA and LF calibration constants were determined. To check the method of concentration measurement for BSA–LF mixture solutions by spectrophotometry, reversed-phase high performance liquid chromatography (RP-HPLC) was used according to the method of Voswinkel and Kulozik [39]. A Zorbax Eclipse XDB-C18 5 μm column was connected to an Agilent 1200 HPLC system with a G1315D diode array detector (Agilent Technologies, France). Eluent A contained 0.1% (v/v) TFA dissolved in water and eluent B was a mixture of 0.0555% (v/v) TFA, 80% (v/v) acetonitrile and 20% (v/v) water, the flow rate was 1.0 mL min^{-1} and temperature was 40 °C. Peak detection was at 226 nm for both proteins. Protein concentration was determined by peak integration of each eluted fraction.

A typical 280 nm UV absorbance curve obtained for BSA and LF mixture adsorption on a Sartobind Q75 device shows two separate breakthrough curves (Supplementary material), the first one corresponds to the non-binding LF, which would be more positively charged and does not bind to the ligands at the membrane surface. The second breakthrough curve corresponds to the binding BSA, which is negatively charged and is retained to the opposite charges on membrane. Consequently, the UV absorbance curve has been used to obtain LF and BSA breakthrough curves using Eqs. (1) and (2), where A is the measured absorbance, $A_{1,0}$ is the UV absorbance corresponding to the loading concentration of the protein not adsorbed onto the membrane, K_i the absorbance calibration constant of protein i (LF or BSA) and c_i is the concentration of protein i.

To verify this method, RP-HPLC was used to measure LF and BSA concentrations in samples taken at various times during the loading step of the LF–BSA mixture (Supplementary material). LF and BSA concentrations were measured in triplicate. The protein breakthrough curves using the UV-absorbance curves compared well to breakthrough curves obtained from RP-HPLC measurements. In the next, we choose the UV absorbance curve method to determine breakthrough curves during protein mixture adsorption.

$$\text{when } A < A_{1,0}; \quad c_1 = \frac{A}{K_1} \text{ and } c_2 = 0 \tag{1}$$

$$\text{when } A \geqslant A_{1,0}; \quad c_1 = \frac{A_{1,0}}{K_1} \text{ and } c_2 = \frac{A - A_{1,0}}{K_2} \tag{2}$$

Furthermore, the zeta potential of 1.00 mg mL^{-1} LF and BSA in 100 mM phosphate buffer at different pH was determined using a Zetasizer Nano-series (Malvern Instruments, Malvern France). All the measurements were performed at least three times and the data were expressed as the mean ± standard deviation (S.D.). The zeta potential was calculated from the electrophoretic mobility by the Helmholtz–Smoluchowski equation [40].

2.3. Process characteristics

System dispersion curves were measured by loading a phosphate buffer containing 5.00% (v/v) acetone as an inert tracer. The flow rate was 12.0 BVmin^{-1}. The absorbance was read at 280 nm. This non-binding experiment using acetone solution was used to determine the dead volume (V_0) of the Sartobind S75 or Q75 device connected to the Aktaprime-plus system, when the breakthrough concentration increased to 10.0% of acetone initial concentration. Using this method, V_0 was found to equal 6.06 mL.

BSA and LF breakthrough curves were measured at different buffer and operating conditions using Sartobind S75 and Q75 devices. In most MC applications, the separation process is stopped when the molecule to be purified starts to appear in the effluent, usually when the concentration reaches 10% of its initial value ($c/c_0 = 0.10$). Therefore, several parameters were determined at 10% breakthrough. The effluent volume ($V_{ef,10\%}$) was the volume read at 10% breakthrough ($V_{10\%}$) minus the dead volume of the Sartobind device and external system (V_0) as shown in Eq. (3). $V_{ef,10\%}$ represents the volume of protein(s) solution that has be loaded until 10% breakthrough occurs.

$$V_{ef,10\%} = V_{10\%} - V_0 \tag{3}$$

The dynamic binding capacity at 10% breakthrough ($DBC_{10\%}$) per unit of Sartobind device was calculated using Eq. (4), where c is the protein (LF or BSA) concentration in the effluent, c_0 is the protein (LF or BSA) loading concentration, $V_{10\%}$ is the read volume of BSA or LF solution at $c/c_0 = 0.10$.

$$DBC_{10\%} = \int_0^{V_{10\%}} (c_0 - c)dV - c_0V_0 \tag{4}$$

Protein (LF or BSA) concentrations in the effluent at 10% breakthrough (c_{ef}) were determined by numerical integration of the breakthrough curve as indicated in Eq. (5). The selectivity, which is one important parameter in the separation process, was determined using Eqs. (6) and (7) for the cation and anion exchangers, respectively, where $c_{0,LF}$ and $c_{0,BSA}$ are the loading protein concentrations, respectively of LF and BSA.

$$c_{ef} = \frac{\int_0^{V_{10\%}} cdV - c_0V_0}{V_{10\%}} \tag{5}$$

$$\alpha_{BSA/LF} = \frac{c_{ef,BSA}/c_{0,BSA}}{c_{ef,LF}/c_{0,LF}} \tag{6}$$

$$\alpha_{LF/BSA} = \frac{c_{ef,LF}/c_{0,LF}}{c_{ef,BSA}/c_{0,BSA}} \tag{7}$$

2.4. Single protein adsorption and BSA–LF mixture separation

BSA and LF concentrations in bovine milk are reported to depend on several factors like the lactation period, and are usually between 0.02 and 0.2 mg mL^{-1} for LF and between 0.2 and 2.6 mg mL^{-1} for BSA [41–43]. Whey protein concentrate is greater than 70% by weight, obtained by ultrafiltration in association with diafiltration [44]. The initial protein concentration of the BSA–LF binary mixture in this work (2.00 mg mL^{-1} and 1.00 mg mL^{-1}, respectively for BSA and LF) referred to conditions that have been previously used [9]. Those conditions simulated the concentrations found in the production of whey concentrate [45]. The influence of the different initial concentrations of proteins was investigated using the initial concentrations of BSA from 1.00 to 4.00 mg mL^{-1} and LF from 0.50 to 2.00 mg mL^{-1}. Moreover, single protein adsorption experiments were operated at both LF and BSA loading concentration of 1.00 mg mL^{-1} to keep the same concentration for both proteins.

For the Sartobind Q75 device, the pH effect was investigated at a reduced ionic strength using 20 mM phosphate buffers. BSA and LF concentrations were monitored by reading the UV-absorbance at 280 nm. All experiments of single protein adsorption were operated at 12.0 BVmin^{-1}.

Afterward, BSA–LF separation was performed by loading BSA–LF mixture solutions at 2/1 of BSA/LF initial concentrations. The loading solution was prepared by mixing the same volume of 2.00 mg mL^{-1} BSA solution and 1.00 mg mL^{-1} LF solution. The loading step was stopped when the loaded volume was 150.0 mL, which ensures that the protein amount is enough to reach 100% breakthrough. The effect of buffer ionic strength, flow rate and protein initial concentration on the BSA–LF mixture separation performance was investigated.

2.5. Elution step

The impact of the different eluents on BSA and LF eluted amount was investigated for both cation and anion exchangers devices. A BSA–LF solution at initial concentration of 2/1 was loaded at 24.0 BVmin^{-1} until $V_{ef,10\%}$. The elution buffer (20.0 mL) was then injected at a flow rate of 6.0 BVmin^{-1}. The amount eluted (BSA or LF) was determined by numerical integration of the elution peak. For both devices, the effect of the ionic strength of the elution buffer was tested (1.00 M and 2.00 M NaCl in phosphate buffer).

In addition, the effect of pH and hydrophobic interaction by adding ethylene glycol were evaluated. For the cation exchange device, 50 mM sodium phosphate buffer was used at two different pH 11.0 or 12.0 above the isoelectric point of LF. An additional elution buffer was tested by adding 25.00% ethylene glycol in 50 mM sodium phosphate buffer at pH 12.0. For the anion exchange device, the elution buffer was 100 mM citrate buffer pH 3.0 (below the isoelectric point of BSA). An additional elution buffer was tested by adding 25.00% ethylene glycol diluted in 100 mM citrate buffer, pH 3.0. Finally, the effect of flow rate on the eluted protein amount was investigated for the best elution buffer found.

2.6. LF–BSA separation cycles on cation exchange membrane

LF–BSA fractionation cycles on Sartobind S75 were operated with the optimal loading buffer, operating and elution conditions. The separation was composed of six steps: (1) equilibration of the MC device using the phosphate buffer for a volume $V_{eq} = 20$ mL, (2) loading of the BSA–LF mixture solution until 10% breakthrough of LF, i.e. for the optimized volume $V_{ef,10\%}$; (3) first washing with phosphate buffer ($V_{w1} = 20$ mL), (4) protein elution ($V_{elu} = 20$ mL), (5) second washing with phosphate buffer ($V_{w2} = 20$ mL), and (6) membrane regeneration with phosphate buffer ($V_{re} = 120$ mL). The different steps where performed at various flow rates: Q_{ef} for the loading and washing steps, Q_{elu} (elution step), and Q_{re} (regeneration step). The process separation was repeated over three cycles.

The membrane regeneration step was performed using the method described in the Sartobind user's guide. 1 M NaOH was loaded to the MC device at $Q_{re} = 1$ BVmin^{-1} for 60.0 BV, followed by 1 M NaCl eluent and phosphate buffer for 10 BV of each solutions. The equilibrium, loading and all washing steps were operated at $Q_{ef} = 24.0$ BVmin^{-1}. The flow rate during the elution step was decreased to $Q_{elu} = 1.0$ BVmin^{-1}. For each process, the total process time (t_p) was defined by Eq. (8) and the productivity of the chromatographic process was calculated using Eq. (9) [30].

$$t_p = \frac{V_{eq} + V_{ef,10\%} + V_{w1} + V_{w2}}{Q_{ef}} + \frac{V_{elu}}{Q_{elu}} + \frac{V_{re}}{Q_{re}} \tag{8}$$

$$\text{Productivity} = \text{Eluted protein mass} \times t_p^{-1} \times BV^{-1} \tag{9}$$

3. Results and discussion

3.1. Cation exchange membrane

3.1.1. Influence of buffer conditions

Using the Sartobind S75 device, single protein adsorption experiments were performed by loading protein (BSA or LF) solution at different buffer pH values between the isoelectric point of BSA and LF. The effect of pH on the single protein adsorption was therefore examined at pH 6.0, 7.0 and 8.0. For all experiments, the flow rate was set at 12.0 BVmin^{-1}.

As shown in Fig. 1, BSA did not bind on the cation exchange membrane because BSA possessed more negative charges than LF at these pH (between 6 and 9); therefore, LF adsorbed preferentially to the membrane. The higher LF binding capacity was obtained at pH 6.0, as LF was less negatively charged (zeta potential of −2.36 mV in 100 mM phosphate buffer) as compared to pH 7.0 and 8.0 (−4.97 and −6.60 mV, respectively). The isoelectric point of BSA being close to 4.7, the zeta potential of BSA was negative at pH between 6.0 and 9.0, and decreased when increasing pH. Moreover, the isoelectric point of LF being given as close to 8.7, it could be foreseen that the zeta potential of this protein would be positive at pH 6.0 and 7.0, which is not the case. In a recent study, Valiño et al. [46] measured various parameters related to BSA and LF, including zeta potential, for a large range of experimental conditions, such as electrolyte type, ionic strength, and protein concentration. The authors observed that the zeta potential decreased with increasing electrolyte concentration. At ionic strength of 0.1 M, from pH 6 to 10, both BSA and LF had negative zeta potential value, which corresponds to our zeta potential data.

The highest $V_{ef,10\%}$ (60.63 mL) was obtained at pH 6.0 with $DBC_{10\%}$ equal to 60.17 mg of LF per unit of Sartobind device. This corresponds to an increase of LF $DBC_{10\%}$ over 46% and 97%, compared to data at pH 7.0 and 8.0, respectively. pH in the range 6–7 have been previously selected for the isolation of LF from whey. For example, Plate et al. [21] treated sweet cheese whey at pH of 6.2 using a cation exchange MC device Sartobind S75.

In addition, the breakthrough curves of single protein (BSA or LF) solutions and binary BSA–LF mixtures was compared at pH 6.0 (Fig. 2). LF breakthrough curves were found identical for both the single and binary protein mixture. In addition, the BSA breakthrough curve of the BSA solution and BSA/LF mixture were identical to the breakthrough curve of the non-binding solute acetone. This confirms that BSA passed through the membrane stack without binding. At this pH, only LF binds to the negatively charged ligands of the cation exchange membrane and there is no competition between BSA and LF adsorption at the binding sites.

The influence of ionic strength was studied by setting the phosphate buffer concentrations at 10, 100 and 200 mM at pH 6.0 (Fig. 3A). The highest LF binding capacity was obtained at 100 mM, compared to the binding capacity at 10 and 200 mM phosphate buffers. In addition, it was observed that the LF breakthrough curve was sharper at the highest phosphate concentration 200 mM compared to 10 mM. Several phosphate buffer concentrations were then tested from 40 to 125 mM (Fig. 3B). The LF binding capacity increased slightly with the increasing phosphate concentrations until 100 mM. A decrease of LF binding capacity was then observed at 125 mM. The phosphate buffer concentrations of 40 and 125 mM provided very similar LF breakthrough curves, with slightly lower LF binding capacity than at 100 mM.

The effect of buffer ionic strength could be explained as follows. Before loading the protein solution onto the ion-exchange membrane, charge sites on proteins and sulfonic acid groups of the membrane are equilibrated by buffer counter-ions. During LF adsorption, these buffer ions are released and may prevent further adsorption by ionic strength increase or pH change. To avoid these negative effects, an increase in buffer concentration can stabilize the pH and improve therefore protein binding. This effect was observed in our study for buffer concentration from 40 mM to 100 mM. However, the buffer ionic strength should not be too high, because the potassium ions could then compete for the same binding sites with LF as observed at buffer concentration of 125 mM and 200 mM.

The selectivity of the BSA/LF mixture separation, $\alpha_{BSA/LF}$, was determined using Eq. (4) and plotted versus the effluent volume until 10% LF breakthrough (Supplementary material). LF was first completely bound to the membrane while BSA passed through the membrane in the effluent. Therefore, $\alpha_{BSA/LF}$ was at first infinite due to the zero content of LF in the effluent. After breakthrough, the selectivity $\alpha_{BSA/LF}$ decreased sharply as LF started to pass in the effluent. At 10% LF breakthrough, the highest selectivity $\alpha_{BSA/LF}$ (147.02) was obtained at 100 mM phosphate buffer with $V_{ef,10\%}$ around 62 mL and $DBC_{10\%}$ at 61.46 mg per device. Therefore, in the range of conditions tested, the optimum buffer conditions for the BSA–LF mixture separation by cation exchange MC were selected to be pH 6.0 and phosphate buffer concentration of 100 mM. The amounts of bound LF at $DBC_{10\%}$ are specified in

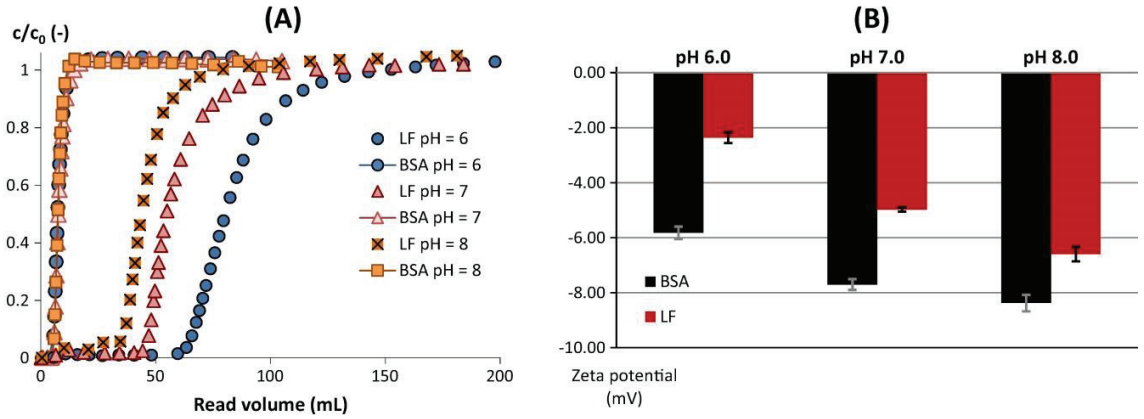

Fig. 1. (A) pH influence on breakthrough curves of single BSA and LF solutions on Sartobind S75 in 100 mM phosphate buffer at flow rate of 12.0 BVmin^{-1}, loading BSA concentration of 1.0 mg mL^{-1} and loading LF concentration 1.0 mg mL^{-1}. (B) Zeta potential of BSA and LF at different buffer pH of 6.0, 7.0 and 8.0, at concentration of 1.0 mg mL^{-1} in 100 mM phosphate buffer.

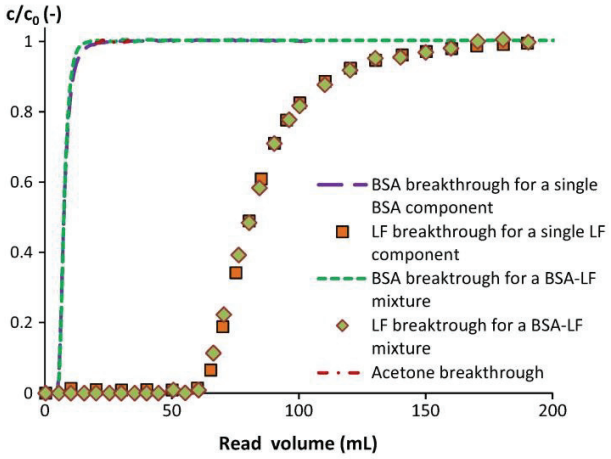

Fig. 2. Comparison between breakthrough curves of (1) single protein (LF and BSA) solutions at loading concentration of 1.00 mg mL^{-1}, (2) BSA–LF mixture at BSA–LF loading ratio of 2:1 and (3) 5.00%(v/v) acetone solution as an inert tracer. Sartobind S75 device, 100 mM phosphate buffer, pH 6.0 and flow rate 12.0 $BVmin^{-1}$.

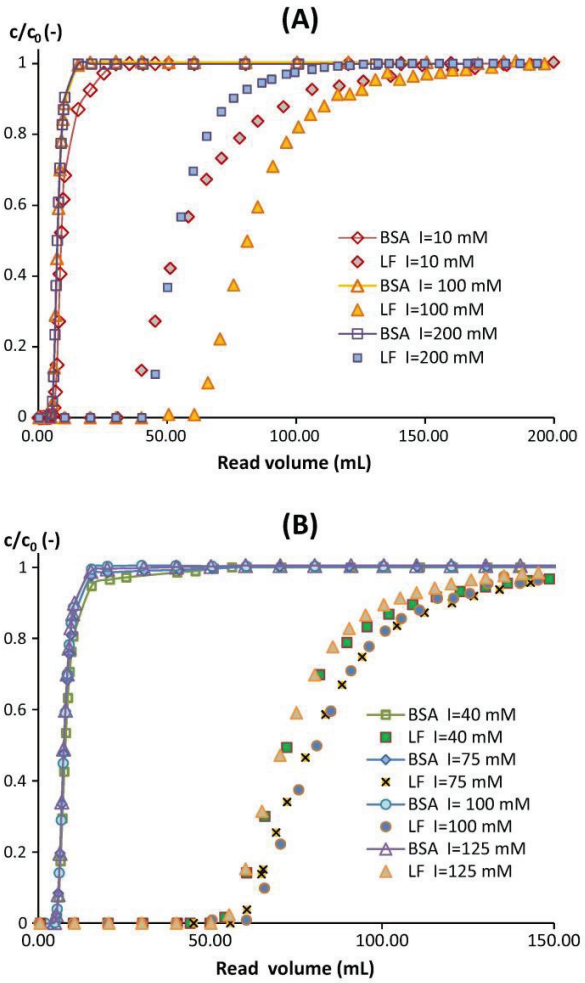

Fig. 3. Influence of ionic strength at pH 6.0 on breakthrough curves of BSA–LF mixture using Sartobind S75 at 12.0 $BVmin^{-1}$ and BSA–LF initial concentrations of 2/1. (A) Phosphate concentrations at 10, 100 and 200 mM. (B) Phosphate concentrations between 40 mM and 125 mM.

Table 1, showing the important effect of buffer condition on MC separation.

3.1.2. Influence of operating conditions

The influence of flow rate on BSA–LF fractionation was investigated at 12.0, 18.0 and 24.0 $BVmin^{-1}$ (Supplementary material), which correspond respectively to superficial velocities of 5.13, 7.70 and 10.27 cm min^{-1}. Optimum pH and phosphate buffer concentration were used, respectively 6.0 and 100 mM. The BSA flux, $\alpha_{BSA/LF}$ at 10% LF breakthrough and LF $DBC_{10\%}$ are given in Table 2. For the different flow rates, breakthrough curves overlapped; LF breakthrough happened around 60.0 mL, which corresponds to LF $DBC_{10\%}$ per BV of 28.50 mg mL^{-1}. This data was higher than the data reported by Sartorius of 25.00 mg mL^{-1} of membrane BV (for lysozyme adsorption in 10 mM potassium phosphate buffer at pH 7.0).

Similarly, van Beijeren et al. [47] observed almost no effect of flow rate in the range 15.0–20.0 mL min^{-1} on breakthrough curves by using the cation exchanger Sartobind S75 at pH 4.5. Moreover, the selectivity, $\alpha_{BSA/LF}$ at 10% LF breakthrough stayed in the same range between 89.97 and 147.02 at the different flow rates. This confirms one major advantage of MC, which can be operated at high flow rate without any decrease in binding capacity and separation performance. BSA flux is calculated from the total membrane area contained in the Sartobind device that is 75 cm^2. Effluent fluxes per membrane area were achieved of 200.0, 304.0 and 400.0 L m^{-2} h^{-1} for flow rates at 12.0, 18.0 and 24.0 $BVmin^{-1}$, respectively. In a recent study, Valiño et al. [9] used a charged ultrafiltration membrane to separate BSA–LF mixture at a maximum flux per membrane area of 77.73 L m^{-2} h^{-1} with an infinite selectivity. When operated at 24.0 $BVmin^{-1}$, the Sartobind S75 device in our study could therefore provide a five-fold higher flux compared to the charged ultrafiltration membrane used by Valiño et al. [9].

The influence of BSA/LF initial concentration was studied at 2/0.5, 2/1, and 2/2 by plotting the breakthrough curves versus LF loading mass (Fig. 4). For all initial concentrations, the breakthrough curves had the same shape, although breakthrough occurred slightly earlier at the concentration of 2/0.5. At the highest LF concentration (2/2), the process was faster and 10% LF breakthrough occurred after 40 s, compared to 76.15 s and 127.08 s, for the BSA/LF concentrations of 2/1 and 2/0.5, respectively. Therefore, loading of high protein concentration solution could be preferable to obtain a fast fractionation process. In a previous study, Valiño et al. [9] reported the loss in the separation selectivity at the BSA/LF concentrations of 2/1 compared to 4/1. This was suggested to be a consequence from the interaction between BSA and LF by forming stoichiometric complexes at the BSA/LF concentrations of 2/1, whose presence might modify the average size and the BSA flux. In our study, no effect of BSA/LF concentrations was observed and the selectivity remained infinite until breakthrough occurred, at the different BSA/LF concentrations.

3.2. Anion exchange membrane

3.2.1. Influence of buffer conditions

Unlike the cation exchange device, the anion exchange device retains BSA molecules at pH between the isoelectric point of BSA and LF. BSA, being negatively charged, binds to the positively charged ligands of the anion exchange membrane; while LF, being less negatively charged, is collected in the effluent. Using the Sartobind Q75 device, the effect of the buffer pH values at 6.0, 7.0 and 8.0 on single protein adsorption performance was investigated (Fig. 5A). The buffers were first prepared using 100 mM phosphate. A low BSA binding capacity was obtained at all pH values because of the competition between salt ions and BSA for the

Table 1
LF and BSA $DBC_{10\%}$, using Sartobind S75 and Q75 devices, respectively, at an initial BSA/LF concentrations of 2/1 and a flow rate of 12.0 $BVmin^{-1}$,[A] except for the experiments at different pH, which were performed by loading single LF and BSA solutions at initial concentrations of 1.00 mg mL^{-1} for both proteins.

Sartobind S75	pH[A] at I = 100 mM			Ionic strength (mM) at pH 6.0					
	6.0	7.0	8.0	10	40	75	100	125	200
LF $DBC_{10\%}$ (mg)	60.17	41.04	30.48	38.96	53.12	57.96	59.96	52.82	38.97

Sartobind Q75	pH[A] at I = 20 mM			pH[A] at I = 100 mM			Ionic strength (mM) at pH 6.0				
	6.0	7.0	8.0	6.0	7.0	8.0	5	10	20	40	60
BSA $DBC_{10\%}$ (mg)	37.22	35.30	28.10	5.48	0.76	5.36	61.13	48.44	37.54	29.56	23.42

Table 2
BSA and LF flux per membrane area, selectivity at 10% breakthrough and $DBC_{10\%}$ at different flow rates using Sartobind S75 with 100 mM phosphate buffer pH 6.0 and using Sartobind Q75 with 5 mM phosphate buffer pH 6.0.

Sartobind S75				Sartobind Q75			
Flow rate ($BVmin^{-1}$)	12.0	18.0	24.0	Flow rate ($BVmin^{-1}$)	12.0	18.0	24.0
BSA flux ($gm^{-2}h^{-1}$)	370.00	544.16	728.00	LF flux ($gm^{-2}\ h^{-1}$)	140.62	224.33	287.46
Selectivity, $\alpha_{BSA/LF}$ at 10% breakthrough	147.02	89.97	123.23	Selectivity, $\alpha_{LF/BSA}$ at 10% breakthrough	70.51	69.94	76.05
LF $DBC_{10\%}$ (mg)	61.22	57.63	60.67	BSA $DBC_{10\%}$ (mg)	61.46	61.26	60.17

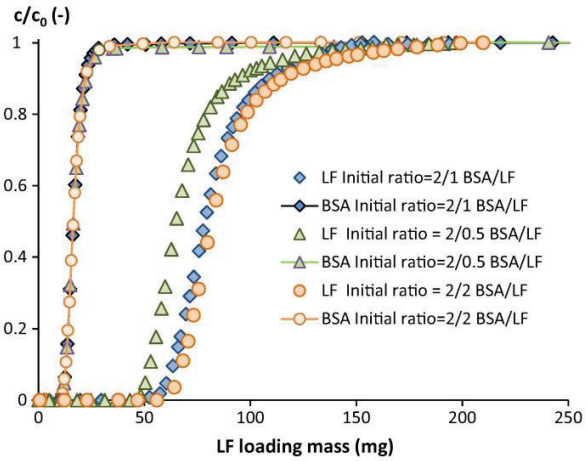

Fig. 4. Loading concentration effect on the BSA–LF mixture breakthrough curves at BSA/LF initial concentrations of 2/1, 2/0.5 and 2/2 on Sartobind S75 in 100 mM phosphate buffer with pH 6.0 at 24.0 $BVmin^{-1}$.

binding sites. The highest $V_{ef,10\%}$ was obtained at pH 6.0 (about 3.00 mL). Using a lower ionic strength phosphate buffer (20 mM), the BSA binding capacity increased (Fig. 5B).

To investigate further the effect of ionic strength, the phosphate buffer concentration was varied from 5 to 60 mM at pH 6.0 (Fig. 6). At lower buffer concentration, breakthrough occurred later and the BSA binding capacity increased. Similar shapes were obtained before 10% breakthrough, although breakthrough curves became more delayed after 10% breakthrough. Therefore, the lowest phosphate buffer concentration of 5 mM at pH 6.0 was retained for BSA/LF fractionation, providing the highest $V_{ef,10\%}$ at 30.67 mL with $DBC_{10\%}$ at 61.46 mg per device. Van Beijeren et al. [47] also reported a strong impact of ionic strength of acetate buffer on BSA adsorption behavior with a Sartobind Q device. The dynamic binding capacity decreased with increasing salt concentration due to the increased binding competition between phosphate ions and BSA for the quaternary ammonium functional groups, which has a strong interaction with the phosphate ions [48]. The values of BSA $DBC_{10\%}$ are given in Table 1 for every buffer condition.

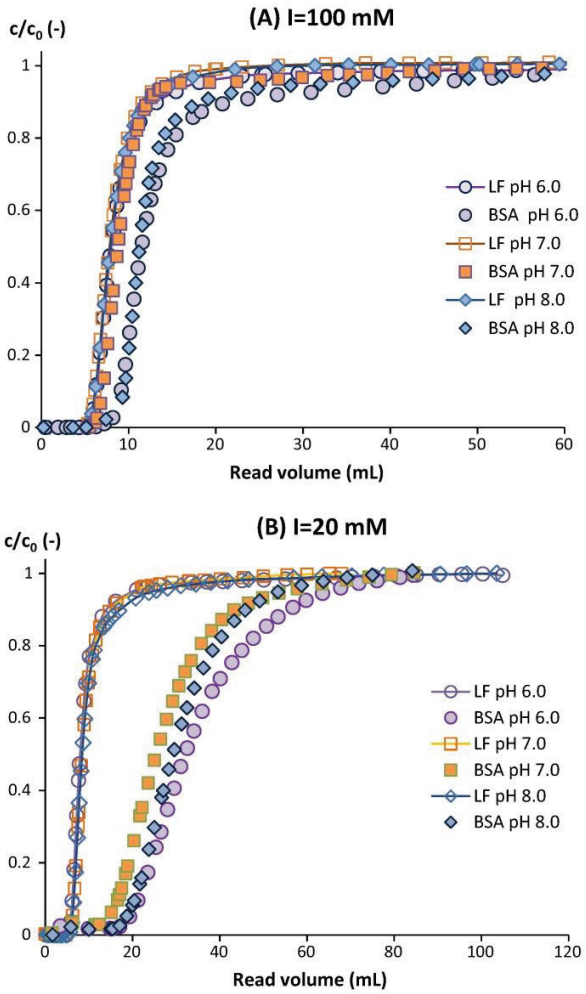

Fig. 5. pH influence on the single BSA and LF breakthrough curves on Sartobind Q75 at 12.0 $BVmin^{-1}$, 1 mg mL^{-1} LF solution and 1 mg mL^{-1} BSA solution. (A) 100 mM phosphate buffer. (B) 20 mM phosphate buffer.

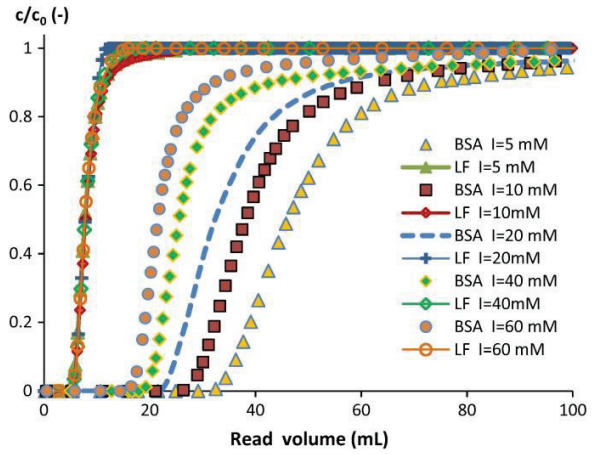

Fig. 6. Ionic strength effect between 10 mM and 100 mM phosphate buffer on the BSA–LF breakthrough curves at pH 6.0 and 12.0 BVmin^{-1} on Sartobind Q75 with a BSA/LF initial concentration of 2/1.

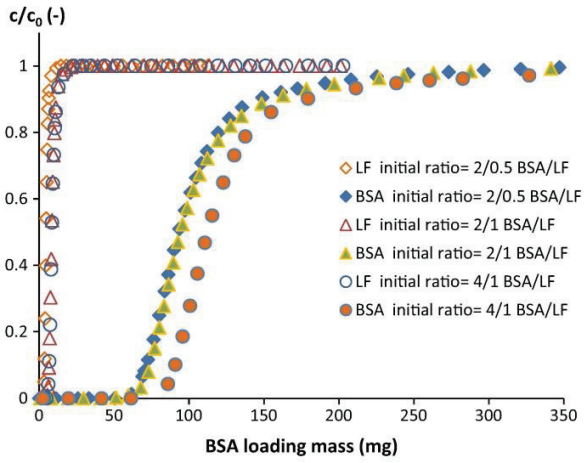

Fig. 7. Concentration effect on the BSA–LF mixture breakthrough curves in 5 mM phosphate buffer with pH 6.0 at the flow rate of 24.0 BVmin^{-1} on Sartobind Q75. The loading BSA–LF concentrations were investigated at 2/0.5, 2/1 and 4/1.

3.2.2. Influence of operating conditions

Using the cation exchange device Sartobind Q75, BSA–LF separation was performed at different flow rates of 12.0, 18.0 and 24.0 BVmin^{-1} (Supplementary material). At the different flow rates, BSA and LF breakthrough curves overlapped. This confirms that MC can be operated at high flow rates without any decrease in binding capacity and selectivity. Similar results are usually reported for BSA binding to Sartobind Q devices (for example van Beijeren et al. [47]). The highest flow rate of 24.0 BVmin^{-1} was then retained for further experiments, because of the fast BSA–LF fractionation process with high separation performance. The process performances are summarized in Table 2. The LF flux per membrane area increased from 140.62 to 287.46 L m^{-2} h^{-1}, for flow rates of 12.0 and 24.0 BVmin^{-1}, respectively. The selectivity of the LF/BSA mixture separation or $\alpha_{LF/BSA}$, was determined using Eq. (7) and found to in the range 69.94–76.05 at the various flow rates. The $DBC_{10\%}$ of BSA was unaffected by the flow rate and stayed constant about 61 mg.

The effect of BSA–LF initial concentrations was investigated at 2/0.5, 2/1 and 4/1 by plotting the breakthrough curves versus BSA loading mass (Fig. 7). At BSA/LF concentrations of 2/0.5 and 2/1, the BSA breakthrough shape and position were unaffected. When the BSA concentration was increased two-fold from 2.00 to 4.00 mg/mL, the BSA binding capacity increased as the BSA breakthrough curve occurred later. The BSA breakthrough shape was not affected by the concentration change.

3.3. Elution step

Eluent selection was investigated for LF from the cation exchange membrane and BSA from the anion exchange membrane (Table 3). All elution experiments were performed at a flow rate of 6.0 BVmin^{-1}. The optimized loading volume, $V_{ef,10\%}$, was 62.0 and 31.0 mL for Sartobind S75 and Q75 devices, respectively. With the cation exchange membrane, the ionic concentrations of 1.00 and 2.00 M NaCl in phosphate buffer pH 6.0 gave relatively low LF eluted amount. A slightly higher LF recovery was observed using phosphate buffer at pH 12.0. However, LF was not eluted using phosphate buffer pH 11.0. The addition of 25.00% ethylene glycol in phosphate buffer pH 12.0 gave the highest LF recovery (around 70.0%). This may be due to the contribution of ionic and hydrophobic interaction in LF desorption, as previously showed by Wolman et al. [30] for LF desorption from dye-membranes. With the anion exchange membrane, the eluted amount of BSA was higher with the citrate eluent pH 3.0, compared to 1.00 and 2.00 M NaCl in phosphate buffer pH 6.0. Similarly to the cation exchange device, the simultaneous effect of pH change and hydrophobic interaction gave the highest BSA recovery (over 72.00%) by adding 25.00% ethylene glycol in citrate buffer pH 3.0.

Finally, the effect of the flow rate was investigated at 6.0, 3.0 and 1.0 BVmin^{-1}. For the cation exchange device, the elution buffer was 25% ethylene glycol in phosphate buffer pH 12.0 and for the anion exchange device 25.00% ethylene glycol in citrate buffer pH 3.0. For both anion and cation exchange membranes, the eluted amount of protein increased with the decreasing flow rate (Table 4), as previously reported [30]. At the flow rate of 1.0 BVmin^{-1}, the protein recovery was about 81% and 93% for the cation and anion exchange devices, respectively. Therefore, a high

Table 3
LF and BSA desorption using different eluents on Sartobind S75 and Q75, respectively. The elution step was operated at 6 BVmin^{-1} with the eluent volume of 20 mL.

Sartobind S75	Eluent	$DBC_{10\%}$ of LF (mg)	Eluted LF mass (mg)	Eluted LF/total loading (%)
	1.00 M NaCl in phosphate buffer pH 6.0	59.44	25.99	40.61
	2.00 M NaCl in phosphate buffer pH 6.0	60.48	29.51	46.11
	Phosphate buffer pH 11.0	59.75	0.00	0.00
	Phosphate buffer pH 12.0	60.18	35.02	54.72
	25.00% ethylene glycol in phosphate buffer pH 12.0	59.60	44.76	69.94
Sartobind Q75	Eluent	$DBC_{10\%}$ of BSA (mg)	Eluted BSA mass (mg)	Eluted BSA/total loading (%)
	1.00 M NaCl in phosphate buffer pH 6.0	60.14	23.64	36.94
	2.00 M NaCl in phosphate buffer pH 6.0	61.39	25.17	39.33
	Citrate buffer pH 3.0	61.64	30.84	48.19
	25.00% ethylene glycol in citrate buffer pH 3.0	60.86	46.49	72.64

Table 4
Flow rate effect on LF and BSA eluted mass on Sartobind S75 and Q75, respectively, using the eluent with hydrophobic and pH change effect.

	Flow rate ($BVmin^{-1}$)	6.0	3.0	1.0
Eluted LF on Sartobind S75 using 25% ethylene glycol in phosphate buffer pH 12.0	$DBC_{10\%}$ of LF (mg)	59.34	59.57	60.29
	Eluted LF mass (mg)	42.87	47.10	52.43
	Eluted LF/total loading (%)	69.14	75.97	81.92
Eluted BSA on Sartobind Q75 using 25% ethylene glycol in citrate buffer pH 3.0	$DBC_{10\%}$ of BSA (mg)	60.86	62.60	62.72
	Eluted BSA mass (mg)	46.49	54.62	58.92
	Eluted BSA/total loading (%)	72.64	87.25	93.95

Table 5
Process time and LF productivity of different BSA–LF separation processes using Sartobind S75 devices.

Process conditions	Process time (min)	Productivity (mg(of LF) mL^{-1} h^{-1})
6 $BVmin^{-1}$ for all steps, except the regeneration step at 1 $BVmin^{-1}$	78.50	936.20
Different flow rates with the regeneration step at 1 $BVmin^{-1}$	78.63	1143.07
Different flow rates with the regeneration step at 3 $BVmin^{-1}$	34.19	2628.84

flow rate during the loading step and a lower flow rate during the elution step were proposed for BSA–LF mixture separation to ensure a fast process and a high protein recovery.

3.4. BSA–LF mixture separation cycles on cation exchange

Using the Sartobind S75 cation exchanger, different separation processes were tested (Table 5). The first process was operated at the same flow rate of 6.0 $BVmin^{-1}$ for the equilibrium, loading, washing and elution steps, according to Sartobind user's guide. This process led to almost the same process time as the process with optimized flow rate at each steps (24 $BVmin^{-1}$ for the loading and washing steps and 1 $BVmin^{-1}$ for the elution step). In addition, the LF productivity using 6.0 $BVmin^{-1}$ of flow rate at all steps was 936.20 mg mL^{-1} h^{-1}, whereas, using different flow rates, a higher LF productivity was obtained equal to 1143.07 mg mL^{-1} h^{-1}. This higher productivity was due to the higher LF eluted mass at the slowest elution flow rate.

However, for both methods, the processing time (around 78.50 min) was mainly attributed due to the slow regeneration step (1.0 $BVmin^{-1}$). Therefore, the BSA–LF mixture separation was further tested at the increased flow rate of 3.0 $BVmin^{-1}$ for the regeneration step. The separation was performed over 3 cycles, with very good repeatability (Fig. 8). The process time was significantly shortened to 34.19 min with an improved LF productivity of 2628.84 mg mL^{-1} h^{-1}. In our study, the productivity was much higher than the one obtained by Wolman et al. [30] using triazinic dye HE-3B-HF-II membranes for LF purification from bovine whey (252.9 mg mL^{-1} h^{-1} at combined flow rates). However, the results are difficult to compare as the LF concentration used in our study was much higher (70 folds), as well as the loaded mass of LF.

4. Conclusion

Using MC at pH between the isoelectric point of BSA and LF, separation between these two proteins was found very effective. Using the cation exchange membrane, LF was totally retained until breakthrough occurred; the higher selectivity being obtained at a strong ionic strength of 100 mM and buffer pH 6.0, with LF $DBC_{10\%}$ about 60 mg per device. At these conditions, BSA passed through the membrane and in the effluent at the optimal flux per membrane area of 728.00 g h^{-1} m^{-2}. Using the anion exchange membrane, an opposite effect was observed. Optimal BSA adsorption was obtained at mild ionic strength of 5 mM and pH 6.0, with BSA $DBC_{10\%}$ of 62.98 mg per device, while LF passed through the membrane at the optimal flux of 287.46 g m^{-2} h^{-1}.

The selectivity of LF and BSA with both anion and cation exchange membranes were independent of flow rate (between 12.0 and 24.0 $BVmin^{-1}$). This confirms the advantage of MC which

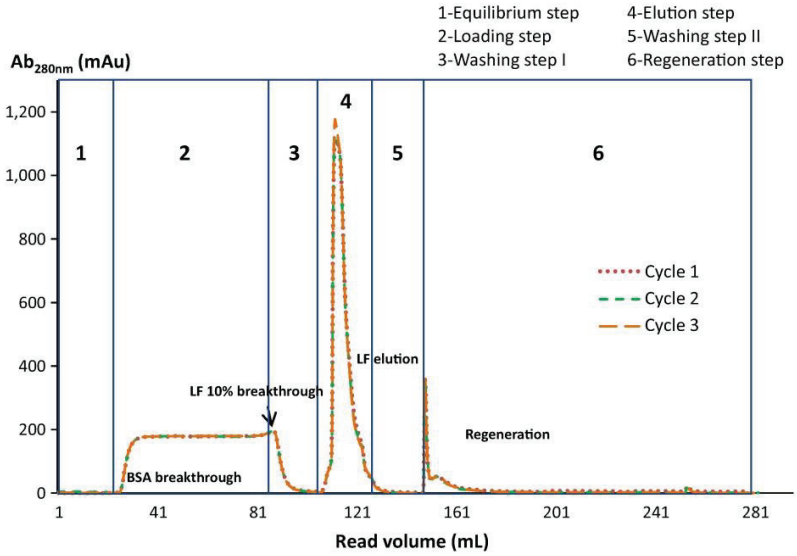

Fig. 8. BSA–LF mixture separation over three repeated cycles with the cation exchange MC Sartobind S75 at 24.0 $BVmin^{-1}$ for the loading and washing steps, 1.0 $BVmin^{-1}$ for the elution step and 3.0 $BVmin^{-1}$ for the regeneration step. The initial concentrations of BSA/LF were 2/1.

can be used at high flow rate without any loss of selectivity. In addition, the selectivity did not decrease with increasing concentration of loaded LF, and even more, the binding capacity at 10% breakthrough increased. These results suggest that high loaded concentrations can also be used.

To optimize the LF eluted mass on the cation exchange device, 25% ethylene glycol in phosphate buffer pH 12.0 was applied at the reduced flow rate of 1 $BVmin^{-1}$. At these conditions, LF recovery was around 80.0%. Similarly to the cation exchange membrane, the anion exchange membrane was tested with 25% ethylene glycol in citrate buffer pH 3.0 as the eluent, which led to the highest BSA recovery about 94.0% at the lowest flow rate of 1.0 $BVmin^{-1}$. Furthermore, the BSA–LF separation procedure using different flow rates (25.0 $BVmin^{-1}$ for the loading and washing steps and 1 $BVmin^{-1}$ for the elution step) led to a fast process and high protein recovery. Process time was shortened and productivity increased by 2-fold by changing the flow rate during the regeneration step to 3.0 $BVmin^{-1}$.

Overall, our results suggest that MC can be a very effective technique for BSA–LF mixture separation and could be applied at industrial scale. The technique could be applied also successfully to the separation of other proteins of similar size and different isoelectric points. However, for industrial applications such as whey treatment, lowering the price of the available MC devices would remain undoubtedly a major challenge.

Acknowledgement

This work was supported by Ministry of Science and Technology (MOST) of Thailand and Campus France with a doctoral scholarship for Chalore Teepakorn. The authors would like to acknowledge Erie Europe (Paris, France) from providing bovine lactoferrin.

Appendix A. Supplementary material

Supplementary data associated with this article can be found, in the online version, at http://dx.doi.org/10.1016/j.seppur.2015.07.046.

References

[1] M.L. Groves, The isolation of a red protein from milk, J. Am. Chem. Soc. 82 (1960) 3345–3350, http://dx.doi.org/10.1021/ja01498a029.
[2] B. Johanson, Isolation of an iron-containing red protein from human milk, Acta Chem. Scand. 14 (1960) 510–512.
[3] J.K. Actor, S.-A. Hwang, M.L. Kruzel, Lactoferrin as a natural immune modulator, Curr. Pharm. Des. 15 (2009) 1956–1973.
[4] A.C.M. van Hooijdonk, K.D. Kussendrager, J.M. Steijns, In vivo antimicrobial and antiviral activity of components in bovine milk and colostrum involved in non-specific defence, Br. J. Nutr. 84 (2000) 127–134, http://dx.doi.org/10.1017/S000711450000235X.
[5] M. Marchetti, C. Longhi, M.P. Conte, S. Pisani, P. Valenti, L. Seganti, Lactoferrin inhibits herpes simplex virus type 1 adsorption to Vero cells, Antiviral Res. 29 (1996) 221–231.
[6] Y. Takayama, Lactoferrin and Its Role in Wound Healing, Springer Science & Business Media, 2011.
[7] T.W. Hutchens, B. Lönnerdal (Eds.), Lactoferrin: Interactions and Biological Functions, first ed., Humana Press, Totowa, N.J., 1997.
[8] M.M.H. El-Sayed, H.A. Chase, Trends in whey protein fractionation, Biotechnol. Lett. 33 (2011) 1501–1511, http://dx.doi.org/10.1007/s10529-011-0594-8.
[9] V. Valiño, M.F. San Román, R. Ibañez, I. Ortiz, Improved separation of bovine serum albumin and lactoferrin mixtures using charged ultrafiltration membranes, Sep. Purif. Technol. 125 (2014) 163–169, http://dx.doi.org/10.1016/j.seppur.2014.01.023.
[10] M. Nyström, P. Aimar, S. Luque, M. Kulovaara, S. Metsämuuronen, Fractionation of model proteins using their physiochemical properties, Colloids Surf., A 138 (1998) 185–205, http://dx.doi.org/10.1016/S0927-7757(96)03892-7.
[11] M.C. Almécija, R. Ibáñez, A. Guadix, E.M. Guadix, Influence of pH in the recovery of lactoferrin from whey with ceramic membranes, Desalination 200 (2006) 475–476, http://dx.doi.org/10.1016/j.desal.2006.03.401.
[12] G. Brisson, M. Britten, Y. Pouliot, Electrically-enhanced crossflow microfiltration for separation of lactoferrin from whey protein mixtures, J. Membr. Sci. 297 (2007) 206–216, http://dx.doi.org/10.1016/j.memsci.2007.03.046.
[13] N. Ndiaye, Y. Pouliot, L. Saucier, L. Beaulieu, L. Bazinet, Electroseparation of bovine lactoferrin from model and whey solutions, Sep. Purif. Technol. 74 (2010) 93–99, http://dx.doi.org/10.1016/j.seppur.2010.05.011.
[14] S. Okonogi, M. Tomita, T. Tomimura, Y. Tamura, T. Mizota, Process for producing bovine lactoferrin in high purity, Google Patents. <http://www.google.com/patents/US4791193>, 1988.
[15] S. Yoshida, Ye-Xiuyun, Isolation of lactoperoxidase and lactoferrins from bovine milk acid whey by carboxymethyl cation exchange chromatography, J. Dairy Sci. 74 (1991) 1439–1444, http://dx.doi.org/10.3168/jds.S0022-0302(91)78301-X.
[16] R. Hahn, P.M. Schulz, C. Schaupp, A. Jungbauer, Bovine whey fractionation based on cation-exchange chromatography, J. Chromatogr. A 795 (1998) 277–287, http://dx.doi.org/10.1016/S0021-9673(97)01030-3.
[17] C.J. Fee, A. Chand, Capture of lactoferrin and lactoperoxidase from raw whole milk by cation exchange chromatography, Sep. Purif. Technol. 48 (2006) 143–149, http://dx.doi.org/10.1016/j.seppur.2005.07.011.
[18] Y. Liang, X. Wang, M. Wu, W. Zhu, Simultaneous isolation of lactoferrin and lactoperoxidase from bovine colostrum by SPEC 70 SLS cation exchange resin, Int. J. Environ. Res. Public Health 8 (2011) 3764–3776, http://dx.doi.org/10.3390/ijerph8093764.
[19] B. Lönnerdal, J. Carlsson, J. Porath, Isolation of lactoferrin from human milk by metal-chelate affinity chromatography, FEBS Lett. 75 (1977) 89–92, http://dx.doi.org/10.1016/0014-5793(77)80059-8.
[20] M.J. Santos, J.A. Teixeira, L.R. Rodrigues, Fractionation and recovery of whey proteins by hydrophobic interaction chromatography, J. Chromatogr. B 879 (2011) 475–479, http://dx.doi.org/10.1016/j.jchromb.2011.01.003.
[21] K. Plate, S. Beutel, H. Buchholz, W. Demmer, S. Fischer-Frühholz, O. Reif, et al., Isolation of bovine lactoferrin, lactoperoxidase and enzymatically prepared lactoferricin from proteolytic digestion of bovine lactoferrin using adsorptive membrane chromatography, J. Chromatogr. A 1117 (2006) 81–86, http://dx.doi.org/10.1016/j.chroma.2006.03.090.
[22] V. Orr, L. Zhong, M. Moo-Young, C.P. Chou, Recent advances in bioprocessing application of membrane chromatography, Biotechnol. Adv. 31 (2013) 450–465, http://dx.doi.org/10.1016/j.biotechadv.2013.01.007.
[23] M.-E. Avramescu, Z. Borneman, M. Wessling, Dynamic behavior of adsorber membranes for protein recovery, Biotechnol. Bioeng. 84 (2003) 564–572, http://dx.doi.org/10.1002/bit.10807.
[24] S.M. Saufi, C.J. Fee, Recovery of lactoferrin from whey using cross-flow cation exchange mixed matrix membrane chromatography, Sep. Purif. Technol. 77 (2011) 68–75, http://dx.doi.org/10.1016/j.seppur.2010.11.021.
[25] R. Ghosh, Protein separation using membrane chromatography: opportunities and challenges, J. Chromatogr. A 952 (2002) 13–27, http://dx.doi.org/10.1016/S0021-9673(02)00057-2.
[26] W. Noppe, F.M. Plieva, I.Y. Galaev, K. Vanhoorelbeke, B. Mattiasson, H. Deckmyn, Immobilised peptide displaying phages as affinity ligands: purification of lactoferrin from defatted milk, J. Chromatogr. A 1101 (2006) 79–85, http://dx.doi.org/10.1016/j.chroma.2005.09.064.
[27] M.R. Etzel, T. Bund, Monoliths for the purification of whey protein–dextran conjugates, J. Chromatogr. A 1218 (2011) 2445–2450, http://dx.doi.org/10.1016/j.chroma.2011.01.025.
[28] C.K. Chiu, M.R. Etzel, Fractionation of lactoperoxidase and lactoferrin from bovine whey using a cation exchange membrane, J. Food Sci. 62 (1997) 996–1000, http://dx.doi.org/10.1111/j.1365-2621.1997.tb15023.x.
[29] L. Voswinkel, U. Kulozik, Fractionation of all major and minor whey proteins with radial flow membrane adsorption chromatography at lab and pilot scale, Int. Dairy J. 39 (2014) 209–214, http://dx.doi.org/10.1016/j.idairyj.2014.06.012.
[30] F.J. Wolman, D.G. Maglio, M. Grasselli, O. Cascone, One-step lactoferrin purification from bovine whey and colostrum by affinity membrane chromatography, J. Membr. Sci. 288 (2007) 132–138, http://dx.doi.org/10.1016/j.memsci.2006.11.011.
[31] S.-Y. Suen, M.R. Etzel, A mathematical analysis of affinity membrane bioseparations, Chem. Eng. Sci. 47 (1992) 1355–1364, http://dx.doi.org/10.1016/0009-2509(92)80281-G.
[32] A. Shiosaki, M. Goto, T. Hirose, Frontal analysis of protein adsorption on a membrane adsorber, J. Chromatogr. A 679 (1994) 1–9, http://dx.doi.org/10.1016/0021-9673(94)80306-4.
[33] K.H. Gebauer, J. Thömmes, M.R. Kula, Breakthrough performance of high-capacity membrane adsorbers in protein chromatography, Chem. Eng. Sci. 52 (1997) 405–419, http://dx.doi.org/10.1016/S0009-2509(96)00426-5.
[34] C. Frerick, P. Kreis, A. Górak, A. Tappe, D. Melzner, Simulation of a human serum albumin downstream process incorporating ion-exchange membrane adsorbers, Chem. Eng. Process. 47 (2008) 1128–1138, http://dx.doi.org/10.1016/j.cep.2007.07.013.
[35] H. Yang, M.R. Etzel, Evaluation of three kinetic equations in models of protein purification using ion-exchange membranes, Ind. Eng. Chem. Res. 42 (2003) 890–896, http://dx.doi.org/10.1021/ie020561u.
[36] C. Boi, S. Dimartino, G.C. Sarti, Modelling and simulation of affinity membrane adsorption, J. Chromatogr. A 1162 (2007) 24–33, http://dx.doi.org/10.1016/j.chroma.2007.02.008.
[37] S. Dimartino, C. Boi, G.C. Sarti, A validated model for the simulation of protein purification through affinity membrane chromatography, J. Chromatogr. A 1218 (2011) 1677–1690, http://dx.doi.org/10.1016/j.chroma.2010.11.056.

[38] Sartobind® Q 75 93IEXQ42DB-12–V – Sartorius AG, (n.d.). <http://www.sartorius.com/en/product/product-detail/93iexq42db-12-v/> (accessed 10.12.14).
[39] L. Voswinkel, U. Kulozik, Fractionation of whey proteins by means of membrane adsorption chromatography, Procedia Food Sci. 1 (2011) 900–907, http://dx.doi.org/10.1016/j.profoo.2011.09.136.
[40] M.-S. Chun, S.-Y. Lee, S.-M. Yang, Estimation of zeta potential by electrokinetic analysis of ionic fluid flows through a divergent microchannel, J. Colloid Interface Sci. 266 (2003) 120–126, http://dx.doi.org/10.1016/S0021-9797(03)00576-9.
[41] L. Sánchez, P. Aranda, Md. Pérez, M. Calvo, Concentration of lactoferrin and transferrin throughout lactation in cow's colostrum and milk, Bio. Chem. Hoppe-Seyler 369 (1988) 1005–1008.
[42] R.J. Harmon, F.L. Schanbacher, L.C. Ferguson, K.L. Smith, Concentration of lactoferrin in milk of normal lactating cows and changes occurring during mastitis, Am. J. Vet. Res. 36 (1975) 1001–1007.
[43] J.M. Steijns, A.C.M. van Hooijdonk, Occurrence, structure, biochemical properties and technological characteristics of lactoferrin, Br. J. Nutr. 84 (2000) 11–17, http://dx.doi.org/10.1017/S0007114500002191.
[44] C. Baldasso, T.C. Barros, I.C. Tessaro, Concentration and purification of whey proteins by ultrafiltration, Desalination 278 (2011) 381–386, http://dx.doi.org/10.1016/j.desal.2011.05.055.
[45] K.W.K. Yee, D.E. Wiley, J. Bao, Whey protein concentrate production by continuous ultrafiltration: operability under constant operating conditions, J. Membr. Sci. 290 (2007) 125–137, http://dx.doi.org/10.1016/j.memsci.2006.12.026.
[46] V. Valiño, M.F. San Román, R. Ibáñez, J.M. Benito, I. Escudero, I. Ortiz, Accurate determination of key surface properties that determine the efficient separation of bovine milk BSA and LF proteins, Separ. Purif. Technol. 135 (2014) 145–157, http://dx.doi.org/10.1016/j.seppur.2014.07.051.
[47] P. van Beijeren, P. Kreis, T. Zeiner, Ion exchange membrane adsorption of bovine serum albumin—Impact of operating and buffer conditions on breakthrough curves, J. Membr. Sci. 415–416 (2012) 568–576, http://dx.doi.org/10.1016/j.memsci.2012.05.051.
[48] C. Teepakorn, K. Fiaty, C. Charcosset, Effect of geometry and scale for axial and radial flow membrane chromatography—Experimental study of bovin serum albumin adsorption, J. Chromatogr. A 1403 (2015) 45–53, http://dx.doi.org/10.1016/j.chroma.2015.05.023.